

Intracellular recording of cardiomyocyte action potentials with nanopatterned volcano-shaped microelectrodes

Présentée le 29 mai 2020

à la Faculté des sciences et techniques de l'ingénieur
Laboratoire de microsystemes 4
Programme doctoral en microsystemes et microélectronique

pour l'obtention du grade de Docteur ès Sciences

par

Benoît Xavier Emmanuel DESBIOLLES

Acceptée sur proposition du jury

Prof. S. Lacour, présidente du jury
Prof. Ph. Renaud, Prof. S. Rohr, directeurs de thèse
Prof. A. Hierlemann, rapporteur
Prof. N. Melosh, rapporteur
Prof. G. Villanueva, rapporteur

*To my father Georges, my mother Isabelle, my sister Olivia,
and to Marta, the most significant finding of this thesis.*

Acknowledgments

Against all expectations, a PhD thesis is not an individual experience but it is a team effort where numerous contributors bring a stone to the edifice and make it resplendent. Yet, I'll be the only one receiving the honors in the end of this wonderful journey. In this section, I intend to sincerely acknowledge each person who contributed to this adventure and give them the credit they deserve.

My deepest gratitude goes to my thesis director Professor Philippe Renaud who gave me the fabulous opportunity to conduct experimental research in the field of micro-nanotechnologies at LMIS4 for several years. Philippe is not only a talented and distinguished scientist, but he is also extremely attentive to the needs related to his team members. Throughout these years, Philippe gave me the ideal amount of freedom allowing me to explore numerous opportunities for my research, while always being incredibly supportive and providing valuable scientific inputs when needed.

It was also a great privilege to work with my thesis co-director Professor Stephan Rohr who is an outstanding open-minded electrophysiologist always enthusiastic for novel technological developments. Stephan taught me, *inter alia*, how to rigorously conduct electrophysiological experiments, interpret scientific data, and report these results in journal articles by investing considerable time into carefully correcting my manuscripts in an incredibly efficient manner.

Special thanks go to my jury members Prof. Lacour, Prof. Villanueva, Prof. Hierlemann, and Prof. Melosh for their availability and for taking the time to evaluate my work.

During this journey, I had the opportunity to work with talented collaborators that made the achievements presented in this thesis possible. I sincerely thank Etienne de Coulon from Bern University for the countless hours we spent together in front of the monitors talking about life while waiting for the slightest perturbation of the signal baseline that would hypothetically justify our investment. Etienne is an exceptional

scientist with a huge experience in multiple fields of science and above all, he is a truly good person and friend. I could not expect a better fellow to share this thesis with. I also wish to thank Regula Flückiger and Christian Dellenbach, both from Bern University, for their decisive help, contagious enthusiasm, and precious comments during experimental procedures. I deeply thank Prof. Georg Fantner from the Laboratory for Bio- and Nano-instrumentation at EPFL for his supervision related to atomic force microscopy (AFM), and particularly his PhD student Mélanie Hannebelle for her impressive AFM skills and for all the time she spent behind the microscope throughout the years, desperately trying to correct for the imperfections of the chips I was providing. Thanks to Rodrigo de Campos Perin from the Laboratory of Neural Microcircuitry for the fruitful discussions related to neuronal electrophysiology as well as Anne-Laure Mahul and Elena Gasparotto from the Laboratory of Molecular Neurobiology and Neuroproteomics for their precious help related to the neuron isolation procedure and culture.

I wish to truly thank Arnaud Bertsch for the countless eye-opening discussions we had together over the years: Why is innovation better rewarded than optimization? Why playing Chopin in 2020 is boring? How can we optimize our diet to achieve a performance in sport? Is tennis a sport? What about tennis shorts in the lab? Can we consider yoga as a religion? What is the real meaning of the tragedy of Hamlet? To any of the points raised above, Arnaud could provide an atypical detailed answer supported by a robust argumentation. He taught me how to observe and have a critical look at the world we are living in, in a manner independent from society. Arnaud played a pivotal role during my thesis whose numerous contributions include creative scientific inputs, precious strategic advices, efficient and high-quality proofreading of my manuscripts, and well-targeted motivational support. I sincerely thank Arnaud Bertsch for having been an incredible mentor over the years and for having done much more than one could ask for.

For the past year, I had the chance to work and interact with Nicolas Maino who will ensure the continuity of my work. Nicolas is an exceptional hard working junior researcher with a remarkable motivation who was instrumental during this last year. His contribution to my thesis was tremendous whether throughout fruitful discussions or services provided in the clean room during high throughput manufacturing periods. I warmly thank Nicolas Maino for being such a great person and friend.

At EPFL, we benefit from astonishing user facilities where we can be trained by experts at the individual level, get access to state-of-the-art instruments, and receive a personal feedback related to our application. A big thank to these platforms that

include the Bioimaging and Optics Platform (BIOP), the Interdisciplinary Center for Electron Microscopy (CIME), and the Atelier de l'institut des Matériaux (ATMX). Especially, I wish to thank Jean-Marc Buchs, Jean-Marie Barblan, Peter Brühlmeier, and José Garciacano from the Atelier de fabrication de Circuits Imprimés (ACI) for their outstanding support related to PCB manufacturing. Warm thanks go to Roland Dupuis and Manuel Leitons from the Atelier de Fabrication Additive (AFA) for kindly sharing their remarkable experience in the field of 3D printing, for manufacturing parts with impressive precision, and for always being ready to help. Finally, my deepest gratitude goes to every single staff member of the EPFL Center of Micronanotechnology (CMi). Throughout these years, I add the wonderful opportunity to spend a considerable amount of time in one of the best academic clean room in the world run by a team of amazing people. I truly thank Julien Dorsaz, Georges-André Racine, Kaspar Suter, and Niccolo Piacentini from the photolithography team for the countless hours spent in front of the VPG200. A big thank to the etching team composed of Cyrille Hibert, Joffrey Pernollet, and Rémy Juttin for rescuing my wafer from the IBE350 day after day. Thanks to Guy Clerc, and Philippe Langlet from the thin films squad for allowing me un-conventional deposition processes. I would like to unconditionally thank Giovanni Monteduro, Patrick Maldiger, Miguel Marmelo, and Jean-Marie Voirol from the equipment team for always fixing the tools after I broke them. Warm thanks to Zdenek Benes for sharing his expertise in electron microscopy as well as his enthusiasm for the CMi photocontest, and to Didier Bouvet for the numerous rescue missions at the AFM. My deep sympathy goes to the interfacing team including Adrien Toros and particularly Giancarlo Corradini for properly handling “la crème de la crème”. A big thank to the logistic team composed of Gatera Kumuntu, Adin Ferhatovic, and Audrey Berset for always bringing on time my last minute orders. Finally, I thank Philippe Flückiger, Marie-Noëlle Verhar, and Céline Cornaz Brébant for running this incredible facility.

The LMIS4 team was an incredible source of motivation throughout the years. Special thanks go to David Bonzon for the countless pieces of advice in electronics, Guillaume Petit-Pierre for being a great source of inspiration, David Forchelet for his unrivalled mental strength, Stefano Varricchio for his subtle jokes, Clarisse Vaillier for her precious help with the cell culture, Richard Meunier for his serenity, Camille Railon for her optimism, Jonathan Cottet for showing me another side of the academic work, Ludovic Serex for making it happen and for always being way too honest, Margaux Duchamp for her unwavering patience in the cell culture room and her distinct skill for handling high voltage sources, Joan Teixidor for being the best muchacho one could ask for, William Courbat for sharing great memories about Berkeley, Fatemeh

Navee for always being willing to help, Thamani Dahoun for her enthusiasm in the laboratory, Jiande Zhou for sharing pieces of her microfluidic setup, and Clementine Lipp for appreciating good clean room work. I wish to also thank the new comers Daniel Migliozi for sharing his Italian culinary experiences, Miguel Solsona for giving me a lesson of humility every Sunday, Lucas Yerly for sharing interesting facts about almost everything, Albert Leroy for bringing happiness in the laboratory, Victor Steininger and Paul Philipp for reassuring me about the rents in Boston, and Colin for being such a good skier. An additional big thank to the startupper Georges Muller, Luc Aeberli, Amélie Bédier, Patrick Burch, Marc Boers, Elodie Dahan, and Dominik Ziegler for all the fruitful and motivating discussions. Special thanks go to the iconic people from LMIS4 Thomas Braschler for sharing his passion of science with such a pleasure, Marc Heuschkel for his precious help at the early stage of my thesis, Harald Van Lintel for the countless distrelec orders, and Sebastien Jiguet for always being enthusiastic and supportive, even while snowboarding with an alpine surf at le Pas de Chavanette, and for being such a great person. I sincerely thank Christine Vuichoud and Lucie Auberson for being incredibly supportive and for doing an outstanding work. I also thank my students Elisabetta Messina, Arnaud Buxtorf, André Dos Santos, Quentin Wannebroucq, Shahriar Shallilel, Pietro Airaghi, and Mathieu Aberle for their important contribution to this thesis. I also wish to warmly thank the members of the neighbouring laboratories LMIS1, LMIS2, NAM, LNE, ANEMS, and BIOS for their direct or less direct contribution to this work.

Throughout these years, I received an incredible support from my friends. I truly and deeply thank my dearest friend Thibault Asselborn for his irreplaceable daily contribution to the team des étoiles for nearly ten years now. Thibault is an incredibly talented person showing impressive skills in basically every field one could possibly imagine, ranging from science to sport passing by music and philosophy but above all, he truly is a great person and an outstanding friend. Since the first week of my bachelor, he pushed me to get better, taught me how to address problems in a singular manner, gave me countless lessons of humility in tennis, ping pong, badminton, and even ski, made me discover Châtel and hate Le Schuss. Together, we experienced so many adventures ranging from crossing the Lemman lake on a fuming sailing boat (without wind) to exploring scary (if not deadly) hostels in Athens, passing by playing plants vs zombies in Hong Kong or eating way too hot bibimbap in South Korea. I take this opportunity to sincerely thank Thibault Asselborn for having positively influenced who I am and for being such a supportive and inspiring brother. I am looking forward to our next adventures. I wish to deeply thank Walid Amanhoud for showing me what it truly means to never give up over the entire duration of our studies. Walid is

an impressive hard working person who was never afraid of facing difficult challenges while showing a remarkable sense of values at all times. He has been an incredible support starting from the first exercise session of Analyses during my Bachelor's first year, up to the development of the particle swarm optimization algorithm presented in my thesis. There is no doubt I would not have made it without him. A big thank to Matthias Neuenschwander for always appreciating whether a cheerful ski excursion in Bürchen or an intense tennis session at lunch break and especially for being such a great Swiss person. Special thanks go to the talented member of the "LUC-ping pong", Thomas Debarre, and to the inspiring leader of the "LUC-AOE", Timon Ganguillet. Thank you also to my childhood friends for all the good times spent together.

To conclude, my deepest gratitude goes to my family. I profoundly thank my parents Georges and Isabelle Desbiolles for their unconditional love and support throughout the years. Thank you for the countless sacrifices you made without hesitation for the sole purpose of giving me the wonderful opportunity to do what I love in my daily life. Thank you Dad for transmitting me your passion for technology and innovation, for showing me every day what hard working truly means, for proving me that it is the key to wonderful achievements, for the countless hours we spent together in Nature, for sharing its beauty with me, and for demonstrating me how to move forward in times of need. Thank you Mom for the innumerable kind attentions, for the countless hours spent together reciting my homework or tapping the pen in rhythm while practicing my solfège, for giving me the taste of discovering new cultures across the globe, for encouraging me to learn foreign languages since my earliest age, for showing me every day what courage and perseverance truly means, for explaining me that not everything is black or white in this world, and for wisely teaching me the surprisingly strong power of trade-offs in my daily life. A thousand thanks to both of you for being such kind, funny, and wonderful parents as well as my inspiring role models. I also wish to deeply thank my sister Olivia Desbiolles for all the trust she put in me since my earliest age. Thank you for all the wonderful adventures we had together as kids including building outstanding tree houses, imagining terrifying ghost trains, or performing incredible swing shows worthy of Broadway, for being such a kind and thoughtful person, for taking such a good care of our family, including me, and for being an unwavering support at any time without asking anything in return. I sincerely thank you for being the outstanding big sister who helped me so much becoming who I am. An additional big thank to Emilio Rodriguez for being a great and generous person always willing to make us enjoy a good meal. I also thank my grandparents Louis Desbiolles for the countless hours spent together seated on the famous bench of Sery, Georgette Desbiolles for being an example of combativity, Maurice Engilberge for teaching me

the strength of memories, and Marguerite Engilberge for the countless kind attentions which include the eagerly awaited weekly chocolate cake. Special thanks go to my uncles and aunts William and Chantal Métral, and Claude and Bernadette Engilberge for the long-standing support and the wonderful moments spent together. I also wish to thank my cousins Maryline and Mickaël Maulet, Christelle and Lionel Jacquemoud, Hervé and Christelle Métral, Marlène and Matthieu Buzzolini, Sylvain and Marine Engilberge, Martin Engilberge, and their respective kids for making our family such a resourceful environment. Special thanks go to Méline Buzzolini for bringing some very special light into my life. Additional thanks go to Isabelle Issert and her family. I sincerely thank my in-laws Cristina Airaghi, for her wonderful hospitality and joie de vivre, Sergio Dellafontana for always appreciating whether an intense ski session or a ping pong challenge, Maria Airaghi for cheering me up with chocolate based candies, and Pietro Airaghi for always doing du “bon boulot”. A big thank to the Italian family Gianmaria and Jole Airaghi, Gianluca Airaghi, Andrea and Renata Airaghi, Stefania and Mario Botto, Davide and Anca Airaghi, Daniela and Lorenzo Calamita, Matteo and Giulia Airaghi, and their respective children as well as Cesare Leccardi for welcoming me warmly.

I wish to conclude this section by sincerely acknowledging the most fascinating discovery of my PhD thesis, Marta Airaghi Leccardi, for being such a marvellous and unique partner of life. Over the last four years, you listened every single day to my derisory work concerns and helped me solving the most challenging ones with your incommensurable creativity. Thank you for your unconditional support, for having remarkably helped me evolve toward the person I am today, and for making me laugh every single day whether by explaining me the true meaning of a cagouille, or by cheerfully interpreting your last favourite song of Patrick Sebastien. Thank you also for always breaking the monotony by coming with the most unexpected and exciting ideas, for admirably taking care of the people we love, for the countless kind attentions including the always appreciated croissant Cailler and the sometime necessary pair of pants, and especially for making me discover another way of loving. I truly love your deep passion for Nature, your beautiful mind associated with your singular personality, your extraordinary perseverance in never giving up, as well as this touching sensibility and kindness which defines you. Together, we already experienced exceptional adventures across the globe ranging from getting attacked by an homeless in San Francisco to almost diving with manta rays off the coasts of Indonesia, and passing by our greatest success, raising giant rabbits in a 2.5 rooms apartments in Lausanne. I am truly proud to share my life with you, Gaston, Mignolo, and even Pépito, and I am looking forward to the inspiring future we’ll build together.

Abstract

Micro-nanotechnology based multielectrode arrays have led to remarkable progress in the field of transmembrane voltage recordings of excitable cells. However, electrode geometries alone have failed to produce a cell-electrode interface that is sufficiently robust and stable over extended periods of time to perform high-quality electrophysiological recordings. This thesis addresses the current limitations of micro-nanoelectrode arrays with a particular focus on whether patterning protruding microelectrodes with nanometer-wide biomimetic self-assembled monolayers that fuse with the cell membrane, significantly improves the quality of the electrophysiological recordings when compared to state-of-the-art technology.

The first step involved developing a novel nanofabrication process exploiting the sputtering of photoresist sidewalls during Ar^+ ion beam etching to rapidly manufacture sub-100-nm complex multimaterial nanostructures at the wafer scale.

Ion beam etching redeposition was subsequently used to manufacture a novel nanopatterned volcano-shaped microelectrode (nanovolcano) array integrating most of the recent technological advances from the literature into an original structure. Electrophysiological studies on neonatal rat cardiomyocyte monolayers demonstrated that nanovolcanoes enabled *in vitro* electroporation-free intracellular recordings of cardiomyocyte action potentials. The recordings lasted more than one continuous hour with amplitudes as high as 20 mV from nearly 30 % of the device's channels.

The second phase investigated whether the use of electroporation improved the performance of nanovolcano arrays in terms of action potential amplitudes, recording durations, and yields. Experiments with neonatal rat cardiomyocyte monolayers grown on nanovolcano arrays showed that electroporation increased the efficiency of nanovolcano recordings as it enabled on-demand multiple registration of intracellular action potentials with amplitudes as high as 62 mV and parallel recordings in up to approximately 76 % of the available channels over consecutive days. The performance of nanovolcanoes showed no dependence on the presence of functional nanopatterns,

indicating that the tip geometry itself was instrumental for establishing the tight seal at the cell-electrode interface. These results suggest that nanovolcanoes could prove useful not only for basic research but also for comprehensive drug testing in cardiac research.

Preliminary studies performed with hippocampal neonatal rat neurons demonstrated that nanovolcano arrays permit the recording of non-attenuated neuronal action potentials in addition to, potentially, subthreshold activity featuring a high signal-to-noise ratio. These results expand the function of nanovolcano arrays to other kinds of electrogenic cells and open new avenues for the field of neuroscience.

During an exploratory phase, a nanovolcano electrode was integrated at the tip of a suspended cantilever (nanovolcano probe) to conduct combined-force electrophysiological recordings. Proof-of-concept experiments on neonatal rat cardiomyocytes demonstrated that extracellular field potentials and contraction displacement curves could be recorded simultaneously. These features render the nanovolcano probe especially suited for mechanobiological studies aiming at linking mechanical stimuli to the electrophysiological responses of single cells.

Keywords: Multielectrode array, on-demand intracellular electrophysiology, nanovolcano, biomimetic nanopattern, electroporation, neonatal rat cardiomyocyte, mechanobiology, scanning probe microscopy, nanofabrication, ion beam etching redeposition.

Résumé

Suite à l'essor des micro-nanotechnologies, les matrices d'électrodes microfabriquées ont apporté de réels progrès pour l'enregistrement du potentiel transmembranaire de cellules excitables. Pourtant, les approches basées uniquement sur la géométrie des électrodes n'ont malheureusement pas permis de garantir un couplage suffisant avec la cellule pour permettre des mesures de qualité. Cette thèse vise à adresser les limitations des matrices de micro-nanoélectrodes en étudiant dans quelle mesure la nanostructuration de couches biomimétiques sur une microélectrode tridimensionnelle améliore de façon significative la qualité des signaux électrophysiologiques mesurés par comparaison avec les technologies existantes.

Dans un premier temps, ce travail propose un nouveau procédé de nanofabrication exploitant la redéposition de matériaux sur les flancs de résine photosensible par gravure ionique. Ceci permet la fabrication de nanostructures complexes composées de plusieurs matériaux en grand nombre.

La redéposition par gravure ionique est ensuite utilisée pour réaliser un nouveau type de matrice de microélectrodes en forme de volcan (nanovolcan) qui intègre la plupart des avancées technologiques décrites dans la littérature. Des études électrophysiologiques réalisées sur des cardiomyocytes de rats ont démontré que les nanovolcans permettent l'enregistrement spontané de potentiels d'action de cardiomyocytes *in vitro*, avec des amplitudes allant jusqu'à 20 mV pour 30 % des canaux composant le dispositif, pour une durée supérieure à une heure.

Dans un second temps, ce travail se propose de rechercher dans quelle mesure l'électroporation améliore les performances des matrices de nanovolcans. Des études réalisées sur des cardiomyocytes de rat ont démontré que, suite à l'électroporation, les nanovolcans ont permis l'enregistrement sur demande des potentiels d'action intracellulaires avec des amplitudes allant jusqu'à 62 mV simultanément depuis environ 76 % des canaux disponibles, et ce pendant plusieurs jours consécutifs. La performance des matrices de nanovolcans n'a montré aucune dépendance vis à vis de la présence de

la monocouche moléculaire structurée à l'échelle nanométrique, indiquant ainsi que la géométrie du nanovolcan est instrumentale pour établir un fort couplage au niveau de l'interface cellule-électrode. Les matrices de nanovolcans ouvrent de nouvelles perspectives dans le domaine de la recherche fondamentale ainsi que pour le profilage pharmacologique destiné à lutter contre les maladies cardiovasculaires.

Des études préliminaires conduites sur des neurones d'hippocampe de rat ont démontré que les matrices de nanovolcans ont permis l'enregistrement de potentiels d'action neuronaux non-atténués ainsi que, potentiellement, d'activités électriques sous le seuil de génération de potentiels d'action. Ces résultats ouvrent ainsi de nombreuses opportunités dans le domaine des neurosciences.

Dans un contexte plus exploratoire, un nanovolcan a été intégré à la pointe d'une poutre suspendue (sonde nanovolcan) pour accomplir des mesures combinées de forces et de signaux électrophysiologiques. Des mesures de potentiels extracellulaires ainsi que des déplacements sub-micrométriques ont été simultanément mesurés lors de contractions de cardiomyocytes de rat. Ces observations rendent la sonde nanovolcan particulièrement adaptée aux études mécanobiologiques qui visent à lier des stimuli mécaniques aux réponses électrophysiologiques de cellules uniques.

Mots clefs : Matrice d'électrodes, électrophysiologie intracellulaire sur demande, nanovolcan, structuration biomimétique, électroporation, cardiomyocyte de rat néonatal, mécanobiologie, microscopie-sonde à balayage, nanofabrication, redéposition par gravure ionique.

Contents

Acknowledgments	v
Abstract	xi
Résumé	xiii
List of Figures	xxi
List of Tables	xxiii
List of Abbreviations	xxv
List of Symbols	xxix
1 Introduction	1
1.1 Scope of the thesis	1
1.2 Electrophysiological methods: state-of-the-art	2
1.2.1 A brief history of electrophysiology	2
1.2.2 The patch clamp technique	8
1.2.3 Optical electrophysiology	13
1.2.4 Multielectrode arrays	18
1.3 Thesis positioning	31
1.3.1 Problem definition	31
1.3.2 Thesis objectives	31
1.3.3 Thesis structure	32
2 Ion beam etching redeposition for 3D multimaterial nanostructure manufacturing	33
2.1 Introduction	33

2.2	Results	35
2.2.1	Single-material nanostructures	35
2.2.2	Multimaterial nanostructures	37
2.2.3	Complex nanostructures	40
2.3	Discussion and applications	43
2.3.1	Biosensing	44
2.3.2	Nanofluidics	45
2.3.3	Nanophotonics	45
2.4	Conclusion	45
2.5	Materials and methods	46
2.5.1	Fabrication of multilayered structures	46
2.5.2	Electron microscopy	46
3	Nanopatterned volcano-shaped microelectrode arrays for spontaneous intracellular recording of cardiomyocyte action potentials	49
3.1	Introduction	49
3.2	Results	51
3.2.1	Microfabrication	51
3.2.2	Electrochemical characterization of the electrode - electrolyte interface	54
3.2.3	Recording system and interfacing optimization for electrophysiological measurements	59
3.2.4	Intracellular action potential recording from networks of cardiomyocytes with nanovolcano arrays	62
3.2.5	Dependence of APD ₅₀ on the frequency of spontaneous activity	64
3.2.6	Stability of nanovolcano recordings	65
3.2.7	Nanovolcano recordings: durations, signal amplitudes, and yield per device	66
3.2.8	Re-use of nanovolcano arrays	67
3.3	Discussion	68
3.4	Conclusion	71
3.5	Materials and methods	71
3.5.1	Microfabrication	71
3.5.2	Device preparation	72
3.5.3	Isolation and culture of primary rat cardiomyocytes	73

3.5.4	Electrophysiology	73
4	Controlled electroporation for long-term on-demand registration of cardiomyocyte action potentials with nanovolcano arrays	75
4.1	Introduction	75
4.2	Results	77
4.2.1	Electroporation modelling	77
4.2.2	Influence of the functionalized nanopattern on electrophysiological recordings made with nanovolcano arrays	80
4.2.3	Effect of the electroporation voltage amplitude on the quality of electrophysiological measurements	83
4.2.4	Long-term on-demand recordings with nanovolcano arrays	84
4.3	Discussion	86
4.3.1	Optimizing the electroporation parameters	86
4.3.2	Performance of functionalized vs. non-functionalized nanovolcano tips	87
4.3.3	Effects of repetitive electroporations	88
4.3.4	On-demand intracellular access for long term recordings	89
4.3.5	Comparison to other micro-nanotechnology based electrode arrays granting intracellular access	89
4.3.6	Limitations of the study and outlook	90
4.4	Conclusion	90
4.5	Materials and methods	91
4.5.1	Microfabrication	91
4.5.2	Device preparation	91
4.5.3	Isolation and culture of primary rat cardiomyocytes	92
4.5.4	Electroporation procedure	92
4.5.5	Electrophysiology	92
4.5.6	Data analysis	92
5	Volcano-shaped SPM probe for combined force-electrogram recordings from cardiomyocytes	95
5.1	Introduction	95
5.2	Results	97
5.2.1	Microfabrication and interfacing	97
5.2.2	Electrochemical characterization	100

5.2.3	Force and electrical measurements on rat cardiomyocytes	102
5.2.4	Recording of cardiomyocyte contraction displacements using the nanovolcano probe	104
5.2.5	Simultaneous recording of contraction displacements and electrogram from cardiomyocytes using the nanovolcano probe . . .	106
5.3	Discussion	107
5.4	Conclusion	109
5.5	Materials and methods	109
5.5.1	Microfabrication	109
5.5.2	Interfacing	111
5.5.3	Electrodeposition of platinum-black	111
5.5.4	Isolation and culture of primary rat cardiomyocytes	111
5.5.5	Device functionalization	112
5.5.6	Combined AFM-optical recordings	112
5.5.7	Electrophysiology	113
6	Intracellular recording of neuron action potentials with nanovolcano arrays: preliminary results	115
6.1	Introduction	115
6.2	Results	116
6.2.1	Spontaneous insertion of nanovolcanoes into neurons	116
6.2.2	Electroporation with nanovolcano arrays on neurons	118
6.2.3	Neuronal culture optimization: glial cell proliferation inhibition	120
6.3	Discussion	121
6.4	Conclusion	122
6.5	Materials and methods	123
6.5.1	Microfabrication	123
6.5.2	Device preparation	123
6.5.3	Isolation procedure and culture of hippocampal neonatal rat neurons	123
6.5.4	Electrophysiology	124
6.5.5	Immunostaining	124
7	Conclusion and perspectives	125
7.1	Summary of performed research	125

7.2	Limitations	126
7.3	Outlook and perspectives	127
7.3.1	Performance improvements	127
7.3.2	Potential opportunities for academia	128
7.3.3	Potential opportunities for the pharmacological industry	130
7.3.4	Perspectives, at a more distant horizon	131
Appendices		133
A Supplementary information related to Chapter 2		135
A.1	Diversity in the shape of nanostructures manufactured by ion beam etching redeposition	135
B Supplementary information related to Chapter 3		137
B.1	Stabilizing the cell-electrode interface by nano-patterning	137
B.2	Modeling of the cell-electrode interface	138
B.3	Effect of the recording system, R_{Seal} , and C_{Stray} on signal shape	141
C Supplementary information related to Chapter 4		143
C.1	Evolution of the signal amplitude with time after electroporation	143
D Supplementary information related to Chapter 5		145
D.1	Setup for simultaneous optical imaging, force, and electrical recordings	145
Bibliography		147
List of publications		177
CV		179

List of Figures

1.1	Exorcising the animal spirit	3
1.2	The instrumental period	5
1.3	The Hodgkin-Huxley model	7
1.4	The patch clamp technique	9
1.5	Optical electrophysiology	14
1.6	Planar microelectrode arrays	19
1.7	Cell-electrode interface model	23
1.8	Optimization of intracellular recording with nanoelectrodes	27
2.1	Structures created by Si redeposition on photoresist sidewalls during Ar^+ ion beam etching	36
2.2	Smoothing of the nanostructure surface roughness by photoresist reflow	37
2.3	Multilayered structures created by the redeposition of different materials	38
2.4	Fast Fourier transform pattern analysis of high resolution TEM images	40
2.5	Complex nanostructures manufactured by the redeposition of several materials	42
2.6	Additional multimaterial complex nanostructures made by Ar^+ ion beam etching	43
3.1	Concept and microfabrication of nanovolcanoes	52
3.2	Layout of the multielectrode array	53
3.3	Multielectrode array assembly	54
3.4	Electrode-electrolyte interface	55
3.5	Recording system and interfacing	60
3.6	Intracellular recording of action potentials from primary rat cardiomyocyte monolayer	63
3.7	APD restitution	65

3.8	Change of action potential shape during continuous recordings by a nanovolcano	66
3.9	Performance of nanovolcano arrays	67
4.1	Electroporation model	79
4.2	Influence of the functionalized Au nanopattern on nanovolcano performance	82
4.3	Effect of electroporation voltage amplitude on the success of intracellular nanovolcano recordings	84
4.4	Long-term recording with non-patterned nanovolcano arrays	85
5.1	Concept and microfabrication of the nanovolcano probe	98
5.2	Mechanical and electrical interfacing of the nanovolcano probe	100
5.3	Electrochemical characterization of the nanovolcano probe	101
5.4	Force and electrical measurements on rat cardiomyocytes	104
5.5	Recording of contraction displacements from rat cardiomyocytes	105
5.6	Simultaneous recording of cardiomyocyte contraction displacements and electrograms	106
6.1	Passive intracellular recording of action potentials from primary rat hippocampal neurons	117
6.2	Intracellular recording of action potentials from primary rat hippocampal neurons after electroporation	119
6.3	Influence of cytosine arabinoside (Ara-C) on glial cells proliferation	120
A.1	Structures of various shapes made by Si redeposition on photoresist sidewalls during Ar ⁺ ion beam etching	136
B.1	Influence of the nanopattern at the cell-electrode interface	138
B.2	Modeling of the cell-electrode interface and of the effect of the recording system	139
C.1	Action potential amplitude temporal evolution after electroporation	144
D.1	Description of the custom AFM-optical system	146

List of Tables

1.1	Summary of the current micro-nanoelectrode arrays features and recording characteristics	30
2.1	Summary of successfully manufactured Si cylinder dimensions	36
2.2	Composition of the redeposited layers presented in Figure 2.3-H measured by EDX	39
2.3	Summary of the redeposition ratios and rates for Si, Ti, and Pt during ion beam etching using Ar ⁺ ions	40
3.1	Theoretical and experimental values of every element composing the electrical equivalent circuit of the electrode-electrolyte interface	58
3.2	Technical specifications of the HS36 headstage used with the Digital Lynx SX acquisition system	61
4.1	Values of the elements composing the electrical equivalent circuit of the electrode-electrolyte interface	78
4.2	Summary of features of transmembrane voltage measurements with micro-nanoelectrodes in primary rat cardiomyocyte monolayers	90
5.1	Experimental values of every element composing the electrical equivalent circuit of the nanovolcano probe electrode-electrolyte interface	101

List of Abbreviations

2D	Two-dimensional
3D	Three-dimensional
ADC	Analog-to-digital converter
AFM	Atomic force microscopy
Al	Aluminium
AP	Action potential
APA	Action potential amplitude
APD₅₀	Action potential duration at 50% repolarization
Ar⁺	Argon ion
Ara-C	Cytosine arabinoside
Au	Gold
BSA	Bovine serum albumin
Ca²⁺	Calcium ion
CCI	Chemical calcium indicator
CL	Cycle length
Cl⁻	Chloride ion
CMC	Cardiomyocyte
CMOS	Complementary metal-oxide-semiconductor
CPE_{DL}	Double layer constant phase element
CPE_W	Warburg constant phase element
Cr	Chromium
Cu	Copper
DAPI	4',6-diamidino-2-phenylindole
DC	Direct current
DRG	Dorsal root ganglion

EAP	Extracellular action potential
EDX	Energy dispersive X-ray spectroscopy
FACS	Fluorescence-activated cell sorting
Fe	Iron
FET	Field effect transistor
FIB	Focused ion beam
FN	Fibronectin
GECI	Genetically encoded calcium indicator
GEVI	Genetically encoded voltage indicator
GFAP	Glial fibrillary acidic protein
GFP	Green fluorescent protein
GH3	Rat pituitary tumor cell line
H₂O	Water
H⁺	Hydrogen ion
HD-MEA	High density multielectrode array
HeLa	Cervical cancer cell line
HiPSC	Human induced pluripotent stem cells
HMDS	Hexamethyldisilazane
IrOx	Iridium oxide
IUPHAR-DB	International union of basic and clinical pharmacology database
K_α	K _α spectral line
K⁺	Potassium ion
L_α	L _α spectral line
LFP	Local field potential
MAP2	Microtubule-associated protein 2
MEA	Multielectrode array
MEMS	Micro-electro-mechanical systems

Na⁺	Sodium ion
PBS	Phosphate buffered saline
PCB	Printed circuit board
PDL	Poly-D-lysine
PFA	Paraformaldehyde
PSO	Particle swarm optimization
Pt	Platinum
RGD	Arginylglycylaspartic acid
RIE	Reactive-ion etching
ROS	Reactive oxygen species
SEM	Scanning electron microscopy
Si	Silicon
SiO₂	Silicon dioxide
SPM	Scanning probe microscopy
TEM	Transmission electron microscopy
TEVC	Two-electrode voltage clamp
Ti	Titanium
VSD	Voltage sensitive dye

List of Symbols

Physical Constants

ϵ_0	Vacuum permittivity	$8.854 \cdot 10^{-12} \text{ F/m}$
π	Pi number	3.1416
e	Euler's number	2.7183
j	Complex unit	$j^2 = -1$
q	Elementary charge	$1.602 \cdot 10^{-19} \text{ C}$

Variables

$\epsilon_{r,SU8}$	Relative permittivity SU8	—
$\epsilon_{r,water}$	Relative permittivity of water	—
ω	Angular frequency	rad/s
A	Electrode area	m^2
A_T	Electrical tracks area	m^2
C_W	Warburg capacitance	Ω
C_{DL}	Double layer capacitance	F
C_G	Gouy-Chapman capacitance	F
C_H	Helmholtz capacitance	F
C_{In}	Amplifier input capacitance	F
C_j	Junctional capacitance	F
C_m	Overall cell membrane capacitance	F
C_{nj}	Non-junctional capacitance	F
C_{Stray}	Stray capacitance	F
D	Diffusion coefficient of H^+ in water	m^2/s
d_{OHP}	Distance of the outer Helmholtz plane	m
dV/dt_{max}	Maximal upstroke velocity	V/s

dV/dt_{min}	Minimal downstroke velocity	V/s
E_K	Reversal potential of potassium channels	V
E_L	Reversal potential of ion channels other than K^+ and Na^+	V
E_{Na}	Reversal potential of sodium channels	V
f	Frequency	Hz
g	Overall cell membrane conductance	S
g_K	Potassium channels conductance	S
g_{Na}	Sodium channels conductance	S
h	Electrode height	m
I	Faradaic current	A
J_0	Exchange current density	A/m^2
L_D	Debye length	m
n_0	Bulk number concentration of ions in PBS	$ions/m^3$
n_{DL}	Double layer constant phase element empirical factor	—
n_W	Warburg constant phase element empirical factor	—
Q_W	Warburg constant phase element magnitude	$\Omega^{-1}s^{1/2}$
r	Electrode radius	m
R_W	Warburg resistance	Ω
R_{CT}	Charge transfer resistance	Ω
R_{In}	Amplifier input resistance	Ω
R_j	Junctional resistance	Ω
R_K	Potassium channels resistance	Ω
R_L	Channel resistance for ion channels other than K^+ and Na^+	Ω
R_{Na}	Sodium channels resistance	Ω
R_{nj}	Non-junctional resistance	Ω
R_{Seal}	Seal resistance	Ω
R_{Spread}	Spreading resistance	Ω
t_T	Electrical track insulating layer thickness	m
V_0	Source potential for impedance spectroscopy	V
V_t	Thermal voltage	V
V_{EP}	Electroporation voltage	V
V_{In}	Voltage at the amplifier input	V

V_j	Voltage the junctional interface	V
V_m	Transmembrane potential	V
V_{OCP}	Open-circuit potential	V
z	Valence of the ion involved in O_2 reduction	—
Z_W	Warburg impedance	Ω
Z_{ce}	Cell-electrode interface equivalent impedance	Ω
$Z_{CPE,DL}$	Double layer constant phase element impedance	Ω
$Z_{CPE,W}$	Warburg constant phase element impedance	Ω
Z_e	Electrode impedance	Ω
$Z_{In,Stray}$	Equivalent impedance of the amplifier-stray components interface	Ω
Z_{In}	Amplifier input impedance	Ω
Z_j	Junctional impedance	Ω
Z_{nj}	Non-junctional impedance	Ω
Z_{Stray}	Stray impedance	Ω
Z_{Sys}	Equivalent impedance of the cell-electrode-amplifier interface	Ω

Chapter 1

Introduction

Since the beginning of time, Nature has given birth to the most sophisticated mechanisms and entities ever created. Historically, these phenomena were often so extraordinary to the human eye, they were considered to have divine origin and were consequently misinterpreted throughout history. In this context, driven by curiosity about the natural world, Science is an ideology essential to society, focusing on objectively studying the workings of Nature and aiming to return it the credit it deserves.

1.1 Scope of the thesis

This thesis lies at the frontiers between three distinct fields of Science: nanotechnology, engineering, and biology. Nanotechnology focuses on the study of the infinitely small. By manipulating physics at the nanoscale – less than a billionth of a meter – this branch of science permits not only the integration of conventional macro tools at this scale but also access to a brand new world of physics. At this scale, gravity is negligible and, instead, electrostatic interactions between atoms or molecules define the physical rules. Engineering nanotechnologies with critical dimensions comparable to the size of the smallest known biological entities enables new forms of interaction with the natural world and opens new paths for biological research.

This work focuses on the potential contribution of technological developments in micro- and nanotechnology to the field of electrophysiology, which principally involves observations of electrical signals in cells and tissues. Over the last decade, micro- and nanoelectrode arrays have led to remarkable advances for transmembrane voltage recordings of excitable cells and received substantial interest from the electrophysiology community. This thesis intends to explore how non-conventional nanofabrication

methods can manufacture the next generation of multielectrode arrays capable of reporting high-quality intracellular electrophysiological recordings from cell networks over extended periods.

1.2 Electrophysiological methods: state-of-the-art

Electrophysiology is the field of medicine that focuses on the study of electrical signals in cells and tissues. It began more than 2000 years ago, when physicians investigated the mechanisms responsible for the transmission of instruction for movement through nerves.

1.2.1 A brief history of electrophysiology

This section outlines the origins of electrophysiology and the ways the Scientific Revolution eradicated common beliefs and defined the foundations of modern electrophysiology.

1.2.1.1 Exorcising the animal spirit

Around 250 BC, Alexandrian physicians believed that unknowable “animal spirits” moving along the nerves were responsible for movement. [1, 2] In 180 AD, in his manuscript “De Motu Musculorum”, the Greek physician Galen of Pergamum (129–216) was the first to codify this by-then well-established concept. [3] However, for the next 1500 years, neither Galen nor his followers could further explain the nature of these spirits or their concrete contribution to movement. Unsurprisingly, this idea founded on belief rather than rational theory did not produce any important discoveries, even though it was part of the physiology and medical knowledge base for nearly 2000 years. [4]

Finally, in 1633, René Descartes (1596–1650) completed his manuscript “De Homine” (Treatise of Man, published posthumously in 1662) [5] and these moving spirits were clearly defined for the first time. For the French philosopher, the animal spirit was a substance analogous to a liquid, “a wind”, or a “very fine flame” and it was localized in the pineal gland. From there, it could be injected via the nerves to the muscles to induce a movement, in the manner of the hydraulic systems making automats move (cf. Figure 1.1-A). [1, 5] Through this precise mechanical analogy, it was implied that a movement could only take place if a muscle was connected to the brain, where the animal spirit was localized, and such movement would inevitably change the muscle volume. Descartes thus transformed a vague concept based on

1.2. Electrophysiological methods: state-of-the-art

commonly held beliefs into a well-defined modern mechanical system that could be experimentally investigated.

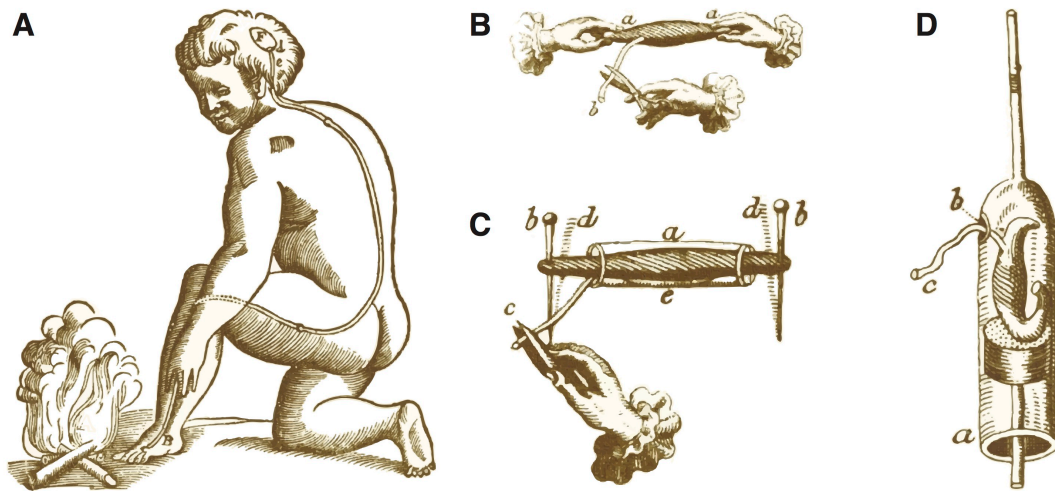


Figure 1.1: *Exorcising the animal spirit.* **A)** Illustration of Descartes' vision of the animal spirit: if the foot is too close to the fire, the animal spirit located in the pineal gland (F) will travel through the nerve to the leg muscles and withdraw the foot from the fire. **B)** Swammerdam's frog nerve-muscle preparation: nerve (b) irritation with scissors, or any other instrument, induces the contraction of the muscle held by its tendons in (a). **C)** Improvement of the nerve-muscle preparation: the distance between the two needles (b) holding the muscle decreases in the event of muscle contraction and thus allows for the quantification of muscle-contracting power. **D)** Experimental setup used by Swammerdam to demonstrate constant muscle volume during contraction: the muscle was placed in an airtight syringe (a) with the nerve (c) protruding through a small hole (b) in the side; following nerve irritation and muscle contraction, the water droplet trapped at the syringe tip did not show any fluctuation in height, demonstrating constant muscle volume during contraction. Reproduced with permission from [1].

Less than three years after Descartes' publication, the young Dutch scientist Jan Swammerdam (1637–1680) presented experimental evidence contradicting the concept of an animal spirit. He first simplified the transmission of movement in animals into the functional sub-unit known as the frog nerve-muscle preparation. As illustrated in Figure 1.1-B, the muscle from a frog leg was carefully dissected and its adjacent nerve isolated and rendered accessible. By “irritating” the nerve extremity with his scalpel, Swammerdam was able to observe muscle contractions that were independent of the brain and therefore experimentally demonstrate that animal spirits were not involved in nerve transmission and muscle movements. [6] This experiment was described as “one of the most important experiments of the century” [7] and is still widely used for educational purposes today. [8] Swammerdam subsequently developed more sophisticated instruments, first quantifying the power of muscle contraction – by adding two needles holding the muscle at the edges of the preparation that bent proportionally to the contraction (cf. Figure 1.1-C) – and then investigating a mus-

Chapter 1. Introduction

cle's volume change during contraction. By inserting his preparation into a sealed syringe presenting a trapped water droplet at its tip (cf. Figure 1.1-D) and finding that a muscle contraction did not change the droplet height, Swammerdam experimentally proved the constant volume of an active muscle and thus definitively refuted Descartes' theory.¹ Instead of accepting the established principles and traditions of his time, Swammerdam had brought non-verified concepts to be tested impartially and empirically, demonstrating the power of modern science as it has been known since the Scientific Revolution.

Swammerdam dismantled the animal spirits myth but did not propose an alternative theory to explain the transmission of movement. The decisive breakthrough came when Luigi Galvani (1737–1798) accidentally discovered electricity's role in muscle contraction by dissecting a frog on the same bench as an “electric machine” (illustrated in Figure 1.2-A). [9] He demonstrated that movement could be induced electrically by stroking an iron plate against a brass hook penetrating the spinal cord of a frog. Based on his experimental observations, Luigi Galvani developed the first theory of “animal electricity”, thus laying the foundations of the then-novel field of science now known as electrophysiology, the study of the electrical properties of cells and tissues. [10, 11]

1.2.1.2 The instrumental period

In 1848, Emil Du Bois-Reymond (1818–1896) was the first to record “action currents” of both the nerves and muscles during muscle contraction using a galvanometer (cf. Figure 1.2-B). He realized that contraction decreased the potential difference between the tissue's intact surface and the cut. For this reason, he called this negative variation “negative Schwankung” (negative fluctuation). [12–14] Johannes Müller (1801–1858), who developed a purely electrical signal-propagation theory, claimed the propagation speed of this negative Schwankung was too high to be measured instrumentally. Only a few years later, Muller was proven wrong by Hermann von Helmholtz (1821–1894), who recorded a nerve-impulse speed of $\sim 25\text{-}40$ m/s by recording the delay between the electrical stimulation and the muscle contraction – “le temps perdu” – using a smoked drum. [15] This relatively low propagation velocity contradicted the notion of a purely electrical nerve-transmission mechanism, in which the speed of the current would be orders of magnitude faster. This contradiction made it difficult for contemporary electrophysiologists to propose a reliable theory accommodating both observations.

¹When Swammerdam published this result, he believed that the absence of muscle-volume variation was experimental incertitude more than physiologically relevant insight but published the “failed” results anyway. It is interesting to note the impact of such an “artifact” in the context of debate about interpreting outliers.

1.2. Electrophysiological methods: state-of-the-art

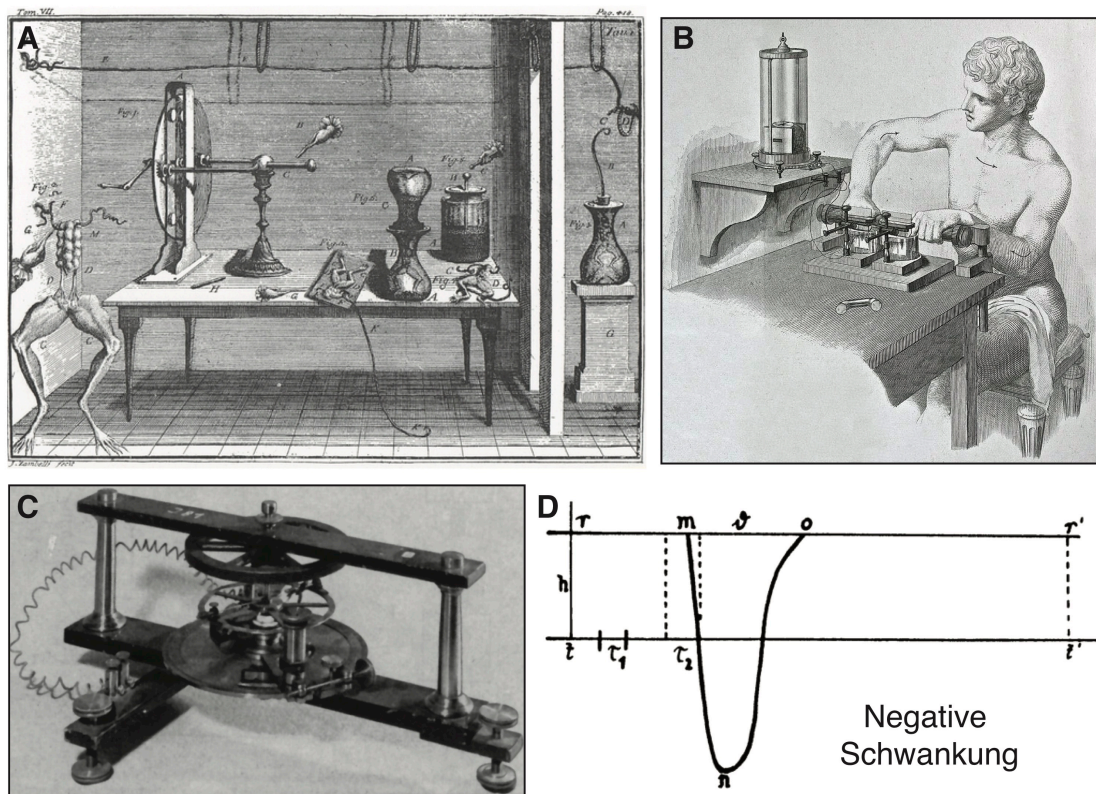


Figure 1.2: *The instrumental period.* **A)** Luigi Galvani’s experimental bench showing his version of the frog nerve-muscle preparation surrounded by “electric machines”. Luigi Galvani often used analogies with Leyden jars, similar to that seen on the right side of the bench, to explain the concept of “animal electricity”. [2] **B)** Emil Du Bois-Reymond measuring the “action current” during muscle contractions using a galvanometer carefully mounted on a separate shelf to prevent disturbances during recording. [12] **C)** The Bernstein rheotome used to record the first nerve resting and **D)** action potential (called “negative Schwankung”) with sufficient temporal resolution to study the kinetic energy of the electrophysiological event. [2] Reproduced with permission.

In 1868, Julius Bernstein (1839–1917) developed a novel scientific instrument – the “differential rheotome” – enabling voltage recordings with a sampling period as low as several tens of microseconds, suitable for recording the kinetic output of fast electrophysiological events. [16] With this instrument (illustrated in Figure 1.2-C), Bernstein was the first to record both a nerve’s resting and action potential (cf. Figure 1.2-D). He observed that the potential of the inside of a nerve at rest was 60 mV lower than that of its surface, but, during contraction, the interior potential surpassed the zero-potential line, with a rising time of 0.3 ms, before returning to its resting potential 0.8-0.9 ms later. [17] Although the mechanism underlying action potential generation and propagation had not yet been elucidated, action potentials were identified as responsible for the transmission of movement through nerves.

Chapter 1. Introduction

1.2.1.3 Membrane excitation theory

Building on previous innovations, Bernstein made significant experimental observations leading to the first developments toward membrane excitation theory, which partly explained the generation of action potentials. In adapting the electrolytic theory of Walther Nernst (1864–1941) to biological systems, Bernstein was already predicting that K^+ selectivity in the nerve membrane was responsible for resting membrane potential. [18]

This theory was completed by Charles Overton (1865–1933), who demonstrated the role of Na^+ in the excitation process. [19] In 1899, Overton proposed the “lipoidal membrane” model for the plasmalemma, [20] a theory which was refined in 1925 by Evert Gorter (1881–1954) and Francois Grendel (1897–1969) and led to the establishment of the lipid bilayer model. [21] Ten years later, James Danielli (1911–1984) and Hugh Dawson (1909–1996) perfected this model by introducing the concept of lipid bilayer containing narrow water-filled pores to allow for the passage of lipid-insoluble molecules such as ions. [22]

Electrophysiological recordings at the single-cell level were essential for validating and completing the current model and became possible after John Z. Young (1907–1997) introduced the giant-squid axon to the electrophysiological community. [23] Due to its large size (up to 1.5 mm in diameter), the giant-squid axon was independently utilized between 1939 and 1942 by Howard Curtis (1906–1972), Kenneth Cole (1900–1984), [24] Alan Hodgkin (1914–1998), and Andrew Huxley (1917–2012) [25] to develop sharp microelectrodes that could be inserted into cells to record the intracellular action potentials. Intracellular recordings showed the giant-squid-axon action potential crossing the zero-potential line, with a resting membrane potential of -50 mV. A decade later, Alan Hodgkin and Andrew Huxley developed the ionic theory of membrane excitation, explaining the generation and propagation of action potentials as we presently know them. In 1963, they received the Nobel Prize in Physiology or Medicine for their work. Using conventional two-electrode voltage clamp measurements, Hodgkin and Huxley demonstrated that the ionic-concentration gradient between the inner and outer part of a cell was responsible for a passive ionic flux across the cell membrane through selective transmembrane aqueous pathways, which in turn was responsible for the action potential. [26–32]

Figure 1.3-A shows a schematic drawing of the giant-squid-axon cell membrane crossed by transmembrane aqueous pathways, now known as ion channels. The Na^+/K^+ ionic pump maintains an electrochemical gradient across the cell membrane and per-

1.2. Electrophysiological methods: state-of-the-art

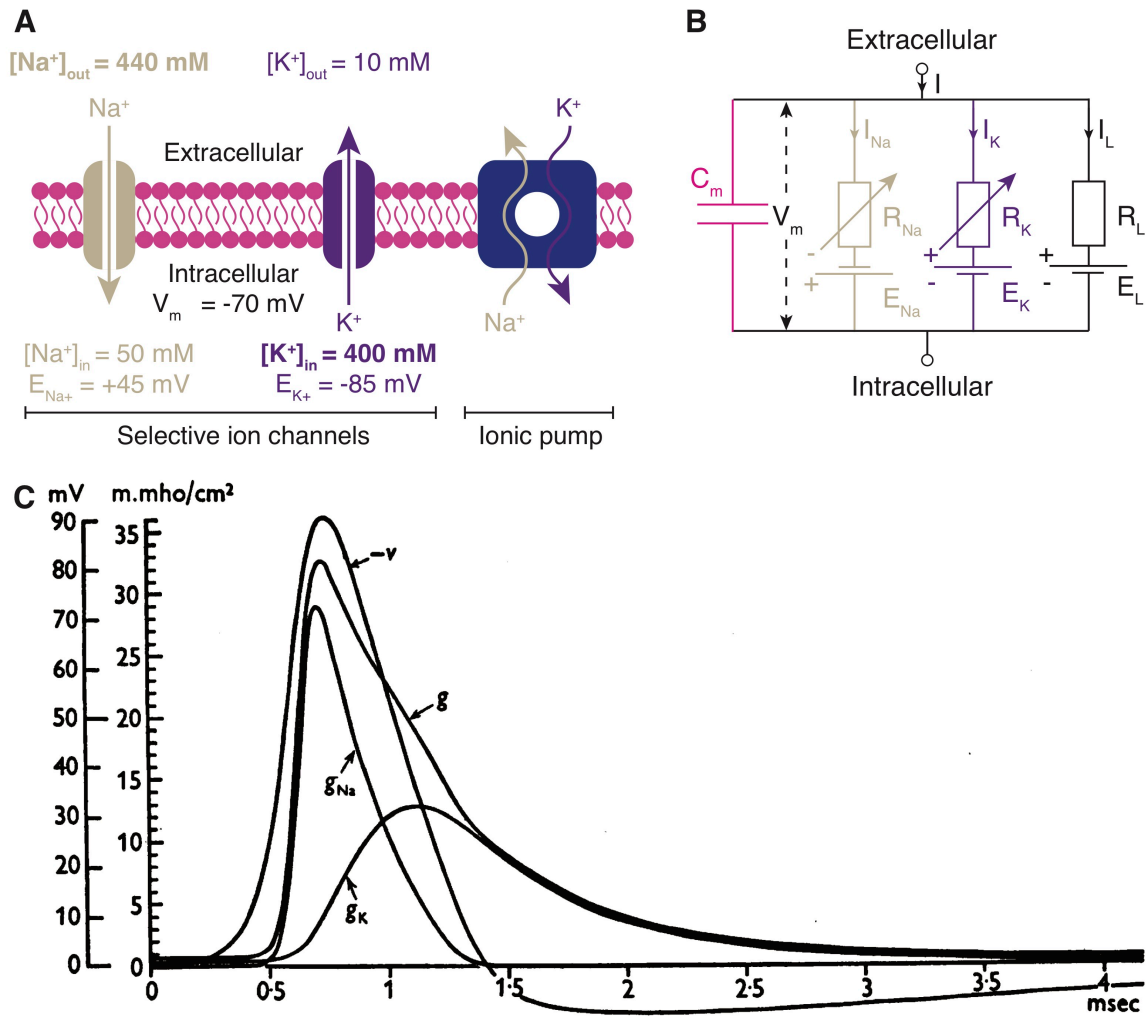


Figure 1.3: *The Hodgkin-Huxley model.* **A)** Schematic drawing illustrating the cell membrane of a giant squid axon composed of transmembrane aqueous pathways, now known as ion channels, selective to Na^+ and K^+ ; the ionic Na^+/K^+ pump maintains the electrochemical gradient across the cell membrane. **B)** Hodgkin-Huxley electrical equivalent circuit of the giant squid axon. C_m represents the lipid bilayer capacitance, R_{Na} and R_K symbolize the variable ion channel resistance influenced by the transmembrane potential, and R_L represents the linear-leakage resistance defined by Cl^- and other ions. The voltage sources E_{Na} , E_K , and E_L represent the reversal ion channel potentials for Na^+ , K^+ , and other ions. **C)** Temporal evolution of Na^+ , K^+ , and overall conductance in the case of action potential ($-v$) for a giant-squid axon is annotated using the labels g_{Na} , g_K , and g . Reproduced with permission from [27].

mits a higher extracellular concentration of sodium ions as well as a lower extracellular concentration of potassium ions. In the Hodgkin-Huxley electrical equivalent model of the giant squid axon (cf. Figure 1.3-B), these electrochemical gradients driving Na^+ , K^+ , and other (mainly Cl^-) ionic flows are represented by batteries labeled E_{Na} , E_K , and E_L . Furthermore, the voltage-dependent conductance experimentally observed for Na^+ and K^+ channels is represented by variable resistance renderings labeled R_{Na} and

Chapter 1. Introduction

R_K . The leakage resistance representation labeled R_L is considered linear and does not vary in the event of action potential. The typical action potential illustrated in Figure 1.3-C causes a rapid increase in the Na^+ ion channel conductance (g_{Na} , where $g_{\text{Na}} = 1/R_{\text{Na}}$), which enables the Na^+ ions to passively diffuse into the intracellular space and positively increase the transmembrane potential. Due to different kinetic properties, K^+ ion channel conductance (g_K , where $g_K = 1/R_K$) increases slightly later and permits potassium ions to passively leave the intracellular space. Subsequently, the transmembrane potential returns to its resting value. Several of the sub-units illustrated in Figure 1.3-A are situated next to each other along an axon. When an action potential is triggered, the conductance fluctuations at the axon's initial segment change the transmembrane potential locally and therefore stimulate the neighboring sub-units, inducing a chain reaction that permits action potential propagation. The initial trigger can be induced by transmembrane channels not necessarily sensitive to voltage but instead to other entities, such as molecules (ligand-gated ion channels).

The Hodgkin-Huxley model permits the theoretical understanding of action potential propagation using a simple biological model such as the giant-squid axon.

1.2.2 The patch clamp technique

The patch clamp methodology led to the first experimental evidence of ion channel existence into cell membranes. Presently, it is still the gold standard to assess electrophysiological characteristics of biological entities ranging from single-cells to single ion channels.

1.2.2.1 The patch clamp origin

In the early 1970s, it was clear that “discrete molecular entities” were responsible for the electrical activity in nerves and muscles. [33] Experiments performed on artificial membranes already demonstrated that proteins isolated from bacteria [34] or antibiotic polypeptides [35] could induce discrete membrane conductance fluctuations. These observations were attributed to the opening and closing of individual pores.

The next logical step was to look for similar discrete currents in small isolated areas of biological membranes (“patch”) by placing a measuring glass micropipette (cf. Figure 1.4-A) onto the surface of a cell, which voltage was clamped using the conventional two-microelectrode voltage clamp circuit as illustrated in Figure 1.4-B. [39, 40] By optimizing the cell surface enzymatic cleaning protocol and the pipette geometry, Erwin Neher and Bert Sakmann obtained a sufficiently high seal resistance of $100\text{ M}\Omega$ to measure for the first time acetylcholine-induced currents from single-

1.2. Electrophysiological methods: state-of-the-art

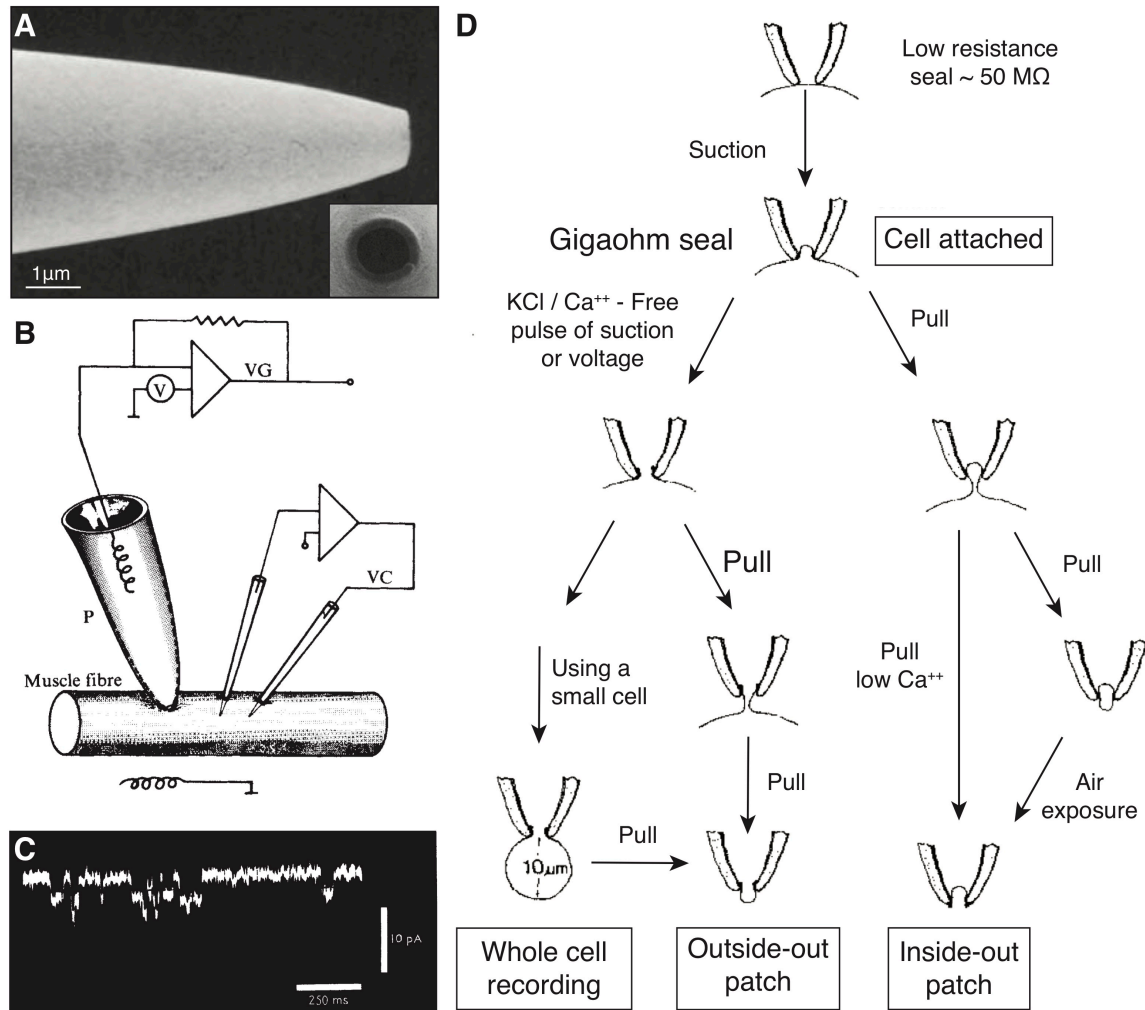


Figure 1.4: *The patch clamp technique.* **A)** Scanning electron micrograph of a typical flame-polished patch clamp pipette tip. The insert shows a tip-on view of the pipette opening. [36] **B)** Schematic drawing representing a glass micropipette placed in contact with a small surface of a voltage clamped muscle fiber. This experimental system was used to record the first single acetylcholine-induced currents, which electrical trace is illustrated in **C)**. [37] **D)** Schematic diagram illustrating the wide variety of patch-clamp configurations. [38] Reproduced with permission.

channels in 1976 (cf. Figure 1.4-C). [37]

Nevertheless, disadvantages of low seal-resistance patch clamp recordings include a limited resolution and a significant noise when the pipette voltage slightly differs from the bath potential. When suction was discovered to increase the seal resistance from tens of megaohms to several gigaohms, most of these limitations were reduced as the resolution improved by an order of magnitude, the variability of channels properties decreased, and the standard two-microelectrode voltage clamp system was not necessary anymore as potentials could directly be applied across the seal. [41, 42] Additionally, due to the high mechanical stability between the pipette tip and the cell

membrane during gigaseal, patches could be excised from their cell and independently studied, therefore opening numerous configurations of patch clamp recordings.

1.2.2.2 Patch clamp configurations

As summarized in Figure 1.4-D, several patch clamp recording configurations were discovered following gigaseal formation by suction. A detailed description of these modes together with some practical ingenuities are available in the manuscript “Patch clamp techniques: an overview” [33] and briefly outlined in this section.

- ◇ **Gigaohm seal formation:** A fire polished glass pipette tip with a typical aperture of $1\ \mu\text{m}$ in diameter (access resistance $\sim 1\text{--}10\ \text{M}\Omega$) is brought in contact with a cell while its resistance is monitored by applying low voltage pulses. During this phase, a slightly positive pressure is usually applied to the pipette in order to clean the landing cell surface and facilitate the seal formation. Once in contact with the cell membrane, the resistance typically increases to a value of $\sim 50\ \text{M}\Omega$. At this point, a negative pressure is applied to the pipette interior ($10\text{--}20\ \text{cm H}_2\text{O}$) inducing a suction of the cell membrane patch into the pipette as well as a sudden increase of the seal resistance to several gigaohms.
- ◇ **Cell-attached patch recording:** Following gigaseal formation, currents passing through the ion channels surrounded by the pipette tip can already be measured with sub-picoampere resolution. In this case, the cell remains intact and the potential across the patch is simply the difference between the cell and the pipette potential.
- ◇ **Inside-out patch recording:** If the pipette is directly withdrawn after gigaseal formation, a membrane patch is excised from the cell letting the cytoplasmic side of the membrane facing the bath solution. In this case, the membrane potential is defined by the difference between the bath and the pipette potential.
- ◇ **Whole-cell recording:** In whole-cell configuration, the membrane patch is ruptured either by applying a strong negative pressure to the pipette interior or by electroporation while the gigaseal is maintained. The cell potential is clamped by the pipette voltage as long as the access resistance is much lower compared to the cell membrane resistance. This is usually the case for small cells. The current passing through the pipette reflects the overall activity of the cell ion channels. Disadvantages of this method includes the washing of secondary messengers and regulatory proteins by diffusion of the pipette solution into the cytoplasm. This limitation can be overcome by perforated patch clamp. [43]

- ◇ **Outside-out patch recording:** Withdrawing the pipette from the cell during whole-cell recording induces the excision of a membrane patch with features similar to whole-cell recording except for a much smaller membrane area. In this variant, subpicoampere currents from single-channels can be measured.

All these different configurations enabled the patch clamp methodology to be used in a wide variety of applications.

1.2.2.3 Patch clamp applications

The patch clamp technique provided the first experimental demonstration of the existence of discrete molecular entities underlying the electrical signaling mechanism in nerves and muscles; therefore terminating once and for all speculations about animal electricity. For their historical breakthrough innovation, Erwin Neher and Bert Sakmann received the Nobel prize in Physiology or Medicine in 1991.

By permitting detailed conductance and kinetic studies of single-channel currents from basically any biological cells, patch clamp recordings led to the discovery of numerous ion channel types with diverse activation mechanisms over the years. [44] For instance, voltage-gated ions channels in nerves and muscles triggered by potential variations across the cell membrane such as Na^+ , K^+ , and Ca^{2+} channels were intensively characterized. [45] Similarly, ligand-gated ion channels modulated by extracellular transmitters such as acetylcholine in the neuromuscular junction or γ -aminobutyric acid in neuronal synapses, [46] or by intracellular ligands [47] (e.g. Ca^{2+} , Adenosine triphosphate, cyclic adenosine monophosphate) were discovered. Additionally, numerous patch clamp recordings were performed on mechanically triggered ion channels (mechanosensory and volume-gated channels, e.g. transient receptor potential channel family) and demonstrated their implications in a wide range of physiological functions such as touch sensitivity and cell volume regulation. [48–50] This is only a very brief insight into the hundreds of ion channel discovered with the patch clamp methodology over the last decades. A more exhaustive list can be found on the international union of basic and clinical pharmacology database (IUPHAR-DB). [51]

Ion channels play an essential role in a wide variety of physiological responses and therefore, their disfunctions are usually associated with diseases (channelopathies). [52] Disfunctions are often caused by specific mutations in the gene coding for the ion channel protein. In this context, the patch clamp technique is essential to link how a single genetical mutation impacts the ion channel electrophysiological response and to understand the functional consequences of the mutation.

The action potential generation in giant squid axons detailed by A. Hodgkin and A. Huxley in their model of the cell membrane excitation was simply caused by two different types of transmembrane voltage-gated ion channels (Na^+ and K^+). In mammalian neuron bodies, patch clamp recordings demonstrated that more than a dozen of diverse types of voltage-gated ion channels were expressed, therefore enabling a much more complex firing behaviour with a wide range of action potential shapes, frequencies, and patterns to encode sophisticated information. [53] Still today, the whole-cell patch clamp recording is the gold standard to record action potentials from single-cells and assess electrophysiological characteristics of electrogenic cells at the transmembrane voltage. [54–58]

1.2.2.4 Patch clamp limitations and automated patch clamp techniques

The patch clamp technique is a unique technology which enables the study of conductance and kinetic properties of single-channels with sub-picoampere resolutions as well as the recording of action potentials from single electrogenic cells at the transmembrane voltage level.

However, patch clamp recordings are still today a practical challenge that requires both an expensive experimental setup together with a well-trained operator. Furthermore, patch clamp recordings are conducted on a single-cell at a time with a usually poor gigaseal formation yield. In this context, the throughput of this technology is typically limited to 8-10 cells a day. [44]

Therefore, manual patch clamp recordings are unfortunately not well suited for pharmacological screening purposes where a high-throughput is required. [59] For this reason, a limited number of automated patch clamp robots (e.g. Flyscreen [60], RoboPatch [61]), equivalent to manual patch clamp recordings in terms of data quality, were developed with an improved yield up to 100 cells a day.

Another automated patch clamp approach, the “planar patch clamp”, consists in microchips patterned with multiple micrometer holes resembling the patch clamp pipette opening ($\sim 1 - 2\ \mu\text{m}$ in diameter), and connected to microfluidic channels. Practically, cells are inserted in suspension while negative pressure is applied through the micro-holes to aspirate one cell per site, form a seal, and then perform whole-cell or perforated recordings. [59, 62] Various types of planar patch clamp technologies were developed since the early 2000s with seal resistances ranging from $\sim 100\ \text{M}\Omega$ to several gigaohms and a number of recording sites up to 384, corresponding to a throughput of nearly ~ 4000 cells per day. [63] A detailed description of these devices as well as a complete comparison of their performances has already been presented in

1.2. Electrophysiological methods: state-of-the-art

the literature. [64] Even though the planar patch clamp technique won the throughput race against both manual and patch clamp robots, its main disadvantage is that it requires stable cell lines known to easily form a gigaseal during manual patch clamp and which highly express the channel of interest. Planar patch clamp devices are usually not suited for electrophysiological studies on primary mammalian cell cultures such as neuronal or cardiac preparations. Additionally, fabricating a large number of individually addressable microfluidic chambers still remains challenging and prevents planar patch clamp devices to permit investigation of network dynamics. [59] Finally, compared to manual patch clamp, automated patch clamp platforms are exceedingly expensive ($> \$100$ k). [64] In comparison with patch clamp pipettes pulled almost for free, the price of single-use planar patch clamp devices is definitely not negligible.

Due to the limited flexibility and high costs of these automated alternatives, the conventional manual patch clamp technique still remains the technique of choice in academia.

1.2.3 Optical electrophysiology

Optical electrophysiology is an alternative method to patch clamp that exploits light to assess electrophysiological characteristics of electrogenic cell networks at the transmembrane voltage level.

1.2.3.1 Concept of optical electrophysiology

Current techniques in optical electrophysiology generally use a molecule (reporter) that transduces an electrical potential (or its consequence) into light. [65] Optical reporters are usually fluorescent molecules expressed by or inserted into cells, which will modify their fluorescent properties (e.g., excitation-emission wavelength shift) according to the electrophysiological activity of the cells of interest. Compared to the patch-clamp technique, optical electrophysiology is usually limited to the recording of transmembrane potentials in excitable cell; a configuration comparable to a whole-cell patch clamp recording with the current fixed to zero.

Probing electrophysiological activity with light is an indirect method that shows significant advantages compared to conventional direct microelectrode measurements. As cell membranes are transparent to light, there is no need of physical contact with a cell to probe its electrophysiological activity, in contrast with patch clamp pipettes that need to form a tight junction with it. Therefore, optical studies are not limited to surface recordings but enable three dimensional (3D) electrophysiological measurements from deep tissues. Additionally, optical techniques usually show a much higher

Chapter 1. Introduction

throughput compared to the patch clamp technique as they can assess electrophysiological activity from cells covering a relatively large area, with a sub-cellular spatial resolution. [66–68] Finally, optical reporters are usually less invasive in comparison with direct measurements using microelectrodes impaled into cells as they are small molecules which emit light that does not interfere with the cell electrical activity.

In this section, we describe in details two main classes of optical reporters widely used in the literature to assess electrophysiological characteristics of electrogenic cell networks: voltage sensors and calcium indicators. Their mechanisms are illustrated in Figure 1.5-A.

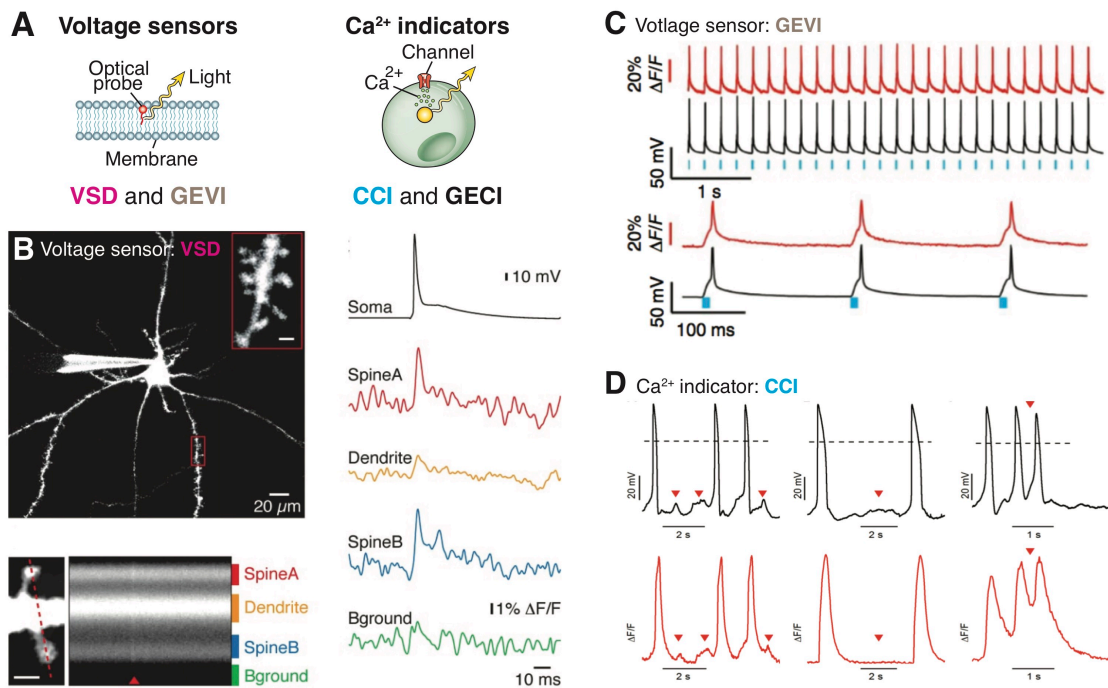


Figure 1.5: Optical electrophysiology. **A)** Schematic drawing of the two main families of optical reporters used in optical electrophysiology: voltage sensors (left panel) that includes voltage sensitive dye (VSD) and genetically encoded voltage indicator (GEVI), and Ca²⁺ indicator (left panel) that includes chemical calcium indicator (CCI) and genetically encoded calcium indicator (GECI). [65] **B)** Optical imaging of neuronal action potentials in dendritic spines with VSD. [69] **C)** Optical stimulation (blue) and recording (red) of neuron action potentials using GEVI. Simultaneous patch clamp measurements (black) demonstrate the high fidelity of the optical signal with respect to the electrical one. [70] **D)** Simultaneous recording of cardiomyocyte action potentials using the patch clamp technique (top panel), and calcium transients with Ca²⁺ indicator (bottom panel) in case of arrhythmia. [71] Reproduced with permission.

1.2.3.2 Voltage sensors

Voltage sensors include optical reporters that convert transmembrane voltage into light. Such reporters can be inserted into cells (e.g., voltage sensitive dyes) or geneti-

cally expressed (e.g., genetically encoded voltage indicators).

Voltage sensitive dye Voltage sensitive dye (VSD) is a family of optical reporters that are usually self-inserted into one leaflet of the lipid bilayer cell membrane and modify their fluorescence emission intensity according to the transmembrane electric field. [72]

Until the last decade, VSDs were the most successful optical reporters as they show a very fast temporal resolution down to the microsecond and permitted in-vitro recordings of cardiomyocyte action potentials over large areas, [73] as well as sub-cellular registration of neuronal action potentials in distal dendrite compartments. [74] More particularly, sub-threshold and action potentials recordings in small neuronal post-synaptic structures called “dendritic spines” (cf. Figure 1.5-B), inaccessible with a patch clamp pipette due to their small dimensions, were achieved by averaging multiple stimulated trials. [69,75] Electrophysiological studies *in vivo* were also conducted using VSD as an optical reporter. [76,77]

However, optical recordings made with VSDs suffer from a low signal-to-noise ratio as VSDs fluorescence change per unit is usually small. Additionally, VSDs labelling internal cell compartments where the electric field is constant, increase the background and therefore reduce the signal-to-noise ratio. Yet, the main limitations of VSD are photobleaching and phototoxicity that limit both the excitation intensity and the duration of the experiment.

Genetically encoded voltage indicators Genetically encoded indicators are an emerging class of optical reporters which underwent an exponential development during the last decade. They include indicators for vesicle release, changes in neurotransmitter concentrations, intracellular calcium dynamics, and particularly for transmembrane potentials. [78] Genetically encoded voltage indicators (GEVIs) consist in fluorescent proteins genetically expressed and manufactured by the cells of interest, which fluorescent properties depend on the transmembrane potential. Compared to VSDs, GEVIs expression can be genetically targeted to sub-populations of cells, hence enabling electrophysiological studies of particular cellular populations, or of sub-cellular compartments such as the plasma membrane to minimize unspecific labeling and therefore increase the signal-to-noise ratio.

Historically, GEVIs favorable voltage sensitivity in comparison with VSDs was undermined by their slow kinetics that prevented the detection of single action poten-

tials. [65] During the past years, GEVIs temporal resolution drastically improved from tens of milliseconds to sub-millisecond, and is presently comparable to electrophysiological recordings with microelectrodes. [79] Recently, electrophysiological studies with GEVIs reported single-trial action potentials from cardiomyocytes [80–82] *in vitro*, as well as *in vivo* measurements with sub-cellular resolution. [83]

Similarly, optogenetic activators or inhibitors can be genetically expressed to selectively stimulate or inhibit the electrical activity of a cell with a beam of light. [84, 85] Therefore, expressing optogenetic actuators together with VEGIs into a single-cell permits the manipulation and recording of its electrophysiological activity using an all-optical setup. Action potentials optically stimulated (in blue) and recorded (in red) from a single neuron expressing both archaerhodopsin-based voltage indicators and channel rhodopsin activators are reported in Figure 1.5-C, and show a high fidelity with respect to patch clamp control measurements (in black). [70]

Genetically encoded voltage indicators and actuators enabled simultaneous transmembrane potential level recordings and manipulations of cell networks, with sub-cellular resolution. These outstanding features certainly render GEVIs suitable to assess electrophysiological characteristics of electrogenic cells over extended periods of time. However, the disadvantages of this method include the fact that experiments are limited to tissues that have been genetically modified to express suitable optogenetic reporters of transmembrane voltage. Additionally, precautions need to be taken regarding the unanticipated physiological response potentially triggered by the genetical expression of exogenous proteins.

1.2.3.3 Calcium indicators

Calcium (Ca^{2+}) is an essential second messenger particularly involved in electrogenic cells such as cardiomyocytes or neurons. [86] For neurons, Ca^{2+} changes in intracellular concentration are often associated to synaptic input and transmembrane potential fluctuations. Since their first development in 1987, chemical Ca^{2+} indicators have been widely used to study electrical activity in neural networks. [87] More recently, a novel type of genetically encoded calcium indicator (GECI) was also used to assess electrophysiological activity of neurons, [88, 89] T-cells, [90] as well as cardiomyocytes. [91] In this section, we will focus on the chemical sub-class of Ca^{2+} indicator used in the literature.

Chemical calcium indicator Chemical calcium indicators (CCIs) are usually lipophilic to facilitate their self-insertion into the cell intracellular space. Once inserted,

1.2. Electrophysiological methods: state-of-the-art

intracellular enzymatic reactions will enable the CCIs to bind with calcium ions, and therefore to become fluorescent due to an emission-excitation wavelength shift following binding. By permitting the simple monitoring of intracellular calcium ion concentration fluctuations in single-cells, without the need of genetic manipulation, CCI is one of the greatest success of synthetic chemistry. [92]

Following well-established protocols, indirect mapping of neural networks electrical activity *in vivo* were regularly achieved using CCI. [93–96] Combined with two-photon microscopy, CCI were demonstrated to be sufficiently sensitive to report single channel openings in dendritic spines. [97] Similarly to other optical methods, the use of calcium indicators was not limited to neurons but could also be used with other types of electrogenic cells such as cardiac cells. [98,99] In Figure 1.5-D, recordings of cardiomyocyte action potentials using a patch clamp electrode are compared with Ca^{2+} influx monitored with CCIs. Even though fluorescence variations nicely follow the action potential outline of a slowly beating cell, the low kinetic properties of intracellular calcium signals prevent the reconstruction of the action potentials from cells firing at higher frequency. For this reason, high fidelity reconstruction of firing patterns in neuronal circuit is challenging with chemical calcium indicators.

1.2.3.4 Overall limitations and perspectives of optical electrophysiology

Optical electrophysiology shows a tremendous potential to assess electrophysiological characteristics of electrogenic cell networks with sub-cellular resolution *in vivo*. Particularly, genetically encoded voltage indicators together with optogenetic actuators not only enabled the passive recording of neuronal synaptic activity but also permitted the single-cell stimulation with sub-cellular resolution using light. Current clamp studies in whole-cell configuration with a non-zero current are presently accessible using an all-optical system.

In comparison with patch clamp recordings, optical methods are not capable of assessing the single-channel activity under different voltage stimuli yet. In other words, performing voltage clamp recordings with an all-optical approach, even in whole-cell configuration, still seems out of reach. Theoretically, an optical voltage clamp could potentially be achieved by expressing two different light-gated ion channels (selective to Na^+ or K^+ for instance) sensitive to different wavelength, together with genetically encoded voltage indicators into a single-cell. [65] By adjusting the two different light source intensities to selectively open either the K^+ or Na^+ channel and maintain a stable voltage clamp using a feedback mechanism based on the potential recorded using the GEVI, any voltage in between the two light gated ion channel reversal poten-

tials could be clamped. Hypothetically, the current could be quantified by measuring the light intensity required to maintain the transmembrane potential clamped. Even though the quantification of the light-activated current might be challenging, an optical voltage clamp would place the optical electrophysiological methods as a potential alternative to patch clamp recordings.

1.2.4 Multielectrode arrays

Multielectrode arrays (MEAs) consist of an assembly of micro-nanoelectrodes that permit electrophysiological studies from non-genetically modified cell networks over extended periods of time, potentially at the transmembrane voltage level. In this section, we distinguish conventional planar microelectrode arrays which report extracellular activity, from protruding micro-nanoelectrode arrays aiming at providing an intracellular readout.

1.2.4.1 Planar microelectrode arrays for extracellular electrophysiology

The concept of conventional microelectrode arrays is briefly described first, high-density microelectrode arrays that enable extracellular recordings at sub-cellular resolution are later discussed.

Concept of planar microelectrode arrays In conventional MEAs, a planar microelectrode is placed in close proximity to a cell to record its electrophysiological activity extracellularly *in vitro* or *in vivo*. Extracellular signals mainly include extracellular action potentials (EAPs), which correspond to potential fluctuations induced by ionic transmembrane Na^+ and K^+ currents during the generation of an action potential, and local field potentials (LFPs) which consist of lower frequency potential fluctuations (< 300 Hz) due to the synchronous electrical activity of electrogenic cells in a tissue. EAPs are typically $100 \mu\text{V}$ in amplitude biphasic voltage pulses that last a few milliseconds for neurons, and go up to a couple of millivolts for cardiomyocytes. [100] Compared to the previously reported technologies, planar MEAs are not invasive and permit the study of spontaneous and stimulated electrical activity from electrogenic non-genetically modified cell networks over extended periods of time.

1.2. Electrophysiological methods: state-of-the-art

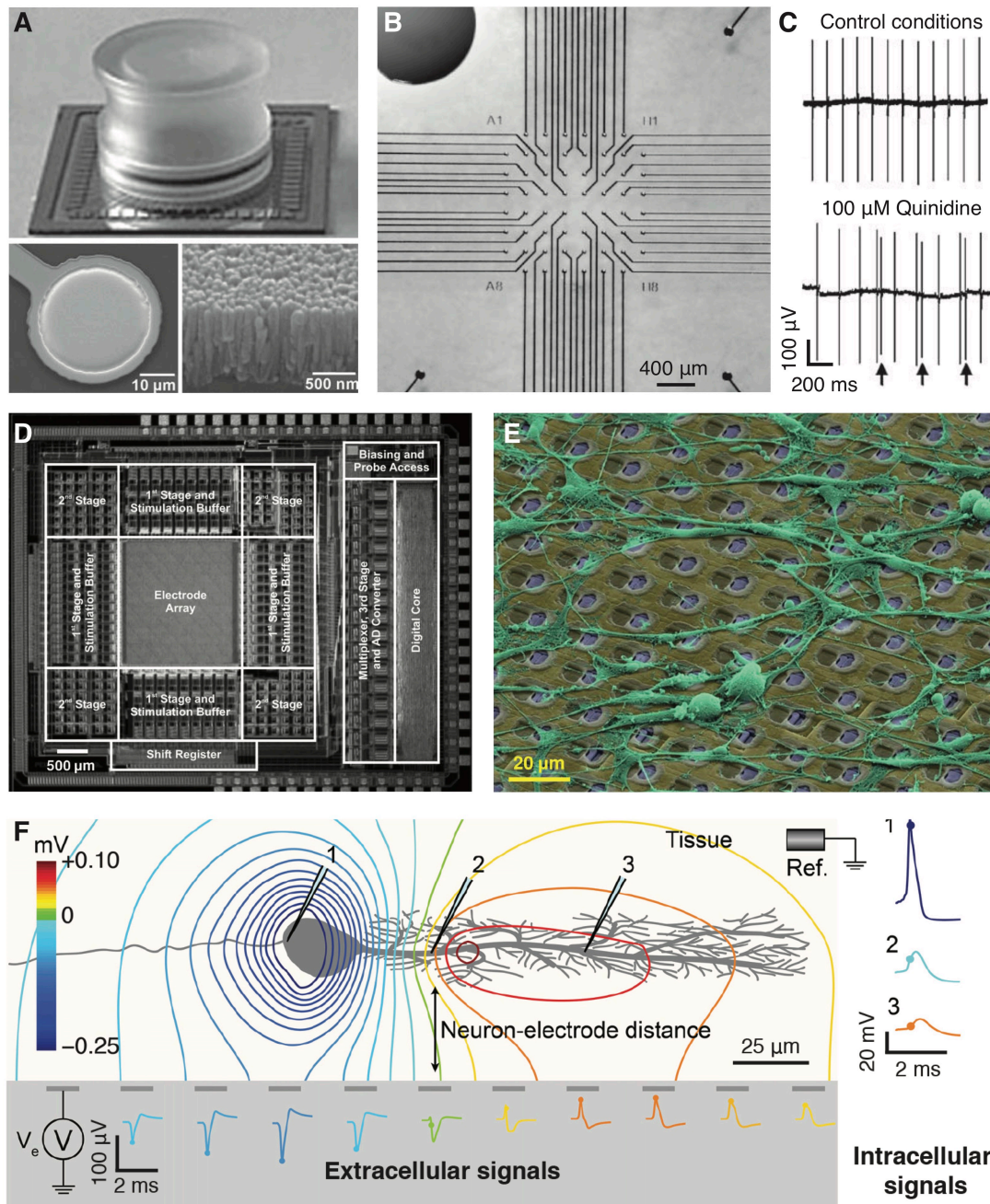


Figure 1.6: *Planar microelectrode arrays.* **A**) Conventional MEA (top panel) composed of 60 TiN planar microelectrodes (bottom left panel). A scanning electron microscopy cross section view of the TiN roughness is proposed in the bottom right panel. [101] **B**) Overview of the 60 microelectrodes composing the arrays (diameter $30\ \mu\text{m}$, pitch $200\ \mu\text{m}$). [101] **C**) Typical extracellular action potentials recorded from spontaneously active ventricular cardiomyocytes with (bottom panel) and without (top panel) Quinidine. The arrows highlight the distortion effect of the Quinidine on the cardiomyocyte contraction rhythm. [101] **D**) Optical image of a high-density MEA with its integrated CMOS electronics. [102] **E**) Scanning electron microscopy image of chicken dorsal root neurons cultured on a high-density MEA. [102] **F**) Illustration of the typical signals recorded from a neuron using either a high-density MEA (extracellular signals) or patch clamp pipettes (intracellular signals). High-density MEAs allow for simultaneous recording of extracellular action potentials at several location of a single neuron. [103] Reproduced with permission.

Since the late 1990s, commercially available MEAs typically composed of 60 electrodes ($\sim 10\text{-}30\ \mu\text{m}$ in diameter) separated by a few hundreds of micrometers pitch were intensively used to assess electrophysiological characteristics of electrogenic cells, especially in the field of neuroscience (e.g., spike sorting and neuron classification, [104,105] firing pattern detection [106–108]) as well as in cardiac research [109] (e.g., conduction wave velocity, [110,111] characterization of cellular electrical properties, [112] responses to mechanical stimuli [113]). For instance, Figure 1.6-A to C present a typical MEA used to record EAPs from cardiomyocyte preparations *in vitro* to investigate the influence of Quinidine on the cardiomyocyte contraction rhythm. *In vitro* and *in vivo* applications of conventional MEAs are reviewed in details in the literature. [101,114]

1.2.4.2 High-density planar microelectrode arrays

The number of microelectrodes per unit area continuously increased since the first development of a single extracellular microelectrode [115,116] to answer the electrophysiologists needs for mapping the electrical activity of large cell networks with a high spatial resolution. Soon, the electrode density was limited by the space occupied by the electrical tracks, passively connecting each microelectrode to the amplifier, which prevented to further decrease the pitch between two electrodes. Developments in the field of microelectronics recently enabled the integration of low-noise CMOS amplifiers directly with the microelectrode arrays; therefore overcoming the connectivity limitations and permitting the development of high-density MEAs (HD-MEAs). [117–120] Compared to conventional MEAs, HD-MEAs show the distinct advantage of enabling low-noise high-quality recordings by minimizing the distance between the microelectrode and the amplifier input, and therefore reducing the impact of parasitic stray components and electromagnetic perturbations (cf. Figure 1.6-D). [102] Additionally, HD-MEAs enable the registration of extracellular signals over large areas with high spatiotemporal resolution. Figure 1.6-E presents a scanning electron microscopy image of chicken dorsal root neurons cultured on a HD-MEA that illustrates the size and density of the microelectrodes with respect to the neurons. For instance, HD-MEAs composed of more than 59'000 microelectrodes separated by a $13.5\ \mu\text{m}$ pitch and simultaneously addressable by group of 2048, enabled the recording EAPs from sub-cellular compartments (axon: $\sim 200\ \text{nm}$) with a temporal resolution down to the microsecond. [121,122]

The high spatiotemporal resolution provided by HD-MEAs opened various opportunities in the field of electrophysiology, [103] especially when mapping firing properties of neuronal sub-compartments. In Figure 1.6-F, typical EAPs simultaneously recorded from several locations of a single neuron are presented and compared to intracellular

recordings. Different shapes of EAPs can be observed according to the recording location. As recently reported by Emmenegger *et al.*, [123] HD-MEAs already made significant discoveries related to the role of the axon in the generation of action potentials. Briefly, mainly neuronal dendrites and somas were for long thought to be responsible of action potential generation whereas the axon was considered as a cable supposed to passively transfer the information. However, studies performed with HD-MEAs reported larger EAPs in the axon initial segments compared to the soma, with different conduction velocity along the axon even with synaptic blockers suggesting specific properties and density of ion channels at different locations of the axon. [124–126] Pathological events related to axon conduction variations could potentially be characterized and novel pharmacological compounds developed with HD-MEAs screenings. Additionally, the neuronal susceptibility to stimulation mapping indicated that electrical stimulation was more efficient at the axon initial segment compared to other regions of the neuron. [127] Similar mapping could potentially be used to selectively and efficiently stimulate specific neurons *a posteriori* with low voltages.

Limitations of planar microelectrode arrays HD-MEAs permit high-throughput electrophysiological studies on electrogenic cell networks at sub-cellular resolution and over extended periods of time, without the need for genetic manipulation. From this perspective, planar microelectrode arrays show a significant advantage compared to the previous technologies. However, planar MEAs are limited to extracellular recordings and do not permit electrophysiological studies at the transmembrane voltage level. For instance, planar MEAs are blind to potential fluctuations below the firing threshold of a neuron and do not permit the visualization of a cardiomyocyte action potential shape, but instead report signals with limited information content. Ideally, multielectrode arrays should permit intracellular recordings from cell networks and over extended periods of time to provide an unequivocal alternative to the gold standard patch clamp method.

1.2.4.3 Micro-nanoelectrode arrays for intracellular electrophysiology

Over the past decade, new approaches based on micro-nanotechnologies were developed with the aim of providing long-term intracellular recordings from cell networks that overcome the shortcomings of standard optical and MEA techniques. They usually consist in multielectrode arrays where conventional planar electrodes are replaced with protruding micro-nanoelectrodes which provide a direct access to the intracellular space following a insertion triggering event (e.g., mechanical insertion, electroporation, optoporation). These technologies show the distinct advantage over conventional

planar microelectrode arrays to potentially report transmembrane voltages from cell networks with a high spatiotemporal resolution and over extended periods of time. Presently, micro-nanoelectrodes arrays mainly focus on the registration of action potentials from electrogenic cell networks with a recording configuration comparable to a whole-cell current clamp ($I = 0$). However, current technologies do not yet permit high-quality recordings comparable to the patch clamp technique as they mainly report attenuated signals, over a limited period of time, and especially with a poor yield. [128–130] Theoretical considerations at the cell-electrode interface need to be made to explain these limiting recording characteristics.

Cell-electrode interface considerations for intracellular electrophysiology

Figure 1.7-A presents the electrical equivalent circuit of a cell adhering on top of a typical protruding nanoelectrode. The electrode-electrolyte interface is represented by the impedance Z_e composed of the resistance R_{CT} reflecting the faradaic charge transfer at the interface, in parallel with a constant phase element CPE_{DL} representing the double layer capacitive coupling. [131] The junctional impedance Z_j of the cell membrane in contact with the nanoelectrode is composed of the junctional resistance R_j symbolizing the cell membrane ion channel resistance at rest, in parallel with the junctional capacitance C_j induced by the lipid bilayer. V_m represents the cell transmembrane potential of interest and V_{In} the potential recorded at the input of the amplifier. Similarly, Z_{nj} represents the impedance of the non-junctional cell membrane. The seal resistance R_{Seal} illustrates the resistive current leaks at the cell-electrode interface and Z_{Stray} , composed of a stray resistance in parallel with a stray capacitance, indicates the current leaks along the electrical tracks. Z_{In} is the input impedance of the amplifier.

An ideal nanoelectrode based recording system enables the cell transmembrane potential V_m to be recorded at the input of the amplifier without any signal loss (i.e. $V_m = V_{In}$). Therefore, the signal attenuation at the cell-electrode interface as well as at the electrode-amplifier interface should be null (i.e. $V_m = V_j$ and $V_j = V_{In}$). To satisfy the first condition (i.e. $V_m = V_j$), the attenuation defined by the voltage divider between the junctional cell membrane impedance (Z_j) and the equivalent impedance of the electrophysiological system interfaced with a cell ($(Z_e + Z_{In} \parallel Z_{Stray}) \parallel R_{Seal}$) needs to be minimized. As the electrophysiological system impedance ($Z_e + Z_{In} \parallel Z_{Stray}$) is usually much larger than the seal resistance (R_{Seal}), the latter is usually the limiting factor and the voltage divider can be simply defined between the junctional impedance and the seal resistance. The attenuation at the cell-electrode interface is therefore minimal if the seal resistance is much higher compared to the junctional

1.2. Electrophysiological methods: state-of-the-art

impedance.

Figure 1.7-B reports electrical traces recorded using nanoneedle-like electrodes on a cardiomyocyte preparation. In the upper panel, the junctional resistance is much higher than the seal resistance ($R_j \gg R_{Seal}$) and therefore, the transmembrane potential is drastically attenuated. Only the fast upstroke action potential components – extracellular action potentials – can be observed as the junctional capacitive impedance is lower at high frequency. In the lower panel, electroporation pulses were applied to damage the junctional membrane and decrease the junctional resistance ($R_j \sim R_{Seal}$). In this configuration, attenuated intracellular-like action potentials can be measured. Note that the signal is attenuated as current technologies are still limited in terms of seal.

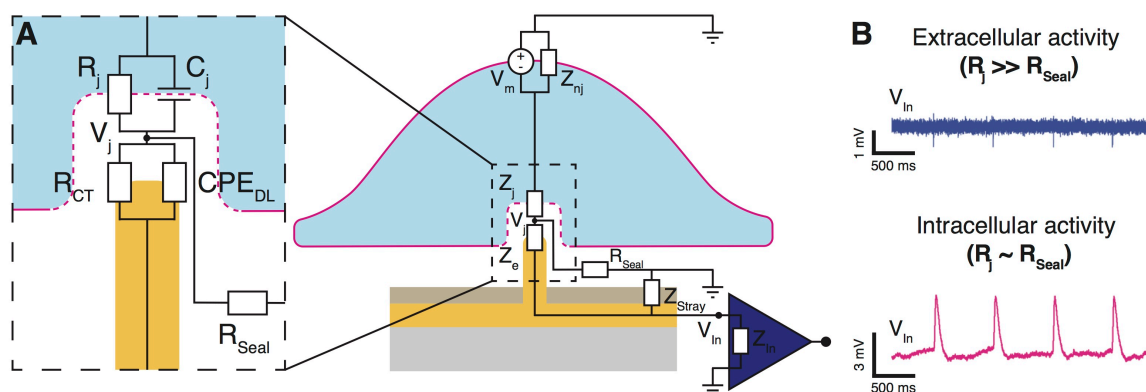


Figure 1.7: *Cell-electrode interface model.* **A)** Electrical equivalent circuit of the cell-electrode interface. Z_e is the electrode impedance composed of a charge transfer resistance R_{CT} reflecting the faradaic charge transfer at the electrode-electrolyte interface in parallel with a constant phase element CPE_{DL} representing the capacitive charge transfer through the double layer at the same interface. Z_j is the junctional impedance which consists of the junctional resistance and capacitance of the cell membrane in parallel. Similarly, Z_{nj} represents the non-junctional cell membrane impedance. R_{Seal} models the seal resistance at the cell-electrode interface, Z_{Stray} symbolizes the capacitive and resistive leaks along the electrical tracks, and Z_{In} models the input impedance of the amplifier. V_m is the transmembrane potential, V_j the potential at the junction, and V_{In} the recorded potential at the input of the amplifier. **B)** Electrical traces recorded from cardiomyocytes using nanoneedle-like electrodes before (extracellular activity, $R_j \gg R_{Seal}$) and after electroporation (intracellular activity, $R_j \sim R_{Seal}$). [130] Reproduced with permission.

Similarly, the second condition (i.e. $V_j = V_{In}$) is satisfied if the impedance of the electrode (Z_e) is negligible compared to the input impedance of the amplifier in parallel with the stray impedance ($Z_{In} \parallel Z_{Stray}$). If the amplifier is well designed, the stray impedance is usually the limiting factor. Additionally, the thermal noise is reduced at low electrode impedance as it is proportional to the square root of the resistance. [103]

Chapter 1. Introduction

Micro-nanoelectrode arrays aiming at measuring non-attenuated transmembrane potentials should guarantee high seal resistance and stray impedance, together with low electrode impedance and junctional resistance. Strategies implemented in the literature to satisfy these conditions are reviewed in the next sections.

Seal resistance maximization As for patch clamp recordings, a high seal resistance is essential to permit the recording of non-attenuated action potentials with micro-nanoelectrode arrays. The gap between the electrode and the cell membrane as well as the size of the aperture mainly limit the seal resistance with micro-nanoelectrodes. A small aperture together with a very small cell-electrode distance tend to increase the seal resistance. [130] Various 3D electrode geometries have been tested in the literature to influence the cell conformation onto protruding electrodes and maximize the seal resistance. As illustrated in Figure 1.8-A-i, transmission electron microscopy (TEM) analysis of cells interfaced with vertical nanowire-like electrodes [132–137] demonstrated that the cell membrane is closer to the protruding nanoelectrode than to flat substrate. [138, 139] Additionally, nanotube-like electrodes [140, 141] reported similar effects while increasing the cell-electrode contact area as the cell membrane is shaped by the hollow structure (cf. Figure 1.8-A-ii). Geometries resembling micromushrooms were also tested to stimulate the electrode engulfment by the cell and strengthen the cell-electrode interface. [142–147] Geometric approaches typically lead to seal resistances in the range of few hundreds of megaohms. [134, 137]

Furthermore, chemical functionalization of the electrodes were also performed to bring the cell membrane closer to the electrode. Conventional cell culture coatings, already used with planar microelectrodes, [148] such as poly-D-lysine (PDL), [149] fibronectin (FN), [132] or arginylglycylaspartic acid (RGD peptides), [142] were also tested on protruding electrodes. More sophisticated membrane mimicking coatings based on lipids were applied to kinked nanowire and nanotube field effect transistors (FETs) to facilitate the merging with cells. As illustrated in Figure 1.8-A-iv (left panel), a promising approach consists in patterning nanoscale hydrophobic bands on otherwise hydrophilic substrates to allow the fusion of manufactured structures with cells. Atomic force microscopy (AFM) experiments performed with a custom-made probe presenting a nanometer-wide gold nanoring covered with an alkanethiol self-assembled monolayer (cf. Figure 1.8-A-iv, right panel) demonstrated a spontaneous insertion and anchoring of the biomimetic probe within the lipid bilayer core. [150–153] As demonstrated by VanderSarl *et al.*, a planar electrode surrounded by an Au nanoring stacked in between two Ti layers which is functionalized with hydrophobic self-assembled monolayers produces gigaohm seals at the cell-electrode interface for

several days. [154] Stealth probe electrodes presenting similar nanopatterns achieved comparable performances. [155]

Junctional resistance minimization From an electrical perspective, providing an intracellular access is equivalent to maximizing the ratio between the seal and the junctional resistances. The junctional resistance minimization is usually triggered by an insertion mechanism such as mechanical pressure, electroporation, optoporation, or can also be achieved spontaneously, if the electrode geometry allows it. Spontaneous intracellular access is generally achieved using vertical nanowire-like electrodes with extreme aspect ratio. [136, 137] These geometric constraints often result either in very high electrode impedances [136] or in invasive structures [137] that prevent the cell to be in a favorable environment (cf. Figure 1.8-B-i).

Other examples in the literature manually insert nanoelectrodes into cells by applying mechanical pressure. [156–158] In Figure 1.8-B-ii, a polydimethylsiloxane substrate covered with cardiomyocytes is pushed toward a kinked nanowire FET until enough mechanical stress is applied to rupture the cell membrane and permit an intracellular access to the nanowire. The scalability of this method is however limited.

Electroporation is the most widely used method to insert on-demand micro-nano-electrodes into cells. [132, 134, 135, 143, 149, 159] It is based on the application of voltage pulses of sufficient magnitude that break the membrane dielectric thereby inducing formation of nanopores. When combined with nanoelectrodes, it is still not clear whether electroporation results into a single or several pores. [130] However, the effective nanopore diameter has been estimated to be ~ 20 nm for a 180 nm in diameter nanotube-like electrode, [141] and between 500 - 700 nm for a 1.5 μm in diameter micromushroom-like electrode. [143] Following electroporation, the recorded signal amplitude significantly increases as the junctional resistance is reduced. Nevertheless, this intracellular configuration is only temporary as the perforated cell membrane reseals over time. This period typically last between a few minutes for vertical nanowire [132, 134] or micromushroom-like electrodes, [142] and can go up to 100 minutes for hollow structures. [141] As illustrated in Figure 1.8-B-iii, hollow structures permit longer durations of stable recording.

More recently, optoporation has been reported to open transient pores into cell membranes without interfering with their electrical activity and demonstrated similar recording characteristics in comparison with electroporation. [140, 160] Disadvantages of optoporation include the need of plasmonic structures to locally enhance the light

electric field as well as a complex optical setup to accurately scan the electrode array with a laser only to trigger intracellular accesses.

Electrode impedance minimization The minimization of the electrode impedance is essential not only to reduce the signal attenuation defined by the voltage divider between the electrode and the stray components, but also to minimize the thermal noise and therefore maximize the signal-to-noise ratio. The electrode geometries usually employed to maximize the seal resistance often imply high electrode impedances (e.g., $R_{CT} \sim 10^{11}\Omega$ for micromushrooms). A simple strategy regularly followed to decrease the overall electrode impedance is to place several nanostructures per electrode (typically 9 nanostructures per electrode). [134] However, if one of the nanostructures is not totally covered by a cell, the seal resistance of the entire electrode is compromised. Additionally, the spatial resolution is also deteriorated. Furthermore, nanoneedle electrodes have been biased with a 1.5 V DC voltage to trigger the faradaic pathway at the electrode-electrolyte interface and reduce their charge transfer resistance R_{CT} . [149] Disadvantages of this method include the generation of toxic reactive oxygen species (ROS) that limit the recording duration. Finally, different materials and coatings were used to diminish the electrode impedance. [161] As illustrated in Figure 1.8-C, platinum black can be electrodeposited to increase the effective area of a microelectrode and therefore reduce its impedance. [135]

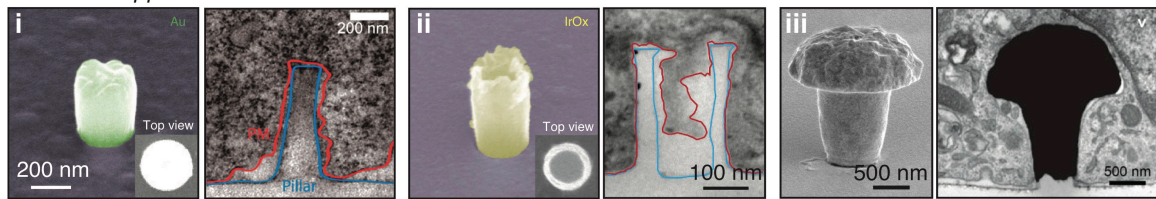
Stray impedance maximization The capacitive and resistive current leaks along the electrical tracks are often neglected when designing a micro-nanoelectrode array to perform intracellular recordings. However, a high stray impedance is essential to prevent signal attenuation between the electrode and the amplifier input. Simple designs considerations such as the addition of a thick insulating layer between the electrical tracks and the extracellular bath or the minimization of their width and length are already efficient to maximize the stray impedance. [154]

Nevertheless, the integration of CMOS amplifiers directly below the micro-nanoelectrode, similarly to HD-MEAs, is the most efficient way to get rid of stray impedances. [134,135] As illustrated in Figure 1.8-D, the distance between the nanoneedle-like electrodes and their embedded amplifier is nearly zero; hence preventing any current leaks between the electrode and the amplifier as well as minimizing the noise due to electromagnetic perturbations. Moreover, as for HD-MEAs, integrated CMOS electronics permit the increase of the electrode number per unit of area.

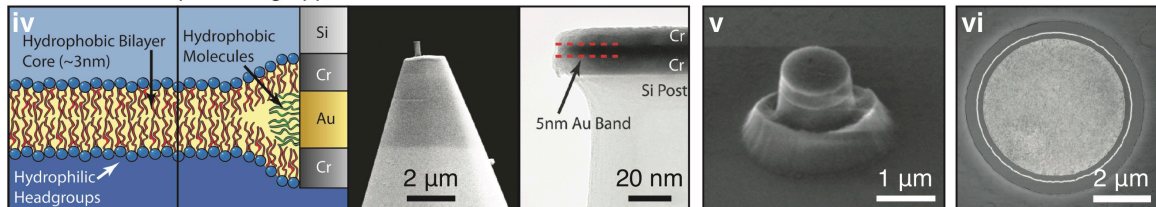
1.2. Electrophysiological methods: state-of-the-art

A Seal resistance maximization

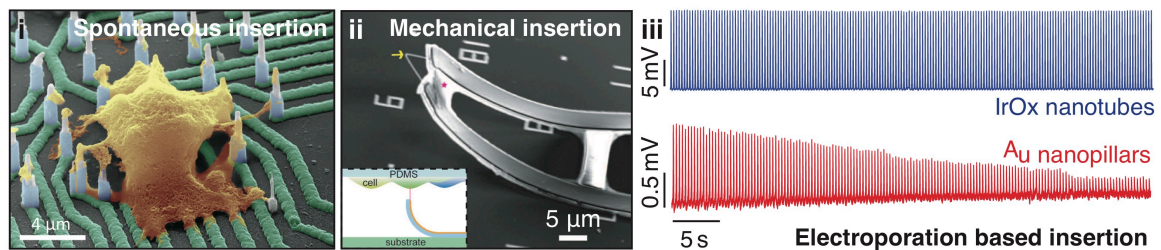
Geometric approaches



Biomimetic nanopatterning approaches



B Junctional resistance minimization



C Electrode impedance D Stray impedance maximization minimization

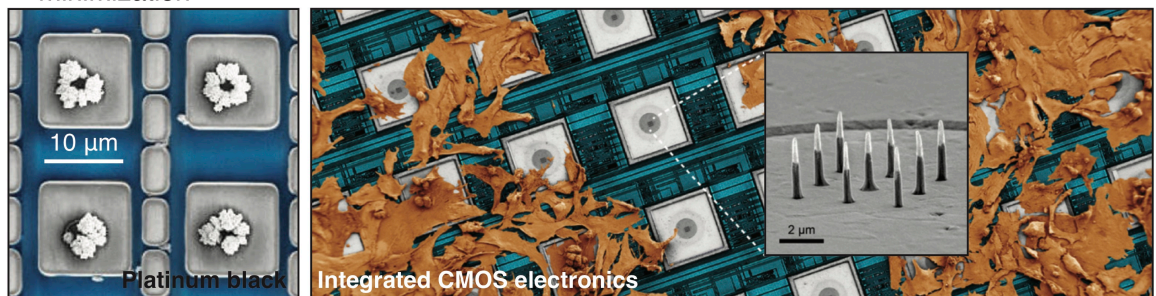


Figure 1.8: Optimization of intracellular recording with nanoelectrodes. **A)** Geometric and chemical approaches adopted in the literature to maximize the seal resistance. Geometric approaches include (i) nanopillar, (ii) nanotube, (iii) micromushroom-like nanoelectrodes. Chemical approaches presented focus on the nanopatterning of biomimetic self-assembled monolayers that fuse with the cell membrane to maximize the seal resistance. (iv) Alkanethiols monolayers selectively self-assembled with a 5 nm-thick Au band protruding from an AFM tip were demonstrated to fuse with the cell membrane and maximize the cell-electrode interface strength. (v and vi) Electrodes integrating this nanopattern achieved gigaseal formation. [130, 141, 145, 152, 154, 155] **B)** Insertion mechanisms based on (i) high aspect ratio electrode geometry, (ii) mechanical pressure, and (iii) electroporation reported in the literature. Electrical traces of cardiomyocyte action potentials following electroporation show that hollow geometries enable longer duration of stable recording compared to nanopillars. [137, 141, 156] **C)** Scanning electron microscopy image of nanoelectrodes coated with platinum black to decrease their impedance. [135] **D)** Protruding nanoneedle-like electrodes directly manufactured on CMOS amplifiers to maximize the stray component impedances. [130] Reproduced with permission.

Summary of the current micro-nanoelectrode arrays recording characteristics and limitations Over the last decade, micro-nanotechnology-based multi-electrode arrays have led to remarkable progress in the field of transmembrane voltage recording of excitable cells. In the last sections, we detailed different approaches adopted to overcome the challenges related to intracellular electrophysiology and more particularly to the seal and junctional resistance, as well as the electrode and stray impedance. In this section, we briefly discuss the intracellular recording characteristics achieved with micro-nanoelectrode arrays until now and their limitations. Table 1.1 summarizes the different micro-nanoelectrode array technologies developed over the last decade as well as the quality of the recorded signals in terms of amplitude, recording duration, and yield.

Vertical nanowires with extreme aspect ratio were developed to provide a spontaneous access to the intracellular space. Once coated with PDL, high-density nanowires could typically achieve seal resistances of a few hundreds of megaohms and were used to report intracellular activity from rodent and human induced pluripotent stem cell (HiPSC) neurons for several days, with amplitudes ranging from a few hundred microvolts to a few millivolts; and exceptionally 99 mV. However, the extreme geometry of these structures induce either a high impedance or a high invasiveness, and additionally high aspect ratio nanowires reported only electrical activity from a single-cells at a time.

Mechanically inserted kinked nanowire and nanotube FET transistors coated with lipids reported quasi non-attenuated action potentials from primary and HiPSC cardiomyocytes as well as primary neurons. These signals in millivolts were estimated from the FETs conductivity change. Limitations of these techniques include a short recording duration that ranges between a few minutes and up to one hour, together with a low-throughput as the devices are mechanically inserted into the cells one by one.

Electroporation based technologies such as nanoneedle, nanopillar, IrOx nanotube, and micromushroom-like electrodes are the most widely used techniques to record intracellular action potentials from cell networks over extended periods of time. For instance, nanoneedle-like electrodes were coated with standard cell culture coatings to optimize the seal resistance (\sim few hundreds of megaohms), composed of 9 nanostructures per electrode to which a DC voltage bias was applied to decrease the electrode impedance, and directly built on CMOS amplifiers to minimize the stray impedances. With this technology, 20 mV amplitude cardiomyocyte action potentials from hundreds of cells were simultaneously recorded for several days as electroporation enables

1.2. Electrophysiological methods: state-of-the-art

on-demand multiple intracellular access over extended periods of time. Even though the recording duration period following electroporation only lasts for ~ 20 minutes with nanoneedle electrodes, IrOx nanotubes and their hollow geometry demonstrated longer intracellular access up to 100 minutes. The maximal intracellular recording yield – defined as the ratio between the number of electrodes reporting intracellular access and the total number of electrodes covered with cells – reported for an electroporation based approach is $\sim 30\%$.

Optoporation based approaches (e.g., plasmonic nanoelectrodes or metaelectrodes) reported similar recording characteristics compared to electroporation techniques, with a slightly higher yield and lower amplitudes.

The micro-nanoelectrode arrays developed over the past decade enabled outstanding advances in the field of intracellular electrophysiology. However, current techniques permitting the investigation of electrophysiological characteristics at the cell network level are still limited in terms of recording amplitude, duration, and yield. In fact, all the geometric based approaches alone failed in providing a seal resistance higher than a few hundreds of megaohms; therefore limiting the quality of the recordings. Nonetheless, planar electrodes surrounded by a biomimetic nanopattern of self-assembled monolayers reported gigaseal formation with a yield up to 80% and an intracellular access for days. Protruding stealth probes presenting a similar nanopattern also demonstrated seal resistances as high as a gigaohm. [155] However, experiments conducted with these technologies were limited to impedance measurements and no records of intracellular electrophysiological activity were found. This can probably be explained by the complex fabrication process either based on focused ion beam (FIB) milling or mechanical polishing that limit the scalability of these techniques. Nevertheless, biomimetic nanopatterns are potentially the key to enable high-quality and stable intracellular recordings with micro-nanoelectrode arrays.

Table 1.1: Summary of the current micro-nanoelectrode arrays features and recording characteristics. Abbreviations are defined in the List of Abbreviations.

Technology and reference	Seal mechanism			Insertion mechanism	Electrode material	Electrode impedance [$R_{CT} C_{DL}$]	Stray impedance optimization	Cells tested	Recording characteristics		
	Electrode geometry	Electrode coating	R_{seal} [M Ω]						Amplitude [mV]	Duration [min]	Yield [%]
Single nanowire [136]	Vertical nanowire	PLL	-	Spontaneous	Si-Pt	'High'	None	GH3	10	0.15	Single cell
High-density nanowire [137]	Vertical nanowire	PDL + laminin	100	Spontaneous	Si	65 M Ω 8 pF	None	Rodent neurons HIPSC neurons	0.1-99 0.1-35	Days Days	Single cell Single cell
FET [156-158]	Kinked nanowire and nanotube	Lipid coating	-	Mechanical	FET	-	None	Chicken CMCs HIPSC CMCs DRG neurons	80 110 70	Seconds 15 3	Single cell Single cell Single cell
Nanoneedle [134, 135]	Vertical nanowire	PDL	100	Electroporation	Au or Pt	300 M Ω 1.2 pF 1.5V bias, 9 electrodes per pad	Integrated CMOS electronics	Rat CMCs Rat neurons	20 10	20 min periods for days 19	30 -
Nanopillar [133]	Vertical nanowire	Fibronectin	-	Electroporation	Pt	$Z_e = 12 \text{ M}\Omega @ 1 \text{ kHz}$ 5 electrodes per pad	None	HL-1	11.8	10 min periods for days	-
IrOx nanotube [141]	Vertical nanotube	Fibronectin	19	Electroporation	IrOx	141 M Ω - 9 electrodes per pad	None	Rat CMCs	15	100 min periods for days	-
Micromushroom [142-147, 162]	Micromushroom	Laminin PEI + laminin RGD peptides	100	Electroporation Spontaneous Spontaneous	Au	100 G Ω -	None	Rat CMCs Rat neurons Aplysia neurons	6 5 25	10 min periods for days Days Days	- 34.5 -
Plasmonic nanoelectrode [140]	Vertical nanotube	Polys-dl-ornithine	0.7	Optoporation	Au	5.5 G Ω 7.2 pF 9 electrodes per pad	Integrated CMOS electronics	HL-1	1.8	90	-
Plasmonic metaelectrodes [160]	Porous material	Fibronectin	-	Optoporation	Porous Au	-	Integrated CMOS electronics	Rat neurons Rat and HIPSC CMCs	1 5	80 40	- 85.4
Nanopatterned planar electrode [154]	None	Biomimetic nanopatterning	1'000	Electroporation	Pt	17.7 M Ω -	5 μm -thick insulating layer	HeLa	-	Days	80

1.3 Thesis positioning

1.3.1 Problem definition

Electrophysiological studies at the single-cell and cell-network levels play a central role in pharmacological screening. Over the last 50 years, the number of new compound approvals remained constant while the average cost of developing and gaining market approval increased exponentially, with an average present-day cost of nearly \$2.6 billion. [163] In neurology, the success rates for drug development associated with psychiatric and neurodegenerative diseases are 7.2 % and 9.6 %. [164] These high failure rates can be partially explained by the lack of high-throughput electrophysiological instruments available to assess electrophysiological characteristics of cell networks at the transmembrane level and over extended periods, which in turn limits provision of the dense-information content essential for the development of novel compounds. In this context, micro- and nanoelectrode arrays aiming to record intracellular activity have the potential to overcome the throughput limitations of the gold-standard patch-clamp technique without requiring genetic manipulation, as it is the case for optical methods. However, micro- and nanoelectrode arrays do not as yet provide stable and high-quality intracellular electrophysiological recordings.

1.3.2 Thesis objectives

The limited intracellular-recording performance of current micro- and nanoelectrode arrays is principally explained by their inability to form a high-seal resistance at the cell-electrode interface. Promising approaches to overcoming this aspect include micro- and nanoelectrodes designed with protruding geometries, or nanopatterned with biomimetic self-assembled monolayers. While geometric approaches alone have been widely investigated in the literature, microelectrodes combining sharp 3D geometries with biomimetic nanopatterns have not been used in electrophysiological studies.

This thesis proposes a novel nanofabrication technique that permits the scalable manufacturing of an original microelectrode integrating most of the recent technological advances. Compared to previous technologies, this new electrode combines a sharp geometry with a nanometer-wide biomimetic pattern aiming at optimizing the cell-electrode interface. Electrophysiological experiments with neonatal rat cardiomyocyte monolayers will be performed to investigate whether the 3D nanopatterned microelectrode array demonstrates improved recording performance compared to current state-of-the-art technologies. In addition, these experiments will assess the relative

contribution of sharp geometry, with respect to biomimetic nanopatterning, to the quality of the signal recorded. Additional applications of the developed technology are explored in the context of mechanobiological studies on cardiomyocytes and electrophysiological recordings from neuronal networks.

1.3.3 Thesis structure

The first part of this thesis details the development of a novel nanofabrication method based on ion beam etching redeposition to manufacture complex 3D multimerial nanostructures at the wafer-scale (Chapter 2). Subsequently, the novel nanofabrication technique is exploited to manufacture a volcano-shaped nanopatterned microelectrode array capable of recording intracellular action potentials from cardiomyocyte monolayers without the need for controlled electroporation (Chapter 3). Chapter 4 investigates whether electroporation improves the performance of nanopatterned microelectrode arrays in terms of action potential amplitudes, recording duration, and yield. Chapter 5 reports on a novel scanning probe microscopy (SPM) probe presenting the nanopatterned microelectrode at its apex; the probe is used in the context of mechanobiology. Finally, preliminary recordings performed on neural networks with nanopatterned microelectrode arrays are presented in Chapter 6.

Chapter 2

Ion beam etching redeposition for 3D multimaterial nanostructure manufacturing

This thesis chapter is adapted from our recently published article: B.X.E. Desbiolles, A. Bertsch, and P. Renaud, “Ion beam etching redeposition for 3D multimaterial nanostructure manufacturing”, *Microsystems and Nanoengineering*, vol. 5 p. 11, 2019.

2.1 Introduction

Recent advances in nanofabrication have led to significant discoveries in a wide range of areas, such as biosensing, nanofluidics, nanophotonics, and nanoelectronics. [165] Most of the nanofabrication techniques used today can be classified in two main categories: bottom-up and top-down. [166] Bottom-up fabrication methods use the interactions between molecules or atoms to build-up complex nanoscale assemblies in two or three dimensions. Atomic layer deposition, [167] molecular self-assembly, [168] and DNA self-assembly [169] are common examples of bottom-up nanofabrication methods. These processes can cover large areas with nanoscale features but suffer from a lack of control, particularly in the geometry of assembled structures.

Top-down approaches are based on the structuration of materials at the nanoscale, starting from a bulk material that was shaped by a series of steps that often include lithography, dry or wet etching, oxidation, and metallization, among others. High-resolution lithography methods are often used, such as optical lithography, [170]

Chapter 2. Ion beam etching redeposition for 3D multimaterial nanostructure manufacturing

e-beam lithography, [171] soft lithography, [172] nanoimprint lithography, [173] stencil lithography, [174–177] and scanning probe lithography. [178] Such methods allow for control over the dimensions, shapes, and characteristics of nanostructures typically over a length scale four orders of magnitude larger than an individual structure. [179] However, limitations include high operating costs, low scalability, and lack of versatility — especially for three-dimensional (3D) nanostructure manufacturing.

Using top-down microfabrication technologies in an “unconventional” but ingenious way allows for the manufacture of sophisticated nanostructures without pushing techniques to the limit or using complex and expensive dedicated manufacturing processes. For example, single-material sub-micron two-dimensional (2D) structures were successfully manufactured by evaporating a thin film onto a substrate covered with self-assembled monolayers of polystyrene microspheres. [180] The microspheres served as a mask for the pattern to be created in the interstitial spaces during the deposition step. The resulting 2D triangular structures were 500 nm in size and covered a large area of the substrate. In order to gain more control over structural shape and decrease the critical dimension, openings were patterned on a suspended gold membrane. Through tilted-angle Au evaporation, 100 nm single-material features of various geometries were obtained on a large-scale and at a low operating cost. [181] Even sub-10 nm nanostructures composed of several materials were fabricated using ingenuities. Chemical-mechanical polishing performed on tapered microstructures covered with a stack of several materials led to 5 nm-thick concentric Ti-Au-Ti nanorings at the wafer-scale. [154] Similar examples can be found in the literature; however, none describe a reliable method to produce complex 3D multimaterial nanostructures at the wafer-scale.

In this work, the use of local sputter-redeposition on photoresist sidewalls during ion beam etching [182–184] is proposed to manufacture multimaterial 3D nanostructures. Using this method, nanostructures of various shapes, profiles, heights, thicknesses, and complexity can easily be fabricated at the wafer-scale in a short period of time. The simplicity of this process, using standard microprocessing tools only, makes the nanofabrication of complex structures fast and accessible.

The potential of the present method was first investigated for silicon (Si) nanostructures. The fabrication of multilayered structures composed of non-silicon materials — hardly achievable using standard nanofabrication processes — is discussed within. The method was also used to manufacture complex structures optimized for specific applications.

2.2 Results

2.2.1 Single-material nanostructures

Figure 2.1-A illustrates the fabrication method studied in this work. A photoresist layer was patterned by standard photolithography onto a Si substrate, which was then bombarded with argon ions (Ar^+) during ion beam etching. Not only did this step lead to the etching of uncovered areas, but it also induced the local redeposition of etched materials onto the photoresist sidewalls. This material redeposition actually created the 3D nanostructures, and a final photoresist stripping completed the fabrication process.

Figure 2.1-B is a scanning electron microscopy (SEM) image of tapered cylinders composed of 60 nm-thick and 1.6 μm -high Si walls arranged in an array. These structures were created by patterning 1.5 μm circular openings in a photoresist layer prior to ion beam etching. The openings can be various shapes, as illustrated in Figure 2.1-C as well as in the Appendix A, Figure A.1. The dimensions achieved for the Si cylinders in this study are summarized in Table 2.1. Walls as thin as 6 nm and as thick as 200 nm were successfully created with heights varying from 200 nm to 15 μm and diameters varying from 300 nm to 200 μm .

The profile of redeposited structures can also be tuned by adjusting the dose of the photolithography step. A high dose leads to straight walls, whereas a low dose induces curved walls, as shown in Figure 2.1-D. By patterning pillars instead of holes, the structure profile can even be inverted (cf. Figure 2.1-D).

As shown in Figure 2.1-E to G, 80 nm-thick intersecting nanowall networks were obtained by defining photoresist lines during photolithography and repeating the presented method twice. The fabrication process was simple, scalable, and led to homogeneous structures at the wafer-scale.

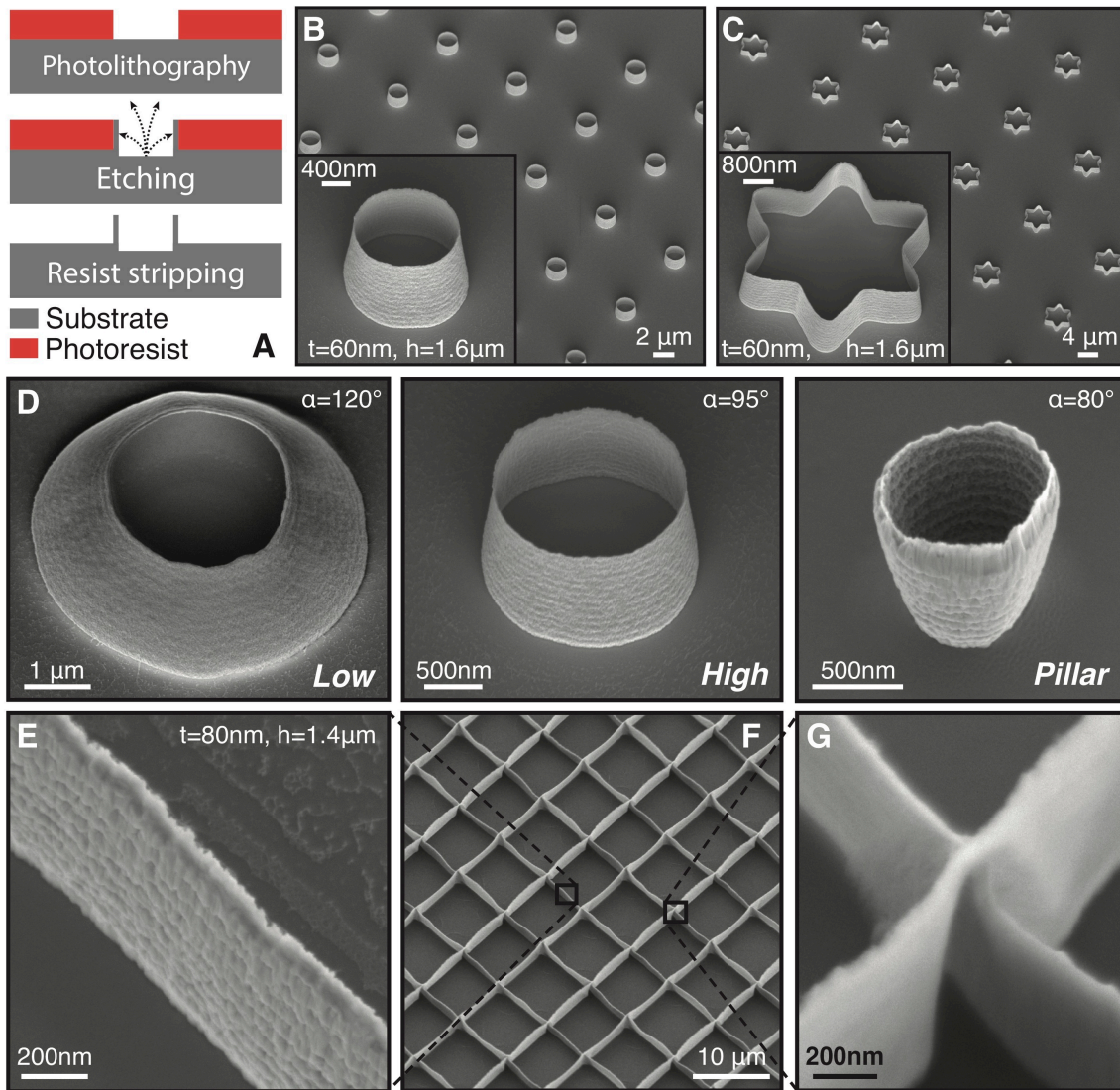


Figure 2.1: Structures created by Si redeposition on photoresist sidewalls during Ar^+ ion beam etching. **A)** Illustration of the process flow used to create Si nanostructures: during ion beam etching, the photoresist sidewalls are sputtered by the etched material and after resist stripping, nanostructures are obtained. SEM images of **B)** cylinder arrays, **C)** star arrays composed of 60 nm-thick and 1.6 μm -high walls, and **D)** profiles obtained by changing the dose from low to high during photolithography. The structure profile can even become negative by performing the redeposition step on a pillar rather than a resist opening. The angle α is defined between the substrate and the cylinder wall. For a vertical wall $\alpha = 90^\circ$. **E)**, **F)**, and **G)** SEM images of 80 nm-thick and 1.4 μm -high intersecting nanowall arrays. Tilt angle of 30° .

Table 2.1: Summary of successfully manufactured Si cylinder dimensions.

	Wall thickness [nm]	Diameter [nm]	Height [nm]
Min	6	300	200
Max	200	200'000	15'000

Note that the nanostructure surfaces are the exact replica of the photoresist side-walls. As demonstrated in Figure 2.2, their surface roughness can be smoothed by reflowing the photoresist before redeposition. It is not an intrinsic limitation of the fabrication process.

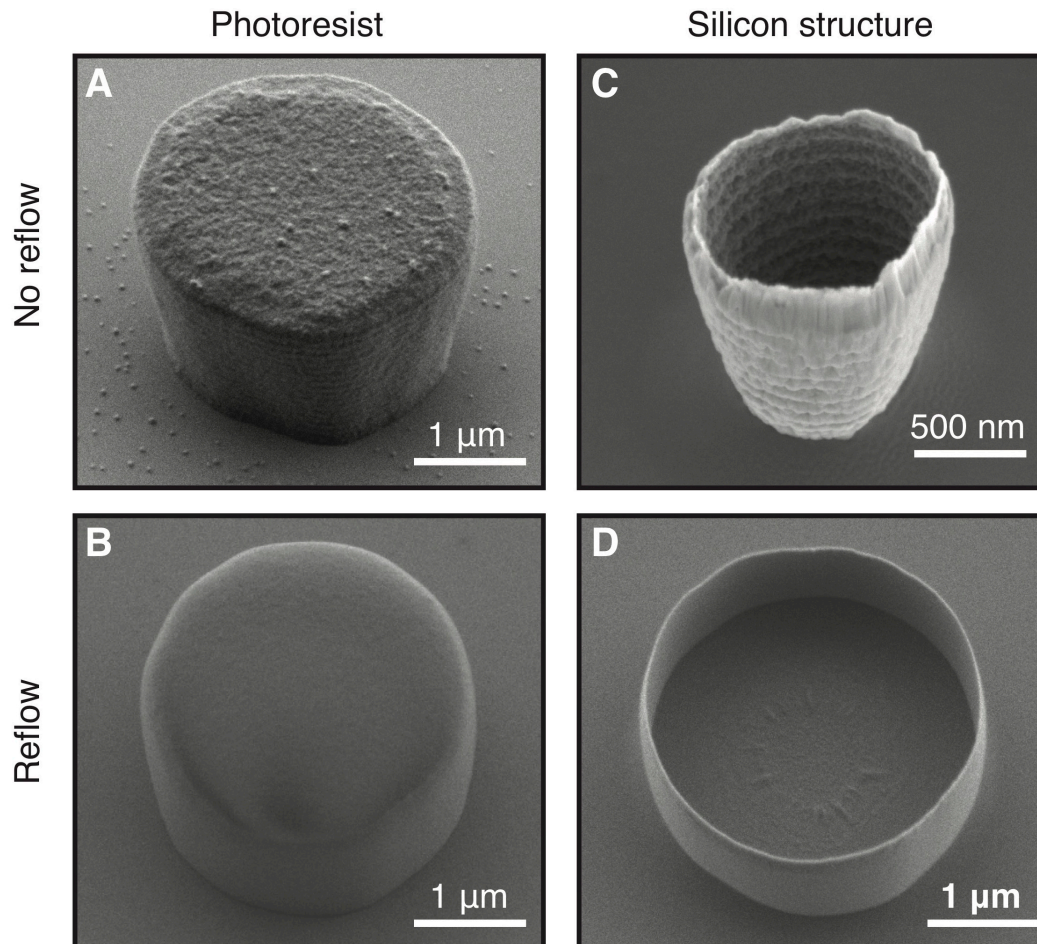


Figure 2.2: *Smoothing of the nanostructure surface roughness by photoresist reflow (160°C for 2 minutes). SEM images of the photoresist mask non-treated A), or treated B), by thermal reflow. C) and D) show typical Si nanostructures obtained respectively without, or with, thermal reflow. Tilt angle of 30°C.*

2.2.2 Multimaterial nanostructures

Multimaterial nanostructures can be produced by combining the studied fabrication method with standard deposition processes, as illustrated in Figure 2.3-A to C. In Figure 2.3-A, several layers of different materials were deposited onto the substrate prior to patterning the photoresist pillars. During ion beam etching, the material of the top layer was first redeposited on the photoresist sidewalls, followed by the materials in deeper layers. The substrate material was redeposited last.

Chapter 2. Ion beam etching redeposition for 3D multimaterial nanostructure manufacturing

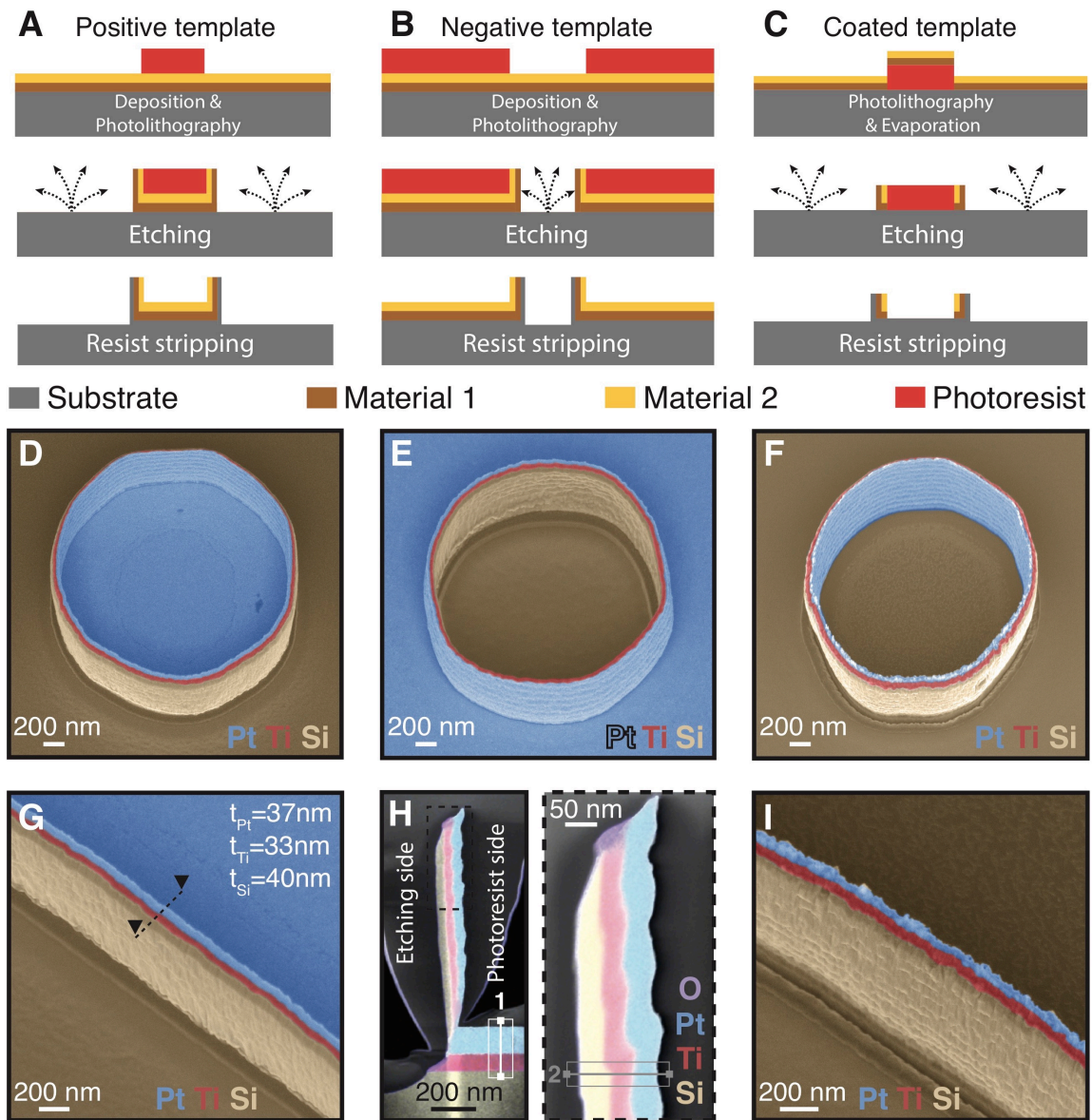


Figure 2.3: Multilayered structures created by the redeposition of different materials. A), B), and C) illustrate three different process flows and D), E), and F) show the respective structures obtained by these three methods, each differing by the location of the different materials used in the final structures. More precisely, **A)** Layers of different materials were deposited before patterning pillars by photolithography; **B)** Layers of different materials were deposited before patterning openings by photolithography; **C)** Layers of different materials were deposited after patterning pillars by photolithography. **G)** Nanowall created using layers of Si, Ti, and Pt corresponding to the fabrication process presented in A); **H)** TEM image combined with an EDX spectroscopy map of a redeposited nanowall cross-section located with dashed lines in G). The photoresist was on the right side of the nanowall during ion beam etching. A carbon layer was locally deposited onto the wall to protect the structure during sample preparation; **I)** Nanowall created using layers of Si, Ti, and Pt corresponding to the fabrication process presented in C). Tilt angle of 30°. The colors in images D) to G) and I) were added in post-processing based on the contrast resulting from the detection of back-scattered electrons. In H), the colors directly result from EDX analysis.

As an example, an SEM image is presented in Figure 2.3-D showing a cylindrical wall obtained using this method on a 2 μm in diameter photoresist template pillar patterned on top of layers of titanium (Ti) and platinum (Pt) deposited on a Si substrate. The interior of the obtained cylindrical structure was composed of Pt, while the outside was composed of Si and delimited by a sharp multimaterial nanowall composed of Si-Ti-Pt layers. In Figure 2.3-B and E, openings in the photoresist were patterned, rather than pillars, using the same sequence of deposited metal layers on a Si substrate (as in Figure 2.3-D). The obtained redeposited structures have similar shapes and dimensions to the one presented in Figure 2.3-D, though the order of the materials in this structure were opposite, with the inner layer of the obtained structure being Si and the outer layer being Pt. The Ti layer remained in the middle of the sharp wall. Similarly, Figure 2.3-C and F demonstrate what occurs when the metal layers are deposited after the photolithography step. Multimaterial cylinders composed of up to six different layers were successfully fabricated, as shown in Figure 2.6-A. If lines are patterned by photolithography, centimeter-long multimaterial nanowalls can be made, as shown in Figure 2.3-G and I. A cross-section of a redeposited multilayered structure was characterized by transmission electron microscopy (TEM) combined with energy dispersive X-ray spectroscopy (EDX). Figure 2.3-H shows how the layers of different materials deposited on the substrate were redeposited on photoresist walls during ion beam etching, with the topmost layer undergoing etching and redeposition first. The redeposition was uniform along the wall and became thinner at the intersection with the planar layers. Native titanium oxide was observed at the end of the Ti layer in contact with air. The detailed composition of each redeposited layer obtained by quantitative EDX analysis is summarized in Table 2.2.

Table 2.2: Composition of the redeposited layers presented in Figure 2.3-H measured by EDX.

Layer	Si[%]	Ti [%]	Pt [%]	Ar [%]	Traces Cu, Cr, Fe [%]
Si	88.5	4.8	3.0	1.5	2.2
Ti	1.8	82.6	11.5	1.4	2.7
Pt	8.3	1.1	87.3	1.0	2.3

Performing EDX line scan analysis on three different samples at the two positions shown in Figure 2.3-H allowed for the accurate measurement of the thickness of each redeposited layer. Table 2.3 presents the redeposition ratio and rate obtained by measuring the thickness of the initial and redeposited layers for each material. Materials that were difficult to etch have slow redeposition rates and high redeposition ratios.

Chapter 2. Ion beam etching redeposition for 3D multimaterial nanostructure manufacturing

Table 2.3: Summary of the redeposition ratios and rates for Si, Ti, and Pt during ion beam etching using Ar^+ ions.

Material	Thickness [nm]		Redeposition ratio [%]	Etching rate [nm/min]	Redeposition rate [nm/min]
	Substrate	Wall			
Si	110	40	36.3	73.3	26.7
Ti	80	33.3	41.6	35.5	14.8
Pt	115	36.6	31.8	92	29.3

Fast Fourier transform pattern analysis of high resolution TEM images demonstrated that the materials composing the walls of the nanostructure were highly amorphous, while those constituting the substrate were more crystalline (cf. Figure 2.4). The ion beam etching step induced a change of crystallinity in the redeposited materials.

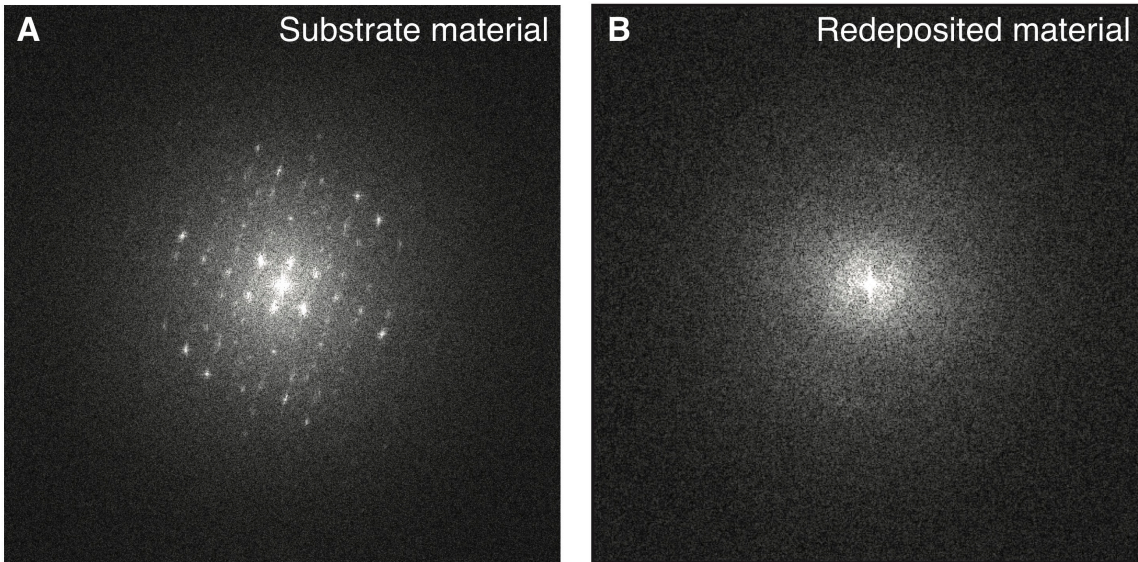


Figure 2.4: Fast Fourier transform pattern analysis of high resolution TEM images. **A)** Diffraction pattern of a Ti layer evaporated on the substrate before the redeposition process. **B)** Diffraction pattern of the same layer after the redeposition process. The Ti layer is more amorphous after ion beam etching redeposition.

2.2.3 Complex nanostructures

Combined with conventional micro-electro-mechanical systems (MEMS) fabrication techniques, this simple fabrication method can lead to the manufacture of complex 3D multimaterial nanostructures. The SEM image presented in Figure 2.5-A shows nanowalls alternately composed of Ti and Si along the longitudinal direction. This was performed by patterning the substrate with Ti lines prior to the fabrication of the nanostructures by redeposition and defining line openings perpendicular to the

Ti lines by photolithography. During ion beam etching, materials from the Ti lines and Si substrate were locally redeposited on the photoresist sidewalls, leading to the formation of nanowalls made alternately of Ti and Si along the longitudinal direction. As Ti was not etched entirely during ion beam etching, Ti lines could still be observed on the substrate. The alternating Ti-Si composition of the nanowalls along the longitudinal direction has been validated by EDX line scan analysis, as shown in Figure 2.5-B.

Nanochannels of any length and shape can be obtained by covering Si nanowalls with a silicon dioxide (SiO_2) layer and subsequently selectively etching the Si nanostructures (cf. Figure 2.5-C). Such nanochannels can be made at the wafer-scale, as illustrated in Figure 2.5-D and E. A cross-section of this type of structure was obtained by focused ion beam (see Figure 2.5-F), which highlighted a sub-200 nm cavity trapped between SiO_2 walls.

Figure 2.5-H presents an SEM image of two 50 nm-thick and 800 nm-high SiO_2 walls separated by an 80 nm gap. This was performed by depositing a Si layer sandwiched between two SiO_2 layers on the substrate before photolithography. After the redeposition, occurring during the Ar^+ ion beam etching process, a multilayer nanowall composed of SiO_2 -Si- SiO_2 was obtained. The Si layer was sacrificial and was etched away to create the nanogap separating the two nanowalls (cf. Figure 2.5-G).

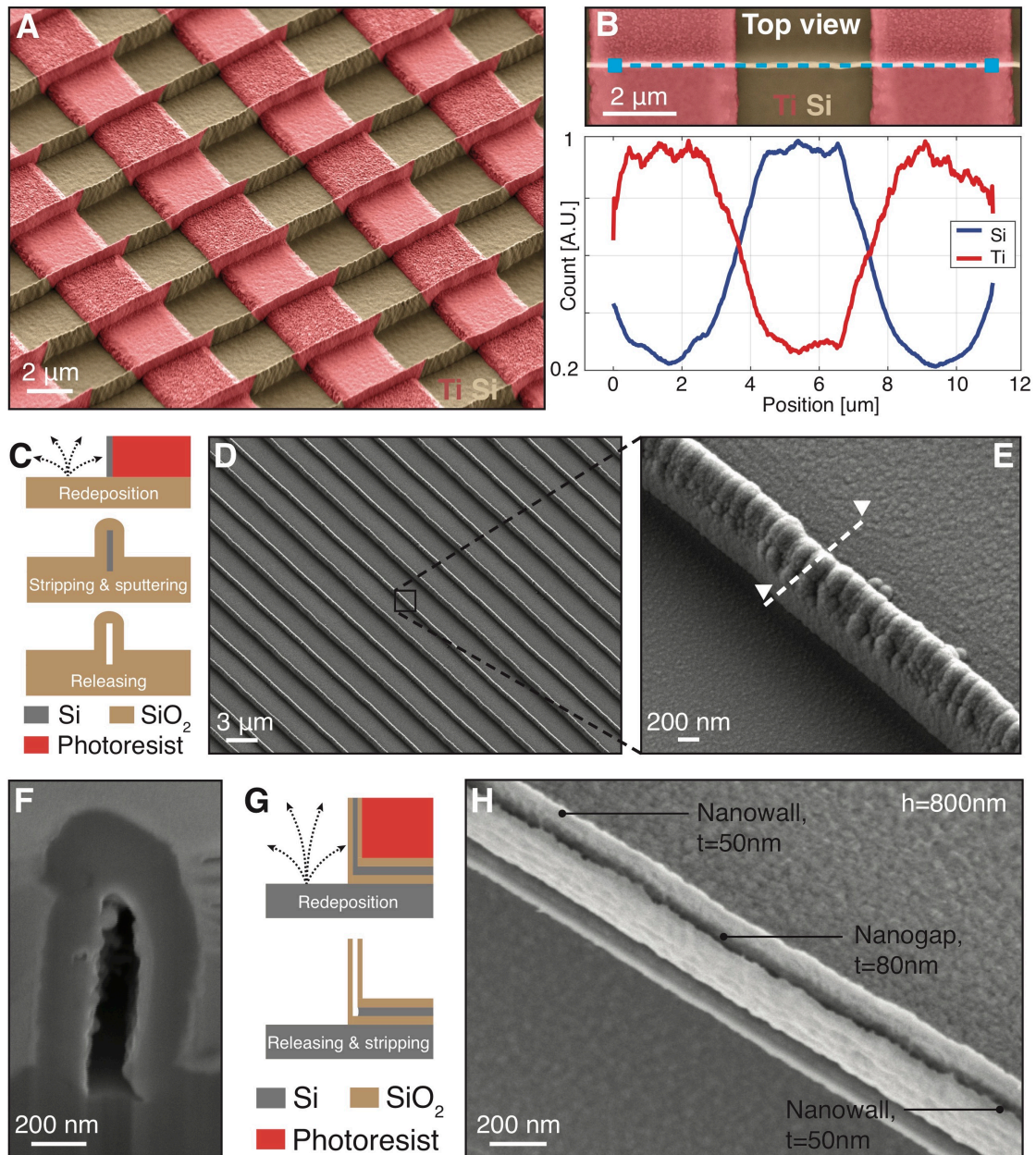


Figure 2.5: *Complex nanostructures manufactured by the redeposition of several materials.* **A)** SEM image of nanowalls alternately composed of Si and Ti along the longitudinal direction. Perpendicular to the walls, pre-patterned Ti lines on the Si substrate were used to build the multimaterial walls during ion beam etching. **B)** EDX line scan analysis of the nanowall material composition. The blue dashed line in the SEM image indicates the location of the analysis. **C)** Illustration of the fabrication process used to manufacture SiO₂ nanochannels. A SiO₂ layer was sputtered on a Si sacrificial template made by ion beam etching redeposition. The template was then removed by isotropic Si dry etching. **D)** and **E)** SEM images of the resulting SiO₂ nanochannels. **F)** SEM image of the nanochannel cross-section indicated by the dashed line in E) after Si release. **G)** Illustration of the fabrication process used to manufacture two SiO₂ nanowalls with a nanogap in between. A Si sacrificial template was fabricated in the middle of two SiO₂ nanowalls by ion beam etching redeposition. After release, the nanogap was obtained. **H)** SEM image of two 50 nm-thick and 800 nm-high SiO₂ nanowalls separated by an 80 nm gap. Tilt angle of 30°.

Repeating such a process twice can lead to multimaterial suspended structures. In Figure 2.6-B, suspended Ti nanowalls alternately joined by a thin membrane can be observed on Si nanowall networks.

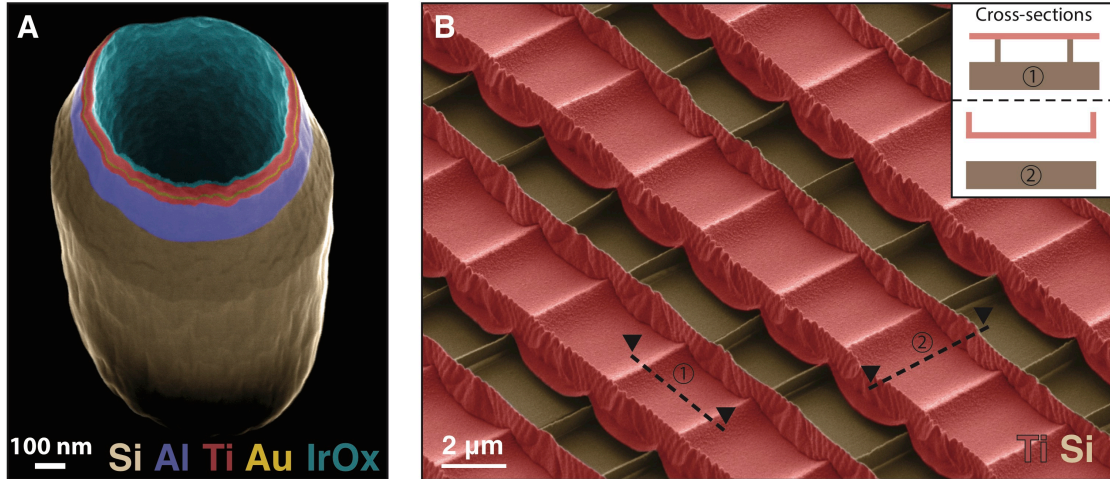


Figure 2.6: *Additional multimaterial complex nanostructures made by Ar^+ ion beam etching. A) SEM image of a multilayered cylinder composed of five different materials: IrOx, Ti, Au, Al, and Si B) SEM image of suspended Ti nanowalls, alternately joined by a thin Ti membrane standing on a Si nanowall networks. The cross-sections 1 and 2 are illustrated in the insert. Tilt angle of 30° .*

2.3 Discussion and applications

Using a simple fabrication method based on the redeposition of materials during Ar^+ ion beam etching, 3D nanostructures can be manufactured at the wafer-scale in a very short amount of time. The shape, dimension, and profile can be engineered to specific applications without using nanolithography techniques, but rather using standard microprocessing tools only, resulting in a decreased cost compared to the use of technologies such as e-beam. Various materials, from metals to ceramics, can be patterned into 3D sub-100 nm nanostructures. Pt, Ti, Si, SiO_2 , Au, IrOx, and Al have been successfully used in the redeposition step. This list can certainly be extended to any sputterable material, resulting in unprecedented freedom in the choice of nanostructure fabrication materials. This diversity brings significant improvements to the current state of the art for nanostructure manufacturing, where materials are limited for many nanopatterning technologies. Additionally, the nanofabrication method described here can be used advantageously to replace more complex manufacturing processes previously presented in the literature.

2.3.1 Biosensing

Gold nanostraws with a geometry similar to the structures presented in Figure 2.1-B were used as plasmonic structures to optoporate cell membranes and provide intracellular access. [140] The nanostraws were fabricated using secondary electron lithography generated by ion beam milling, a top-down technique allowing precise control over the geometry of the hollow structure, though this process was hardly scalable. With some adjustments, the method presented here could be used to fabricate such gold nanocylinders at the wafer-scale.

Not only does this fabrication method allow for the manufacture of 3D nanostructures composed of non-standard materials, but it also enables the easy patterning of multimaterial 3D nanostructures, potentially increasing applications. With minor adjustments, the multimaterial walls presented in Figure 2.5-A could be used to fabricate 3D electrodes, thermal oscillators, or electrostatic actuators. Specifically, the structure shown in Figure 2.3-E is very similar to the multimaterial feature built by Van Dersarl *et al.*, [154] where “un-conventional” top-down techniques were used to fabricate a 10 nm-thick protruding gold nanoring sandwiched between two Ti layers and one SiO₂ layer surrounding a planar electrode. The purpose was to optimize the cell-electrode interface and improve the electrophysiological recording quality. This was done by performing chemical-mechanical polishing on a micro-patterned surface covered with Ti-Au-Ti-SiO₂ layers. Even if the fabrication method used was ingenious, it was limited by the lack of homogeneity induced during the polishing step. In order to provide greater homogeneity to the structures over the entire wafer area, the redeposition process described here would be advantageous to fabricate similar structures using openings in photoresist layers as a template for multimetal redeposition.

This novel technology also provides new opportunities for the detection of electrochemically active molecules using nanoscale redox cycling structures, where two electrodes separated by a nanogap are usually used to collect the electrochemical current induced by redox reactions at the interface. Interestingly, the sensor sensitivity is improved by reducing the nanogap dimensions, due to a shorter diffusion time between the two electrodes. [185] In the literature, embedded nanochannels made by conventional nanofabrication techniques, [186, 187] or protruding sensors produced by focused ion beams [185] are used. However, the embedded geometry often prevents a fast and direct collection of biological molecules, whereas the fabrication of focused ions beam based devices is not scalable. Following the fabrication process illustrated in Figure 2.5-G - with Pt-SiO₂ stacks instead of SiO₂ - protruding and insulated vertical electrodes, separated by a nanogap could potentially be manufactured at the

wafer-scale by ion beam etching redeposition. These electrodes could easily be integrated with microfluidic chips and guarantee a minimal distance with the molecule of interest, enhancing the temporal resolution of the recording. Furthermore, it has been demonstrated that the smoothening of the photoresist sidewalls before ion beam etching leads to a more homogeneous redeposition with a smoother surface roughness. This could drastically decrease the minimal nanogap dimension achievable with this technology and significantly improve the sensor sensitivity.

2.3.2 Nanofluidics

The selective removal of a specific layer in a multimaterial nanostructure allows for an increase in the degree of complexity of achievable features. As shown in Figure 2.5-C to F, nanofluidic channels can be fabricated over a large area by using redeposited silicon as a sacrificial layer. In the literature, similar nanochannels from 50 nm to 300 nm-wide were obtained by reactive ion etching of a quartz substrate protected by a photoresist mask previously patterned using a stepper. [188]

2.3.3 Nanophotonics

Manufactured in a similar manner, the structures in Figure 2.5-H are comparable to the vertically-oriented plasmonic nanogaps fabricated by metal deposition and anisotropic etching used for surface-enhanced Raman spectroscopy. [189] The method presented here is an alternative to fabricating these types of nanopatterns in a short period of time without the intervention of expensive and time-consuming processes, making such devices more accessible.

By repeating the redeposition process, the obtained structures become even more sophisticated. Suspended multimaterial nanowall networks can be obtained quickly at the wafer-scale. Such structures appear similar to the photonic components found in the literature. In particular, it was demonstrated that the direct patterning of titanium dioxide using femtosecond laser pulses led to comparable patterns. [190] Using the redeposition of the photoresist sidewalls during ion beam etching could potentially simplify the fabrication process and make it more scalable.

2.4 Conclusion

In this chapter, a novel “unconventional” nanofabrication method exploiting the redeposition during Ar^+ ion beam etching was proposed to manufacture 3D multima-

terial sub-100 nm nanostructures at the wafer-scale. This simple fabrication process provided a rapid and lower-cost alternative to conventional nanofabrication techniques, with outstanding freedom in the choice of materials. Complex nanostructures such as nanochannels, multimaterial nanowalls, as well as suspended multimaterial networks were successfully fabricated in a few steps using the presented method. The potential applications were discussed based on similar examples from the literature. This nanofabrication method being integrable within other process flows may allow for new technological developments in the field of nanotechnologies.

2.5 Materials and methods

2.5.1 Fabrication of multilayered structures

A standard four-inch Si substrate (thickness 525 μm , orientation $\langle 100 \rangle$, p-doped) was sputter-coated by 100 nm of Ti and 100 nm of Pt using a Spider600 sputter-coater (Pfeiffer Vacuum, France). The substrate was spin-coated with a 1.4 μm thick layer of AZ nLof 2020 photoresist (MicroChemicals, Germany) using an EVG150 spin-coater/developer (EVG, Austria) and was exposed with an i-line VPG200 direct laser writer (Heidelberg, Germany) using doses between 50 mJ/cm^2 and 150 mJ/cm^2 . After a post-exposure bake at 110 $^\circ\text{C}$ with a 50 μm proximity gap for 75 seconds, the wafer was developed over 46 seconds using an AZ 726 MIF commercial developer (MicroChemicals, Germany) and was dispensed using an EVG150 coater/developer. The sample was then bombarded with Ar^+ ions at an incident angle of 0° using an IBE350 ion beam etcher (Veeco, USA). Materials from the substrate were etched and redeposited on the photoresist sidewalls. The photoresist was finally stripped using a 500W O_2 plasma (O_2 flow 400 mL/min) for 7 minutes with a TePla300 microwave plasma system (PVA TePla, Germany). Structures higher than 3 μm were fabricated using a thick layer of AZ 40 XT photoresist (MicroChemicals, Germany).

2.5.2 Electron microscopy

All scanning electron microscopy images were taken with a Merlin SEM (Zeiss, Germany). In order to highlight the difference in contrast between the two materials, secondary electrons and back-scattered electrons were collected during image acquisition. For the EDX analysis leading to Figure 2.5-B, the voltage used was 3 kV, which was sufficient to observe L_α Ti (0.452) and the K_α Si (1.739) X-ray characteristics. Scanning transmission electron microscopy images and the corresponding EDX analysis (cf. Figure 2.3-H) were done using a Tecnai Osiris TEM (FEI, USA). In order to

2.5. Materials and methods

obtain reliable map data, the acquisition time was set to 10 min/image during EDX analysis.

Chapter 3

Nanopatterned volcano-shaped microelectrode arrays for spontaneous intracellular recording of cardiomyocyte action potentials

This thesis chapter is adapted from our recently published article: B.X.E. Desbilles, E. de Coulon, A. Bertsch, S. Rohr, and P. Renaud, “Intracellular recording of cardiomyocyte action potentials with nanopatterned volcano-shaped microelectrode arrays”, *Nano Letters*, vol. 19, pp. 6173-6181, 2019.

3.1 Introduction

Cardiovascular disease is the primary cause of morbidity and mortality worldwide and responsible for more than 40 % of deaths in Europe alone. [191] Among both disabling and fatal events, cardiac arrhythmias play a central role and research efforts aimed at elucidating underlying mechanisms are extensive. They range from experiments at the subcellular level to experiments with large animals. Within this spectrum, electrophysiological studies performed at the single-cell and cell network level form an important intermediate platform. [192] Experimental approaches used for studies at the cellular and cell network level include patch clamp recordings of single-cells [193] and optical [194] or electrogram [113, 195] recordings for assessing cell network behavior in terms of action potential generation, propagation and establishment of reentrant activity. Electrogram recordings with extracellular multielectrode arrays (MEAs) are

Chapter 3. Nanopatterned volcano-shaped microelectrode arrays for spontaneous intracellular recording of cardiomyocyte action potentials

non-invasive and permit long-term measurements. They are primarily used for assessing network activity in cultured cell monolayers or slice preparations. Their disadvantage consists of the lack of reporting transmembrane voltage changes which are of interest when trying to relate specific activity patterns to changes in action potential configuration and the occurrence of early or delayed afterdepolarizations. This disadvantage is overcome by multisite optical recordings of transmembrane voltage with voltage sensitive dyes (VSDs) or genetically encoded voltage indicators (GEVIs; optogenetic reporters). [196] Disadvantages of optical techniques include VSD phototoxicity that limits the duration of experiments to a few minutes [73] and, for GEVIs, the circumstance that experiments are limited to tissues that have been genetically modified as to express suitable optogenetic reporters of transmembrane voltage. Also, neither of these methods reports absolute values of transmembrane voltage.

Over the last decade, new approaches based on micro-nanotechnologies were developed with the aim of providing long-term intracellular recordings from cell networks that overcome the shortcomings of standard optical and MEA recording techniques. [128–130] Approaches proposed consisted of sharp nanopillar [132–134, 140, 141], gold micro-mushroom [146, 147], or plasmonic [160] electrode arrays, where the penetration of the sensing electrode into the cell is triggered by electro- or optoporation. With these techniques, simultaneous intracellular recording of action potentials from cardiomyocyte networks could be obtained after the penetration triggering event. Field-effect transistors mounted on nanowires and mechanically inserted inside electrogenic cells were shown to produce similar results. [156–158]

Until now, electrode geometries designed with the aim to permit passive insertion into cell membranes have failed to produce a cell-electrode interface that is stable over extended periods of time. [197] A promising approach that overcomes this problem consists of patterning nanoscale hydrophobic bands on otherwise hydrophilic substrates that allow the insertion of manufactured structures into cells. [150–152, 155] As demonstrated by VanderSarl *et al.*, a planar electrode surrounded by an Au nanoring stacked in between two Ti layers which is functionalized with hydrophobic self-assembled monolayers produces gigaohm seals at the cell-electrode interface for several days. [154]

In the present study, a novel type of microelectrode that integrates the recent technological advances developed by Almquist *et al.* [150] into an original structure is proposed to perform opto/electroporation-free intracellular recording from cell networks. Because of its resemblance with a volcano, the novel nanopatterned microelectrode was named “nanovolcano” – “nano” standing for “nanopatterned”. As illustrated in

Figure 3.1-A, the inner surface of the 2 μm -wide nanovolcano consists of a large conductive three-dimensional area made of Pt that ensures a low access-impedance to the intracellular space. The outside of the structure is covered with a 50 nm-thick insulating SiO_2 layer that diminishes the current leak from the electrode. Furthermore, a 10 to 20 nm-thick Au nanoring, functionalized with self-assembled monolayers of alkanethiols and stacked in between two Ti layers, protrudes from the structure to fuse with the cell membrane thereby optimizing the cell-electrode interface (see Appendix B, section B.1). Finally, the 100 nm-thick multilayered nanovolcano wall is shaped similar to nanopillars that induce high curvature regions in the cell membrane which maximize the coupling between the cell and the microstructure. [138]

Neonatal rat cardiomyocytes were cultured for several days on the nanovolcano arrays and electrophysiological recordings were performed to investigate whether nanovolcanoes provide intracellular access to the cells. Signals recorded from up to 30 % of the nanovolcanoes displayed the typical shape of rat cardiomyocyte action potentials thereby demonstrating that the nanopatterned microstructures provided successful intracellular access to the cells.

3.2 Results

3.2.1 Microfabrication

The nanovolcano was manufactured by exploiting the local redeposition on the photoresist sidewalls occurring during argon ion beam etching. [198] As illustrated in Figure 3.1-B, openings with a diameter of 2 μm were patterned into a negative photoresist layer by standard photolithography thereby exposing the multilayered Ti-Pt-Ti-Au-Ti- SiO_2 -coated glass substrate. During argon ion beam etching, part of the etched material from the substrate was redeposited on the sidewalls of the photoresist opening which resulted in the build-up of the multilayered wall of the nanovolcano. The redeposition of the stacked layers of materials occurred in reverse order, starting from the top most layer (SiO_2) and being stopped when the Pt layer was partially etched. A final resist stripping step completed the nanovolcano manufacturing process and resulted in the structure shown by the scanning electron microscope (SEM) image in Figure 3.1-C. Following the formation of nanovolcanoes, 3 μm -wide conductive tracks were patterned by conventional ion beam etching to independently interface each microelectrode to the peripheral connecting pads. To reduce capacitive current leaks from these tracks, a 4.5 μm -thick SU8-insulating layer was structured such as to result in 20 μm -wide openings around each nanovolcano.

Chapter 3. Nanopatterned volcano-shaped microelectrode arrays for spontaneous intracellular recording of cardiomyocyte action potentials

The redeposited multilayered structure was characterized by transmission electron microscopy (TEM) combined with energy dispersive X-ray spectroscopy (EDX). Figure 3.1-D and E show redeposition of the etched substrate layers on the photoresist sidewalls during ion beam etching with the topmost layer undergoing etching and redeposition first. The inner side of the wall is conductive and contiguous with the active electrode area, whereas the outer side (SiO_2) is insulating (IrOx was used instead of Pt for TEM imaging in Figure 3.1-E). The two titanium layers on either side of the gold nanoring prevent its diffusion through the structure. The gold nanoring thickness was 18 nm as determined by EDX on a single linescan (cf. dashed line in Figure 3.1-E). The redeposition was uniform along the entire wall.

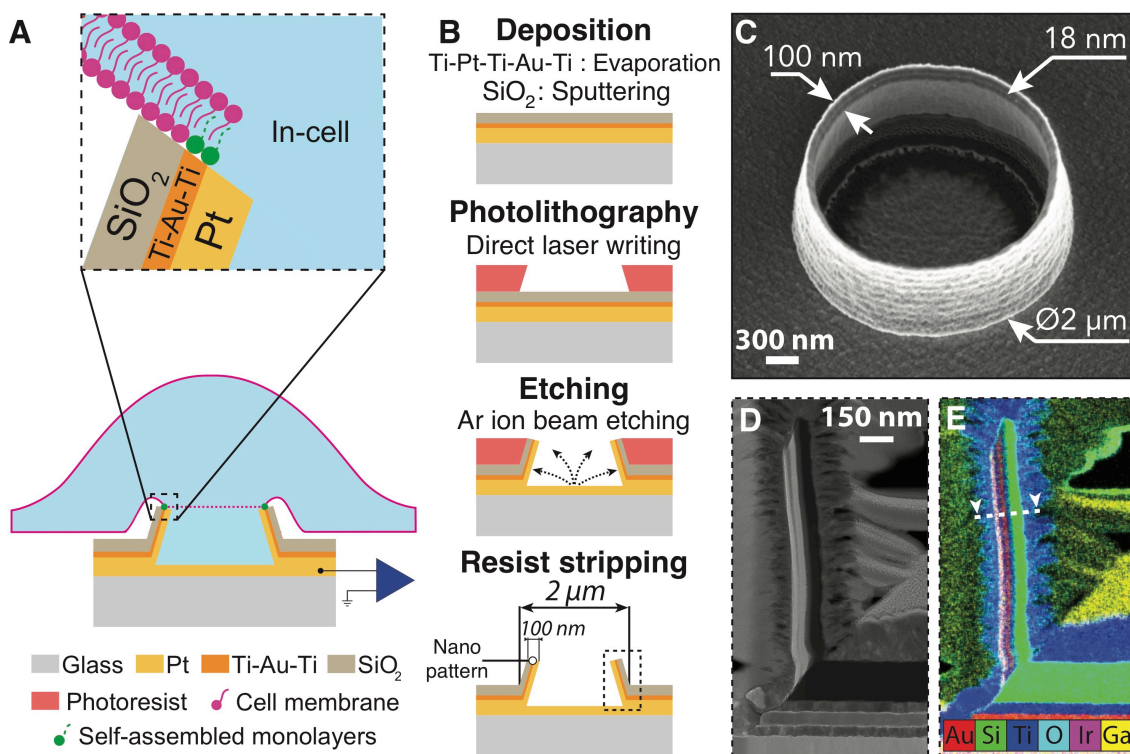


Figure 3.1: *Concept and microfabrication of nanovolcanoes.* **A)** Schematic drawing showing the overall structure of the nanovolcano and the interface to a cell. The dashed lines represent the junctional cell membrane at the cell-electrode interface. **B)** Microfabrication process flow used to manufacture the nanopatterned microelectrode. During ion beam etching, the material etched from the substrate is redeposited onto the photoresist sidewalls and the nanovolcano emerges after photoresist stripping. **C)** SEM image of the microelectrode. **D)** and **E)** TEM image combined with EDX spectroscopy map of the redeposited multilayered wall. The thickness of each redeposited layer was measured along the dashed line.

Throughout the thesis, different layouts of the nanovolcano array were developed where mainly the pitch, and the dimension and number of planar electrodes per device were adjusted. The nanovolcano geometry, however, was kept constant. Figure 3.2

depicts the latest version of the layout used in this thesis. The array is composed of 32 recording microelectrodes (28 nanovolcanoes and 4 planar Pt electrodes with a diameter of $40\ \mu\text{m}$), 2 stimulation dipoles, and 4 reference electrodes. The microelectrodes are separated by a pitch of $500\ \mu\text{m}$.

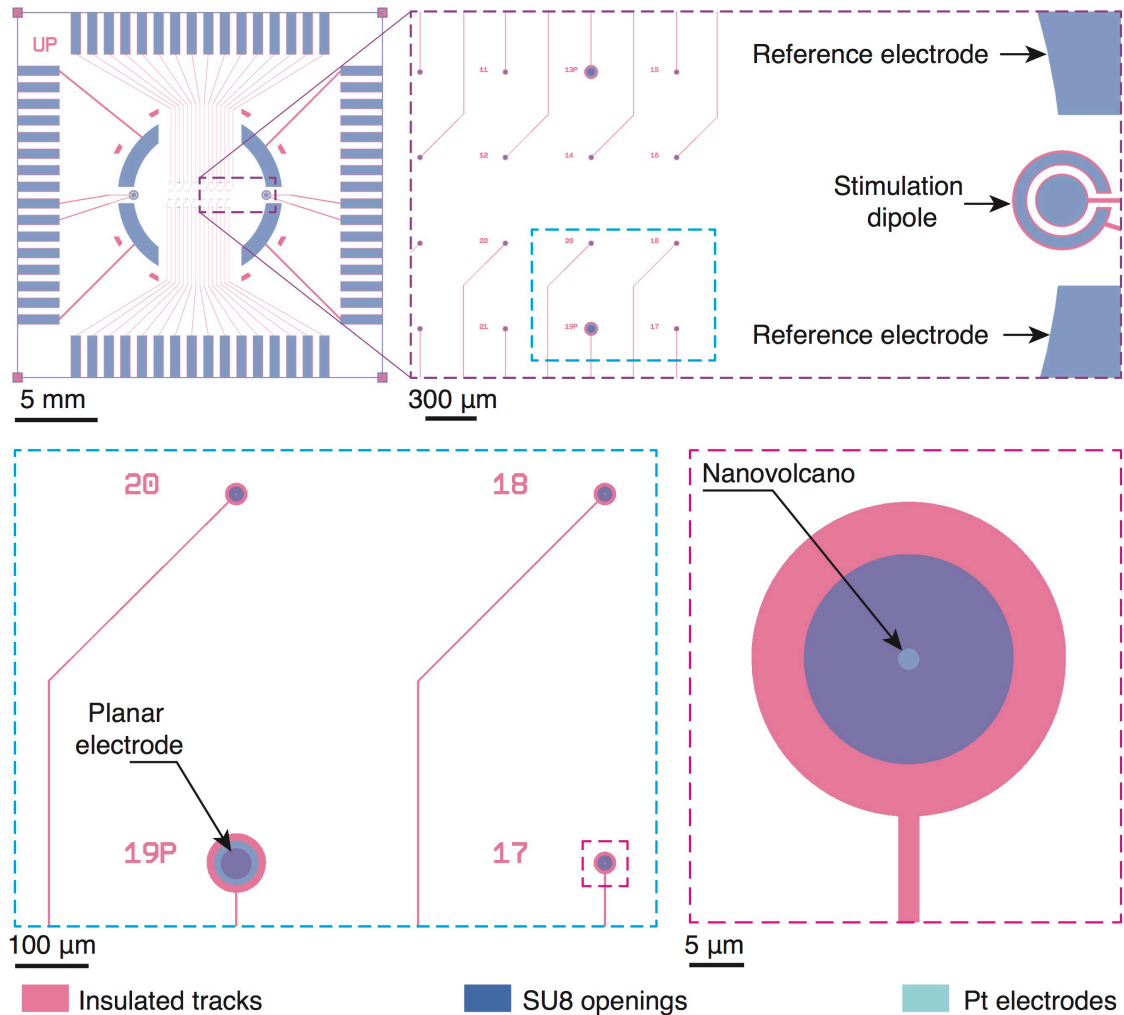


Figure 3.2: *Layout of the multielectrode array.* Electrically conductive tracks (pink) connect each electrode to the interfacing pads of the chip. The inserts show an enlarged view of the recording and stimulation electrodes (top right panel), the planar electrodes used as control recording sites (bottom left panel), and the nanovolcano (bottom right panel).

Figure 3.3-A illustrates a typical glass wafer patterned with 9 nanovolcano arrays in the end of the fabrication process. The chips were subsequently diced and assembled with a glass ring forming the cell culture well as depicted in Figure 3.3-B and C.

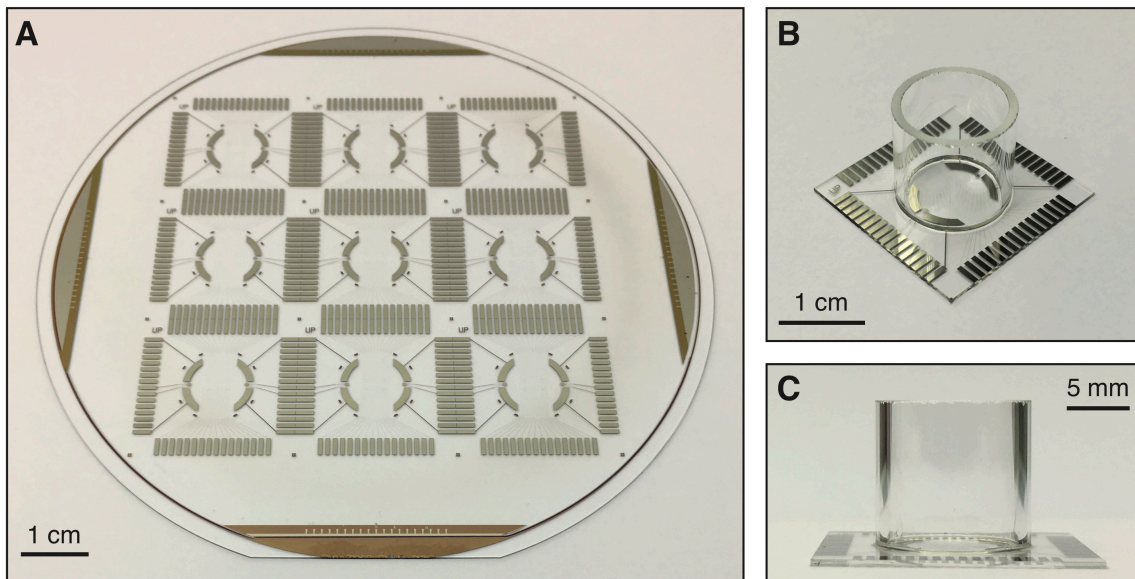


Figure 3.3: *Multielectrode array assembly.* **A)** Typical glass wafer patterned with 9 nano-volcano arrays at the end of the fabrication process. **B)** Tilted and **C)** side view of the nanovolcano array device assembled with a glass cell culture well.

3.2.2 Electrochemical characterization of the electrode - electrolyte interface

Figure 3.4-A shows the electrical equivalent model of the electrode-electrolyte interface. As detailed in Chapter 1, it is composed of a non-linear resistance, R_{CT} , that represents faradaic charge transfer secondary to redox reactions. In series with this resistance, a Warburg element, CPE_W , reflects the diffusion of ions at the interface. A parallel constant phase element, CPE_{DL} , represents the double layer capacitance underlying capacitive charge transfer. The stray capacitance, C_{Stray} , denotes the capacitive current leaks along the insulated tracks. The spread resistance is neglected.

The nanovolcano-electrolyte interface properties have been analytically determined and experimentally measured using electrochemical impedance spectroscopy based on a 100 mV sinusoidal signal (frequency swept between 0.01 Hz and 1 MHz) applied to the chip in presence of phosphate buffer saline (PBS) at room temperature.

3.2.2.1 Experimental measurement by electrochemical impedance spectroscopy

The electrochemical impedance spectroscopy data are presented in Figure 3.4-B and show a typical electrode-electrolyte behavior. [131] After fitting, values for each element composing the equivalent electrical circuit have been extracted and are sum-

marized in Table 3.1.

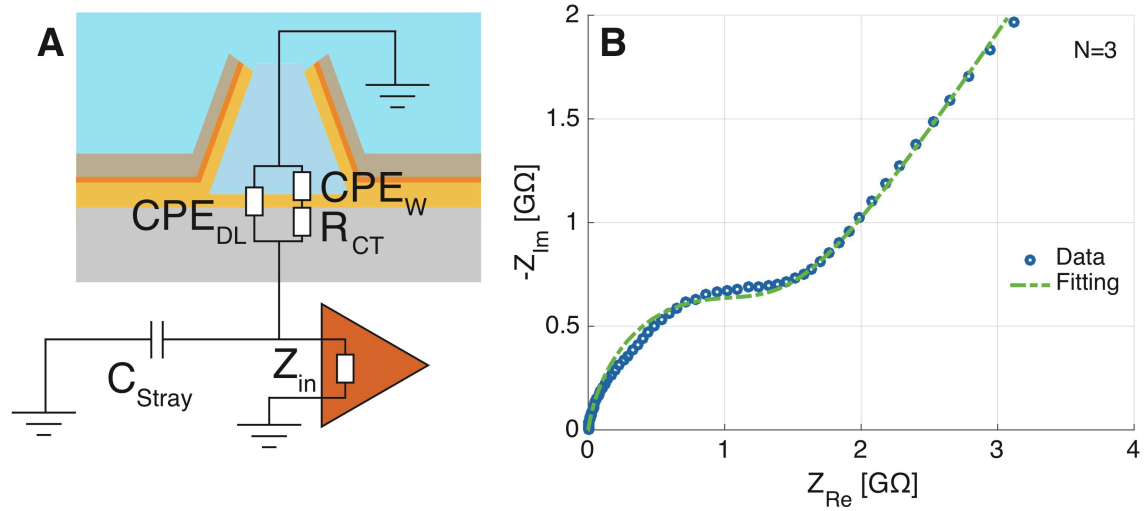


Figure 3.4: *Electrode-electrolyte interface.* **A)** Equivalent electrical model of the microelectrode-electrolyte interface (for abbreviations cf. text). **B)** Electrochemical impedance spectroscopy of a single nanovolcano in PBS. N is the number of nanovolcanoes tested.

3.2.2.2 Theoretical modeling

As shown in the literature, the value of each of the elements composing the electrode-electrolyte interface can be analytically predicted. [131,199]

Double layer constant phase element The constant phase element impedance, $Z_{CPE,DL}$, representing the double layer capacitance impedance at the interface can be expressed as:

$$Z_{CPE,DL} = \frac{1}{C_{DL}(j\omega)^{n_{DL}}} \quad (3.1)$$

Where ω is the angular frequency (rad/s) and n_{DL} the empirical factor representing the surface irregularities ($n_{DL} \sim 0.91$ from literature [131]). The double layer capacitance, C_{DL} , is defined as the Helmholtz capacitance, C_H , being in series with the Gouy-Chapman capacitance, C_G as described in the Gouy-Chapman-Stern model:

$$C_{DL} = \frac{C_H C_G}{C_H + C_G} = 17.3 \text{ pF} \quad (3.2)$$

Chapter 3. Nanopatterned volcano-shaped microelectrode arrays for spontaneous intracellular recording of cardiomyocyte action potentials

with:

$$C_H = \frac{\epsilon_0 \epsilon_{r,water} A}{d_{OHP}} = 17.3 \text{ pF} \quad (3.3)$$

ϵ_0 : Vacuum permittivity = $8.85 \cdot 10^{-12}$ F/m

$\epsilon_{r,water}$: Relative permittivity of water = 78 [131]

d_{OHP} : Distance of the outer Helmholtz plane from the electrode = 5 \AA [131]

r : Electrode radius = 1 \mu m

h : Electrode height = 1.5 \mu m

A : Electrode area = $\pi r^2 + 2\pi r h = 12.6 \text{ \mu m}^2$

and:

$$C_G = \frac{\epsilon_0 \epsilon_{r,water} A}{L_D} \cosh\left(\frac{zV_0}{2V_t}\right) = 51.2 \text{ nF} \quad (3.4)$$

L_D : Debye length = $\sqrt{\frac{\epsilon_0 \epsilon_r V_t}{2n_0 z^2 q}} = 0.19 \text{ \AA}$

V_t : Thermal voltage = 25.9 mV [131]

n_0 : Bulk number concentration of ions in solution = $9.3 \cdot 10^{25}$ ions/m³ [131]

z : Valence of ions in solution = 4 [131]

q : Elementary charge = $1.602 \cdot 10^{-19}$ C

V_0 : Applied electrode potential = 100 mV

Charge transfer resistance Faradaic charge transfer of Pt electrodes in PBS is due to the electrolysis of H₂O and the reduction of O₂ and can be defined as:



The faradaic current, I , passing through the electrode can be expressed as:

$$I = J_0 A e^{\frac{zV_0}{2V_t}} = 10.0 \text{ pA} \quad (3.6)$$

where $J_0 = 35 \cdot 10^{-5} \text{ A/m}^2$ is the exchange current density [200] and $V_0 = 100 \text{ mV}$ the over-potential applied.

The charge transfer resistance, R_{CT} , can be obtained by taking into account the inverse of the derivative of I :

$$\frac{dI}{dV_0} = \frac{J_0 A z}{2V_t} e^{\frac{zV_0}{2V_t}} \quad (3.7)$$

$$R_{CT} = \left[\frac{dI}{dV_0} \right]^{-1} = \frac{2V_t}{J_0 A z e^{\frac{zV_0}{2V_t}}} = 1.3 \text{ G}\Omega \quad (3.8)$$

Warburg element The Warburg impedance, Z_W , reflects non-instantaneous diffusion of reactants to the interface. It can be defined by a resistor, R_W , in parallel with a capacitor, C_W : [199]

$$Z_W = \left[\frac{1}{R_W} + j2\pi C_W \right]^{-1} \quad (3.9)$$

where:

$$R_W = \frac{10^3 V_t A}{z^2 q n_0 \sqrt{\pi f D}} \quad (3.10)$$

and:

$$C_W = \frac{1}{2\pi R_W} \quad (3.11)$$

with f representing the frequency of the electrical signal and D the diffusion coefficient of H^+ in water that amounts to $0.824 \text{ m}^2/\text{s}$. [201]

Z_W can be expressed as a standard constant phase element with a phase of -45° as follows:

$$Z_{CPE,W} = \left[\frac{1}{R_W} + j2\pi C_W \right]^{-1} = \frac{1}{\frac{1}{R_W} + j2\pi \frac{1}{2\pi R_W}} = \frac{R_W}{1+j} \quad (3.12)$$

as: $\sqrt{j} = (e^{j\frac{\pi}{2}})^{\frac{1}{2}} = \cos(\frac{\pi}{4}) + j\sin(\frac{\pi}{4}) = \frac{1}{\sqrt{2}} + j\frac{1}{\sqrt{2}} = \frac{1+j}{\sqrt{2}} \leftrightarrow 1+j = \sqrt{2}\sqrt{j}$

$$Z_{CPE,W} = \frac{R_W}{\sqrt{2}\sqrt{j}} = \frac{1}{\frac{z^2 q n_0 \sqrt{D}}{10^3 V_t A} \sqrt{2\pi f j}} \quad (3.13)$$

Chapter 3. Nanopatterned volcano-shaped microelectrode arrays for spontaneous intracellular recording of cardiomyocyte action potentials

$$Z_{CPE,W} = \frac{1}{Q_W(j\omega)^{n_W}} \quad (3.14)$$

with: $Q_W = \frac{z^2 q n_0 \sqrt{D}}{10^3 V_t A} = 3.3 \cdot 10^{-9} \Omega^{-1} s^{\frac{1}{2}}$ and $n_W = \frac{1}{2}$

Stray capacitance The stray capacitance along the tracks connecting the electrodes to the pads can be modeled as follows:

$$C_{Stray} = \frac{\epsilon_0 \epsilon_{r,SU8}}{t_T} A_T \quad (3.15)$$

where $\epsilon_{r,SU8} = 3.5$ is the relative permittivity of the SU8 insulating layer, $t_T = 4.5 \mu\text{m}$ is the thickness of the insulating layer, and $A_T = 0.045 \text{ mm}^2$ refers to the overall area of the tracks.

3.2.2.3 Theory vs experiment comparison

The values for each element composing the electrode-electrolyte interface equivalent circuit are summarized in Table 3.1. Overall, predicted and experimentally measured values agree. The difference obtained for the Warburg element may be related to the difficulty to obtain a reliable estimate of the H^+ diffusion coefficient.

Table 3.1: Theoretical and experimental values of every element composing the electrical equivalent circuit of the electrode-electrolyte interface.

Element	Experiment	Theory
R_{CT}	1.3 G Ω	1.3 G Ω
C_{DL}, n_{DL}	18.6 pF, 0.85	17.3 pF, 0.91
Q_W, n_W	$4.8 \cdot 10^{-10} \Omega^{-1} s^{1/2}$, 0.5	$3.3 \cdot 10^{-9} \Omega^{-1} s^{1/2}$, 0.5
C_{Stray}	0.3 pF	0.3 pF

3.2.3 Recording system and interfacing optimization for electrophysiological measurements

Prior to the electrophysiological experiments, theoretical considerations regarding the influence of the recording system and its interfacing on the quality of the registered signals have to be discussed, especially in terms of distortion, amplitude, and noise.

3.2.3.1 Recording system

As discussed in the introductory Chapter 1, the choice of the recording system is pivotal to record high-quality electrophysiological potentials with micro-nanoelectrode arrays. Mainly, its bandwidth, input impedance, capability to perform simultaneous recordings from several channels, and dynamic range will impact the registered electrical signals.

Bandwidth considerations Cardiomyocyte action potentials are typically composed of a fast upstroke component followed by a slower repolarization phase. In the frequency domain, such a signal typically lies in between 0 Hz and 5 kHz. To prevent significant distortions of intracellular signals affecting particularly the repolarization phase at low frequency, and the upstroke component at high frequency, the amplifier bandwidth needs to match the action potential spectrum.

Input impedance consideration The input impedance of the amplifier Z_{In} , defined by the resistance R_{In} in parallel with the capacitance C_{In} , needs to be much higher than the electrode impedance Z_e to minimize the signal attenuation at the input of the amplifier. As detailed in subsection 3.2.2, the nanovolcano impedance corresponds to the charge transfer resistance ($R_{CT} = 1.3 \text{ G}\Omega$) in parallel with a double layer constant phase element CPE_{DL} ($C_{DL} = 18.6 \text{ pF}$, $n_{DL} = 0.85$). Respectively, R_{In} needs to be much higher than $1.3 \text{ G}\Omega$ and C_{In} lower than 18.6 pF .

Multichannel recording In order to independently record electrical signals from every nanovolcanoes composing the device simultaneously, the recording system needs to permit simultaneous voltage recordings from 32 channels.

Dynamic input range and analog-to-digital converter resolution Intracellular action potentials recorded with micro-nanoelectrode arrays reported in the literature showed a wide variety of signal amplitudes ranging from a few hundred microvolts

Chapter 3. Nanopatterned volcano-shaped microelectrode arrays for spontaneous intracellular recording of cardiomyocyte action potentials

to tens of millivolts. Ideally, action potential amplitudes can be as high as 100 mV. For this reason, the dynamic input range of the recording system needs to be at least 100 mV, with an analog-to-digital converter (ADC) bit number sufficiently high to also enable low signal amplitude recordings.

Neuralynx recording system A Neuralynx setup composed of a Digital Lynx SX acquisition system (cf. Figure 3.5-A) and a DC-coupled HS36 headstage (cf. Figure 3.5-B) was used to perform electrophysiological experiments throughout the entire thesis. The high-input impedance headstage enables simultaneous voltage recording from 32 microelectrodes within a DC range of ± 1 V and a dynamic range of ± 130 mV. The recording system technical specifications are summarized in Table 3.2 and meet the requirements for intracellular recordings with nanovolcano arrays. The software Cheetah (Neuralynx, USA) was used to visualize and save the data.

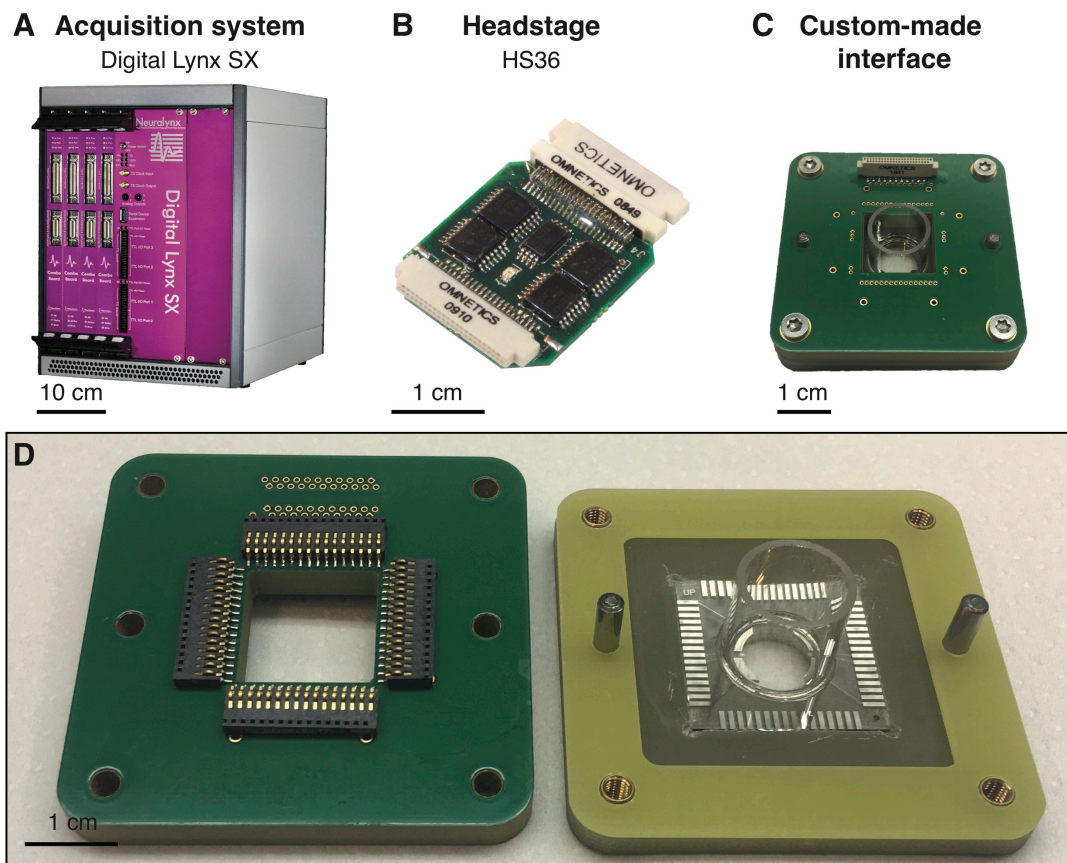


Figure 3.5: *Recording system and interfacing.* Illustration of the Digital Lynx SX acquisition system **A**) as well as the HS36 headstage **B**) developed by Neuralynx and used to perform electrophysiological recordings with nanovolcano arrays. Optical images showing an assembled **C**) and a disassembled **D**) view of the custom-made interface developed to connect the nanovolcano arrays to the HS36 headstage.

Table 3.2: Technical specifications of the HS36 headstage used with the Digital Lynx SX acquisition system.

Feature	Value
Bandwidth	0 - 8 kHz
Input impedance	1 T Ω 2 pF
Channel number	32
Dynamic range	\pm 130 mV
DC range	\pm 1 V
ADC bit number	24
Sampling frequency	32 kHz
Stimulation lines	2

3.2.3.2 Interfacing optimization

The connection between a multielectrode array and its recording system plays a central role in the quality of the electrophysiological signals registered as it may reduce the stray impedance of the system. Figure 3.5-C illustrates the custom-made interface developed to connect the nanovolcano array to the HS36 headstage.

It is composed of a bottom piece (cf. Figure 3.5-D, right panel) which receives the device and enables the nanovolcano interfacing pads to be aligned with the spring loaded connectors from the top part (cf. Figure 3.5-D, left panel). The top part consists of a multilayered PCB that makes the electrical connections between the spring loaded connectors and a standard 44-pins omnetic connector, compatible with the HS36 headstage.

The PCB is composed of a 1.4 mm-thick substrate patterned on both sides with 100 μ m-wide conductive tracks, separated from the top and bottom shielding ground planes by a 1.6 mm-thick insulating spacing layer of IT180. The relatively large distance between the PCB conductive tracks and the ground planes, together with their small dimensions guarantee a low stray capacitance while minimizing the electrical noise induced by external electromagnetic perturbations. The high resistivity properties of IT180 (volume resistivity $\sim 10^{10}$ M Ω cm) allows for a stray resistance much higher compared to the input resistance of the amplifier.

The developed interface permits a reliable connection between the nanovolcano array and the HS36 headstage while minimizing both the signal attenuation along the interface and the noise.

3.2.4 Intracellular action potential recording from networks of cardiomyocytes with nanovolcano arrays

To validate the device, monolayers of neonatal rat ventricular cardiomyocytes were cultured on the nanopatterned array for 48 h to 72 h prior to the electrophysiological recordings. As shown in Figure 3.6-A, the cell monolayers displayed uniform adherence to the entire substrate including the region of the two standard planar electrodes and the four nanovolcanoes.

Figure 3.6-B shows a series of sequential intracellular action potentials (APs) recorded by a nanovolcano from a spontaneously active cardiomyocyte monolayer. The shape of the signal is typical for APs of cultured rat cardiomyocytes. [202] Action potential upstrokes coincided, as expected, with extracellular field potentials (electrograms) recorded simultaneously by nearby planar extracellular electrodes of the array. Recordings of a series of intracellular APs obtained simultaneously from several nanovolcanoes of the same device are shown in Figure 3.6-C with the corresponding AP parameters (amplitude, APA; duration at 50 % repolarization, APD₅₀, and maximal action potential upstroke velocity, dV/dt_{max}) shown in Figure 3.6-D. To ease comparison with conventionally measured values of dV/dt_{max} , maximal upstroke velocities were calculated after normalization of the signal amplitudes (% action potential amplitude, %APA/ms). Under the assumption of a typical non-attenuated action potential amplitude of 100 mV, [203] %APA/ms corresponds to the commonly used unit V/s. While APs recorded by different nanovolcanoes were similar in respect to APD₅₀ (244.9 ± 50 ms, N = 147) and dV/dt_{max} (21.7 ± 2.7 %APA/ms, N = 147), they differed in respect to the amplitude which ranged from 1.5 mV to 20.3 mV. This variability is likely explained by differences in the coupling parameters of the nanovolcano to the cells. The differences in the midpoints of action potential upstrokes depicted in the expanded inset of Figure 3.6-C demonstrate presence of propagated electrical activity which is typical for cardiomyocyte monolayers.

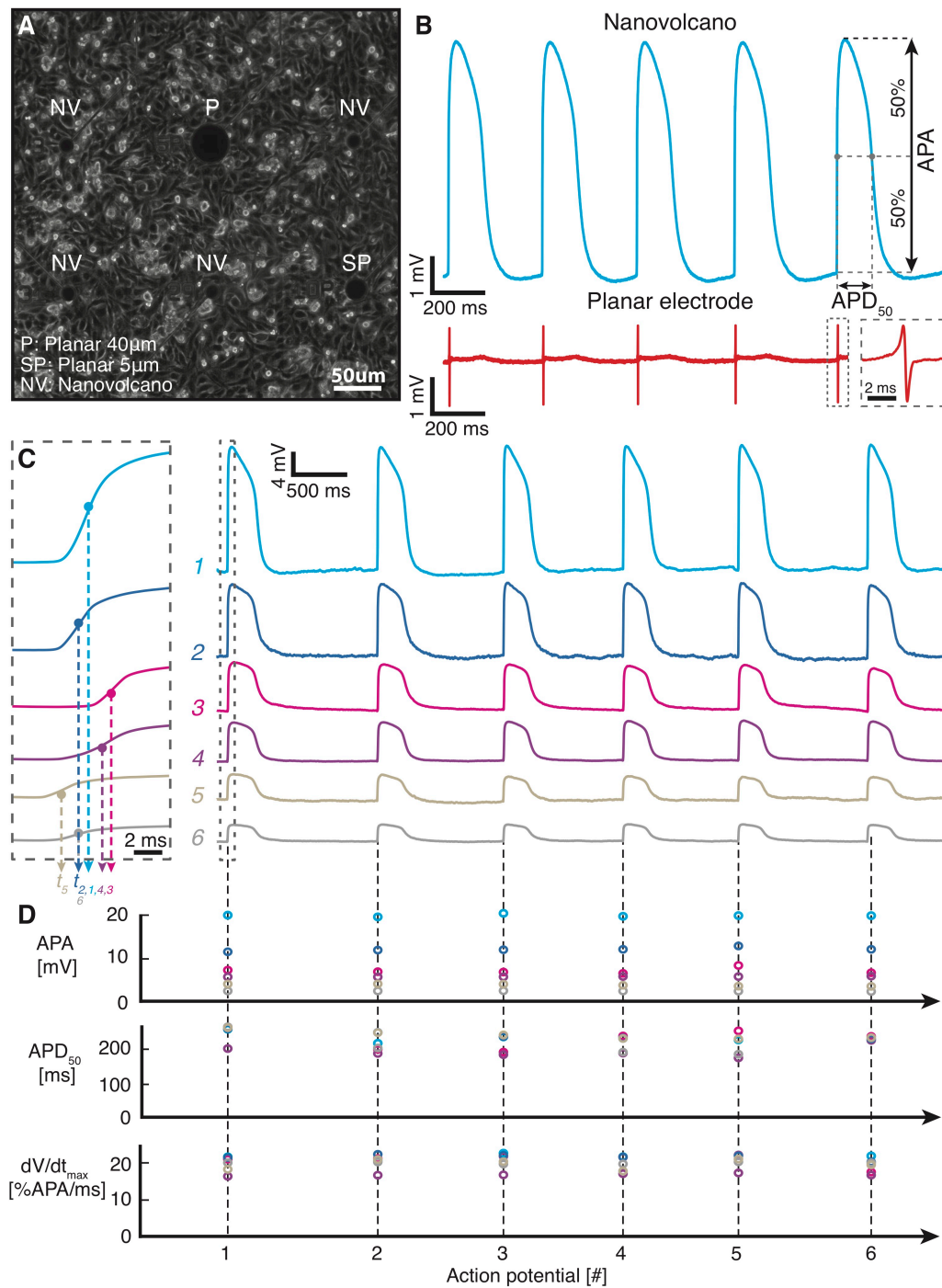


Figure 3.6: *Intracellular recording of action potentials from primary rat cardiomyocyte monolayer.* **A)** Phase contrast image of a representative 3-day-old primary rat cardiomyocyte monolayer culture grown on the nanovolcano array. **B)** Intracellular recording of action potentials with a nanovolcano (upper trace) and simultaneously measured electrograms from a nearby planar electrode (lower trace) during spontaneous electrical activity (APA: action potential amplitude; APD_{50} : action potential duration at 50 % repolarization). **C)** Simultaneous recording of spontaneous action potentials from six different channels of a nanovolcano array with action potential upstrokes shown at an expanded timescale on the left. Temporal shifts between activation midpoints indicate the presence of propagated electrical activity. **D)** Temporal evolution of action potential parameters of the signals presented in C) (dV/dt_{max} : maximal upstroke velocity).

3.2.5 Dependence of APD₅₀ on the frequency of spontaneous activity

The instantaneous frequency of spontaneous action potentials was assessed by measuring the period between successive action potentials (= cycle length, CL). CLs varied over time as shown in Figure 3.7-A for a 3 min fragment of a 60 min lasting recording. The distribution of CLs (range: 0.2 – 17 s; bin width: 200 ms) determined for the entire recording of 60 min is shown in Figure 3.7-B. Differences in CLs permitted to investigate whether nanovolcanoes are suited to detect frequency dependent changes in APD₅₀ (APD restitution) in order to further validate the physiological relevance of the recorded data. For this purpose, APD₅₀ values of each AP were correlated to the preceding CL. As shown in Figure 3.7-C for individual APs recorded by a single nanovolcano, APD₅₀ values decreased with decreasing CL thereby exhibiting the salient feature of APD restitution. When binning APD₅₀ values of all signals recorded from the same nanovolcano over the entire recording period, an increase of APD₅₀ with increasing CL was observed that leveled off at CLs > 800 ms (Figure 3.7-D). For the preparation shown, the change in APD₅₀ ranged from 96.6 ± 14 ms (CL: 287.7 ± 9.3 ms; N = 57) to 139 ± 18 ms (CL: $850.3 \text{ ms} \pm 29.6$ ms; N = 137; $p = 8.8 \cdot 10^{-38}$) which reproduces findings reported before for APD restitution of neonatal rat cardiomyocyte monolayers using conventional measurement techniques. [113]

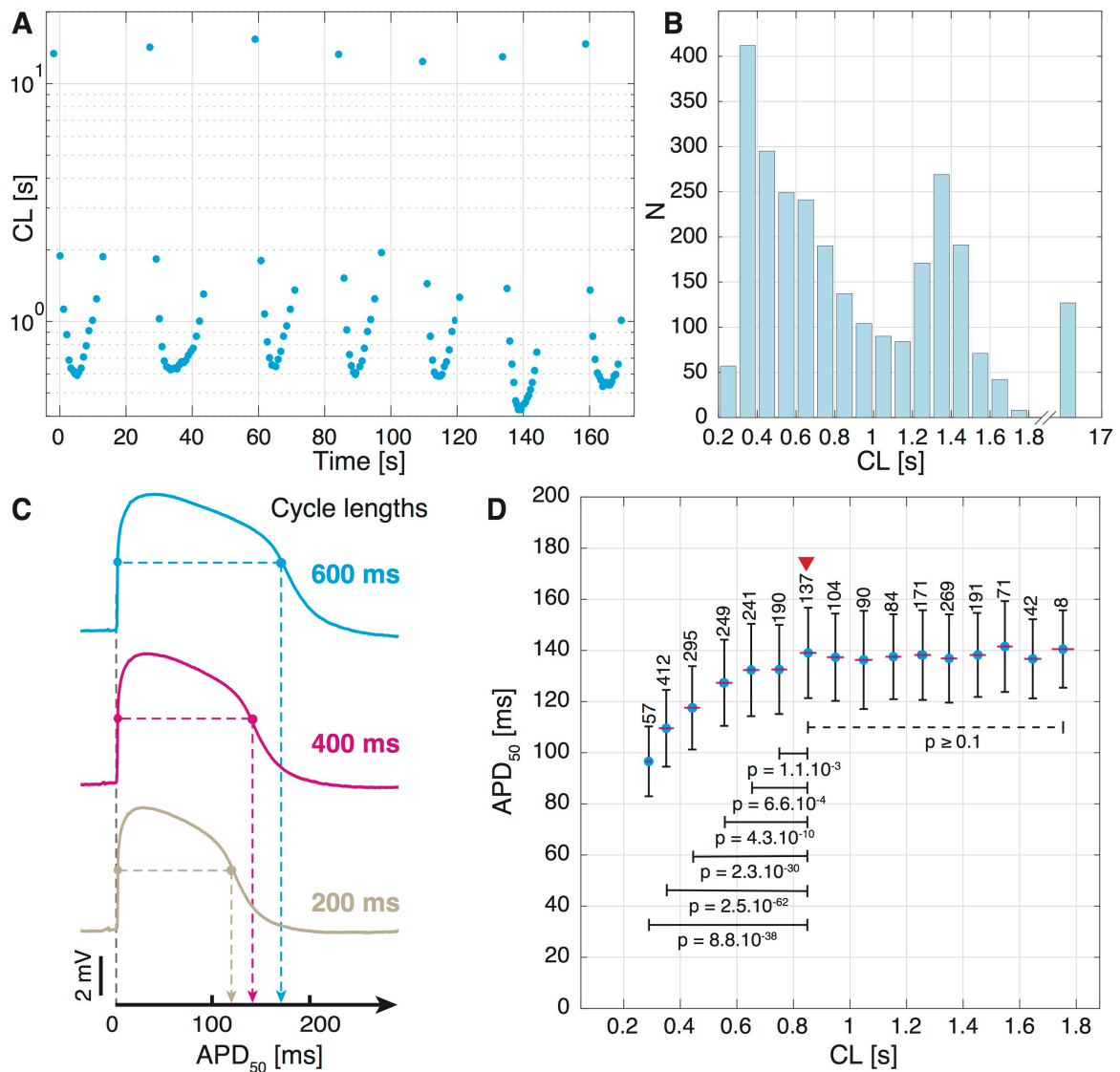


Figure 3.7: APD restitution. **A**) Timecourse of cycle lengths (CL) of a spontaneously active preparation (3 min fragment shown is typical for the entire recording). **B**) Distribution of CLs of the same preparation as determined during 60 min of continuous recording (bin width: 200 ms). **C**) Action potential shapes at different CLs. **D**) Dependence of APD₅₀ on CL (mean \pm SD; N indicated above values; p-values are given in respect to the data point marked with a red triangle).

3.2.6 Stability of nanovolcano recordings

Nanovolcanoes permitted continuous long-term recordings for up to 1 hour without appreciable changes in general AP shape (Figure 3.8-A; left 3 signals). Stability of the recordings is reflected by the analysis of AP parameters presented in Figure 3.8-B to D. While APAs decreased by 9.7 % from 7.02 ± 0.39 mV (interval: 10-20 min; N = 460) to 6.34 ± 0.41 mV (interval: 60-70 min; N = 339; $p = 3.21 \cdot 10^{-94}$), APD₅₀ remained unchanged (136.2 ± 25.5 ms vs. 134.9 ± 21.7 ms; $p = 0.44$). The transient decrease

Chapter 3. Nanopatterned volcano-shaped microelectrode arrays for spontaneous intracellular recording of cardiomyocyte action potentials

of APD_{50} between 20 and 30 min is likely explained by the simultaneously occurring transient increase of the frequency of spontaneous activity and, hence, APD restitution. Maximal upstroke velocities decreased by 1.3 % from 23.56 ± 1.20 %APA/ms (interval: 10-20 min) to 22.25 ± 1.22 %APA/ms (interval: 60-70 min; $p = 3.56 \cdot 10^{-4}$). The absence of a change of APD_{50} and the moderate decline of APA and dV/dt_{max} over time indicate that cell viability was little if any affected by the nanovolcano recording. The final phase of the successful nanovolcano recording is illustrated by the two signals shown on the right of Figure 3.8-A. It was heralded by a sudden drop of the APA (t = 66 min) followed by the appearance of extracellular field potentials (t = 70 min) which likely indicates spontaneous membrane resealing. No coupling-uncoupling cycles were observed when reassessing the signals of nanovolcanoes 24 h after an initial successful intracellular access.

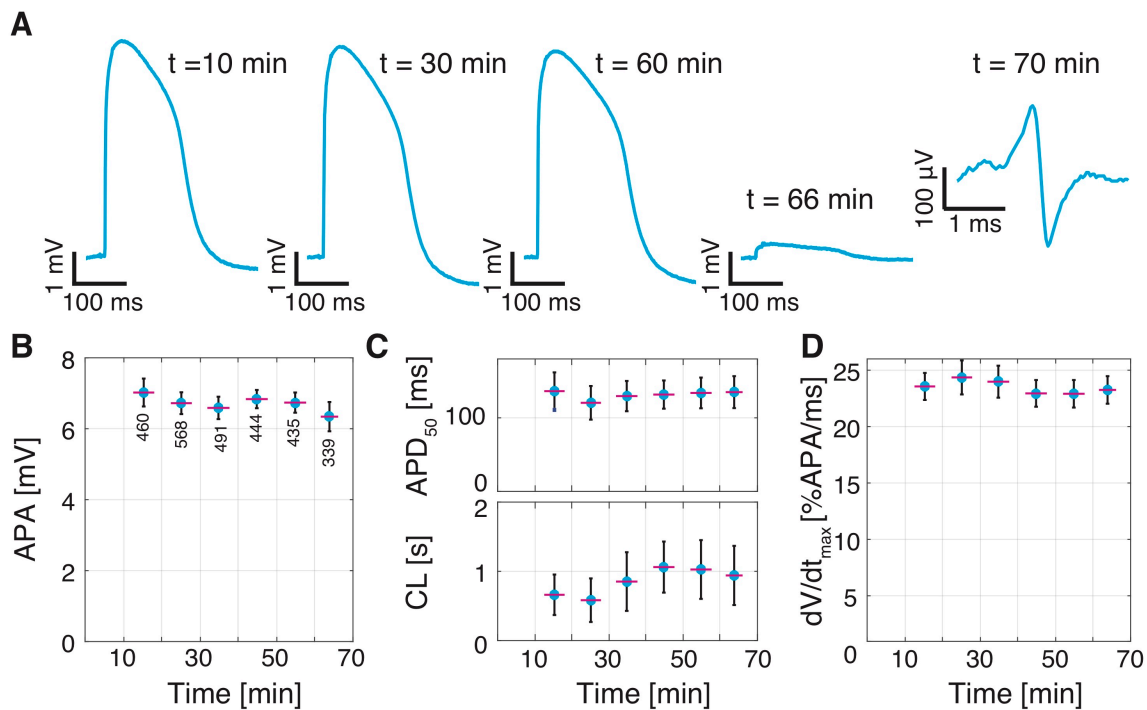


Figure 3.8: Change of action potential shape during continuous recordings by a nanovolcano. **A)** Action potentials recorded at the times indicated. **B)** Evolution of APA, **C)** APD_{50} and CLs, and **D)** dV/dt_{max} (mean \pm SD, N given below values in panel B).

3.2.7 Nanovolcano recordings: durations, signal amplitudes, and yield per device

The distribution of action potential amplitudes, recording durations, and yield of nanovolcanoes with successful in-cell access per device are summarized in Figure 3.9. Figure 3.9-A presents the recording duration for every nanovolcano with intracellular

access per device. Successful recordings lasted from 3 min to 66 min (18.2 ± 21 min, mean \pm SD; $N = 16$). The recording yield, defined as the number of nanovolcanoes reporting intracellular activity divided by their total number, ranged from 3 % to 29 % (15 ± 11 %, mean \pm SD; $N = 4$). Figure 3.9-B shows the amplitude distribution of all action potentials recorded by nanovolcanoes. Amplitudes ranged from 0.5 mV to 20 mV (6.59 ± 1.8 mV, mean \pm SD; $N = 3087$).

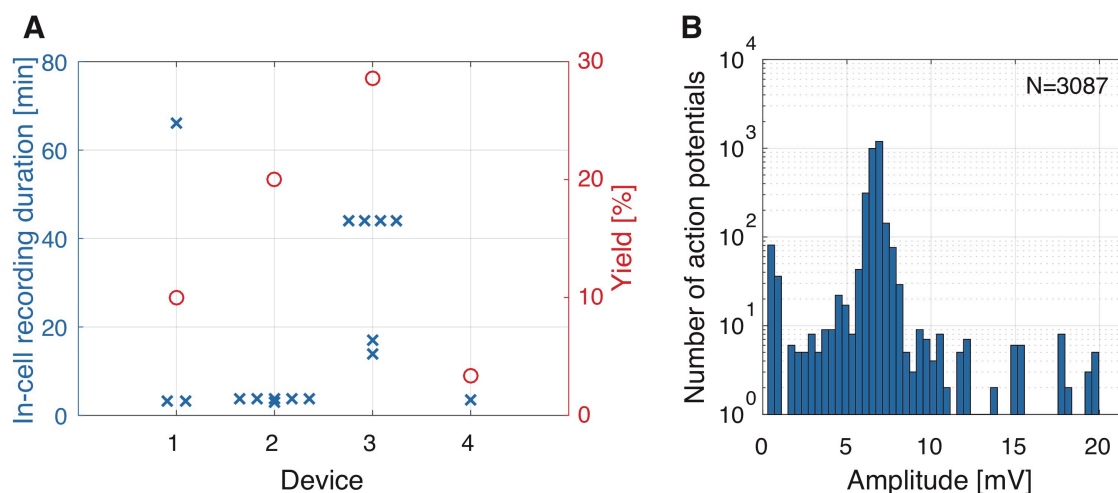


Figure 3.9: Performance of nanovolcano arrays. **A)** Durations of successful in-cell recordings and yield of nanovolcanoes with successful intracellular access per device. **B)** Distribution of the amplitudes of all action potentials recorded by nanovolcanoes with in-cell access.

3.2.8 Re-use of nanovolcano arrays

In order to investigate device reusability, used nanovolcano arrays were enzymatically cleaned with a HBSS solution containing 0.6 mg/mL pancreatin (P 3292, Sigma) and 2.5 % trypsin (Sigma, T4674) for 3 h at 37 °C. After rinsing with HBSS, a second round of enzymatic cleaning using Tergazyme (Alconox, 2 %) was performed. For this purpose, the well was filled with 1 mL of cleaning solution and kept on an orbital shaker for 2 h at room temperature. Thereafter, the devices were subjected to 3 rounds of thorough rinsing with double distilled water. Scanning electron microscopy showed that, typically, ~ 60 % of the nanovolcanoes survived the cleaning process as evidenced by an intact structure with a clean gold nanopattern. The remaining nanovolcanoes were either detached from the substrate or showed dirt remnants. Given the poor outcome of the cleaning process, re-use of the nanovolcano arrays is not recommended.

3.3 Discussion

The novel type of microelectrode developed in this work combines numerous recent technological advances into a single structure. By contrast to previous micro-nanoelectrodes, the high aspect ratio of the sharp nanovolcano wall permits a tight junction between the cell membrane and the electrode without limiting the active area of the recording electrode. [128] This results in a relatively low electrode impedance and, accordingly, high signal-to-noise ratios. The robustness of the cell-electrode interface is also ensured by the electrically insulating walls preventing current leakage and by the functionalized nanoscale pattern that enables fusing of the nanovolcano to the cell membrane.

Manufacturing of the multimaterial nanopatterned microstructure would be a major challenge when using conventional processes only. However, by exploiting ion beam etching redeposition, manufacturing can be simplified to a reliable and scalable four-step method that is compatible with complementary metal-oxide-semiconductor (CMOS) technologies. Accordingly, the nanovolcanoes can be manufactured directly on CMOS chips thereby opening the perspective to be further developed into a self-standing intracellular electrophysiology platform. [117,121,204] The fabrication process is simple, scalable and leads to homogeneous structures at the wafer-scale.

By varying the geometry of the photoresist openings, planar control electrodes with different dimensions were integrated in the device following the same fabrication process. Electrograms recorded by these electrodes were used as baseline indicator for the presence of electrical activity and confirmed that planar electrodes having active areas similar to the nanovolcanoes permit artifact-free extracellular field potential (electrogram) recordings.

After seeding, primary neonatal rat ventricular cardiomyocytes showed uniform attachment to the entire surface of the device and formed a well coupled cell monolayer. Morphology and electrical activity of the cell monolayers cultured on the nanostructured substrate was not different from control monolayers grown on standard glass coverslips thereby demonstrating biocompatibility of the microstructure. [205] Depending on the degree of contamination with cardiac myofibroblasts, cardiomyocyte monolayers were either quiescent or showed synchronized spontaneous activity. [206] The device presented demonstrates for the first time passive transmembrane accesses to primary rat cardiomyocytes and therefore significantly improves upon previous micro-nanotechnology based multielectrode arrays where electroporation, [132–134, 140, 141, 146, 147] optoporation, [160] or mechanical pressure [156, 157]

need to be applied to provide an intracellular access. Moreover, by providing direct and stable recordings for more than one hour, nanovolcanoes achieved results comparable to the state-of-the-art technologies in terms of recording duration. [134, 140, 141].

Overall, more than 3000 intracellular action potentials were successfully recorded from cardiomyocyte monolayer cultures grown on four different devices. Action potentials could be recorded simultaneously from up to 30 % of the nanovolcanoes composing the device. This maximal yield suggests that arrays of nanovolcanoes are potentially suited for the spatially resolved assessment of transmembrane signals in networks of cardiomyocytes. Prospectively, this yield could be increased by optimizing the nanovolcano geometry (diameter, height, wall thickness, and inclination) as well as the nanopatterned self-assembled monolayers in order to maximize the penetration probability of the structure. Additionally, the spatial resolution of the device is only limited by the overall size of the microelectrode pad (30 μm -wide) and the electrical tracks (3 μm -wide). The microelectrode pad size could be decreased to the diameter of a single nanovolcano thereby permitting a significant increase of microelectrode density and spatial resolution of the device.

Nanovolcano recordings of intracellular APs showed, with the exception of attenuated APAs, a typical AP shape as well as APD_{50} and dV/dt_{max} characteristics that match APs recorded using conventional sharp electrode or patch clamp techniques. [203] Also, nanovolcanoes permitted the characterization of APD restitution which illustrates the physiological relevance of this measurement approach. [113]

Even though attenuated, APAs reached amplitudes as high as 20 mV (20 % APA of an actual AP) which is significantly higher than amplitudes reported for state-of-the-art micro-nanotechnology based multielectrode arrays such as gold micro-mushrooms (max APA: 5mV), [147] plasmonic nano- (max APA: 1.8 mV) [140] or meta-electrodes (max APA: 5 mV). [160] The superior performance of nanovolcanoes may be explained by the fact that they have access resistances as low as 1.3 $\text{G}\Omega$ which is over a hundred times smaller than those of gold micro-mushrooms [128] and is negligible compared to the input impedance of the amplifier used (1 $\text{T}\Omega$). Accordingly, nanovolcanoes have the potential to record non-attenuated intracellular action potentials if the ratio of junctional-to-seal resistance is further minimized. Such optimization may be achieved by varying the nanovolcano geometry as well as the composition of the self-assembled monolayers. The potential impact of these measures on AP shape and amplitude is described in Appendix B, section B.2 and B.3.

Ideally, intracellular electrodes would permit uninterrupted long-term recordings

Chapter 3. Nanopatterned volcano-shaped microelectrode arrays for spontaneous intracellular recording of cardiomyocyte action potentials

of the electrical activity of networks of excitable cells. With nanovolcanoes, maximal recording periods were limited to slightly more than an hour. During this time, APA, dV/dt_{max} and APD_{50} showed little if any change. In the example shown in Figure-3.8, this stable period was followed, by a sudden and drastic decrease of APAs and, ultimately, the replacement of APs by electrogram-like signals. Given that the peak-to-peak amplitudes of these electrograms ($262 \pm 62 \mu\text{V}$, $N = 23$) were similar to electrograms recorded simultaneously by neighboring extracellular nanovolcanoes of the same device ($253 \pm 118 \mu\text{V}$; $N = 45$), a spontaneous closing of the cell membrane that restores the situation of non-intracellular nanovolcanoes seems plausible. The alternative explanation, a loss of the seal, cannot be ruled out. The investigation of the latter possibility is hampered by the fact that the seal resistance (R_{Seal}) is in series with the high charge transfer resistance (R_{CT}) of the nanovolcanoes which precludes an accurate determination of a change of R_{Seal} during the loss of signal. While we have no direct evidence favoring a specific mechanism giving rise to spontaneous in-cell access by the nanovolcanoes, the high stress imposed on the cell membrane by the nanowall combined with an abrupt release of static charges accumulating at the electrode may explain the spontaneous process. In this context, the sharp geometry of the nanovolcano in conjunction with the nanopatterned self-assembled monolayers may maximize the chances of static charge-induced electroporation. If we further assume that a static discharge was preferably induced by turning on the amplifier system, this may explain why we never observed transitions from extracellular to intracellular recordings during our experiments. Conversely, resealing of the static charge induced pores reported by others [132, 141] may explain the loss of intracellular access over time.

Our work agrees with previous studies showing that hollow structures significantly improve the recording duration compared to other structures aimed at gaining intracellular access. For instance, 3D hollow plasmonic electrodes were shown to provide intracellular access for up to 80 minutes after optoporation [140] while iridium oxide nanotube electrodes retained intracellular access for 100 minutes after electroporation. By contrast, gold nanopillars lost in-cell access already after one minute. [141] As demonstrated by Lin *et al.*, the cell membrane curvature induced by hollow geometries increases the pore resealing time and, hence, the intracellular recording. [141] As reported in this study, the nanovolcanoes perform similar to hollow electrodes in regard to the duration of successful in-cell access which supports the idea that hollow geometries delay the closure of the pore.

Finally, the low electrode impedance at low frequency permits a substantial charge

injection into the cells and potentially makes the nanovolcano a tool for creating new horizons in the field of intracellular amperometric sensing. [207–209].

3.4 Conclusion

In this chapter, we present a new type of nanopatterned microelectrode demonstrating significant advances compared to state-of-the-art microelectrodes for multisite intracellular electrophysiology. Improvements include a microstructure that enables spontaneous in-cell access and a self-assembled monolayer supporting stabilization of the cell-electrode interface. Further, the structure features a large electrode area and, hence, a low impedance. Despite the complexity of the nanopatterned structure, the manufacturing of nanovolcanoes at the wafer-scale is straightforward as it exploits non-conventional redeposition processes occurring during standard ion beam etching.

Proof-of-principle experiments with primary rat cardiomyocyte cell cultures demonstrate that the nanovolcanoes provide spontaneous intracellular access without application of penetrating triggers such as opto- or electroporation. Upon gaining intracellular access, the nanovolcanoes successfully reported transmembrane voltage changes over extended periods of time. Apart from permitting the assessment of changes in AP shape in general, the nanovolcano recordings have the distinct advantage over extracellular multielectrode array recordings that they allow for the investigation of highly pathological events like early and delayed afterdepolarizations that are central to cardiac arrhythmogenesis. This feature may render nanovolcanoes especially suited for pharmacological screening purposes aimed at detecting adverse cardiac side effects of novel compounds.

3.5 Materials and methods

3.5.1 Microfabrication

A standard glass float wafer (100 mm in diameter, 550 μm -thick) was covered by successive evaporations of Ti-Pt-Ti-Au-Ti (10-250-50-50-50 nm) using an EVA760 e-beam evaporator (Alliance Concept, France), followed by an additional deposition of a 150 nm-thick SiO_2 layer performed with a Spider600 sputter-coater (Pfeiffer Vacuum, France). Subsequently, the substrate was spin-coated with a 1.6 μm -thick AZ nLof 2020 photoresist layer (MicroChemicals, Germany) exploiting an EVG150 automatic spin-coater/developer (EVG, Austria), into which 2 μm -diameter openings were pat-

Chapter 3. Nanopatterned volcano-shaped microelectrode arrays for spontaneous intracellular recording of cardiomyocyte action potentials

terned with an i-line VPG200 direct laser writer (Heidelberg, Germany) operating at a dose of 80 mJ/cm². After a post-exposure bake at 110 °C with a 50 µm proximity gap for 75 s, the wafer was developed for 46 s using an AZ 726 MIF commercial developer (MicroChemicals, Germany) dispensed using an EVG150 coater/developer. The sample was then bombarded with Ar⁺ ions at an incidence angle of 0° using an IBE350 ion beam etcher (Veeco, USA). At this step, materials from the substrate were etched and redeposited on the photoresist sidewalls. The photoresist was finally stripped using a 500 W O₂ plasma (O₂ flow 400 mL/min) for 7 min with a TePla300 microwave plasma system (PVA TePla, Germany).

Electrically conductive tracks were patterned in a 3 µm-thick AZ 9221 photoresist layer (MicroChemicals) spin-coated with a Rite Track 88 series automatic coater (Rite Track, USA), exposed with a VPG200 direct laser writer at a dose of 280 mJ/cm², and developed for 102 s using a Rite Track 88 series automatic developer (Rite Track). Thereafter, a 2 min reflow at 120 °C was performed on a Sawatec HP200 hotplate (Sawatec, Switzerland) prior to etching the substrate positioned at an incidence angle of -35° with respect to the ion beam generated in an IBE350 ion beam etcher. The photoresist was stripped in 500 W O₂ plasma (O₂ flow 400 mL/min) for 7 min created by a TePla300 microwave plasma system.

Finally, a 4.5 µm-thick GM1050 SU8 insulating layer (Gersteltec, Switzerland) was spin-coated using a Sawatec LSM250 manual coater (Sawatec, Switzerland) and soft-baked at 130 °C for 5 min on a Sawatec HP200 hotplate. After a 20 mJ/cm² exposure using a VPG200 direct laser writer, the SU8 layer was post-exposure baked on a Sawatec HP200 hotplate for 20 minutes at 85 °C before being manually developed in propylene glycol methyl ether acetate (PGMEA) for 1.5 min and rinsed for an additional minute in isopropanol. A final hard-bake for 2 h at 135 °C on a Sawatec HP200 hotplate completed the fabrication process.

SEM images were taken with a Merlin SEM (Zeiss, Germany) at 1.5 kV and 50 pA. Both the back-scattered and secondary electrons were detected to enhance the contrast difference between the different layers of the wall. Scanning TEM as well as the corresponding EDX analysis were acquired with a Tecnai Osiris TEM (FEI, USA).

3.5.2 Device preparation

The device was completed by mounting a glass ring onto the chip that formed the cell culture well using epoxy resin (Epo-Tek 302-3M; Epoxy technology, USA). The microelectrode arrays were sterilized for 30 s with O₂ plasma (100 W, 650 mTorr;

Diener Electronic, Germany) before they were submerged for 30 min in a 20 mmol/L hexanethiol solution in pure ethanol for self-assembled monolayer formation. After ethanol rinsing, the chips were thoroughly rinsed in sterile deionized water. Prior to cell seeding, the substrate was coated with collagen type IV (C5533, Sigma, Germany). All recordings presented in this study were acquired using new devices.

3.5.3 Isolation and culture of primary rat cardiomyocytes

Primary neonatal rat (Wistar, 1 day old) ventricular cardiomyocytes were obtained using established procedures. [210] Experiments were performed by Etienne de Coulon, Regula Flückiger Labrada, and Prof. Stephan Rohr from the Laboratory of Cellular Optics II (University of Bern), in accordance with federal guidelines for animal experimentation under the license BE27/17 of the state veterinary department of the canton Bern. In short, hearts from eight to ten neonatal rats were excised and ventricles trimmed in ice-cold Hank's balanced salt solution (HBSS) without Ca^{2+} and Mg^{2+} (3-02F29-I, BioConcept, Switzerland) containing trypsin (0.1 %; Sigma, T4674) and pancreatin (120 $\mu\text{g}/\text{mL}$; P 3292, Sigma). Ventricles were minced into small tissue pieces and subjected to 4-5 consecutive dissociation steps in a stirred vessel at 36 °C. After each step, the supernatant was collected, stored on ice and new dissociation solution was added to the tissue pieces. The dissociated cells were centrifuged and resuspended in medium M199 containing Hank's salts (M7653, Sigma), penicillin (20 U/mL; P7794, Sigma), vitamin B12 (2 $\mu\text{g}/\text{mL}$; Sigma, V2876), bromodeoxyuridin (100 $\mu\text{mol}/\text{L}$; B-5002, Sigma), vitamin C (18 $\mu\text{mol}/\text{L}$; A-4544, Sigma), epinephrine (10 $\mu\text{mol}/\text{L}$; E4250, Sigma), L-glutamin (680 $\mu\text{mol}/\text{L}$; G7513, Sigma), and 10 % neonatal calf serum (S 0125, Biochrom, Bioswisstec, Switzerland). Cardiomyocytes were enriched by pre-plating for 120 min in cell culture flasks. Cell numbers in the supernatant were determined using a hemocytometer and adjusted by dilution to result in a density of ~ 3500 cardiomyocytes per mm^2 . After seeding, the cultures were incubated at 36 °C in an atmosphere containing 0.8 % CO_2 . After 24 h, the cell culture medium was renewed and the serum level reduced to 5 %. Experiments were conducted 48 to 72 h post-seeding. At this time, the cellular electrophysiology of cardiomyocytes has recovered from the isolation process and overgrowth with non-cardiomyocytes like myofibroblasts is still moderate.

3.5.4 Electrophysiology

Electrophysiological experiments were conducted at the University of Bern, together with Etienne de Coulon and Prof. Stephan Rohr. Recordings with 48 to

Chapter 3. Nanopatterned volcano-shaped microelectrode arrays for spontaneous intracellular recording of cardiomyocyte action potentials

72 hours old cultures were performed in an incubator (37 °C; 0.8 % CO₂). A DC-coupled recording system (Digital Lynx SX with HS36 headstage; Neuralynx, USA) was used to record intracellular action potentials and electrograms. Apart from bandwidth limitations imposed by the array and the recording system ($R_{In} = 1 \text{ T}\Omega$; $C_{In} = 2 \text{ pF}$), signals shown correspond to actual non-filtered data.

Chapter 4

Controlled electroporation for long-term on-demand registration of cardiomyocyte action potentials with nanovolcano arrays

This thesis chapter is adapted from our recently submitted article: B.X.E. Desbilles,* E. de Coulon,* N. Maino, A. Bertsch, S. Rohr, and P. Renaud, “Nanovolcano-microelectrode-arrays: Controlled electroporation enables long-term on-demand registration of transmembrane action potentials”, *Under review in Microsystems and Nanoengineering*, 2020.

4.1 Introduction

Cell membrane electroporation is a well-established method for gaining access to the cell interior. It is based on the application of voltage pulses of sufficient magnitude that break the membrane dielectric thereby inducing formation of nanopores. [211, 212] Over the past decades, biological and medical applications of electroporation [213, 214] mainly focused on therapeutic gene transfer, [215–217] extraction of molecules, [218–220] and electrochemotherapy [221–223]. More recently, electroporation became a method of choice for providing micro-nanoelectrodes with intracellular access capabilities. In the context of nanoelectrophysiology, electroporation combined with multielectrode arrays (MEAs) has the potential to overcome some limitations of the current gold standard, i.e., whole-cell patch clamp recording. This technology of-

Chapter 4. Controlled electroporation for long-term on-demand registration of cardiomyocyte action potentials with nanovolcano arrays

fers only limited throughput, the recording duration is generally short and performing experiments is associated with high personnel costs. [224] By contrast, the use of electroporation in conjunction with arrays of nanoneedle-like electrodes recently allowed for simultaneous recording of intracellular action potentials from hundreds of electrotonically coupled rat cardiomyocytes over several days. [134, 149, 225] Recordings made with electrodes of various geometries such as micromushrooms [143, 146, 147, 162] or nanotubes [141] demonstrated similar electrophysiological characteristics. Current limitations of these technologies include substantial signal attenuation, short intracellular recording durations, and low yield.

In the last chapter, we described a novel type of nanopatterned volcano-shaped hollow microelectrode named “nanovolcano” which is suited to perform transmembrane voltage measurements from networks of excitable cells without the need of active electroporation. [226] The inner surface of the slightly conical hollow nanovolcanoes having a diameter of 2 μm consists of a large three-dimensional Pt electrode that offers low impedance access to the cell interior. The outer surface of the nanovolcano is insulated by a 50 nm-thick SiO_2 layer. A 10 to 20 nm-thick gold layer flanked by two Ti layers is intercalated between the Pt and the SiO_2 layers that form the nanovolcano wall. The gold layer is exposed along the upper rim of the nanovolcano and is functionalized with alkanethiol self-assembled monolayers. [150] This functionalization has been shown before in planar electrodes to support formation of gigaohm seals lasting for several days. [154] Further supporting seal formation and as reported for nanopillars before, [138, 197] the 100 nm-thin upper rim of the nanovolcano induces high-curvature regions in the membrane of contacting cells that is expected to maximize the coupling between the cell and the electrode.

We have shown that nanovolcanoes permit the recording of transmembrane action potentials (APs) from spontaneously active monolayer cultures of primary neonatal rat cardiomyocyte cultures without applying active electroporation. [226] The yield of AP recordings with amplitudes up to 20 mV was close to 30% and continuous recordings for up to 1 h were achieved. Static charge-induced electroporation was suspected to be the main mechanism responsible for the spontaneously occurring sporadic intracellular access of nanovolcanoes. If this hypothesis is correct, controlled electroporation applied to all nanovolcanoes of the array should improve the yield of electrodes showing intracellular access. Moreover, controlled electroporation may improve the amplitudes of the recorded signals by reducing the access resistance and permit longer duration measurements. Hypothetically, the quality of recordings may furthermore profit from the thiol functionalization of the gold ring being in contact with the cells.

In the present study, we investigated these questions using spontaneously active monolayer cultures of neonatal rat ventricular cardiomyocyte. [206] Optimal electroporation waveforms and frequencies were derived from a theoretical model of the cell-electrode interface. The usefulness of thiol functionalization was tested by comparing the performance of nanovolcanoes produced with and without this feature. Controlled electroporation with nanovolcano arrays enabled on-demand intermittent intracellular access for two days with recorded AP amplitudes ranging up to 62 mV and yields as high as $\sim 76\%$. Non-patterned nanovolcanoes showed similar performances compared to nanovolcanoes containing the functionalized gold nanorings.

4.2 Results

4.2.1 Electroporation modelling

A theoretical model representing the cell-electrode interface was established to analytically determine the optimal voltage waveform and frequency necessary to reliably electroporate cell membranes with nanovolcano electrodes. Figure 4.1-A illustrates the electrical equivalent circuit of the cell-nanovolcano interface. The electrode-electrolyte interface is composed of a non-linear resistance, R_{CT} , that represents faradaic charge transfer secondary to redox reactions, in parallel with a constant phase element, CPE_{DL} , that represents the double layer formed by the accumulation of opposite charges at the electrode-electrolyte interface underlying capacitive charge transfer. The stray capacitance, C_{Stray} , denotes the capacitive current leaks along the insulated conductive tracks. The junctional cell membrane covering the microelectrode is modeled by its junctional capacitance, C_j , and the parallel resistance, R_j . The non-junctional membrane impedance is neglected. The seal resistance, R_{Seal} , depicts the current leaks at the cell-electrode interface. To simplify the model and consider the worst-case scenario, the resting membrane potential of the cell was not taken into account. Accordingly, V_j directly reflects the potential applied across the cell membrane. The values for each element forming the cell-electrode interface equivalent circuit are summarized in Table 4.1. Components related to the electrode-electrolyte interface were experimentally measured in Chapter 3 (i.e. R_{CT} , CPE_{DL} , and C_{Stray}) whereas the junctional cell membrane capacitance, C_j , and resistance, R_j , were taken from the literature. [227]

Chapter 4. Controlled electroporation for long-term on-demand registration of cardiomyocyte action potentials with nanovolcano arrays

Table 4.1: Values of the elements composing the electrical equivalent circuit of the electrode-electrolyte interface.

Element	Value
R_{CT}	1.3 G Ω
C_{DL}, n_{DL}	18.6 pF, 0.85
C_{Stray}	0.3 pF
C_j	30 fF
R_j	47 G Ω

In order to induce dielectric breakdown of cell membranes, the junctional potential across the cell membrane (V_j) must reach 300 - 400 mV. [227, 228] Due to the voltage divider formed by the electrode impedance at the electrode-electrolyte interface ($Z_e = R_{CT} \parallel \text{CPE}_{DL}$) and the impedance representing the remainder of the cell-electrode interface ($Z_{ce} = R_{Seal} \parallel C_j \parallel R_j$), V_j is attenuated compared to the electroporation voltage (V_{EP}) applied at the terminals of the device. This attenuation should be minimized to keep V_{EP} low and prevent local hydrolysis in the junctional space. V_j is expressed according to V_{EP} in the next equation:

$$V_j = \frac{Z_{ce}}{Z_{ce} + Z_e} V_{EP} \quad (4.1)$$

where:

$$Z_{ce} = R_{Seal} \parallel R_j \parallel C_j = \frac{R_j R_{Seal}}{(R_j C_j j\omega + 1)(R_{Seal} + \frac{R_j}{R_j C_j j\omega + 1})} \quad (4.2)$$

and:

$$Z_e = \text{CPE}_{DL} \parallel R_{CT} = \frac{R_{CT}}{R_{CT} C_{DL} (j\omega)^n + 1} \quad (4.3)$$

Equation 4.1 was used in Figure 4.1-B to analytically determine the evolution of the attenuation ratio V_j/V_{EP} as a function of the frequency of the sinusoidal electroporation signal applied at different values of R_{Seal} ranging from 10 M Ω to 1 G Ω . At low frequency, the voltage divider determined by R_{Seal} dominates the attenuation because the junctional impedance, and especially R_j is much higher. Therefore, an electroporation signal oscillating at 1 Hz is attenuated by a factor 128 if $R_{Seal} = 10$ M Ω , or by a factor 2 if $R_{Seal} = 1$ G Ω . With increasing V_{EP} frequency, the attenuation factor decreases because the double layer ($Z_{\text{CPE}_{DL}}$) and the junctional cell membrane (Z_j) impedance get smaller. At sufficiently high frequencies, C_j replaces R_{Seal} as the dominant factor and, because CPE_{DL} is larger than C_j , no attenuation is present anymore.

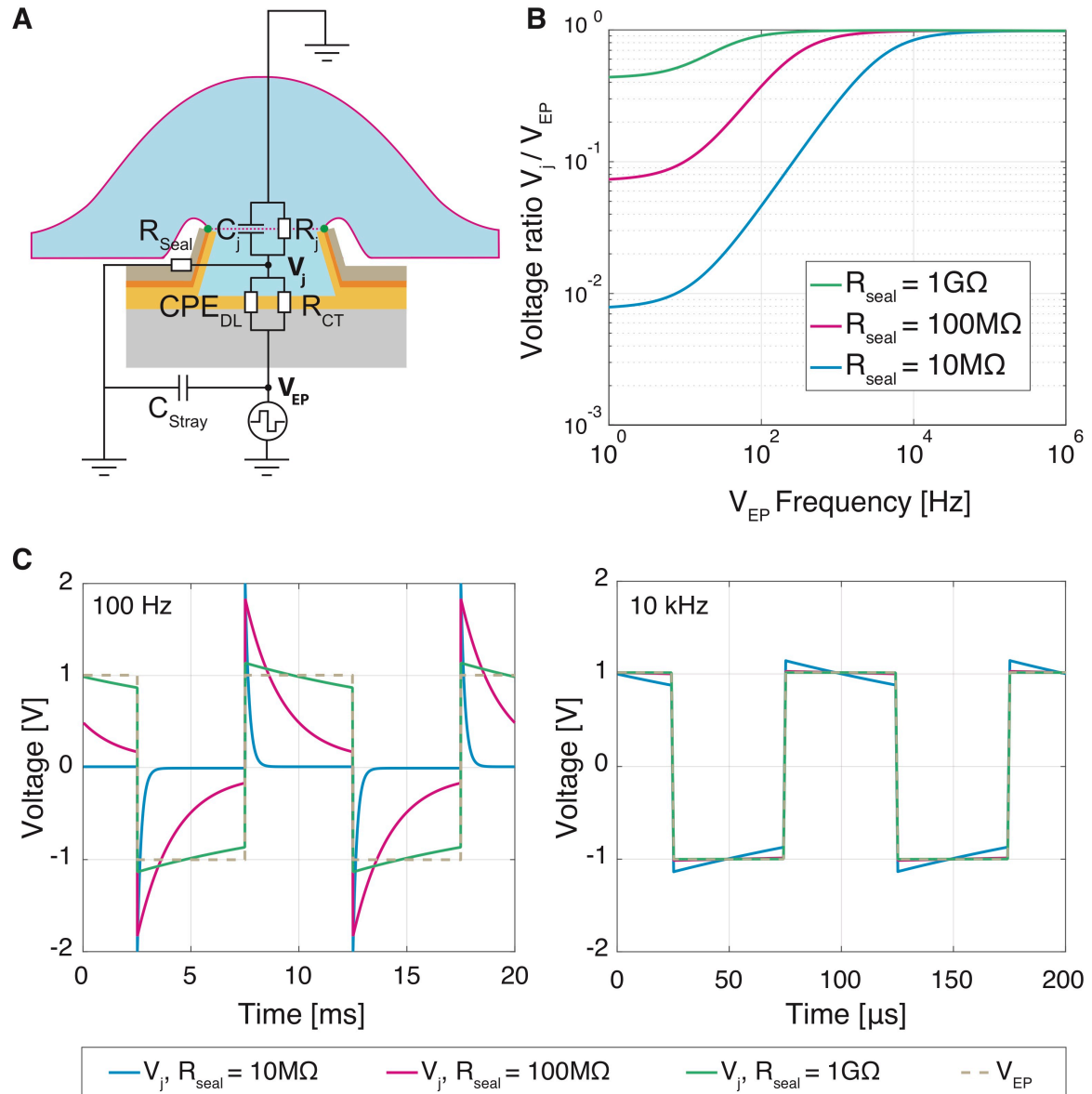


Figure 4.1: *Electroporation model.* **A)** Equivalent electrical circuit of the cell-nanovolcano interface during electroporation. CPE_{DL} is a constant phase element representing the double layer at the electrode electrolyte interface, R_{CT} is the charge transfer resistance reflecting the faradaic charge transfer at the same interface, C_j and R_j model the junctional capacitance and resistance of the cell membrane respectively, R_{Seal} the seal resistance at the cell-electrode interface, and C_{Stray} represents the capacitive current leaks along the electrical tracks. **B)** Frequency-dependence of the junctional voltage amplitude ratio (V_j / V_{EP}) of an electroporation pulse for different seal resistances (R_{Seal}). **C)** V_j waveforms in response to square biphasic electroporation pulses (V_{EP} , stippled line) applied at 100 Hz (left panel) and 10 kHz (right panel) for different values of R_{Seal} (blue: 10 M Ω ; magenta: 100 M Ω ; green: 1 G Ω).

Figure 4.1-C shows the shape of 100 Hz and 10 kHz biphasic square electroporation pulses with amplitude V_{EP} together with V_j induced across the cell membrane. As opposed to sinusoidal waves, biphasic square waves have the distinct advantage of

Chapter 4. Controlled electroporation for long-term on-demand registration of cardiomyocyte action potentials with nanovolcano arrays

reaching electroporation-relevant levels of V_j nearly instantaneously and then maintaining these levels during most of the signal period. At 100 Hz and $R_{Seal} < 1 \text{ G}\Omega$, V_{EP} high frequency components are efficiently transmitted to the junctional space whereas the lower frequency parts are drastically attenuated. At 10 kHz, the cell membrane voltage follows V_{EP} with high fidelity even for low seal resistances, therefore ensuring a more efficient electroporation process for a similar overall pulse train duration. According to this finding, we used 10 kHz biphasic electroporation voltage pulses with an overall train duration of one second in this study. Higher frequencies were avoided to prevent current leaks through the stray capacitance.

4.2.2 Influence of the functionalized nanopattern on electrophysiological recordings made with nanovolcano arrays

Two features of the volcano-shaped microelectrodes likely determine the quality of the electrophysiological recordings: (a) the high curvature formed by the rim of the nanovolcano is thought to force the cell membrane to follow its shape thereby increasing the contact area and, (b), the self-assembled alkanethiol monolayer on the gold nanoring exposed at the top of the nanovolcano is hypothesized to support tight adhesion of the cell membrane. Both of these features are expected to increase R_{Seal} and, hence, raise the signal amplitude. Here, we investigated the relative importance of the two features for establishing a high R_{Seal} . For this purpose, nanovolcanoes with and without thiol-functionalized gold nanorings were produced as shown schematically in Figure 4.2-A and in scanning electron micrographs in Figure 4.2-B. Both types of nanovolcanoes have similar geometries except for thinner walls in case of nanovolcanoes being devoid of a Ti-Au-Ti layer (50 nm instead of 100 nm). Each nanovolcano array was composed of 28 recording sites separated by a pitch of 500 μm .

The experimental protocol used to compare the performance of the two types of nanovolcanoes consisted of applying square voltage waves as defined above (1 V peak-to-peak amplitude, 10 kHz frequency) simultaneously to every microelectrodes of a given device for an overall duration of 1 s prior to the electrophysiological recordings on spontaneously active cardiomyocyte monolayers. The efficacy of electroporation was assessed by determining the amplitude of the APs (APA), the recording duration and the yield. A new electroporation was started when all nanovolcanoes of a given device had lost their signals which resulted in sequential electroporation runs separated by 5 min to 45 min. Typical examples of successful intracellular recordings of action potentials obtained by either type of nanovolcano are shown in Figure 4.2-C. Electrophysiological characteristics presented in the study were extracted from such

traces with selection criteria being defined in the Materials and methods section.

An overall analysis of APAs recorded immediately after given electroporations is presented in Figure 4.2-D for devices with and without functionalized gold rings ($N = 1$ each). Each data point represents the average of APAs of the first three APs recorded by nanovolcanoes with intracellular access. Following the first electroporation (repetition number 1), each type of device reported intracellular activity in 14 channels (yield_{Au} : 73.7 %, $\text{yield}_{\text{NoAu}}$: 63.6 %) with APAs ranging from 0.8 mV to 6.8 mV (nanopatterned) and 0.3 mV to 36.9 mV (non-patterned). Signals recorded by all nanovolcanoes with intracellular access declined over time with a typical example being shown in Figure C.1 of the Appendix, section C. After intracellular signals were lost in all channels of a given device, electroporation was repeated (repetition number 2 to 4). APAs as well as the number of channels showing in-cell activity decreased with each further electroporation. After four consecutive electroporation events, the nanopatterned device did not show intracellular activity anymore whereas, in case of non-patterned volcanoes, 2 channels continued to show activity albeit with very small APAs (< 1 mV). Recording durations, i.e., the time until signals completely disappeared, are presented in Figure 4.2-E. Following the initial electroporation, they ranged from 44 s to 11.3 min (patterned devices) and from 16 s to 8.4 min (non-patterned devices). With each further electroporation, recording durations decreased. Intracellular access yield as defined by the number of channels showing intracellular activity divided by the total number of non-saturated channels per device are shown in Figure 4.2-F. Similar yields were observed after the first electroporation for both patterned (73.7 %) and non-patterned (63.6 %) devices. As was the case for APAs and recording durations, the yield decreased with each consecutive electroporation.

The results indicate that non-patterned nanovolcanoes tend to have similar performance than those with thiol-functionalized gold rings. This suggests that the nanovolcano geometry is the dominant parameter in establishing conditions favorable for obtaining intracellular access. For this reason, only non-patterned devices were used for the remainder of the study.

Chapter 4. Controlled electroporation for long-term on-demand registration of cardiomyocyte action potentials with nanovolcano arrays

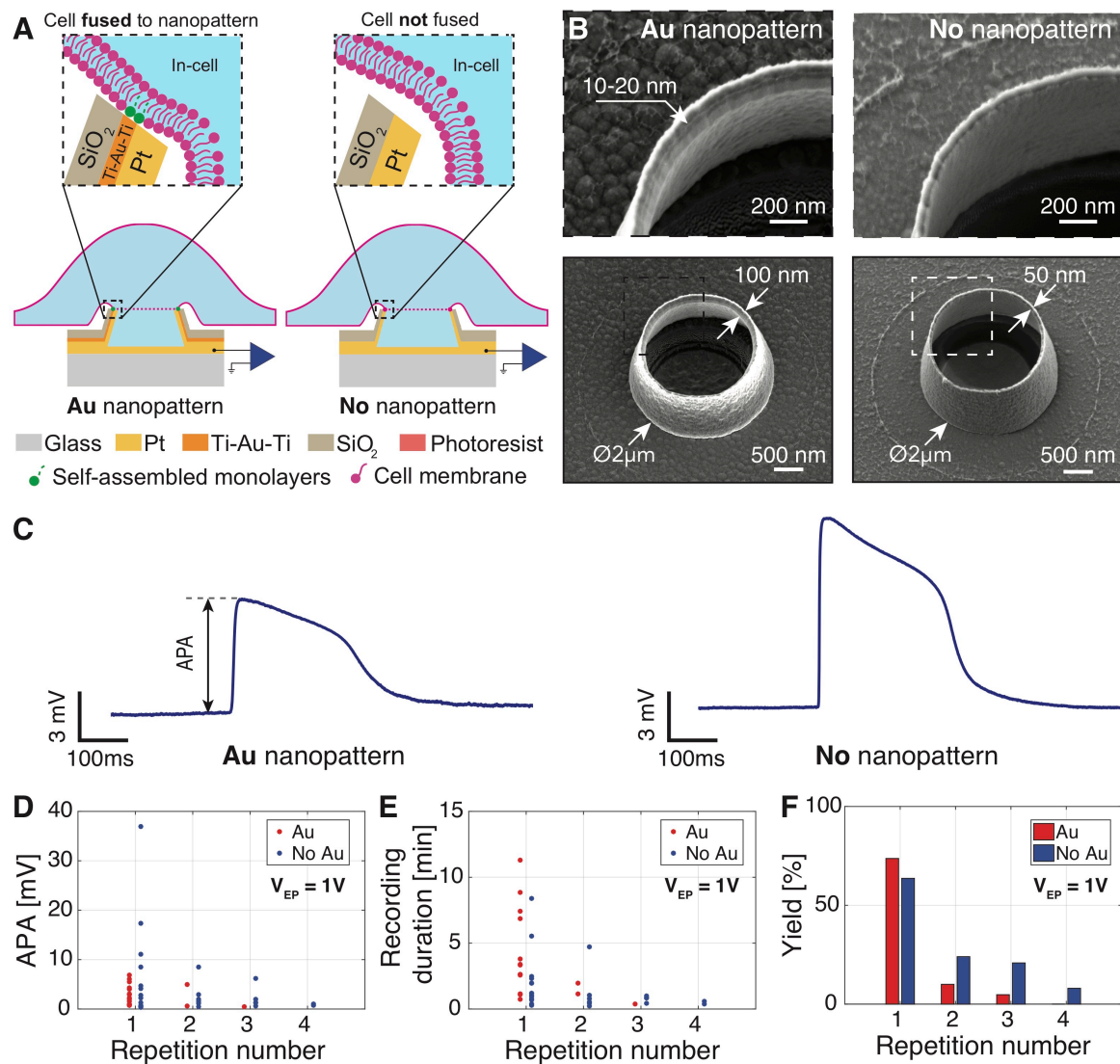


Figure 4.2: Influence of the functionalized Au nanopattern on nanovolcano performance. **A)** Schematic drawings showing the overall structure of a nanovolcano with (left panel) or without (right panel) a functionalized Au nanopattern in contact with the cell. The inserts depict the schematic configuration of the respective cell-electrode interfaces. The electroporated junctional cell membrane is represented by dashed lines. **B)** SEM images of the nanovolcano with (left panels) and without (right panels) the Au nanopattern. The expanded views show the nanowall rim of both types of nanovolcanoes. **C)** Cardiomyocyte action potentials recorded using nanovolcanoes with (left panel) and without (right panel) the Au nanopattern (APA: action potential amplitude). **D)** Evolution of APAs during subsequent electroporations (each data point represents the average of the first three APAs recorded by different nanovolcanoes with intracellular access). **E)** Intracellular recording durations per nanovolcano as a function of consecutive electroporations. **F)** Dependence of the yield (number of nanovolcanoes showing in-cell APs / total number of non-saturated nanovolcanoes per device) on the number of consecutive electroporations.

4.2.3 Effect of the electroporation voltage amplitude on the quality of electrophysiological measurements

Biphasic square voltage pulses with amplitudes ranging from 1 V to 4 V were applied to non-patterned nanovolcano arrays covered with spontaneously active cardiomyocyte monolayers to investigate the effect of the electroporation voltage on the yield and quality of the recorded APs. The interval between consecutive electroporations was determined by the time after which none of the microelectrodes of a given device showed intracellular activity anymore (range: ~ 5 min and ~ 45 min). Figure 4.3 shows APAs, recording durations, and yield of successful recordings obtained at increasing electroporation voltages with four different devices. APAs up to 40 mV were successfully recorded with highest amplitudes recorded at $V_{EP} = 3$ V. With each repetition of electroporation, APAs were further reduced. In case of $V_{EP} = 4$ V, no intracellular activity was detected after the second repetition suggesting that this voltage caused irreversible cell damage. Similar to the dependence of APAs on electroporation voltage, recording durations depicted in Figure 4.3-B suggest that intermediate electroporation voltages (2 V - 3 V) performed best in maximizing periods of intracellular access. With respect to the yield of successful intracellular access following the first electroporation, V_{EP} s ranging from 1 V to 3 V induced access in up to 76.5 % ($V_{EP} = 2$ V) of the nanovolcanoes. Recordings obtained after the first electroporation with $V_{EP} = 2$ V are shown in Figure 4.3-D. The yield of gaining intracellular access declined with each further electroporation with $V_{EP} = 3$ V showing the least decrease. Electroporation voltage amplitudes of 4 V produced the lowest yields and failed to initiate successful recordings after 2 electroporation events. Overall, a V_{EP} of 3 V performed best in regard to APAs, recording durations and yield of intracellular access during repeated electroporations.

Chapter 4. Controlled electroporation for long-term on-demand registration of cardiomyocyte action potentials with nanovolcano arrays

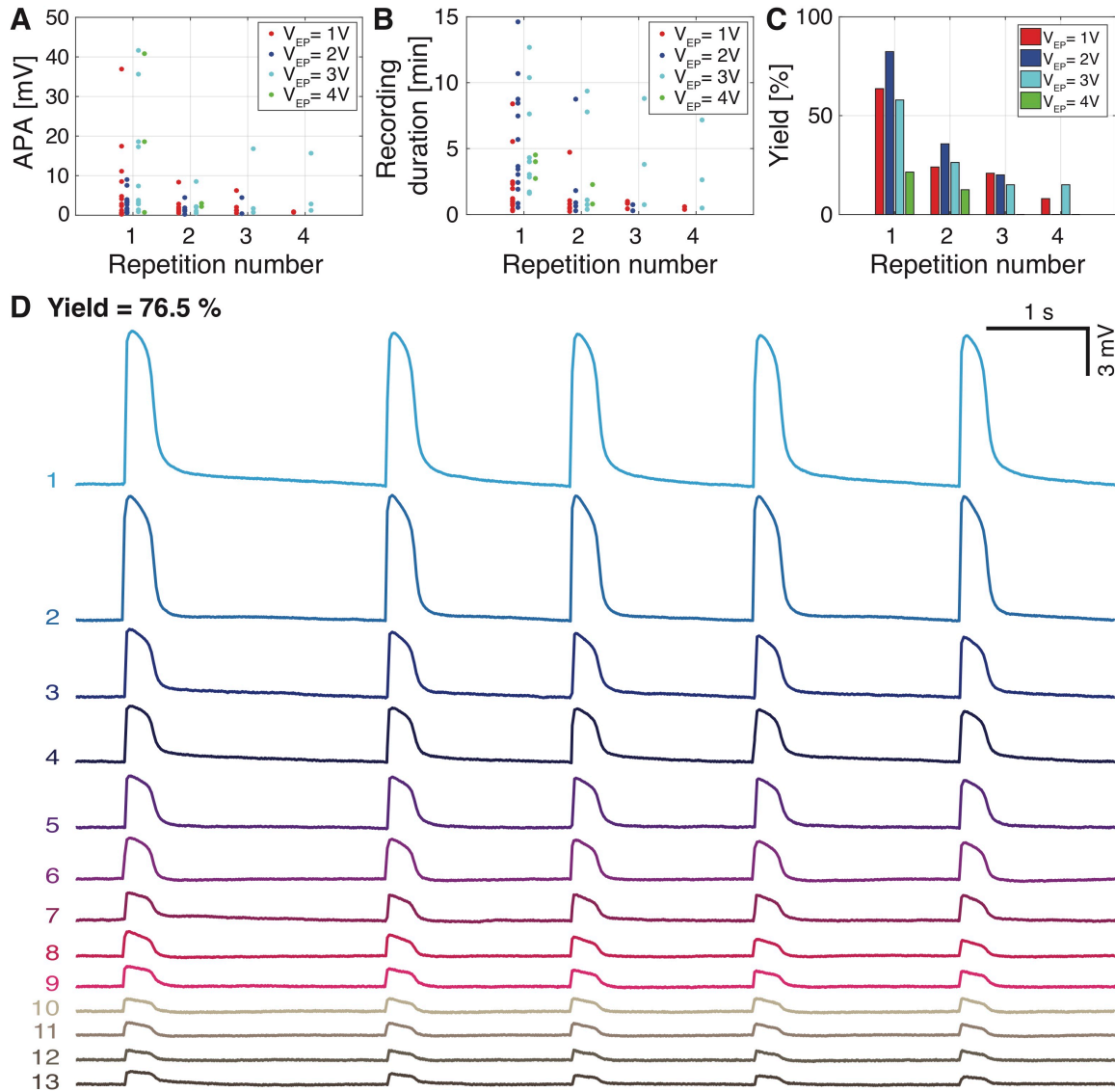


Figure 4.3: Effect of electroporation voltage amplitude (V_{EP}) on the success of intracellular nanovolcano recordings. Evolution of **A**) APA, **B**) recording duration, and **C**) yield of intracellular access during consecutive electroporations for V_{EP} s ranging from 1 V to 4 V. **D**) Simultaneous recording of action potentials from 13 different channels of a nanovolcano array as obtained after the first electroporation at a $V_{EP} = 2V$ (yield of 76.5 %).

4.2.4 Long-term on-demand recordings with nanovolcano arrays

Electroporation protocols were repeated on the same preparations on successive days to investigate the possibility of using nanovolcano arrays in long-term experiments. Recording characteristics were investigated during four sequential electroporation events ($V_{EP} = 3V$) that were repeated after 24 hours (Figure 4.4) in one device.

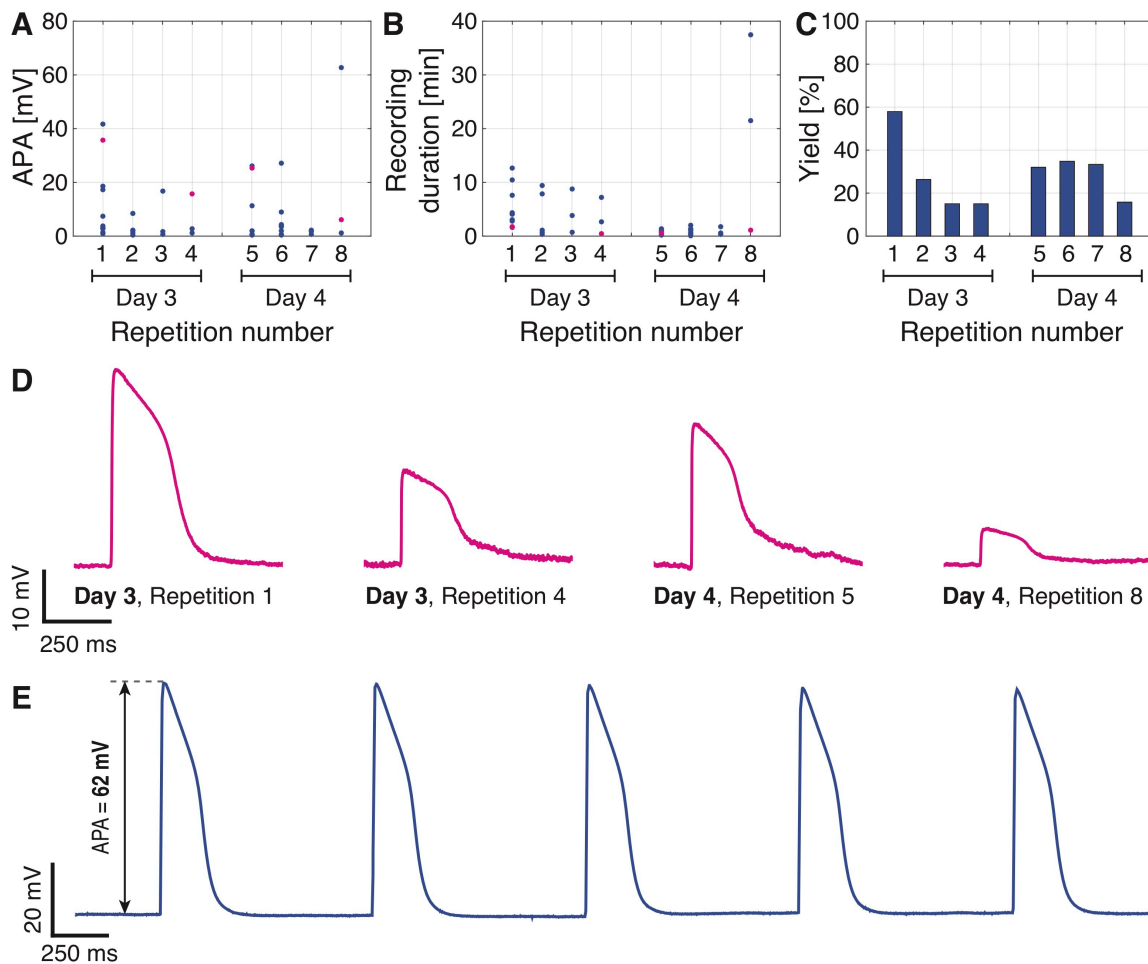


Figure 4.4: Long-term recording with non-patterned nanovolcano arrays. Evolution of **A)** APA, **B)** recording duration, and **C)** yield with two series of electroporations (4 each) performed on successive days ($V_{EP} = 3V$). **D)** Action potentials recorded by a single nanovolcano on subsequent days following multiple electroporations. The signals shown correspond to the data points highlighted in magenta in **A)** and **B)**. **E)** Recording of spontaneous action potentials with an exceptionally high amplitude of ~ 62 mV on day 4 after the preparation underwent 8 electroporations.

Within the two electroporation sequences performed on different days, APAs, recording durations and yield decreased in a qualitatively similar manner to the data shown above for experiments conducted on the same day (Figure 4.3). When comparing the electroporation sequence on day 3 to that of day 4, APAs showed a slight tendency to recover (sequence 4 vs. sequence 5; Figure 4.4-A) whereas recording durations further declined with the exception of 2 recordings in sequence 8 (Figure 4.4-B). The yield showed a decline similar to that observed in other devices during the electroporation sequence on day 3. On day 4, the success rate stayed rather constant during sequential electroporations, i.e., average success rate did not differ from day 3 (Figure 4.4-C). Figure 4.4-D shows intracellular APs recorded from a single nano-

Chapter 4. Controlled electroporation for long-term on-demand registration of cardiomyocyte action potentials with nanovolcano arrays

volcano undergoing multiple electroporations on consecutive days ($V_{EP} = 3$ V). The corresponding datapoints are highlighted in magenta in Figure 4.4-A and 4.4-B. Figure 4.4-E depicts intracellular recordings of spontaneous action potentials as recorded on day 4 with a maximal APA = 62 mV, an average AP duration at 50 % repolarization $APD_{50} = 166 \pm 0.5$ ms and a maximal upstroke velocity $dV/dt_{max} = 22.8 \pm 1.4$ %APA/ms ($V_{EP} = 3$ V, repetition 8).

Overall, these results demonstrate that nanovolcanoes paired with electroporation permit on-demand intracellular access in cultures of excitable cells during extended periods of time.

4.3 Discussion

We recently introduced nanovolcanoes as a tool to perform multisite intracellular electrophysiological recordings following spontaneous insertion of arrays of nanodevices into networks of excitable cells. [226] Here, we show that controlled electroporation improves the yield of successful intracellular recordings with nanovolcano arrays and permits long-term on demand measurements of transmembrane electrical activity in excitable tissues.

4.3.1 Optimizing the electroporation parameters

Optimal electroporation parameters were derived from an analytical model of the cell-electrode interface based on the electrical properties of nanovolcanoes (measured experimentally) and from the general electrical properties of cell membrane characteristics. [227] The model permitted an estimation of the optimal electroporation signal frequency for an efficient perforation of the cell membrane at low voltages. The calculation was based on seal resistances reported previously for similar micro-nanoelectrodes (few hundred of megaohms). [134,137] It predicted that an electroporation frequency of 10 kHz is optimal to minimize both the electroporation signal attenuation across the electrode-electrolyte interface and the extent of hydrolysis. This prediction was experimentally confirmed as electroporation voltage amplitudes as low as 600 mV applied at 10 kHz provided successful intracellular access. Furthermore, the use of 10 kHz biphasic square electroporation pulses induced a symmetrical and mainly capacitive charge transfer at the electrode-electrolyte interface [131] thereby causing charge balance [161] and preventing the generation of toxic reactive oxygen species (ROS). [229] Both of these effects are known to minimize cell damage after electroporation. [228] Even though a single electroporation pulse was sometimes found to be sufficient to

gain intracellular access with nanovolcanoes, a pulse train duration of one second was finally adopted to maximize the yield. [230]

Regarding the electroporation voltage amplitude, $V_{EP} = 3$ V provided an adequate balance between a sufficient reduction of the junctional resistance and the prevention of induction of damages to the seal. As reported in the literature, [154] electroporation damages seal resistances and the poor recording characteristics reported with $V_{EP} = 4$ V is a likely example for this circumstance.

4.3.2 Performance of functionalized vs. non-functionalized nanovolcano tips

The non-conventional ion beam etching redeposition [198] based nanofabrication process underlying nanovolcano manufacturing provided sufficient freedom to develop non-patterned devices, i.e., nanovolcanoes devoid of the intra-wall gold layer. Following thiol functionalization, this gold layer was expected to improve the sealing of the cell membrane to the nanovolcano rim. The non-patterned devices permitted to investigate the relative importance of thiol-functionalization vs. the high curvature of the nanovolcano rim for establishing successful intracellular access. Non-functionalized nanopatterned devices were not used on purpose because the Ti-Au-Ti nanoring itself could have affected the results and, hence, biased the study.

Average APAs recorded after the first electroporation amounted to 3.0 ± 2.1 mV and 6.6 ± 10.1 mV for non-patterned and patterned nanovolcanoes, respectively. The corresponding yield and recording durations amounted to 73.7 % / 243.9 ± 195.9 s (patterned) and 63.6 % / 124.4 ± 134.7 s (non-patterned; $N = 14$ for all data). Whereas the relatively large variability of values precludes unequivocal conclusions as to the relative performance of the two types of nanovolcanoes, the overall trend suggests that the geometry of the nanovolcano tip in contact with the cell likely played a dominant role by inducing a tight seal of the cell membrane around the protruding nanostructure. [138,197]

The relatively large variation APAs, recording durations, and yield among the nanovolcanoes of a given device may have several reasons: (i) fabrication dependent differences in the exact nanostructure of the top of the nanovolcano may have affected the quality of R_{Seal} with consequences for all assessed parameters; (ii) the position of individual nanovolcanoes in respect to the monolayer of cardiomyocytes may have resulted in microelectrodes being ideally positioned below a given cell and others being situated at cell-cell borders and, hence, having less chances to establish

Chapter 4. Controlled electroporation for long-term on-demand registration of cardiomyocyte action potentials with nanovolcano arrays

a high-quality seal. [231] (iii) A few of the nanovolcanoes may have been in contact with non-cardiomyocytes (myofibroblasts) that are well known “contaminants” of primary heart cell cultures. [232] These non-excitable cells are electrotonically coupled to cardiomyocytes and, as a consequence, display passive “action potentials” with attenuated amplitudes. According to these potential factors inducing variability in recordings, improvements may be made by (i) introducing a polishing procedure to obtain reproducible and seal promoting flat surfaces of the nanovolcanoes, (ii) control of the cell positioning with respect to the nanovolcanoes with hydrodynamic traps, [233,234] and, (iii) producing cardiomyocyte only cell cultures by, e.g., fluorescence-activated cell sorting (FACS) sorting. Moreover, probing signals to investigate the cell-electrode coupling quality might be applied and the results used to compensate APAs according to a calibration curve established beforehand.

Overall and apart from performing at least similar if not better than patterned nanovolcanoes, non-patterned nanovolcanoes devices have the distinct advantage on being based on a simplified preparation procedure which facilitates their production and storage in case of a potential scale up.

4.3.3 Effects of repetitive electroporations

Compared to previous results obtained with nanovolcanoes gaining spontaneous intracellular access (maximal APA of 20 mV; maximal yield of 30%; maximal recording duration of 66 min), [226] electroporation substantially improved the recording success. APAs up to 40 mV were frequently observed with one recording showing an APA of 62 mV which corresponds to 2/3 of a non-attenuated cardiomyocyte APA. [203] Also, the yield of nanovolcanoes reporting intracellular electrical activity more than doubled to 76.5 %. Similar to the decline of APAs in case of nanovolcanoes gaining spontaneous access to the cell interior, APAs declined after electroporation as well indicating that, for both modalities, the cell membrane spanning the opening of the nanovolcano tended to reseal. That electroporation only provides intermittent intracellular access has been reported before. [132, 141] With each consecutive electroporation, APAs, recording duration and yield showed a decline: when comparing the first with the last (fourth) electroporation ($V_{EP} = 3$ V), APAs decreased by ~ 50 %, recording durations by ~ 30 % and the yield by ~ 75 %. The decrease of APAs may be explained by deterioration of the cell-nanovolcano contact and, hence, a decrease of R_{Seal} . Interestingly, when pausing electroporation for 24 hours, both the APAs and yield showed a slight recovery suggesting partial restitution of the cell-electrode interface.

4.3.4 On-demand intracellular access for long term recordings

Compared to our previous work, the possibility to re-open membranes by electroporation increased the apparent overall recording duration by permitting discontinuous on-demand intracellular access for at least two days. These results indicate that electroporation performed with nanovolcanoes is mainly localized to the small membrane patch defined by the nanovolcano geometry and therefore permit a gentle access to the intracellular space without altering the cell viability. In this study, intracellular access frequently lasted tens of minutes and up to 38 minutes before the cell membrane resealed. Prospectively, the resealing time could be slow-down by optimizing the nanovolcano geometry or modifying its inner surface material. In the literature, hollow nanoelectrodes made of IrOx showed intracellular recording duration up to 100 minutes, much longer compared to Au pillars with similar dimensions. [141]

Repetitive measurements on the same site is an essential advantage over conventional patch clamp measurements of action potentials as it permits the screening of pharmacological compounds at high-throughput and over extended periods of time.

4.3.5 Comparison to other micro-nanotechnology based electrode arrays granting intracellular access

Micro-nanotechnologies based electrode arrays aim to assess electrophysiological characteristics of networks of excitable cells over extended periods of time with recording qualities approaching those of standard intracellular measurements. Table 4.2 compares the respective performance of recently presented micro-nanotechnology based multielectrode arrays. In all experiments, data were collected from primary rat cardiomyocyte cell cultures with intracellular access being induced by electro- or optoporation. By comparison, nanotube-like electrodes composed of IrOx enabled the longest continuous intracellular recordings (~ 100 minutes) followed by nanovolcanoes, plasmonic metaelectrodes, nanoneedles and micromushrooms. APAs were largest in the nanovolcanoes while maximal yield was best in plasmonic metaelectrodes, closely followed by nanovolcanoes. By contrast to the other technologies, APs measured with nanovolcano arrays did not suffer from high-pass filtering distortion due to the recording system and therefore, can be exploited, e.g., for pharmacological studies aiming at detecting side effects of drugs on AP shape in general and AP duration in particular.

Chapter 4. Controlled electroporation for long-term on-demand registration of cardiomyocyte action potentials with nanovolcano arrays

Table 4.2: Summary of features of transmembrane voltage measurements with micro-nanoelectrodes in primary rat cardiomyocyte monolayers.

Insertion method	Technology	Max. APA [mV]	Max. Duration		Max. Yield [%]	Distortion / Bandwidth [Hz]
			Single access [min]	Multiple access		
Electroporation	Nanovolcano	62	66 [226]	Days	76.5	No / 0-8000
	Nanoneedle [134]	20	20	Days	30	Yes / 1-5000
	Micromushroom [147]	6	10	Days	-	Yes / 1-10000
	IrOx nanotubes [141]	15	100	Days	10	Yes / 0.01-3000
Optoporation	Metaelectrodes [160]	5	40	Minutes	85.4	-

4.3.6 Limitations of the study and outlook

In this study, electrophysiological recording performances of two different nanovolcano architectures were investigated under different electroporation modalities with one device being used per each condition. This low number does not allow for a systematic statistical comparison of the data. The unequivocal results obtained, however, permit to draw qualitative conclusions and to detect trends when comparing the micro-nanoelectrode devices.

Future developments of nanovolcano arrays may focus on manufacturing the micro-electrodes directly on integrated CMOS amplifiers in order to maximize signal-to-noise ratios and facilitate the electroporation procedure. Moreover, this approach would permit to increase the density of nanovolcanoes per device which is now limited by the electrical tracks. Such an approach has been described for nanoelectrodes before (1024 recording sites with dedicated amplifiers). [134] Apart from producing larger datasets at minimized experimental cost, a high-density array would extend the system capabilities in the context of permitting spatially resolved measurements of electrical activation patterns.

4.4 Conclusion

In this chapter, we demonstrate that electroporation significantly improves the recording characteristics of transmembrane action potentials measured with nanovolcano arrays. An analytical model is proposed to predict the electroporation voltage attenuation across the electrode-electrolyte interface and suggests optimal electroporation parameters to perforate cell membranes with low voltage amplitudes. Electroporation is shown to drastically improve the quality of the electrophysiological recordings

reported with the nanovolcanoes arrays in terms of APAs, recording duration, and yield. The signal quality is shown not to be dependent on the presence of functionalized nano-patterns incorporated into the tip of the nanovolcano which indicates that the “sharp” geometry of the top of the nanovolcanoes is sufficient to establish optimal seal conditions at the cell-electrode interface. Importantly, electroporation enables on-demand intracellular access during consecutive days indicating that interactions of the nanovolcanoes with the cells is largely non-destructive and opening the perspective to follow electrical activity over periods of time being relevant for assessing developmental aspects of the preparations under investigation.

4.5 Materials and methods

4.5.1 Microfabrication

Nanovolcano arrays were manufactured following the nanofabrication process described in detail in the previous Chapter 3, with the help of Nicolas Maino (Microsystems Laboratory 4, EPFL). Briefly, a standard fused silica wafer (100 mm in diameter, 550 μm -thick) was covered with a multilayered metal stack by successive evaporations prior to be coated by a 150 nm-thick layer of sputtered SiO_2 . For nanovolcanoes on which a thiol pattern was self-assembled (“patterned nanovolcanoes”), the multilayered stack consisted of Ti-Pt-Ti-Au-Ti- SiO_2 (10-250-50-50-50-150 nm). For nanovolcano arrays without the self-assembled thiol pattern (“non-patterned nanovolcanoes”), a stack of Ti-Pt- SiO_2 (10-250-150 nm) was used instead. 2 μm in diameter openings were patterned into a 2 μm -thick AZ nLOf 2020 negative photoresist layer (MicroChemicals, Germany) by direct laser writing and Ar^+ ion beam etching redeposition was used to manufacture the nanovolcano sidewalls. [198] 3 μm -wide electrical tracks that connected every nanovolcano to its interfacing pad were patterned by photolithography and conventional ion beam etching. Finally, a 4.5 μm -thick SU8 insulating layer was coated and patterned by direct laser writing, providing 20 μm in diameter openings surrounding each microelectrode of the wafer.

4.5.2 Device preparation

Nanovolcano arrays were assembled with a glass ring forming the cell culture well using polydimethylsiloxane (Sylgard 184 Silicone Elastomer kit 10:1; Dow Corning, USA) as glue, cured for 2 hours at 80 $^\circ\text{C}$. Nanopatterned arrays were sterilized for 30 s by O_2 plasma (100 W, 650 mTorr; Diener Electronic, Germany) prior to be submerged for 1 hour in a 20 mmol/L hexanethiol solution in pure ethanol for self-

Chapter 4. Controlled electroporation for long-term on-demand registration of cardiomyocyte action potentials with nanovolcano arrays

assembled monolayer formation. After ethanol rinsing, the microelectrode arrays were thoroughly rinsed with sterile deionized water. As demonstrated before, hexanethiols do not attach to the Pt electrode. [154] For non-patterned devices, the hexanethiol solution was replaced by pure ethanol. Finally, the substrate was coated with collagen type IV (C5533, Sigma, Germany) before cell seeding. Only new devices were used during this study.

4.5.3 Isolation and culture of primary rat cardiomyocytes

Primary neonatal rat (Wistar, 1 day old) ventricular cardiomyocytes were isolated and cultured on nanovolcano arrays as detailed in Chapter 3. These procedures were performed in compliance with federal guidelines for animal experimentation under license BE27/17 of the Bernese veterinary department.

4.5.4 Electroporation procedure

Prior to the first electroporation, a control recording was performed to guarantee absence of intracellular activity due to static charge-induced electroporation. [226] Thereafter, biphasic voltage pulses with a period of 100 μ s and an amplitude ranging from 1 V to 4 V with respect to the four reference electrodes integrated in the device were simultaneously applied to every channel of the device using a A-M Systems Model 2100 pulse stimulator (A-M Systems, USA) for an overall duration of 1 s before initiating the electrophysiological recordings.

4.5.5 Electrophysiology

Electrophysiological experiments were conducted together with Etienne de Coulon and Prof. Stephan Rohr at the University of Bern. Recordings were started 48 hours after cell seeding. At this time, cardiomyocytes had formed a uniform cell monolayer that exhibited spontaneous synchronized electrical activity and contamination by proliferating non-cardiomyocytes was still moderate. Experiments were performed in a dry incubator (37 °C; 0.8 % CO₂) using a DC-coupled HS-36 headstage ($R_{In} = 1 \text{ T}\Omega$, $C_{In} = 2 \text{ pF}$; bandwidth = 0 – 8 kHz) together with a Digital Lynx SX acquisition system (Neuralynx, USA). Preparations were covered with a lid to prevent evaporation.

4.5.6 Data analysis

A custom-made Matlab2016a (MathWorks, USA) script was developed to extract the electrophysiological parameters of interest from the recorded signals (APA, APD₅₀,

and dV/dt_{max}) as well as the recording duration per channel and intracellular yield per device. Every electrical trace analyzed and presented in this work correspond to the non-filtered raw data.

In order to objectively define the duration of intracellular recording per channel, an AP was considered intracellular until its APA decreased below $250\ \mu\text{V}$ or until the maximum of the first derivative thereof became smaller than three times the absolute value of its minimum indicating that the upstroke of the signal is similarly fast as the downstroke as is typical for extracellular recordings.

Recordings from channels showing saturation were excluded from the analysis. Saturation occurring in a few channels was likely the results of the combination of the relatively large impedance of the nanovolcanoes with the DC-coupled headstage of the recording system.

Chapter 5

Volcano-shaped SPM probe for combined force-electrogram recordings from cardiomyocytes

This thesis chapter is adapted from our recently submitted article: B.X.E. Desbiolles, M.T.M. Hannebelle, E. de Coulon, A. Bertsch, S. Rohr, G.E. Fantner, and P. Renaud, “Volcano-shaped SPM probe for combined force-electrogram recordings from excitable cells”, *Submitted*, 2020.

5.1 Introduction

Mechanobiology is an emerging field at the frontiers between biology and engineering that focuses on studying the role of mechanical properties of biological specimens and the effect of forces acting on those specimens in physiology. [235–238] Over the last three decades, atomic force microscopy (AFM) [239] has been widely used to map mechanical properties and responses of biological systems to mechanical cues. [240–244] AFM exhibits force sensitivities in the piconewton range [245] with nanometer-scale lateral resolutions. [246] It is compatible with a broad range of biological samples ranging from single molecules to cells and tissues. The mechanical properties of mammalian cells were extensively studied using AFM based approaches [247–254]. For instance, cell differentiation [255, 256] or fibrosis [257] was shown to be dependent of the substrate stiffness. AFM was also used to study mechanical stresses during bacterial division, [258] turgor pressure [259] and adhesion. [260]

The key challenge in mechanobiology consists of linking functional responses of

Chapter 5. Volcano-shaped SPM probe for combined force-electrogram recordings from cardiomyocytes

complex biological systems to mechanical stimuli. [261] AFM based approaches alone are essentially blind to mechanically triggered biological responses such as changes in cellular electrophysiology and, accordingly, complementary techniques need to be developed to convey multimodal capabilities to the AFM. Presently, this is achieved by combining AFM with optical microscopy of cells expressing or being loaded with fluorescent indicators of physiological parameters like transmembrane potentials [196] (e.g., voltage-sensitive dyes, genetically encoded voltage indicators) or ion concentrations [262] (e.g., calcium indicators). As an example, cells expressing mechanosensitive ion channels can be mechanically stimulated by AFM and their electrophysiological response be monitored in real time using fluorescent calcium imaging. [263] Disadvantages of optical techniques include, apart from the requirement of cell manipulation and the introduction of indicators that themselves may adversely affect cellular function, phototoxicity that limits the duration of experiments. [73] Other studies combined AFM recordings of contraction displacement of cardiomyocytes with extracellular field potential (electrograms) measurements provided by multielectrode arrays (MEA). [264, 265] Similarly, planar patch-clamp devices were used to record transmembrane potentials of mechanically stimulated cells. [266, 267] Even though direct recordings of electrical activities were achieved, the limitation of these techniques mainly consist in their complexity and the lack of freedom when selecting a specific cell, because that cell has to be located exactly on top of a given microelectrode. To overcome these challenges, Ossola *et al.* used the FluidFM probe [268, 269] as a force-controlled nanopipette to simultaneously record force and ion channel activities in a whole-cell configuration, therefore pioneering the field of AFM-based force-controlled electrophysiology. [270] In this study, the electrical access to the cell was granted via an embedded microfluidic channel filled with saline solution that connected the tip opening to the recording system. Depending on the experimental question asked, this methodology has the disadvantage of washing-out intracellular small molecules thereby compromising, e.g., the integrity of the second messenger signaling cascade. [271] Moreover, a fluidic access to the cell significantly complicates the experimental setup as fluidic connections and pressure controllers are needed. Additionally, the embedded microchannel significantly limits the minimal cantilever thickness achievable; therefore limiting the bandwidth and the sensitivity during force measurements.

Cells are constantly interacting with each other and with their environment through chemical, mechanical and electrical factors. The latter include mechanical forces, cellular stiffness, electrical potentials and ion currents that determine the cell behavior. Here we propose a new fluidic-free instrument that combines, within a single probe, measurement capabilities for both electrical and mechanical factors determining cell.

Central to the device is a novel type of probe for scanning probe microscopy (SPM) consisting of a protruding three-dimensional (3D) volcano-shaped microelectrode at its apex that enables fluidic-free combined force and electrophysiological recordings from single-cells or tissues. The device is termed “nanovolcano probe” as it integrates our recently developed nanovolcano electrode [226,272] at the tip of an AFM cantilever.

Force and impedance were concurrently measured when engaging onto neonatal rat cardiomyocytes to confirm the proper functioning of the probe in a conventional AFM setup. Thereafter, the nanovolcano probe was used to investigate whether it could be used to record simultaneously mechanical and electrophysiological activity from single-cells. Successful recording of electrograms together with cardiomyocyte contraction displacements demonstrated that the nanovolcano probe enables combined force-electrogram recordings. These findings render the nanovolcano probe particularly suitable for mechanobiological studies aiming at linking electrophysiological responses with mechanical stimuli at the single-cell level.

5.2 Results

5.2.1 Microfabrication and interfacing

The nanovolcano probe concept and design are summarized in Figure 5.1-A. The inner surface of the 8 μm -wide nanovolcano consists of a large electrodeposited platinum-black electrode that minimizes the access impedance to the cell. The outside of the structure is covered with a 20 nm-thick insulating SiO_2 layer that prevents current leaks from the electrode. Furthermore, a 5 to 10 nm-thick gold nanoring stacked in-between two Ti layers and functionalized with self-assembled monolayers of alkanethiols forms the site of contact with the cell membrane and is thought to optimize the cell-electrode interface [150–152, 154, 155]. The microelectrode is attached to a 2.2 μm -thick SiO_2 cantilever, that is coated on the backside with a 50 nm-thick Cr-Au reflective layer allowing for conventional optical beam deflection measurement in an AFM. [273]

As illustrated in Figure 5.1-B, conventional ion beam etching was used to pattern 3 μm -wide conductive tracks on a Si substrate covered with a 2 μm -thick layer of thermally grown SiO_2 that was subsequently insulated with 200 nm of sputtered SiO_2 . The nanovolcano was then manufactured at the tip of the Ti-Pt-Ti-Au-Ti- SiO_2 pattern by ion beam etching redeposition. [198,226] To this end, openings with a diameter of 8 μm were patterned into a 6 μm -thick negative photoresist layer. During ion beam etching,

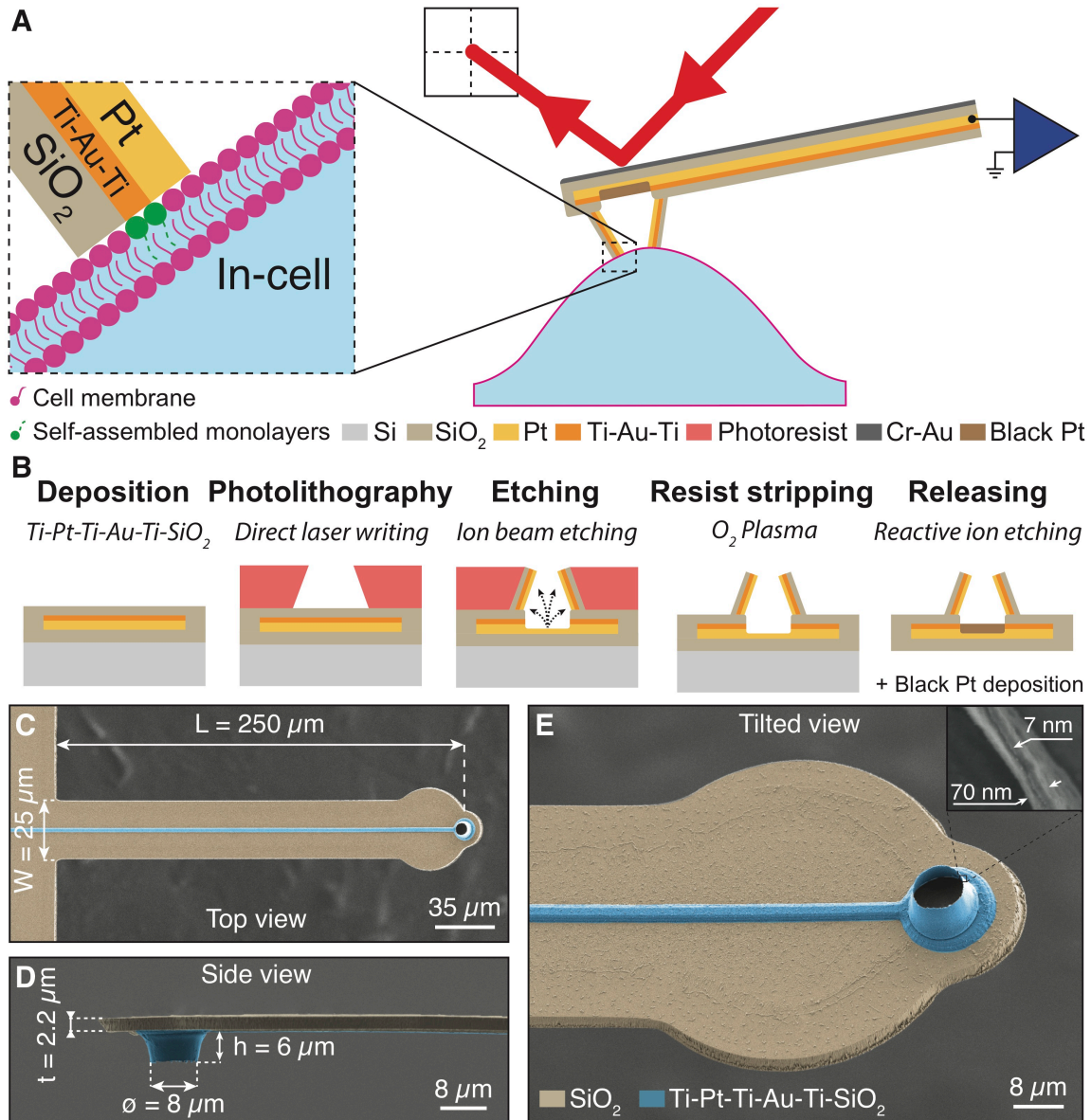


Figure 5.1: *Concept and microfabrication of the nanovolcano probe. A)* Schematic drawing showing the nanovolcano probe in contact with a cell. The cantilever deflection as well as the electrical signal from the nanovolcano are measured simultaneously. The insert shows the cell-electrode interface in detail. **B)** Microfabrication process used to manufacture the nanovolcano probe. Insulated metallic tracks are patterned onto a 2 μm-thick SiO₂ layer covering the Si substrate. During ion beam etching, the material etched from the substrate is redeposited on the photoresist sidewalls therefore forming the nanovolcano after resist stripping. The SiO₂ cantilever is subsequently defined and released by reactive ion etching. **C-E)** SEM images showing top view, side view, and tilted view (angle of 30°) of the nanovolcano probe. The volcano electrode structure and the conductive tracks are colored in blue.

a part of the etched material from the substrate was redeposited onto the photoresist sidewalls, thereby creating the multilayered nanovolcano wall after resist stripping by O₂ plasma. The SiO₂ cantilever was then defined, with a wider circular shape close

to the tip to maximize the laser reflection, and released by reactive ion etching (RIE). Due to the compressive stress accumulated in the SiO₂ layer during thermal growth, the released cantilever bent in the opposite direction from the substrate. In a final fabrication step, stressed layers of Cr-Au (50-50 nm) were evaporated onto the backside of the cantilever to compensate for their bending and to render them reflective.

Scanning electron microscope (SEM) images of the finalized nanovolcano probe are shown in Figure 5.1-C to E. As illustrated by Figure 5.1-C and D, the SiO₂ cantilever dimensions were chosen such as to ensure a stiffness comparable to cells (for the nanovolcano probe: $k_{\text{Measured}} = 0.45 \text{ N/m}$). The nanovolcano electrode placed at the tip of the cantilever was fabricated with a relatively large diameter to ensure a low electrode-electrolyte impedance whereas its height guaranteed that the nanovolcano touched the sample first during AFM manipulation. The inset in Figure 5.1-E shows the 7 nm-thick gold nanoring flanked by two titanium layers in the middle of the 70 nm-thick multilayered nanovolcano wall.

The nanovolcano probe was interfaced to a shielded printed circuit board (PCB) connected to a 800 μm -diameter coaxial cable and screwed to a custom-made AFM cantilever holder as illustrated in Figure 5.2-A. Figure 5.2-B shows the nanovolcano probe glued to the PCB and wire-bonded to the gold coated PCB pad making a direct connection to the inner wire of the coaxial output, and therefore guaranteeing a standard electrical connection to the nanovolcano. A glob top was used to electrically insulate the chip-PCB interface when the system is immersed in liquid (cf. Figure 5.2-C). Details regarding the interfacing protocol are described in the Materials and methods section.

Overall, this interface prevents any electrical shortcut when working in a liquid environment, and shields the recorded electrical signals from external electromagnetic noises, therefore allowing for low-noise recordings. The cantilever holder keeps the nanovolcano probe tilted at an angle of 11° with respect to the horizontal, as required for the optical deflection measurement with AFM.

Finally, platinum-black was locally electrodeposited into the nanovolcano to decrease its electrode-electrolyte impedance. A complete electrochemical characterization of the nanovolcano probe is provided in the next section.

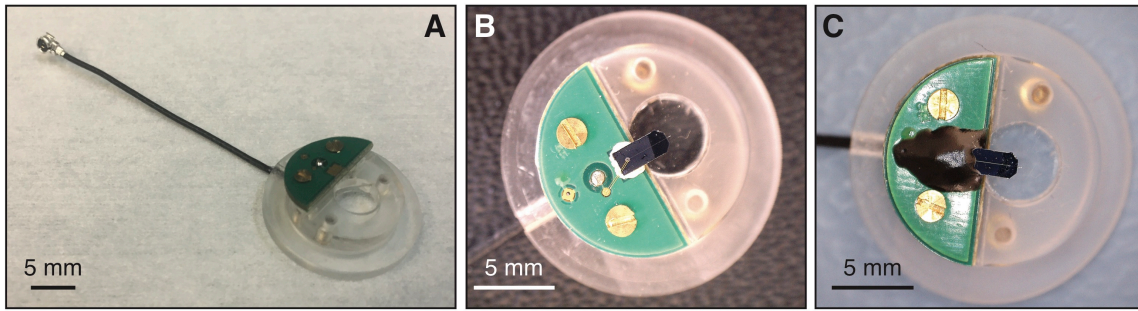


Figure 5.2: *Mechanical and electrical interfacing of the nanovolcano probe. A)* Picture of the custom-made AFM holder without the nanovolcano probe assembled. **B)** Top-view image of the nanovolcano probe mechanically assembled and wire-bonded to the custom-made holder. **C)** Top-view image of the interface with the glob top used to insulate the chip-PCB electrical contact.

5.2.2 Electrochemical characterization

Electrode-electrolyte interface Figure 5.3-A shows the electrical equivalent model of the electrode-electrolyte interface. As previously described, it is composed of a non-linear resistance, R_{CT} , that represents faradaic charge transfer secondary to redox reactions, in parallel with a constant phase element CPE_{DL} representing the double layer capacitance underlying the capacitive charge transfer. R_{Spread} represents the resistance induced by the confinement of the electric field lines near the microelectrode. The stray capacitance, C_{Stray} , denotes the capacitive current leaks along the insulated tracks.

The electrode-electrolyte interface properties have been experimentally measured using electrochemical impedance spectroscopy (EIS) based on a 100 mV sinusoidal signal applied to the nanovolcano probe in presence of phosphate buffer saline (PBS) at room temperature. The EIS data are shown in Figure 5.3-B and show a typical electrode-electrolyte behavior. [131] Values for each element composing the electrical equivalent circuit have been extracted and are summarized in Table 5.1.

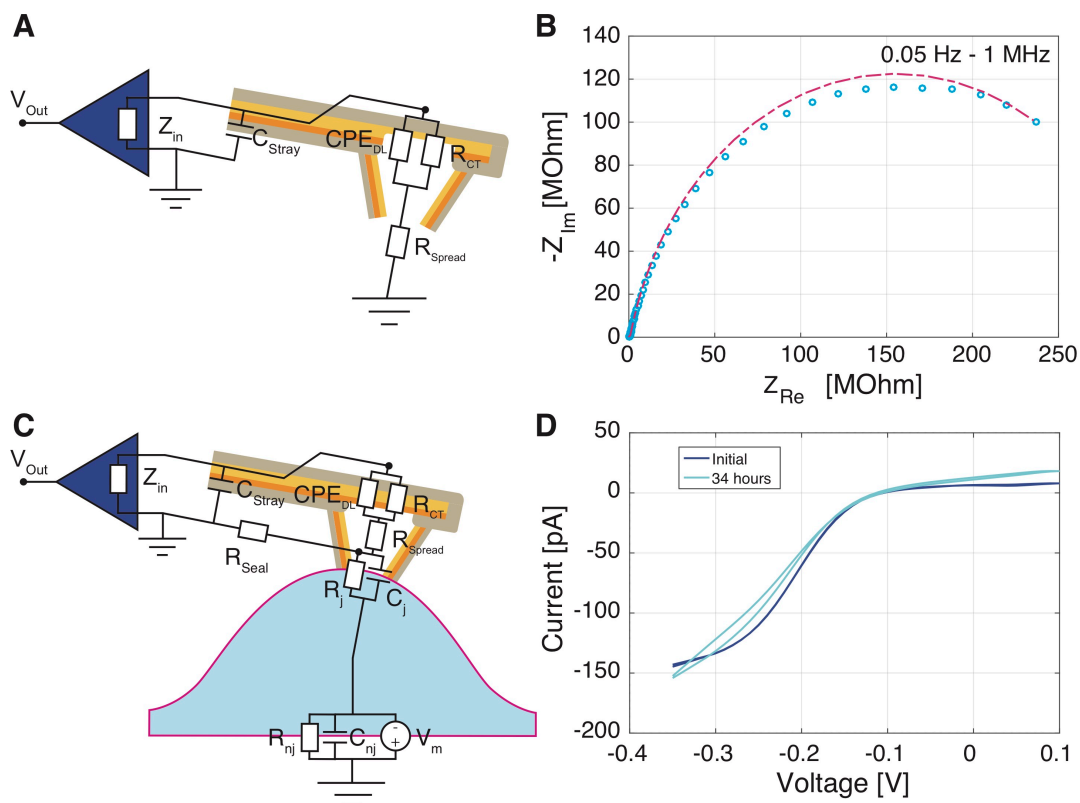


Figure 5.3: *Electrochemical characterization of the nanovolcano probe.* **A)** Equivalent electrical model of the electrode-electrolyte interface. **B)** Electrochemical impedance spectroscopy of a single nanovolcano probe in PBS. **C)** Equivalent electrical model of the cell-electrode interface. **D)** Cyclic voltammogram of the nanovolcano probe right after immersion in a solution of 5 mM hexaamine ruthenium chloride and 100 mM potassium nitrate in deionized water (dark blue) and after 34 hours of continuous chronoamperometry at a fixed potential of -0.35 V (light blue).

Table 5.1: Experimental values of every element composing the electrical equivalent circuit of the nanovolcano probe electrode-electrolyte interface.

Element	Value
R_{CT}	$315 \text{ M}\Omega$
C_{DL}, n_{DL}	$4.15 \text{ nF}, 0.82$
R_{Spread}	$74.4 \text{ k}\Omega$
C_{Stray}	30 pF

Cell-electrode interface Figure 5.3-C represents the electrical equivalent circuit once the nanovolcano probe is in contact with a cell. In this situation, the junctional membrane resistance R_j and capacitance C_j are added in parallel with the seal resistance R_{Seal} – representing the leaks at the cell-electrode interface – at the tip of the nanovolcano probe. V_m is the cell transmembrane potential whereas R_{nj} and C_{nj}

respectively represent the non-junctional cell membrane resistance and capacitance.

While engaging the probe onto the cell, no variation of the resistance is expected at low frequency as the seal resistance R_{Seal} is likely lower compared to the charge transfer resistance R_{CT} . However, at higher frequency, the impedance of the electrode-electrolyte interface ($CPE_{DL} \parallel R_{CT}$) becomes negligible as most of the current passes through the low double layer impedance. At this frequency, impedance measurements should directly represent the spreading resistance R_{Spread} in serial with the other components of the cell-electrode interface ($R_{Seal} \parallel R_j \parallel C_j$). For this reason, the impedance seen by the nanovolcano probe should increase when approaching the cell surface.

Long-term characterization The long-term stability of the nanovolcano probe was characterized by Scuba Probe Technologies LLC. The nanovolcano probe was immersed into a solution of 5 mM hexamine ruthenium chloride and 100 mM potassium nitrate in deionized water. As shown in Figure 5.3-D, a first cyclic voltammogram was acquired between -0.35 V to 0.1 V vs. Ag/AgCl at a scan rate of 50 mV/s using a 3 electrodes setup (dark blue curve). For the next 34 hours, the nanovolcano potential was hold at -0.35 V while similar cyclic voltammograms were registered every 20 minutes as control. The light blue cyclic voltammogram in Figure 5.3-D shows nearly no significant differences compared to the initial one, thereby demonstrating that the nanovolcano probe was functional for 34 hours.

5.2.3 Force and electrical measurements on rat cardiomyocytes

The nanovolcano probe was mounted on a custom-made setup composed of a tip-scanning AFM positioned above an optical inverted microscope and a custom sample holder to keep the biological sample in physiological conditions (see Materials and methods section). Experiments with neonatal rat cardiomyocytes were performed to validate that both force and impedance signals can be recorded simultaneously by the nanovolcano probe.

Cardiomyocytes were cultured at low density for 48 to 72 hours prior to the experiment. During experiments, the cantilever position and deflection were recorded while the nanovolcano probe was repeatedly brought in contact with a cell of interest followed by pulling away using the AFM piezoelectric actuator. A typical result of such an experiment is shown in Figure 5.4-A: the probe was initially lowered towards the cell by $\sim 11 \mu\text{m}$ while applying a maximal force of 772 nN before being withdrawn

again at $t = 0.25$ s. The maximally applied force is three orders of magnitude larger than the force usually used as a setpoint for non-destructive AFM imaging (a few hundred pN). However, because the contact area between the nanovolcano rim and the cell under investigation is about three orders of magnitude larger than the contact area of a pyramidal cantilever tip, local strain and stress applied to the cell are below the cell damage threshold for the nanovolcano measurements as well. The ramp curve depicting the force-position relation (Figure 5.4-B) shows a typical smooth increase of the force between $7\ \mu\text{m}$ and $11\ \mu\text{m}$ indicating indentation of the cell by the nanovolcano. The hysteresis visible in the force curve is due to mechanical energy dissipated by the cell, whereas the step during withdrawing highlights the detachment of the cantilever from the cell.

Simultaneous with the force measurements, square wave amperometry was performed through the nanovolcano probe to observe the impedance variation when engaging onto a cell. A 5 mV square wave oscillating at 20 Hz was applied between the nanovolcano and a counter electrode located in the bath while measuring the resulting current. Capacitive current peak amplitudes and current pulse time constants were extracted and plotted in Figure 5.4-C as the tip approached the cell and then was withdrawn again. As hypothesized in the previous section 5.2.2, both the “high frequency impedance” and the time constants significantly increased when the probe came close to the cell. Impedance increased by 189 % and time constants by 160 %. No variations of the resistive current at low frequency was observed. Figure 5.4-D shows the variation of impedance with respect to the cantilever position. A significant increase of high frequency impedance can be noted for cantilever displacements larger than $3\ \mu\text{m}$ that saturates at $10.5\ \mu\text{m}$. Amperometric measurements allow for an earlier cell detection compared to force recording. Forces in the nN range were applied and currents with < 10 pA amplitude were measured. This experiment was successfully repeated on seven different cells with two different cantilevers.

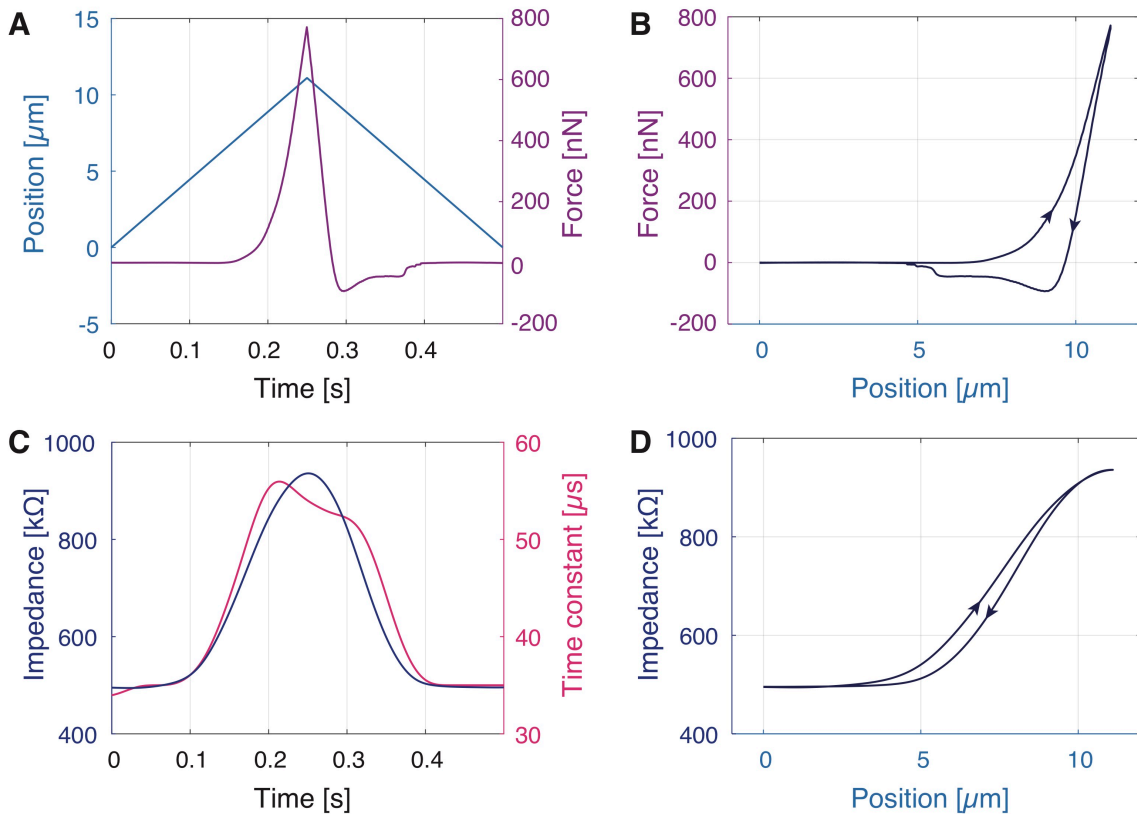


Figure 5.4: Force and electrical measurements on neonatal rat cardiomyocytes. **A)** Evolution of the nanovolcano cantilever position along the z-axis (left axis, light blue) and the resulting force applied to the cell (right axis, purple) with time. The first contact with the cell was initiated at $t = \sim 0.15$ s and position $\sim 7 \mu\text{m}$ (maximum force = 772 nN). **B)** Ramp curve showing the force – position relationship. **C)** Evolution of the nanovolcano probe impedance (left axis, dark blue) and time constant (right axis, magenta) with time, measured by pulsed amperometry. **D)** Ramp curve showing the impedance – position relationship.

5.2.4 Recording of cardiomyocyte contraction displacements using the nanovolcano probe

Following the basic characterization of the nanovolcano probe, we tested its suitability for performing measurements of contraction displacements from spontaneously active primary neonatal rat ventricular cardiomyocytes. The time-lapse images in Figure 5.5-A show one contraction of a spontaneously active cell studied with the nanovolcano probe maintained at a constant height. The blue pixels illustrate variation of intensity compared to the previous frame and therefore highlight the contraction-related movement of the cell. At t_0 , the cardiomyocyte is quiescent. It initiates its contraction at $t_{1,2}$, stays contracted during $t_{3,4}$ before relaxing again at t_{5-9} . The bottom panel in Figure 5.5-A represents the sum of the derivative for every pixels from

the video in the region of interest presented in the top panel. This measure is conventionally used to quantify cardiomyocyte contractions [274,275] and serves as visual control for the nanovolcano measurements.

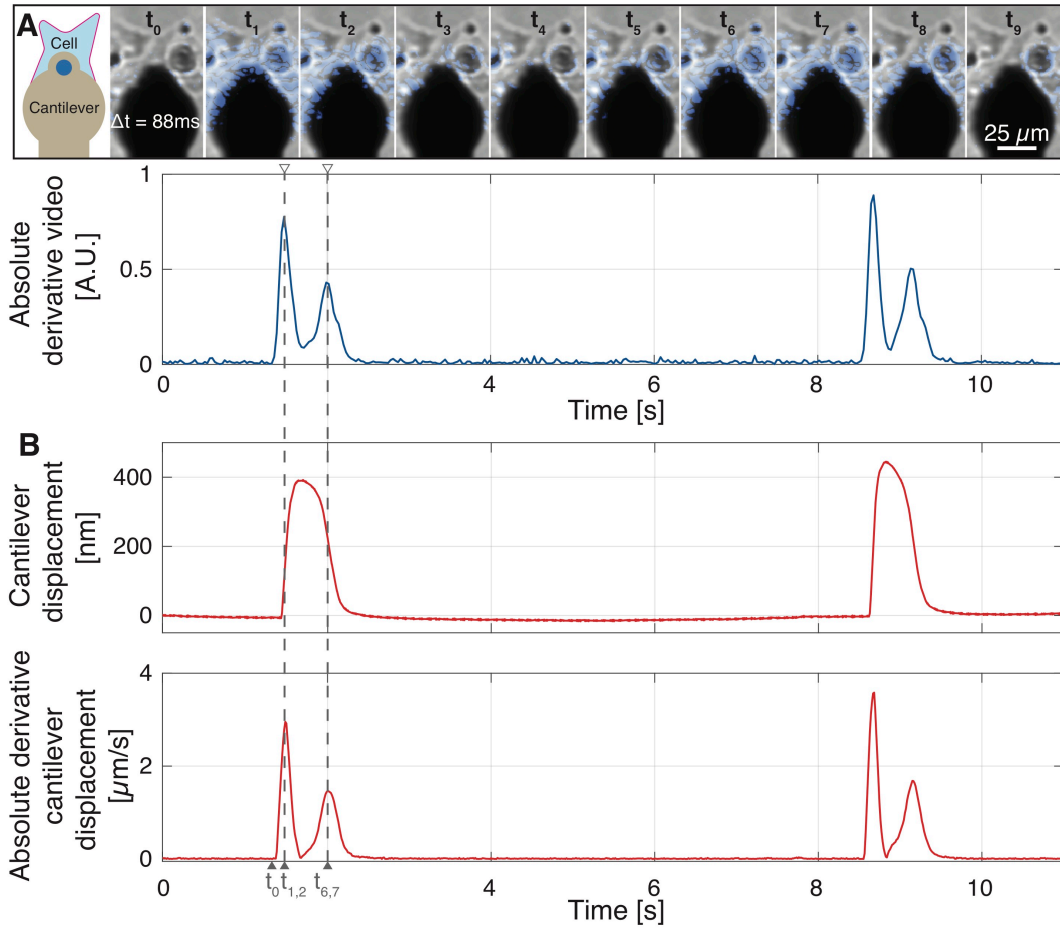


Figure 5.5: Recording of contraction displacements from primary rat cardiomyocytes. **A)** Upper panel: Schematic drawing (left) and series of time lapse images showing the nanovolcano probe engaged on a beating cardiomyocyte (right). Pixels showing intensity variations compared to the previous frame are highlighted in blue and indicate cardiomyocyte contraction. [274,275] Lower panel: temporal evolution of the sum of the derivatives of every pixels for the entire area depicted in the upper panel. **B)** Cantilever displacement (top panel) and its absolute derivative (bottom panel) from the same cardiomyocyte. The first contraction starts at t_0 and corresponds to the time-lapse images presented in A). The cantilever displacement absolute derivative matches the absolute derivative of the video signal.

Cantilever displacements recorded in parallel are shown in Figure 5.5-B (top panel). The first contraction (corresponding to the time-lapse data) has an amplitude of 367 nm and a duration (at 10 % of the amplitude) of 646 ms. Similarly, the second contraction had an amplitude of 422 nm and displayed a duration of 614 ms. The panel below depicts the corresponding derivatives (absolute values). For both activations, contraction rates amounted to 2.9 $\mu\text{m/s}$ and 3.5 $\mu\text{m/s}$, respectively. Relaxation

was slower and amounted to $1.5 \mu\text{m/s}$ and $1.7 \mu\text{m/s}$, respectively. The absolute derivatives of the cantilever displacement and those derived from the video data reliably matched.

5.2.5 Simultaneous recording of contraction displacements and electrogram from cardiomyocytes using the nanovolcano probe

Neonatal rat ventricular cardiomyocytes were also used to investigate the possibility of recording contraction displacement together with electrophysiological activity using the nanovolcano probe. As demonstrated in Figure 5.6, both contraction displacements (cf. Figure 5.6-A) and electrograms (cf. Figure 5.6-B) could simultaneously be recorded by the nanovolcano probe. Electrograms showed typical biphasic shapes and displayed amplitudes ranging from $-38 \mu\text{V}$ to $-75 \mu\text{V}$ that slightly preceded contraction. During a 25 s long recording session, contraction amplitudes of $250 \pm 35 \text{ nm}$ with a duration at 50 % amplitudes of $225 \pm 35 \text{ ms}$ (mean \pm SD) were observed together with electrograms showing downstroke amplitudes of $47 \pm 9 \mu\text{V}$ ($N = 49$). Electrograms recorded from a second cell gave similar results.

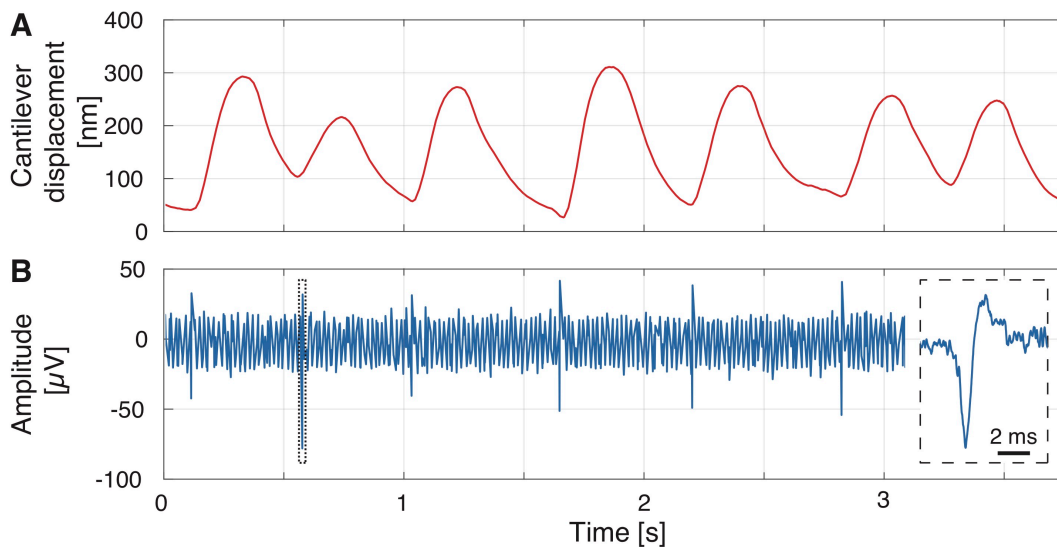


Figure 5.6: *Simultaneous recording of cardiomyocyte contraction displacements and electrograms. A)* Cantilever displacement simultaneously recorded with **B)** electrograms from a spontaneously active cardiomyocyte using the nanovolcano probe. The insert presents an expanded view of the region of the electrogram framed with dashed lines.

5.3 Discussion

The novel SPM probe presented in this study enables direct combined force and electrical signal recordings by placing a 3D microelectrode at the tip of an AFM cantilever. By contrast to previous technologies, no microfluidic channels were needed to transmit the electrical signal from the tip to the recording system, therefore bypassing the high fluid resistance and simplifying the experimental system. [270] The protruding electrode at the cantilever tip combines several technological advances in a single structure: (1) the platinum-black coated nanovolcano interior ensures a relatively low electrode impedance and, hence, optimizes signal-to-noise ratios; (2) the electrically insulating nanovolcano walls prevent current leakage from the electrode which contribute to the robustness of the cell-electrode interface robustness.

The 3D multimaterial nanopatterned microelectrode was manufactured following a reliable and scalable non-conventional four-step fabrication process based on ion beam etching redeposition that was completed with the patterning and release of the cantilever by conventional reactive ion etching techniques. All manufacturing steps used to produce both the nanopatterned electrode and the cantilever are compatible with complementary metal oxide semiconductor (CMOS) technologies. Accordingly, it is feasible to integrate CMOS amplifiers on the nanovolcano probes in the future to minimize electrical signal attenuation and noise. In contrast to previous technologies using FIB milling, [270,276] the fabrication process is simple, scalable, and leads to homogeneous structures at the wafer-scale (> 250 chips per wafer). Compared to regular nanovolcano arrays, the photoresist layer used to manufacture the 3D microelectrode presented in this study is thicker which results in a wider undercut after development. As a consequence, the redeposited materials composing the nanovolcano wall are electrically insulated from the electrode area (cf. Figure 5.1-B) thereby preventing the gold nanoring to be coated during platinum-black electrodeposition.

Compared to conventional conductive AFM tips, nanovolcano probes show the distinct advantage of being insulated up to the very end of the tip, allowing for a confined measurement with minimal current leaks. Furthermore, the volcano geometry enables low access impedance in physiological saline solutions compared to conductive AFM tips and therefore permits electrophysiological recordings.

Simultaneous force and impedance recordings on neonatal rat cardiomyocytes confirmed that pulsed amperometry could be used to gauge the engaging process and allows for gentle engaging on soft biological samples. As already reported in the literature, the probing depth of a microelectrode is mainly influenced by its spreading

Chapter 5. Volcano-shaped SPM probe for combined force-electrogram recordings from cardiomyocytes

resistance and proportional to its radius. [131] For this reason, cells were detected by impedance measurements $\sim 4\ \mu\text{m}$ (\sim microelectrode radius) prior to mechanical contact. These experiments demonstrated that the nanovolcano probe was suited to map the impedance properties of mechanically stimulated cells at the single-cell level, hence providing opportunities in the field of mechanobiology.

When performing experiments with primary neonatal rat ventricular cardiomyocytes, their morphology and contractility did not change during the duration of the experiments, thereby suggesting that the materials used to manufacture the probe were non-toxic to the cells. [205] For the first time, electrograms together with contraction displacements were successfully recorded using a single probe and were confirmed by simultaneous optical recordings. Positive monophasic cantilever displacements with an amplitude and duration similar to the ones observed with conventional probes were reported. [264] Simultaneously, biphasic voltage pulses corresponding to electrograms showed shapes, durations, and amplitudes consistent with extracellular activities recorded with standard MEAs. [109] Even though, amplitudes close to 1 mV are commonly reported in the literature for cardiomyocyte monolayers, recording performed on single cardiomyocyte with conventional MEAs showed similarly low amplitudes ($< 100\ \mu\text{V}$). [277]

Future developments of the nanovolcano probe should focus on permitting combined force and intracellular electrophysiological recordings such as action potentials or ion channel activity. This might be challenging as, compared to extracellular recording, a high seal resistance is essential in intracellular electrophysiology to maintain the punctured cell activity and enable high-quality recordings. In this study, the seal resistance was estimated to be much lower than the nanovolcano probe access resistance ($R_{Seal} < 315\ \text{M}\Omega$). The nanometer-wide alkanethiols nanopattern hypothesized to strengthen the cell-electrode interface was seemingly not sufficient to provide the gigaseal required to perform decent intracellular electrophysiology. Nevertheless, a systematic investigation of the nanopattern contribution to the seal formation could be performed with diverse types of self-assembled monolayers, not only based on alkane chains but also on positively charged molecules (e.g., poly-amine) or proteins (glutaraldehyde). On the other hand, a chemical-mechanical polishing step of the nanovolcano tip could be added in the microfabrication process to significantly reduce its roughness; therefore potentially improving the interface strength. In this context, the nanovolcano probe is certainly of interest to characterize the cell-electrode interface electrical properties by *in-situ* impedance spectroscopy.

5.4 Conclusion

In this work, we present an instrument for combined optical, force, and electrical measurements using a novel type of SPM probe composed of a nanopatterned volcano-shaped protruding electrode. Parallel mechanical, optical, and electrical measurements of single-cells were acquired thereby presenting a new approach for integrated mechano-electrical investigations.

The protruding microelectrode is electrically insulated to prevent current leaks at the cell-electrode interface. Additionally, a platinum-black coating of the large electrode area results in a relatively low impedance at the electrode-electrolyte interface. The complex 3D multimaterial microstructure was successfully manufactured at the tip of a suspended cantilever, exploiting a straightforward process that is reliable at the wafer-scale. It combines a non-conventional redeposition process occurring during ion beam etching with standard microfabrication techniques.

Experiments with neonatal rat cardiomyocytes demonstrate that the nanovolcano probe enables *in-situ* impedance recordings of mechanically stimulated cells with conventional liquid AFM setups. Proof-of-principle experiments confirm that combined measurement of force and electrical signals can be achieved with the presented probe. Electrograms and contraction displacements from spontaneously active cardiomyocyte were simultaneously recorded with similar characteristics to the one measured with conventional methods.

These features render the nanovolcano probe particularly suitable for mechanobiological studies aimed at linking functional electrophysiological single-cell responses with mechanical stimuli.

5.5 Materials and methods

5.5.1 Microfabrication

The microfabrication of the nanovolcano probe was performed with the help of Mathieu Aberle from the Microsystem Laboratory 4 (EPFL). A 380 μm -thick double-side polished silicon wafer (100 mm in diameter) coated with 2 μm of SiO_2 obtained by wet thermal oxidation was covered by successive evaporations of Ti-Pt-Ti-Au-Ti (10-250-100-100-100 nm) using an EVA760 e-beam evaporator (Alliance Concept, France). Electrically conductive tracks were patterned in a 750 nm-thick layer of AZ ECI 3007 positive photoresist layer (MicroChemicals, Germany) spin-coated with a Rite Track

Chapter 5. Volcano-shaped SPM probe for combined force-electrogram recordings from cardiomyocytes

88 series automatic coater (Rite Track, USA), exposed with an i-line VPG200 direct laser writer (Heidelberg, Germany) at a dose of 93 mJ/cm^2 and developed for 36 s in an AZ 726 MIF commercial developer (MicroChemicals) using a Rite Track 88 series automatic developer (Rite Track). Thereafter, a 2 min reflow at $120 \text{ }^\circ\text{C}$ was performed on a Sawatec HP200 hotplate (Sawatec, Switzerland) prior to etching the substrate positioned at an angle of incidence of -35° with respect to the ion beam generated in an IBE350 ion beam etcher (Veeco, USA) for 9 min 30 s. The photoresist was stripped in a 500 W O_2 plasma (O_2 flow 400 mL/min) for 7 min created by a TePla300 microwave plasma system (PVA TePla, Germany). The conductive tracks were subsequently insulated by 200 nm of SiO_2 sputtered with a Spider600 sputter-coater (Pfeiffer Vacuum, France).

A monolayer of hexamethyldisilazane (HMDS) was deposited on the top-most SiO_2 layer using a primer hotplate VB20 (ATMsse, Germany) before spin-coating a $6 \mu\text{m}$ -thick layer of negative photoresist AZ nLof 2070 (MicroChemicals) using an OPTIspin SB20 manual coater (ATMsse) rotating at 3500 rpm. $8 \mu\text{m}$ -diameter openings were patterned in the photoresist layer using an i-line VPG200 direct laser writer (Heidelberg) operating at a dose of 105 mJ/cm^2 . After a postexposure bake at $110 \text{ }^\circ\text{C}$ with a $50 \mu\text{m}$ proximity gap for 75 s, the wafer was developed for 91 s using an AZ 726 MIF developer (MicroChemicals) dispensed using an EVG150 automatic coater/developer (EVG, Austria). The sample was then bombarded with Ar^+ ions for 15 min at an angle of incidence of 0° using an IBE350 ion beam etcher (Veeco). During this step, materials from the substrate were etched and redeposited on the photoresist sidewalls. The photoresist was finally stripped by O_2 plasma (10 min, 500 W, O_2 flow 400 mL/min) in a Tepla300 microwave plasma system (PVA TePla), letting the nanovolcanoes protrude from the insulated tracks.

Both the cantilever and chip body were then patterned into a $15 \mu\text{m}$ -thick AZ 40 xT photoresist layer (MicroChemicals) coated with an ACS200 gen 3 automatic coater-developer (Süss, Germany), exposed with an i-line VPG200 direct laser writer (Heidelberg) at a dose of 93 mJ/cm^2 , and developed in an AZ 726 MIF developer (MicroChemicals) for 80 s using an ACS200 gen 3 automatic coater-developer (Süss). Following an overnight bake at $85 \text{ }^\circ\text{C}$ in a Heraeus T6060 oven (Heraeus, Germany), the cantilever shape was transferred into the $2.2 \mu\text{m}$ -thick SiO_2 layer by a 7 min long reactive ion etching process ($\text{He}/\text{H}_2/\text{C}_4\text{F}_8$ based chemistry) performed using a SPTS APS dielectric etcher (SPTS, United Kingdom). The cantilever and chip body outlines were subsequently etched throughout the $380 \mu\text{m}$ -thick Si wafer by Bosch processing in an AMS200 dry etcher (AMS, Austria), until reaching the $2 \mu\text{m}$ -thick backside Al

etching stop layer deposited beforehand with an EVA760 e-beam evaporator (Alliance Concept). Finally, the SiO₂ cantilever was released by Si isotropic dry etching performed in an AMS200 reactive ion etcher (AMS). The photoresist was then removed by O₂ plasma (10 min, 500 W, O₂ flow 400 mL/min) performed in a TePla300 microwave plasma system (TePla), followed by a 15 min long piranha etch (H₂SO₄:H₂O₂, 3:1) to remove both dry etching residues as well as the backside Al membrane.

The 2.2 μm-thick SiO₂ handlers connecting the chips to the substrate were manually removed to place the cantilevers upside down in an EVA760 e-beam evaporator (Alliance Concept) and coat their backside with 50 nm-thick layers of Cr and Au.

5.5.2 Interfacing

The nanovolcano probe was mechanically assembled on a custom-made PCB using a H20E epoxy cured for 3 hours at 80 °C (Epoxy Technology, USA). The PCB was then mounted onto a custom-made AFM holder prior to wire-bonding the chip contact pad (electrically connected to the nanovolcano) with the PCB gold coated pad (linked to a standard U. FL coaxial cable) using a HB05 wedge and ball bonder (TPT, Germany). The chip-PCB interface was electrically insulated using a H70E-2 glob top epoxy (Epoxy Technology) that was dispensed manually and cured at 80 °C for 1 h 30 min.

5.5.3 Electrodeposition of platinum-black

Platinum-black was locally deposited into nanovolcanoes by pulsed potentiostatic deposition as described before. [278] Briefly, the nanovolcanoes were electrochemically treated by varying the electrode potential from -0.2 V to +1.2 V vs. Ag/AgCl (scan rate of 100 mV/s) for 20 cycles in a 0.5 M H₂SO₄ solution. Subsequently, the microelectrodes were immersed into a solution of hexachloroplatinic acid (17.5 mmol/L, 262587, Sigma) and lead(II) acetate trihydrate (0.03 mmol/L, 467863-50G, Sigma) prior to applying -700 mV voltage pulses with respect to the open-circuit potential (V_{OCP}) for an overall duration of 45 s ($t_{on} = 0.2$ s, $t_{off} = 0.4$ s, number of pulses = 225).

5.5.4 Isolation and culture of primary rat cardiomyocytes

Primary neonatal rat (Wistar, 1 day old) ventricular cardiomyocytes were isolated using established procedures (detailed in Chapter 3) in compliance with federal guidelines for animal experimentation under license BE27/17 of the Bernese Veterinary Department. The resulting cell suspension was centrifuged at 1000 rpm for 5 min, re-suspended in DMEM (41965-039, Gibco) containing 10 % fetal bovine serum

Chapter 5. Volcano-shaped SPM probe for combined force-electrogram recordings from cardiomyocytes

(16140071, ThermoFisher Scientific) and 1 % penicillin/streptomycin, and seeded in 6 cm-diameter petri dishes at a density of ~ 350 cells/mm². Cells were incubated at 37 °C in an atmosphere containing 5 % CO₂. The cell medium was renewed every 24 hours. Experiments were conducted 48 to 72 h post-seeding. At this time, the cellular electrophysiology of cardiomyocytes has recovered from the isolation process and overgrowth with non-cardiomyocytes such as myofibroblasts is still moderate.

5.5.5 Device functionalization

The nanovolcano probes were sterilized for 30 s with O₂ plasma (100 W, 650 mTorr; Diener Electronic, Germany) prior to being immersed for 1 hour in a 20 mmol/L hexanethiol solution in pure ethanol for self-assembled monolayer formation. After ethanol rinsing, the probes were thoroughly rinsed in sterile deionized water.

5.5.6 Combined AFM-optical recordings

AFM experiments were performed in the Laboratory for Bio- and Nano-Instrumentation of Prof. Georg Fantner (EPFL) with the help of Mélanie Hannebelle. A detailed description of the system combining AFM, optical, and electrical recordings is presented in the Appendix D, section D.1.

In short, the combined AFM-optical setup is a custom system [279] associating a tip-scanning AFM (Dimension Icon, Bruker, Germany) and an optical microscope (IX73 or IX81, Olympus, Japan) equipped with a 20x objective and a camera (ixon Ultra 897, Oxford Instruments, United Kingdom). The camera was used in frame transfer mode with a 20 Hz acquisition rate. The AFM was used in contact mode without (constant height mode) or with feedback enabled (constant deflection mode). Height and deflection were recorded while imaging with a scan size of 0 nm, a scan rate of 40 Hz, and 1024 samples per line, which corresponds to a sampling rate of about 80 kHz. The images were pre-processed using gwyddion, [280] before further processing with a custom Matlab script to convert the “trace” and “retrace” AFM images into height and deflection as a function of time.

Two different nanovolcano probes were used to collect the data presented in this study. Impedance measurements were performed with probes 1 and 2. Probe 2 was subsequently cleaned by O₂ plasma (100 W, 650 mTorr, 30 s; Diener Electronic), inspected by SEM, functionalized, and re-used to record electrophysiological signals from cardiomyocytes.

5.5.7 Electrophysiology

Electrophysiological recordings were performed at room temperature on preparations kept in Hank's balanced salt solution supplemented with 10 mmol/L Hepes (pH 7.2). An Axopatch 200B microelectrode amplifier together with a CV 203 BU headstage (Molecular Devices, USA) were used to perform pulsed amperometry and to record electrograms from cardiomyocytes (bandwidth: 0 – 100 kHz). The analog to digital conversion was performed by a Powerlab 4/25 acquisition card (AD Instruments, Australia) at a sampling frequency of 200 kS/s. Extracellular signals were post processed with a Butterworth bandpass filter (100 Hz - 500 Hz).

Chapter 6

Intracellular recording of neuron action potentials with nanovolcano arrays: preliminary results

6.1 Introduction

So far, primary rat cardiomyocytes were used to characterize the novel nanovolcano technology as they are robust cells which can be easily cultured in monolayers – therefore guaranteeing each microelectrode of the device to be covered with a cell – and show a simple well-known electrophysiological behavior that can be optically confirmed by the detection of the cardiomyocytes mechanical contractions to discriminate signal from noise.

It is however more difficult to work with neurons as they are more fragile cells compared to cardiomyocytes, need to be cultured at lower density, and have a complex irregular electrophysiological response made of both action potentials and sub-threshold potentials. [53] Sub-threshold excitatory and inhibitory post-synaptic potentials correspond to synaptic inputs from the neighboring cells that induce an electrical response below the neuron firing threshold potential. Because conventional planar multielectrode arrays are blind to such low-frequency and amplitude potential variations and only detect action potentials, some brain areas are considered to be silent as 90 % of the neurons are not firing or at very low rates. [281] Recording sub-threshold potentials at the transmembrane level from these areas would certainly bring significant information regarding the role of this silent majority [128] and therefore provide advances to both fundamental research and pharmacological screenings aiming at the development

of novel chemical compounds against neurological disorders. [282]

Presently, patch clamp electrodes are conventionally used to record sub-threshold activity. [193] However, this technology is severely limited by its low-throughput as it only permits transmembrane recordings from a single-cell at a time. To improve the throughput, voltage sensitive proteins and dyes were used to report action potentials [283] and sub-threshold activity [284] from neurons. Disadvantages of optical techniques include phototoxicity and a poor signal-to-noise ratio, or genetic manipulation. [285] As an alternative to measure sub-threshold activity from cell networks, nanoelectrode arrays mainly based on nanoneedle or micromushroom-like electrodes were developed and recently demonstrated first sub-threshold recordings proof-of-concepts. [135, 137, 149, 286] However, these techniques also suffer from a high signal attenuation and therefore result in the recording of sub-threshold potential traces showing a poor signal-to-noise ratio making, data interpretation difficult.

Now that the volcano-shaped microelectrodes were validated on cardiomyocyte monolayers, we propose to broaden their application by using nanovolcano arrays to assess electrophysiological activity of neuronal cell networks at the transmembrane potential level and explore the current limitations of this technology with neurons.

This thesis chapter presents preliminary experiments aimed at investigating if the nanovolcano technology can be used to record intracellular signals from neurons, identifying its actual limitations, and to give insights on how the developed technology and experimental protocols should be adapted to be used in this particular field.

Primary rat hippocampal neurons were insulated and cultured on nanovolcano arrays for several weeks (7 - 21 days) prior to the electrophysiological experiments. Preliminary recording sessions with and without electroporation were conducted to investigate the quality of the signals recorded with nanovolcano on neurons in both conditions. Culture optimization was explored as a potential alternative to maximize the nanovolcano recording yield with neurons.

6.2 Results

6.2.1 Spontaneous insertion of nanovolcanoes into neurons

Primary rat hippocampal neurons were cultured for 7 to 21 days on nanopatterned volcano arrays prior to the electrophysiological recordings to investigate the spontaneous insertion of nanovolcanoes into neurons. Figure 6.1-A shows a transmission

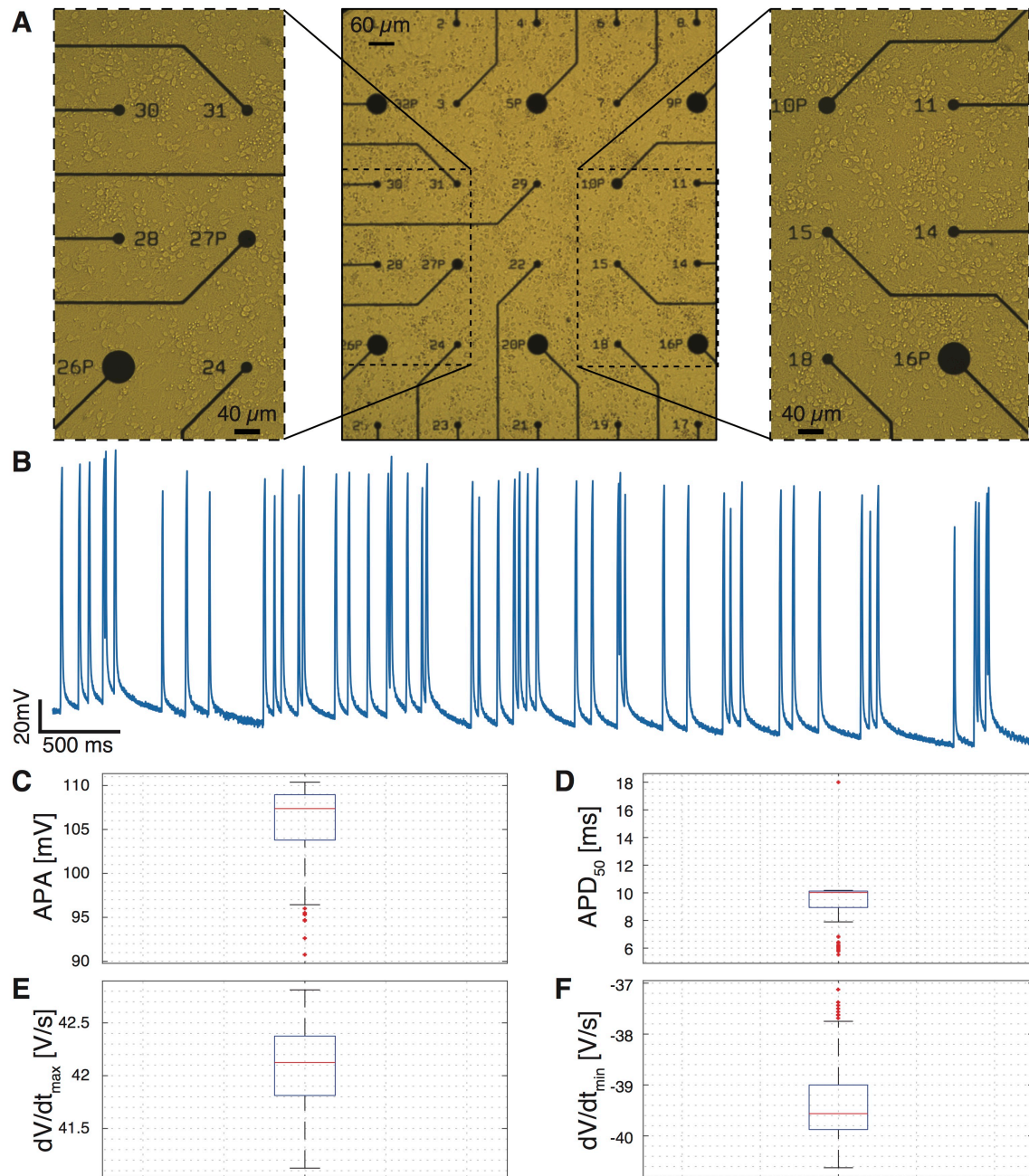


Figure 6.1: *Passive intracellular recording of action potentials from primary rat hippocampal neurons.* **A)** Transmission images of a representative 14-day-old primary rat hippocampal neuronal culture grown on nanovolcano arrays. **B)** Electrical trace of neuron action potentials recorded with the nanovolcano arrays. Box plots representing the recorded action potential **C)** amplitude (APA), **D)** duration at 50 % repolarization (APD_{50}), **E)** maximal upstroke velocity (dV/dt_{max}), and **F)** minimal downstroke velocity (dV/dt_{min}) for a 25 s long recording session ($N = 149$). On each box, the red central line represents the median, the bottom and the top edges show respectively the 25th and 75th percentiles, the whiskers indicate the most extreme values not considered as outliers. The red “+” represent the outliers.

Chapter 6. Intracellular recording of neuron action potentials with nanovolcano arrays: preliminary results

optical image of a typical neuronal culture on a nanovolcano array 14 days after seeding. The cells displayed uniform adherence over the substrate.

Figure 6.1-B shows the electrical trace of intracellular action potentials recorded with a single nanovolcano showing typical shapes and electrophysiological characteristics. As demonstrated in Figure 6.1-C to F, average action potential amplitude (APA) as high as 105.4 ± 4.7 mV, action potential duration at 50% repolarization (APD₅₀) of 9.2 ± 1.7 ms, and upstroke maximum (dV/dt_{max}) and downstroke minimum (dV/dt_{min}) velocity of 42.1 ± 0.4 V/s and -39.3 ± 0.7 V/s respectively were reported over the 25 s long recording session (N = 149); therefore demonstrating that nanovolcanoes can spontaneously provide an intracellular access to neurons. However, action potentials were lost after 25 seconds of recording and only a single nanovolcano showed spontaneous intracellular insertion into neurons over a dozen of nanovolcano arrays tested, with 26 nanovolcanoes per device. Even though the recording duration and yield of spontaneous insertion into neurons is low with nanovolcano arrays, the presented recording is of high quality as it shows non-attenuated action potentials.

6.2.2 Electroporation with nanovolcano arrays on neurons

A train of 10 negative current pulses, 10 ms long with amplitudes of 1 nA were applied prior to the electrophysiological session in order to perforate nanopores into the neuronal cell membrane and provide an intracellular access to the microelectrode. Figure 6.2 presents electrophysiological recordings of intracellular neuron action potentials coming from two independent nanovolcanoes in two different devices. In Figure 6.2-A, attenuated action potentials with typical burst behaviors are presented. Electrophysiological characteristics include APA = 12.9 ± 1.0 mV, APD₅₀ = 37.6 ± 5.7 ms, $dV/dt_{max} = 0.51 \pm 0.14$ V/s and $dV/dt_{min} = 0.16 \pm 0.01$ V/s over 16 seconds long recording session (N = 49). Compared to previous and conventional neuron action potentials, this electrical trace showed a longer APD₅₀ as well as slower maximal upstroke and minimal downstroke velocity. Even though neuron action potentials with similar characteristics were reported in the literature, [137] we hypothesize that these slower characteristics are due to filtering effects at the cell-electrode interface (e.g., cell membrane not well perforated) and do not represent physiological behaviors.

Figure 6.2-B shows the electrical traces of intracellular action potentials recorded with a nanovolcano from a different device compared to Figure 6.2-A. Conventional electrophysiological characteristics such as APA = 16.9 ± 2.5 mV, APD₅₀ = 5.3 ± 4.1 ms, $dV/dt_{max} = 42.3 \pm 1.8$ V/s and $dV/dt_{min} = -41.8 \pm 3.3$ V/s were measured during a 2 seconds long recording experiment (N = 15). Compared to previ-

ously reported traces, low-frequency and amplitude potential variations prior to action potentials can be observed after electroporation, suggesting sub-threshold potentials recordings with nanovolcanoes. However, even after electroporation, only two nanovolcanoes showed intracellular activity out of dozen of devices tested. Electroporation through nanovolcanoes does not improve the recording yield and duration with neurons.

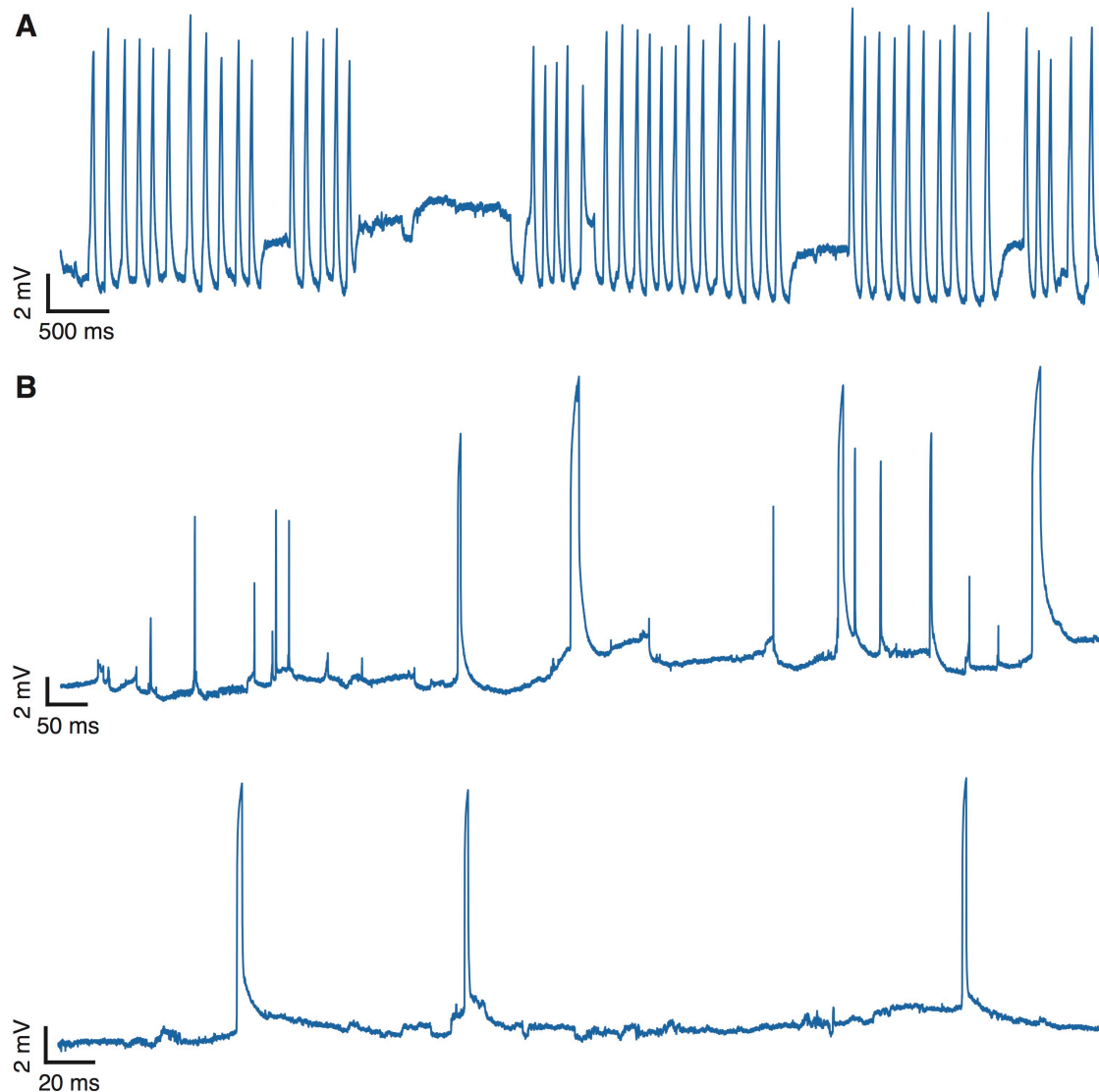


Figure 6.2: *Intracellular recording of action potentials from primary rat hippocampal neurons after electroporation.* Electrical traces of neuronal action potentials highlighting **A)** typical burst behaviors (day 7), **B)** possible sub-threshold potentials after electroporation (day 17) recorded with two nanovolcanoes coming from two different devices.

6.2.3 Neuronal culture optimization: glial cell proliferation inhibition

Following the isolation procedure from P0 rats, both neurons and glial cells (mainly astrocytes and oligodendrocytes) are cultured on the microelectrode arrays. In order to maximize the number of neurons with respect to other non-electrogenic cell types in our culture and improve the very low recording yield with nanovolcano arrays, the impact of cytosine arabinoside (Ara-C) on glial cells proliferation was investigated. Ara-C was temporarily added into the cell medium culture during the first three days after seeding. Confocal images showing immunostaining of neuronal cultures without (cf. Figure 6.3-A) or with (cf. Figure 6.3-B) Ara-C are presented in Figure 6.3 after 14 days of culture. Anti-MAP2 (microtubule-associated protein 2) antibodies were used for neurons, anti-GFAP (glial fibrillary acidic protein) for glial cells, and DAPI molecules (4',6-diamidino-2-phenylindole) for nuclei. The ratio between the neuron and glial cell area were respectively 0.41 without Ara-C and 1.2 with Ara-C. Ara-C significantly reduces the proliferation of glial cells with respect to neurons and therefore maximize the probability to obtain an electrogenic neuron on top of a nanovolcano and could potentially improve the low nanovolcano recording yield with neurons.

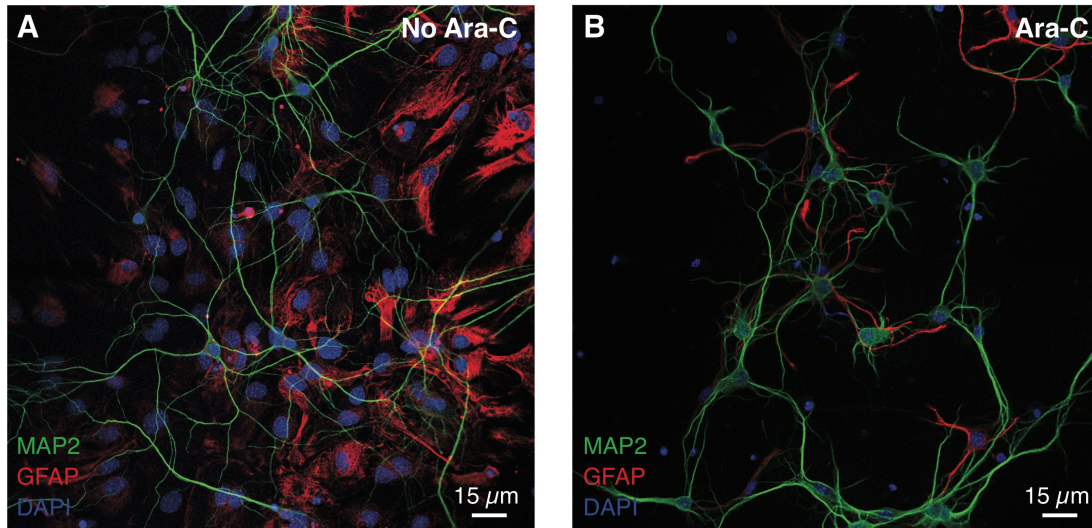


Figure 6.3: *Influence of cytosine arabinoside (Ara-C) on glial cells proliferation.* Immunostaining for neuron marker MAP2, glial marker GFAP, and nuclei DAPI **A)** with and **B)** without cytosine arabinoside after 14 days of culture on glass coverslip. See main text for abbreviations.

6.3 Discussion

In this study, we performed preliminary electrophysiological recordings from neural networks using nanovolcano arrays to broaden the applications of the developed technology. Primary rat hippocampal neurons showed uniform adhesion over the entire surface of the device for up to 21 days showing no discrepancies compared to neurons seeded on controlled Poly-D-Lysin coated glass coverslips and literature. [287] Inter-connected neuronal extensions confirmed interactions in between cells composing the neural networks.

Non-attenuated action potentials were recorded without applying electroporation pulses using nanovolcano arrays with electrophysiological characteristics similar to signals recorded using conventional patch clamp electrodes (APA included) [53] and slightly higher APA compared to the best amplitudes reported in the literature with nanoelectrode arrays. [137] In this configuration, static charge-induced electroporation is suggested as the main insertion mechanism and partially explains the low yield and recording duration observed as it is not controlled.

By applying controlled electroporation pulses, attenuated action potentials as well as lower frequency potential fluctuations resembling sub-threshold potentials could be observed on two different nanovolcanoes from different devices seeded with neurons. This is potentially a significant result as sub-threshold excitatory and inhibitory postsynaptic potentials are invisible to conventional planar multielectrode arrays [128] and rarely observed with micro-nanoelectrode arrays due to their low amplitudes. [135, 137, 149] Nonetheless, it is extremely difficult, if not impossible, to rigorously discriminate sub-threshold potentials from potential fluctuations due to seal variations. For this reason, control experiments should be performed with pharmacological inhibitors of glutamatergic synaptic transmission such as cyanquixaline prior any successful recording of sub-threshold potentials with nanovolcano arrays can be confirmed. Similarly, additional experiments with glutamate and tetrodotoxin should be performed to manipulate the neural network electrical activity and rigorously validate the electrophysiological nature of the recorded signals. At present, such experiments are limited by the very low recording yield and duration reported using nanovolcanoes with neurons.

Electroporation did not bring significant improvements in terms of recording yield. Furthermore, recording of extracellular fields potentials with control planar electrodes integrated in the devices also showed a very low yield, similar to the one observed with nanovolcanoes. This suggest that the reported limitations might not be entirely due

Chapter 6. Intracellular recording of neuron action potentials with nanovolcano arrays: preliminary results

to the nanovolcano intrinsic properties but to external factors related to the quality of the neuronal culture to perform electrophysiological recordings with multielectrode arrays. To improve the recording yield, one should first maximize the number of electrogenic neurons in the culture compared to non-electrogenic cells types such as the glial cells. Especially because these cells form a carpet between the neurons and the microelectrodes that minimizes the probability to obtain an electrically active cell on top of a nanovolcano. As expected from the literature, temporary addition of Ara-C into the cell culture medium showed significant improvements of the ratio between neurons and glial cells. [288] Another option would be to harvest cells from E18 rats instead of P0 as the number of glial cells should be much lower. [135] Furthermore, in contrast to cardiomyocyte monolayers, the substrate is not entirely covered with neurons as hippocampal neuronal cells show optimal behaviors at lower density. [288] For this reason, the probability to obtain a cell on top of a microelectrode is quite low and minimizes the achievable yield with nanovolcanoes. An accurate positioning of neurons on top of each microelectrode of the device by hydrodynamic trapping [234, 289] or dielectrophoresis [290] could potentially improve the recording yield. Alternatively, the number of nanovolcano or cell per device could drastically be increased for a similar result. In the literature, high-density nanoelectrodes arrays with 1024 electrodes were developed to solve this issue. [135]

Furthermore, adapting the electroporation protocol from 10 ms, 1 nA negative current pulses to 3 V biphasic voltage waves oscillating at 10 kHz as modeled in the previous Chapter 4 with cardiomyocytes, could potentially improve the recording yield and duration as it should maximize the voltage drop across the interface. Unfortunately, this could not be tested with neurons because of time constraints. For similar reasons, a single-channel microelectrode amplifier was used to conduct the recording sessions on neurons. Using a multichannel amplifier would certainly facilitate the recording sessions, improve their throughput, and therefore minimizing the chance of missing an intracellular signal.

6.4 Conclusion

In this chapter, we investigate the potential of nanovolcanoes to record action potentials from neurons at the transmembrane voltage level. Primary rat hippocampal neurons are cultured on nanovolcano arrays for 7 to 21 days prior to electrophysiological recordings of the neural network spontaneous activity. Preliminary results show that non-attenuated action potentials can be measured with electrophysiological characteristics similar to action potentials recorded with patch clamp electrodes using

static charge-induced electroporation as a main insertion mechanism. Electrophysiological recordings following active electroporation with nanovolcano arrays show high signal-to-noise ratio neuron action potentials as well as low-frequency potential fluctuations resembling sub-threshold activity; potentially opening numerous opportunities for pharmacological screening purposes aimed at developing novel compounds against neurological disorders.

Even though the preliminary results presented in this study are encouraging and demonstrate that nanovolcanoes can be used to assess intracellular electrophysiological activity from neurons, the recording duration and most importantly the yield are both low. Nevertheless, these recording characteristics are certainly not limited by the nanovolcanoes themselves yet but by external factors. To objectively assess the intrinsic nanovolcano array recording limitations with neurons, one should first guarantee to obtain an electrically active neuron on every microelectrode of the device. Improvements can be made by optimizing the neuronal culture purity, cell positioning, and density of electrode per device.

6.5 Materials and methods

6.5.1 Microfabrication

Nanovolcano arrays were manufactured following procedures previously established in Chapter 3.

6.5.2 Device preparation

As previously described, nanovolcano arrays were sterilized for 30 s with O₂ plasma (100 W, 650 mTorr; Diener Electronic, Germany) prior to be submerged with a 20 mmol/L hexanethiol solution in pure ethanol for self-assembled monolayer formation. After ethanol and deionized water rinsing, substrate were incubated with Poly-D-Lysin (354210, Corning) for 1 hour and rinsed with deionized water.

6.5.3 Isolation procedure and culture of hippocampal neonatal rat neurons

Hippocampal neurons were harvested by Anne-Laure Mahul and Elena Gasparotto (Laboratory of Molecular Neurobiology and Neuroproteomics, EPFL) following established protocols. [291] Experiments were performed in accordance with federal guide-

Chapter 6. Intracellular recording of neuron action potentials with nanovolcano arrays: preliminary results

lines for animal experimentation under license 3290 of the state veterinary department of canton Vaud. Briefly, hippocampi were harvested from P0 rats, dissociated in papain, and triturated with a glass pipette. Following centrifugation, cells were plated at a density of 200'000 cells/cm² in adhesion growth medium. 3 hours later, medium was substituted with neurobasal supplemented with B27. Subsequently, half-medium exchange was performed every three days.

6.5.4 Electrophysiology

Electrophysiological experiments were conducted together with Pietro Airaghi (Microsystems Laboratory 4, EPFL). Recordings were performed at room temperature using an Axopatch 200B microelectrode amplifier together with a CV 203 BU headstage (Molecular Devices, USA; bandwidth: 0 - 100 kHz). A Powerlab 4/25 acquisition card (AD Instruments, Australia) was used to convert the signal from analog to digital at a sampling frequency of 40 kS/s. Electrical traces shown correspond to the actual non-filtered data.

6.5.5 Immunostaining

The immunostaining protocol was rigorously followed by Nicolas Maino (Microsystems Laboratory, EPFL) from Beaudoin *et al.* [292] Briefly, cells were fixed with 500 μ L of paraformaldehyde (PFA, 4% in phosphate buffered saline (PBS; 14190-094, ThermoFisher Scientific) at 37 °C; 158127-100G, Sigma) for 10 min at room temperature. Subsequently, PFA was substituted by 500 μ L of triton solution (0.1%; T8787-100ML, Sigma) for 10 min. After PBS rinsing, 500 μ L of bovine serum albumin (BSA; A7906-10G, Sigma) were added and incubated for one hour to prevent non-specific binding. Following an additional PBS rinsing, 100 μ L of primary antibody mixture, composed of anti-GFAP (1:2000; M4403-50UL, Sigma) and anti-MAP2 (1:2000; G4546-100UG, Sigma) in 1 % BSA in PBS, was added and incubated for 1 hour. Thereafter, the preparation was washed three times with PBS and incubated for an additional hour with the secondary antibody solution composed of donkey anti-mouse (1:2000; A10037, ThermoFisher Scientific) and anti-rabbit (1:2000; A-21206, ThermoFisher Scientific) antibodies in 1 % BSA in PBS. Finally, the DAPI solution (1:10000 in PBS; 28718-90-3, Sigma) was incubated for 15 minutes and washed three times with PBS before imaging.

Chapter 7

Conclusion and perspectives

This thesis addresses the current limitations of micro-nanoelectrode arrays in the context of electrophysiological studies performed on excitable cells at the transmembrane voltage level. In the context of achieving high-quality electrophysiological recordings from cell networks over extended periods, a novel microelectrode combining protruding geometry with a biomimetic nanopattern is studied as a potential alternative to both the patch clamp method and all the recently developed micro- and nanofabricated electrodes.

7.1 Summary of performed research

Technological developments presented in this work include a novel nanofabrication technique exploiting the local sputtering of the photoresist sidewalls during Ar^+ ion beam etching to rapidly manufacture complex three-dimensional (3D) multimaterial nanostructures at the wafer-scale. This non-conventional nanofabrication method potentially opens numerous opportunities for the production of a variety of nanostructures that can be of interest in the fields of biosensing, nanofluidics, and nanophotonics.

Specifically, ion beam etching redeposition enables the scalable manufacturing of an original nanopatterned volcano-shaped microelectrode (nanovolcano) array implementing most of the recent technological advances described in the literature when interfacing electrogenic cells, in a single structure. Design improvements include a 3D large-area low-impedance electrode surrounded by protruding, insulating sharp walls aimed at reducing current leaks at the cell-electrode interface. Additionally, the protruding electrode presents a nanopatterned biomimetic self-assembled monolayer thought to fuse with the cell membrane to maximize the coupling between the

cell and the microstructure. Experiments with neonatal rat cardiomyocyte monolayers demonstrated that nanovolcanoes permit spontaneous in-cell access and enable electroporation-free intracellular recordings of cardiomyocyte action potentials with characteristics similar to the state-of-the-art technology.

Controlled electroporation resulted in significant improvements in the quality of the signals recorded with nanovolcano arrays and permitted on-demand multiple intracellular access over consecutive days. Overall, nanovolcano arrays showed superior recording performances compared to other electroporation-based approaches, especially in terms of signal amplitude, recording duration, and yield. Interestingly, the quality of the signal recorded with nanovolcano arrays showed no dependence on the presence of the biomimetic nanopattern, suggesting that the nanovolcano geometry alone is instrumental to the formation of a tight seal at the cell-electrode interface. The high quality of the electrophysiological signals recorded with nanovolcano arrays can, therefore, be directly attributed to the original microelectrode shape, design, and material composition.

Preliminary studies conducted using hippocampal neonatal rat neurons suggest that nanovolcano arrays can be used to assess the electrophysiological characteristics of neuronal cells and potentially at the sub-threshold level if further optimization of the cell culture is performed. These preliminary results prospectively extend the application of nanovolcano arrays to other electrogenic cell types, especially in the field of neuroscience.

During a more exploratory phase, the nanovolcano electrode was manufactured at the tip of a suspended cantilever (nanovolcano probe) to take force-controlled electrophysiological recordings. Contraction displacement and extracellular field potentials were simultaneously recorded from single cardiomyocytes using the nanovolcano probe, thereby, in the context of mechanobiological studies, demonstrating the probe's suitability for linking functional electrophysiological single-cell responses with mechanical stimuli.

7.2 Limitations

Although nanovolcano arrays demonstrated outstanding recording capabilities, the technology does not yet permit the repeatable registration of non-attenuated action potentials from excitable cells. Nanovolcano arrays, in general, are restricted by the considerable variability of the measured signal's amplitude between channels, probably linked to the heterogeneity in the coupling quality at the cell-electrode interface, which

likely depends on the nanovolcano's position relative to the cell.

Presently, nanovolcano arrays only permit intermittent intracellular access. Although this enables the study of electrophysiological characteristics over extended periods, it prevents applications where long-term continuous recordings are necessary for the detection of single events. Additionally, the cell membrane resealing throughout the intermittent intracellular period prevents a stable recording over time, therefore rendering data interpretation related to action potential amplitudes difficult.

For proof-of-concept experiments, nanovolcano arrays were designed with limited spatial resolution. Increasing the density of nanovolcanoes per device could potentially enable electrophysiological studies at the transmembrane-voltage level with subcellular resolution.

Finally, compared to the patch clamp technique, nanovolcano arrays only permit whole-cell current clamp recordings with a current fixed to zero, hence limiting their applications to action potentials recording from electrogenic cells. Novel recording configurations such as voltage clamp should be established with nanovolcanoes to broaden their application toward ion channel based electrophysiological studies of non-electrogenic cells and provide a reliable high-throughput alternative to the patch clamp method.

7.3 Outlook and perspectives

Technological improvements aiming to overcome the current limitations of nanovolcano arrays are discussed in this section. The potential impacts of the developed technology on academia and the pharmacological industry are evaluated later, and a discussion regarding the long-term implications of nanovolcano arrays concludes the section.

7.3.1 Performance improvements

Future developments of the proposed technology should focus on allowing the registration of non-attenuated action potentials while improving the repeatability and the stability of the recordings performed with nanovolcano arrays. Given the micro-electrode geometry was demonstrated to be pivotal at the cell-electrode interface, a systematic optimization of the nanovolcano geometry – in terms of diameter, nanowall thickness, and height – could significantly improve the signal amplitude, stability, and variability. For instance, extreme nanowall aspect ratios could improve the cell-

microstructure coupling while prohibiting cell membrane reconstruction after electroporation.

In a second phase, the quality of the cell-electrode interface should be investigated by impedance spectroscopy prior to electrophysiological measurement. This would preemptively compensate for the attenuation of the recorded signal amplitudes for every channel composing the device. In contrast to theoretical compensation, this method would be based on direct experimental measurement, including a preliminary calibration procedure established for nanovolcano arrays beforehand. Repeating the compensation procedure would not only prevent signal attenuations and decrease recording variabilities between channels but also allow researchers to correct for signal amplitude decrease over time.

Finally, nanovolcano arrays should be integrated with CMOS amplifiers to diminish the potential signal attenuation along the electrical tracks, improve its spatial resolution, and generate high-content electrophysiological data at a minimal experimental cost. From a technological point of view, integrating nanovolcanoes with CMOS electronics should be straightforward, as ion beam etching redeposition is CMOS compatible and only requires four additional conventional microfabrication steps. A smaller electrode inter-distance increases the probability of at least one microelectrode being well-positioned relative to the cell, therefore reducing the variability of recording quality in between cells. Furthermore, high-density nanovolcano arrays could probably permit subcellular resolution electrophysiological studies at the transmembrane voltage level and therefore enable the study of the propagation of action potentials in a single-cell.

7.3.2 Potential opportunities for academia

In addition to permitting the assessment of electrophysiological characteristics of cardiomyocyte monolayers over extended periods and contributing to cardiac research, nanovolcano arrays could provide opportunities to explore new fields of research and conduct novel experiments.

Proof-of-concept experiments using neurons In this thesis, electrophysiological studies combining nanovolcano arrays with neurons produced preliminary recordings of non-attenuated action potentials along with suggesting the possibility of recording sub-threshold potentials. Limitations of this study include a very low number of successful intracellular signals, mainly due to the neuronal culture being contami-

nated by non-electrogenic glial cells. This experiment should be repeated using higher density nanovolcano arrays with E18 prenatal neurons, which are known to have a lower proportion of glial cells. Demonstrating high signal-to-noise ratio recordings of action potentials and especially sub-threshold activity in neuronal networks over extended periods would not only permit the nanovolcano technology to expand its range of applications to electrogenic cell types other than cardiomyocytes but also, most importantly, open possibilities in the field ranging from fundamental research to pharmacological screening.

Two-electrode voltage clamp with nanovolcanoes To propose a robust high-throughput alternative to the patch clamp technique, nanovolcano arrays should not only have recording capabilities competitive with the gold standard but also enable similar recording configurations, ranging from whole-cell current clamps to voltage clamps. The relatively large electrode impedance of microelectrode arrays usually limits voltage clamp applications. This is because the voltage divider defined by the electrode and the seal resistance attenuates the applied voltage, thereby preventing the transmembrane potential being fixed at the desired value. [135] In the case of nanovolcanoes, it is technically possible to integrate two electrodes into a single nanovolcano and use the developed technology to perform two-electrode voltage clamp (TEVC) experiments. In this situation, one electrode is set to the desired potential while the second injects sufficient current to reach the set steady value. This allows the cell transmembrane voltage to be accurately clamped to a specific value independent of seal resistance, and current variations linked to ion channel activity can be directly measured. Performing two-electrode voltage clamp experiments could allow investigations of voltage-gated ion channel activities in non-electrogenic cells, opening new horizons in the field of high-throughput electrophysiology.

Nanofluidic intracellular access with nanovolcanoes The nanovolcano geometry is particularly suitable for integrating different types of micro-nanosensors to its inner part. For instance, a nanochannel could be manufactured at the base of the nanovolcano to permit specific molecules to be selectively delivered to or collected from the cytoplasm at the single-cell level. The fabrication process would comprise using conventional methods to manufacture nanopores on an insulating membrane [293,294] prior to fabricating the nanovolcano arrays. By combining intracellular electrophysiological recordings with direct nanofluidic intracellular accesses, the next iteration of the nanovolcano could enable the study of single-cell electrophysiological responses following chemical stimulation with novel compounds developed for the treatment of

specific pathologies.

Among the potential for future studies discussed, performing two-electrode voltage clamp experiments with nanovolcano arrays is most likely to revolutionize the field of electrophysiology because it would enable the assessment of ion channel activity in adherent mammalian cells at high-throughput. Current micro-nanotechnologies such as nanoneedle, nanotube, and micromushroom multielectrode arrays are inherently limited in this regard because their geometries do not permit the integration of two electrodes in a single structure. This branch of electrophysiology could thus represent a niche for nanovolcanoes because of a geometry that specifically promotes the integration of several micro-nanosensors in a single structure, making them ideal for access to the in-cell environment. In this context, nanovolcanoes have the potential to substantially contribute to this field of research and could have a more significant impact than current state-of-the-art technologies.

7.3.3 Potential opportunities for the pharmacological industry

Over the last decade, confronted with the need for high-throughput electrophysiology, the pharmacological industry has invested considerably in automated patch clamp systems – permitting the investigation of ion channel activity from 100 to 1000 cells per day – and in planar microelectrode arrays assessing the electrophysiological properties of cell networks. Given their well-established procedures, a hypothetical replacement for these conventional tools seems unlikely unless novel technologies permit measurements within specific electrophysiological parameters inaccessible to current instruments, enabling them to play a central role in pharmacological screenings.

Presently, nanovolcano arrays permit electrophysiological studies of electrogenic cells at the transmembrane voltage level over extended periods. This has the distinct advantage over the patch clamp technique of permitting experiments at the cell network level. Future technological developments will potentially improve nanovolcano array recording stability and repeatability. In addition, spatial resolution should reach the subcellular level. At this stage, the next generation of nanovolcano arrays will potentially provide a robust alternative to the conventional planar microelectrode arrays used for pharmacological screening purposes at the cell network level, as they will provide substantially more information, especially considering the relatively small modification to the industrial infrastructure.

However, to provide a reliable alternative to the pharmacological industry's patch

clamp robots, future developments of nanovolcano arrays should include assessment of non-electrogenic cell single ion channel activity at the subcellular resolution. Such a significant breakthrough could revolutionize the pharmacological industry and motivate the replacement of its expensive conventional tools for the benefit of micro-nanoelectrode arrays.

7.3.4 Perspectives, at a more distant horizon

Relatively little technological improvements of nanovolcano arrays might already open numerous opportunities for academia and prospectively for pharmacological screenings at the industrial level. In this section, we envision the possible impact of the next-generation micro-nanoelectrode arrays on society.

In the future, nanovolcano arrays will potentially permit the study of the entire electrophysiological spectrum with subcellular resolution at the cell network level. Experiments performed on neuronal networks will provide significant knowledge about how information is generated, processed, and stored in human brains. These results could help answer complex, long-standing questions about matters ranging from low-level computation processes in neuronal sub-units to the birth of consciousness. [295] Understanding how single neurons exchange, compute, store, and learn information in a network will revolutionize cognitive science by enabling the study of consciousness and investigations of individual personality. Such discoveries will inevitably enable improved treatment of neurological disorders, including both neurodegenerative diseases and, no less importantly, behavioral difficulties.

Additionally, knowledge collected from biological neuronal networks could significantly contribute to human progress if used for technological development. Artificial intelligence based on virtual neural networks would be vastly expanded and deliver innovative solutions to complex societal problems. Using electrophysiological observations to implement artificial neural networks replicating organic networks could revolutionize current artificial intelligence algorithms and open new pathways in this field of research. [296] Biological neuronal networks themselves could be programmed with micro-nanoelectrode arrays following Hebb's principle of using synaptic plasticity [297] to accomplish a particular task. Given this is not possible with conventional artificial intelligence algorithms, it would open an entirely new field of research.

Appendices

Appendix A

Supplementary information related to Chapter 2

A.1 Diversity in the shape of nanostructures manufactured by ion beam etching redeposition

Figure A.1 illustrates the diversity of nanostructure geometries that can be obtained by varying the photoresist opening shapes prior to ion beam etching.

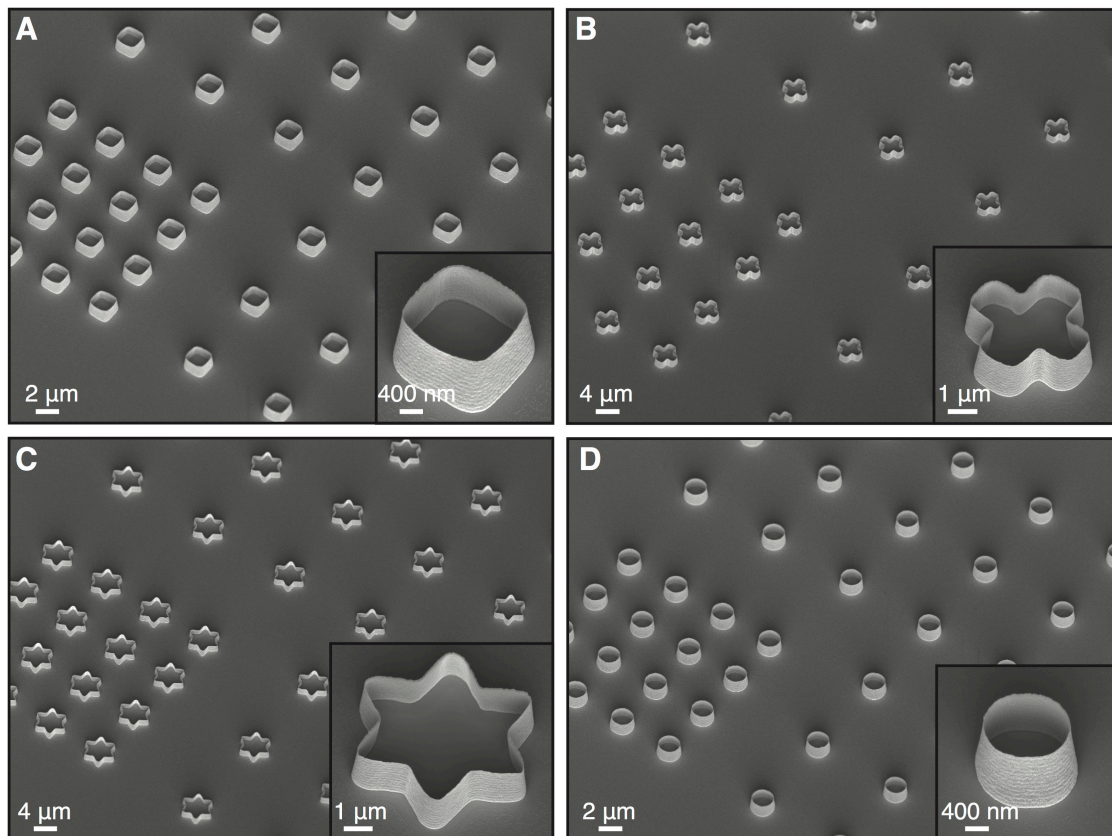


Figure A.1: Structures of various shapes made by Si redeposition on photoresist sidewalls during Ar^+ ion beam etching. SEM images of **A)** square arrays, **B)** cross arrays, **C)** star arrays, and **D)** cylinder arrays composed of 60 nm thick walls. Tilt angle of 30° .

Appendix B

Supplementary information related to Chapter 3

B.1 Stabilizing the cell-electrode interface by nanopatterning

As demonstrated by VanderSarl *et al.*, [154] the patterning of nanoscale hydrophobic bands on otherwise hydrophilic substrates prevents the diffusion of the lipophilic membrane dye DiI at the location surrounded by the nanopattern which demonstrates a stabilizing effect on the cell-electrode interface (cf. Figure B.1-B to D). In Figure B.1-A, similar results were obtained using the protruding nanopatterned microelectrodes presented in this work.

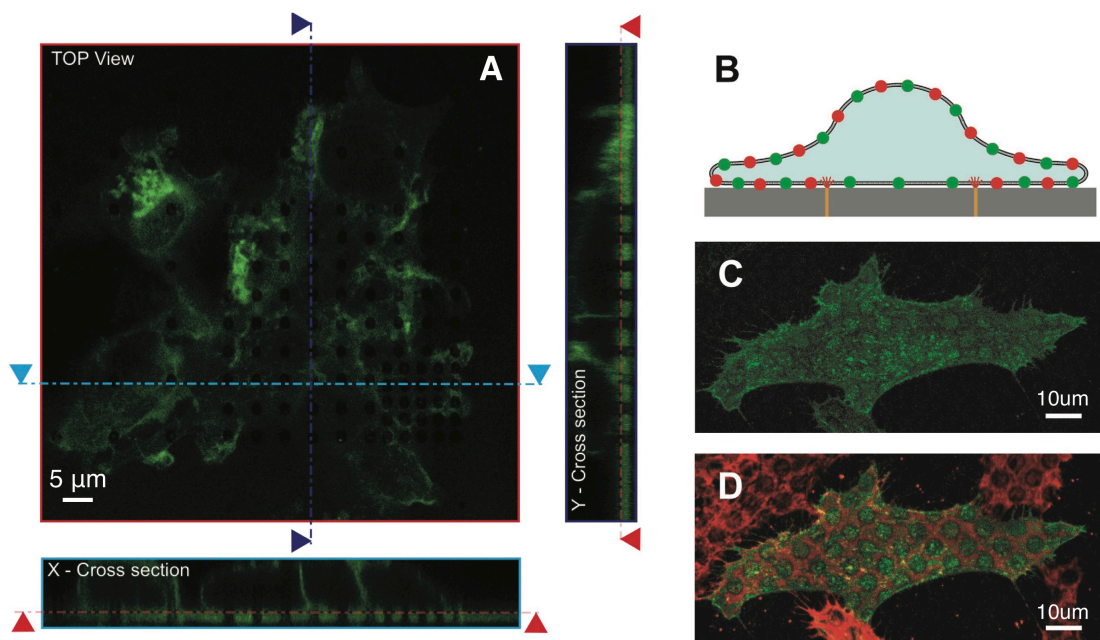


Figure B.1: *Influence of the nanopattern at the cell-electrode interface.* **A)** Confocal image of fixed HEK cells showing DiI membrane dye exclusion at the location of the protruding nanopatterned tips of the nanovolcanoes. **B)** Schematic drawing and **C)** confocal image of a cell with a green fluorescent protein (GFP) membrane label adhering onto a planar electrode surrounded by a self-assembled nanoring. **D)** Subsequent addition of a red membrane label is blocked from diffusing into areas encircled by the self-assembled monolayer. B), C) and D) are reproduced with permission from VanderSarl *et al.* [154]

B.2 Modeling of the cell-electrode interface

As illustrated in Figure B.2-A, the potential $V_{In}(\omega)$ at the input of the recording amplifier in the frequency domain can be expressed by analyzing the potential in the junctional space $V_j(\omega)$ with respect to the original intracellular action potential $V_m(\omega)$. Note that the Warburg element as well as the half-cell potential at the interface were considered to be zero.

B.2. Modeling of the cell-electrode interface

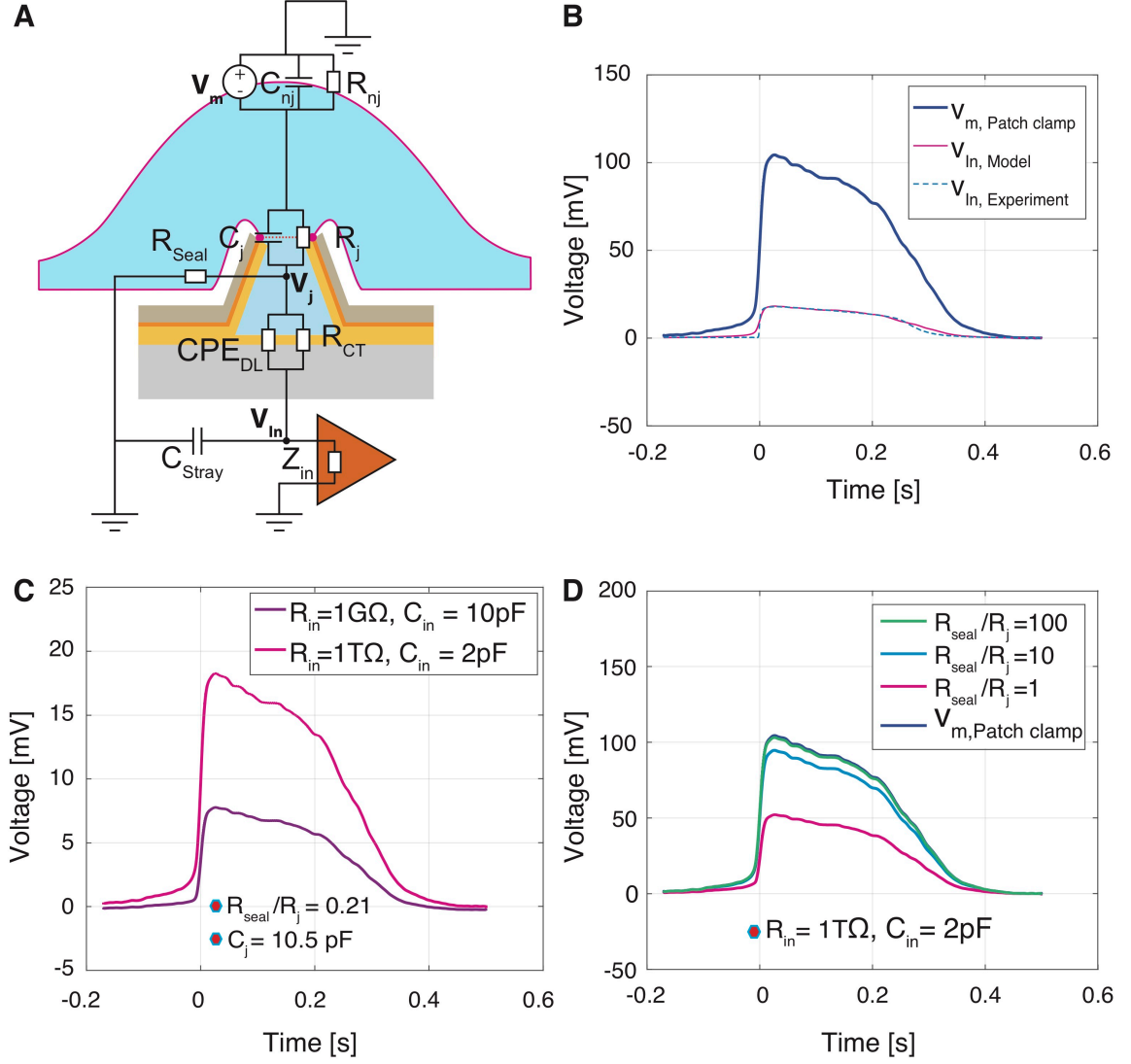


Figure B.2: Modeling of the cell-electrode interface and of the effect of the recording system. **A)** Equivalent electrical model of the cell-electrode interface. **B)** Graph comparing the reference action potential of a rat cardiomyocyte coupled to a myofibroblast as recorded with the whole-cell patch clamp technique ($v_{m, \text{Patch clamp}}$), the action potential recorded with the nanovolcano ($v_{In, \text{Experiment}}$) and the reference action potential passed through the equivalent electrical model of the cell-electrode interface ($v_{In, \text{Model}}$). **C)** Influence of the input impedance of the amplifier on the signal shape. **D)** Effect of the seal resistance R_{seal} with respect to the junctional resistance R_j , on the recorded signal.

$$V_j(\omega) = \frac{Z_{Sys}}{Z_{Sys} + Z_j} V_m(\omega) \quad (\text{B.1})$$

where:

$$Z_j(\omega) = \frac{R_j}{1 + j\omega R_j C_j} \quad (\text{B.2})$$

Appendix B. Supplementary information related to Chapter 3

With R_j being the junctional resistance and C_j the junctional capacitance of the cell membrane, Z_{Sys} can be defined as:

$$Z_{Sys}(\omega) = (Z_{In,Stray} + Z_e) \parallel R_{Seal} = \frac{R_{Seal}(Z_{In,Stray} + Z_e)}{R_{Seal} + Z_{In,Stray} + Z_e} \quad (\text{B.3})$$

with:

$$Z_e(\omega) = \frac{R_{CT}}{1 + (j\omega)^{n_{DL}} R_{CT} C_{DL}} \quad (\text{B.4})$$

and:

$$Z_{In,Stray}(\omega) = Z_{In} \parallel C_{Stray} = \frac{R_{In}}{1 + j\omega R_{In}(C_{In} + C_{Stray})} \quad (\text{B.5})$$

where R_{In} is the input resistance (1 T Ω), C_{In} the input capacitance of the amplifier (2 pF), and R_{Seal} the seal resistance.

The potential $V_{In}(\omega)$ can be computed from $V_j(\omega)$ as follows:

$$V_{In}(\omega) = \frac{Z_{In,Stray}}{Z_{In,Stray} + Z_e} V_j(\omega) \quad (\text{B.6})$$

The temporal signal can finally be expressed by applying the inverse Fourier transform to the frequency dependent signal $V_{In}(\omega)$:

$$v_{In}(t) = \mathcal{F}^{-1}(V_{In}(\omega)) \quad (\text{B.7})$$

As presented in Chapter 3, most of the parameters of the cell-electrode interface were determined by electrochemical impedance spectroscopy. Only R_{Seal} , R_j and C_j are missing to complete the interface modeling. The direct experimental determination of these values using the nanovolcanoes is presently not feasible. In order to estimate these parameters, a reference action potential recorded using the standard patch clamp technique was fed into the electrical equivalent model of the cell-electrode interface and its output was compared to the action potential measured experimentally with the nanovolcano. Iteratively, R_{Seal} , R_j and C_j were adjusted by a particle swarm optimization (PSO) algorithm until the output of the system fitted with the experimental signal. As R_{Seal}/R_j and C_j are independent variables, it is consistent to get

B.3. Effect of the recording system, R_{Seal} , and C_{Stray} on signal shape

an estimation of these parameters by a simple fitting. In Figure B.2-B, the reference action potential is shown before ($v_{m, \text{Patch clamp}}$) and after passing through the model ($v_{In, \text{Model}}$). Under the assumption of $R_{Seal}/R_j = 0.21$ and $C_j = 10.5$ pF, the signal recorded by the nanovolcano ($v_{In, \text{Experiment}}$) and the output of the model ($v_{In, \text{Model}}$) show an excellent fit. Of note, the action potential shown was recorded from a cardiomyocyte that was electrotonically coupled to a myofibroblast. [298] We chose this model because it approximates, at the two cell level, the cellular composition of the cell monolayers used in the nanovolcano experiments. These monolayers contained, as evidenced by the presence of spontaneous electrical activity, myofibroblasts that were electrotonically coupled to the cardiomyocytes. [206] Spontaneous activity was present in the cardiomyocyte-myofibroblast model as well and was characterized by a typical pacemaker potential preceding the action potential upstroke. This pacemaker potential was missing in the nanovolcano signals which indicates that they recorded propagated action potentials remote from the pacemaking region of the cell monolayer.

As all the parameters required to define the cell-electrode interface have been estimated, it is now possible to analytically study the influence of specific system components in order to predict the full potential of the developed technology.

B.3 Effect of the recording system, R_{Seal} , and C_{Stray} on signal shape

Filtering Extracellular microelectrode array amplifiers usually exhibit a limited bandwidth (typically 0.1 Hz to 5 kHz) that induces significant distortions of intracellular signals which affect especially the repolarization phase. To circumvent this problem, we used a DC-coupled Digital Lynx SX acquisition system combined with a HS36 headstage (Neuralynx, USA) instead in this study. The bandwidth of this system (0 to 8 kHz) prevents signal distortion.

Amplifier input impedance Amplifiers used for recording extracellular field potentials generally have an input impedance that is too small to prevent signal attenuation when recording with nanovolcanoes. As highlighted by equation B.6, Z_e has to be negligible compared to $Z_{In, Stray}$ in order not to attenuate the voltage V_j at the amplifier input. Figure B.2-C presents the advantages of using a high input impedance amplifier such as the HS36 headstage used in this study ($R_{In} = 1 \text{ T}\Omega$ and $C_{In} = 2$ pF) to prevent signal attenuation at the electrode-electrolyte interface. The non-filtered signal $V_{In}(t)$ has been computed from equation B.7 for both cases of an amplifier with

Appendix B. Supplementary information related to Chapter 3

low and high input impedance, respectively. For the same cell-electrode configuration, a higher input impedance amplifier can improve the signal amplitude by a factor superior to two which renders amplifiers like the HS36 headstage an ideal choice for intracellular electrophysiology based on micro-nanotechnologies.

Influence of R_{Seal}/R_j Conducting particle swarm optimization on experimentally recorded action potentials suggested a ratio of R_{Seal}/R_j of 0.21 for the nanovolcanoes. From Equation B.1, Z_{Sys} has to be higher than Z_j in order to guarantee a low attenuation of V_m . Practically, if the amplifier is well chosen, R_{Seal} is likely the limiting factor of Z_{Sys} and, hence, should be maximized with respect to Z_j to optimize the signal amplitude. In Figure B.2-D, the non-filtered signal $V_{In}(t)$ has been computed for different R_{Seal}/R_j ratios based on Equation B.7. A constant high input impedance amplifier was used for the computations. A higher ratio leads to a recorded signal closer to the original action potential. An increase by a factor of ten would already result in significant improvements in term of amplitude and physiological relevance, whereas a factor of 100 would be close to ideal. In that case, recording of normal amplitude signals would be feasible. Higher ratios could potentially be achieved by increasing the seal resistance or by trying to reduce R_j (e.g., by optimizing the geometry and the self-assembled monolayers). For practical reasons, the amplifier should exhibit a large DC range and the signals should be converted with high-resolution analog to digital converters (ADCs).

Influence of the stray capacitance As shown in Equation B.6 the stray capacitance also attenuates V_j . Accordingly, C_{Stray} should be kept as small as possible to maintain signal amplitudes. In our case, the stray capacitance ($C_{Stray} = 0.3$ pF) was negligible when compared to the input capacitance of the amplifier ($C_{In} = 2$ pF) and, hence, did not significantly affect signal amplitude.

Appendix C

Supplementary information related to Chapter 4

C.1 Evolution of the signal amplitude with time after electroporation

Figure C.1 presents a typical example of the decay of APAs after electroporation. A relatively rapid initial decay is followed, after ~ 2 minutes, by a longer and more stable recording phase. After 8 minutes, signals with typical AP shapes are superseded by signals showing both intracellular and extracellular signal characteristics which is likely explained by progressive re-sealing of the cell.

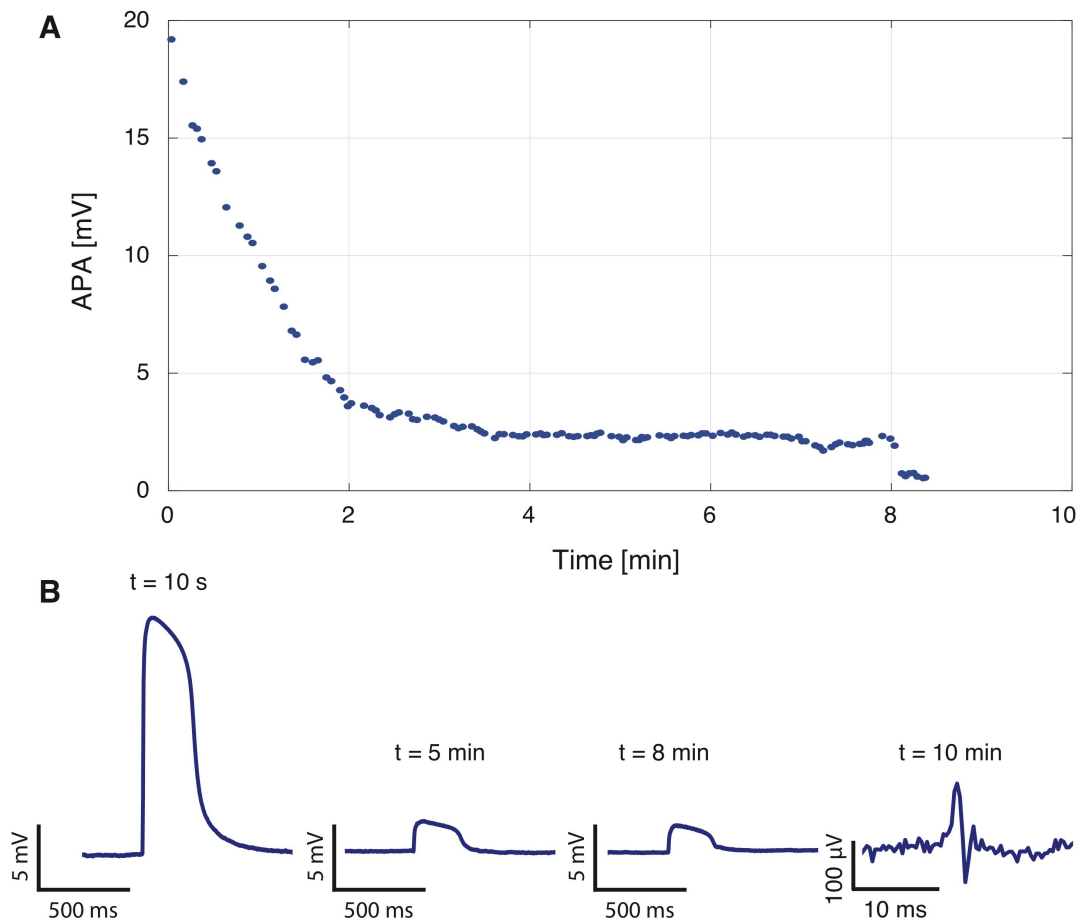


Figure C.1: *APA temporal evolution after electroporation.* **A)** Typical time course of the decline of the action potential amplitude (APA) as reported by a single nanovolcano after electroporation ($V_{EP} = 1V$, repetition 1). **B)** Electrical trace of the corresponding action potentials at different time points.

Appendix D

Supplementary information related to Chapter 5

D.1 Setup for simultaneous optical imaging, force, and electrical recordings

A custom setup was necessary to obtain simultaneously optical images as well as mechanical forces and electrical recordings (Figure D.1-A). The cells were seeded to a 6 cm in diameter petri dish, which was mounted in a custom sample holder. The cells were then covered with liquid medium (Figure D.1-A). The sample holder rests on a large aluminum structure placed on a noise cancelling table (not represented in the figure) to ensure minimal mechanical noise. The nanovolcano probe was placed on top of the sample using the custom cantilever holder described in Chapter 5, connected to a commercial tip-scanning AFM head (Figure D.1-B). The cantilever deflection is measured using an optical laser readout. The force applied by the cell to the cantilever is calculated based the cantilever deflection signal, knowing the cantilever stiffness and deflection sensitivity. The nanovolcano cantilever electrode is connected through a coaxial cable to a microelectrode amplifier and a digital acquisition system to record the electrical signal. An inverted microscope was placed under the sample holder to allow for simultaneous optical imaging.

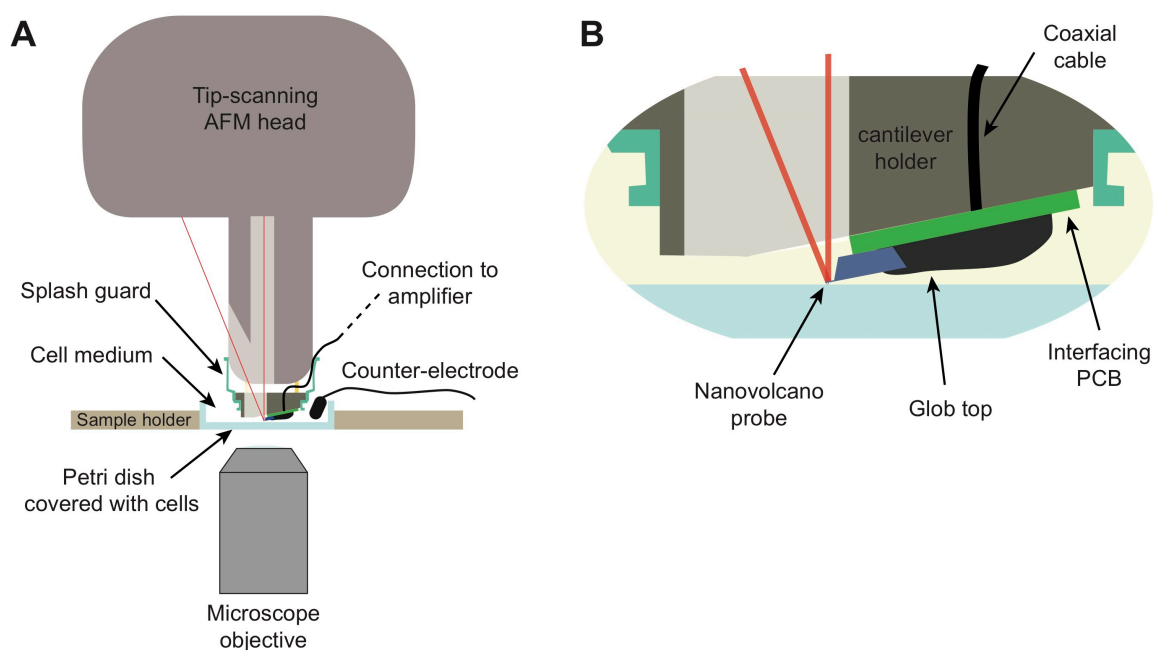


Figure D.1: *Description of the custom AFM-optical system. A)* Schematic drawing showing a cross-section view of the custom-made AFM-optical system. **B)** Expanded cross-section view of the custom-made cantilever holder mounted on the AFM head.

Bibliography

- [1] M. Cobb, “Exorcizing the animal spirits: Jan Swammerdam on nerve function,” *Nature Reviews Neuroscience*, vol. 3, no. 5, pp. 395–400, 2002.
- [2] A. Verkhratsky, O. A. Krishtal, and O. H. Petersen, “From Galvani to patch clamp: The development of electrophysiology,” *Pflugers Archiv European Journal of Physiology*, vol. 453, no. 3, pp. 233–247, 2006.
- [3] A. Galen, *De Motu Musculorum*. 1549.
- [4] I. Glynn, “Two millennia of animal spirits,” *Nature*, vol. 402, no. 6760, pp. 353–353, 1999.
- [5] R. Descartes, *De Homine*. 1662.
- [6] J. Swammerdam, *In Ranis*. 1665.
- [7] J. Jaynes, “The problem of animate motion in the seventeenth century,” *Journal of the History of Ideas*, vol. 31, pp. 219–234, 1970.
- [8] F. L. Holmes, “The old martyr of science: The frog in experimental physiology,” *Journal of the History of Biology*, vol. 26, no. 2, pp. 311–328, 1993.
- [9] L. Galvani, *De Viribus Electricitatis in Motu Musculari Commentarius*. 1791.
- [10] L. Galvani, *Dell’Uso e dell’Attività dell’Arco Conduttore*. 1794.
- [11] M. Piccolino, “Animal electricity and the birth of electrophysiology: The legacy of Luigi Galvani,” *Brain Research Bulletin*, vol. 46, no. 5, pp. 381–407, 1998.
- [12] G. Finkelstein, “Mechanical neuroscience: Emil du Bois-Reymond’s innovations in theory and practice,” *Frontiers in Systems Neuroscience*, vol. 9, pp. 1–4, 2015.
- [13] E. Du Bois-Reymond, *Untersuchungen über Thierische Electricität*. 1848.

Bibliography

- [14] A. Verkhratsky and V. Parpura, “History of electrophysiology and the patch clamp,” *Methods in Molecular Biology*, vol. 1183, pp. 1–19, 2014.
- [15] H. von Helmholtz, “Note sur la vitesse de propagation de l’agent nerveux dans les nerfs rachidiens,” *Comptes rendus de l’Académie des Sciences*, vol. 30, pp. 204–206, 1850.
- [16] J. Bernstein, “Ueber den zeitlichen verlauf der negativen schwankung des nervenstroms,” *Pflüger, Archiv für die Gesamte Physiologie des Menschen und der Thiere*, vol. 1, no. 1, pp. 173–207, 1868.
- [17] J. Bernstein, *Untersuchungen über den Erregungsvorgang im Nerven und Muskel-system*. 1871.
- [18] J. Bernstein, *Elektrobiologie - Die Lehre von den Electricischen Vorgängen im Organismus auf Moderner Grundlage Dargestellt*. 1912.
- [19] E. Overton, “Betrag zur allgemeine muskel und nervenphysiologie. II über die unentbehrlichkeit von natrium- (oder litium-) ionen für den contractionsact des muskels,” *Pflugers Arch*, vol. 92, pp. 346–380, 1902.
- [20] C. E. Overton, “Über die allgemeinen osmotischen eigenschaften der zelle, ihre vermutlichen ursachen und ihre bedeutung für die physiologie,” *Vierteljahrsschrift der Naturforschenden Gesellschaft in Zurich*, vol. 44, pp. 88–135, 1899.
- [21] B. Y. E. Gorter, “On bimolecular layers of lipids on the chromocytes of the blood,” *Journal of Experimental Medicine*, vol. 41, pp. 439–443, 1925.
- [22] J. Danielli and H. Davson, “A Contribution to the theory of permeability of thin films,” *Journal of Cellular Physiology*, vol. 5, pp. 495–508, 1935.
- [23] J. Young, “Structure of nerve fibres and synapses in some invertebrates,” *Cold Spring Harbor Symposia on Quantitative Biology*, vol. 4, pp. 1–6, 1936.
- [24] H. J. Curtis and K. S. Cole, “Membrane resting and action potentials from the squid giant axon,” *Journal of Cellular and Comparative Physiology*, vol. 19, no. 2, pp. 135–144, 1942.
- [25] A. L. Hodgkin and A. F. Huxley, “Action potentials recorded from inside a nerve fibre,” *Nature*, vol. 144, no. 3651, pp. 710–711, 1939.
- [26] A. L. Hodgkin, A. F. Huxley, and B. Katz, “Measurement of current-voltage relations in the membrane of the giant axon of *Loligo*,” *The Journal of Physiology*, vol. 116, no. 4, pp. 424–448, 1952.

-
- [27] A. L. Hodgkin and A. F. Huxley, "A quantitative description of membrane current and its application to conduction and excitation in nerve," *The Journal of Physiology*, vol. 117, no. 4, pp. 500–544, 1952.
- [28] A. L. Hodgkin and A. F. Huxley, "Propagation of electrical signals along giant nerve fibers," *Proceedings of the Royal Society of London. Series B*, vol. 140, no. 899, pp. 177–183, 1952.
- [29] A. L. Hodgkin and A. F. Huxley, "Movement of sodium and potassium ions during nervous activity," *Cold Spring Harbor Symposia on Quantitative Biology*, vol. 17, pp. 43–52, 1952.
- [30] A. L. Hodgkin and A. F. Huxley, "The dual effect of membrane potential on sodium conductance in the giant axon of *Loligo*," *The Journal of Physiology*, vol. 116, no. 4, pp. 497–506, 1952.
- [31] A. L. Hodgkin and A. F. Huxley, "Currents carried by sodium and potassium ions through the membrane of the giant axon of *Loligo*," *The Journal of Physiology*, vol. 116, no. 4, pp. 449–472, 1952.
- [32] A. L. Hodgkin and A. F. Huxley, "The components of membrane conductance in the giant axon of *Loligo*," *The Journal of Physiology*, vol. 116, no. 4, pp. 473–496, 1952.
- [33] M. Cahalan and E. Neher, "Patch clamp techniques: An overview," *Methods in Enzymology*, vol. 207, pp. 3–14, 1992.
- [34] R. C. Bean, W. C. Shepherd, H. Chan, and J. Eichner, "Discrete conductance fluctuations in lipid bilayer protein membranes," *The Journal of general physiology*, vol. 53, no. 6, pp. 741–757, 1969.
- [35] S. B. Hladky and D. A. Haydon, "Discreteness of conductance change in bimolecular lipid membranes in the presence of certain antibiotics," *Nature*, vol. 225, no. 5231, pp. 451–453, 1970.
- [36] B. Sakmann and E. Neher, *Single-Channel Recording*. Springer, 1983.
- [37] E. Neher and B. Sakmann, "Single-channel currents recorded from membrane," *Nature*, vol. 260, pp. 799–802, 1976.
- [38] B. Sakmann, "Patch Clamp Techniques for Studying Ionic Channels in Excitable Membranes," *Annual Review of Physiology*, vol. 46, no. 1, pp. 455–472, 1984.

Bibliography

- [39] A. Strickholm, “Impedance of a small electrically isolated area of the muscle cell surface,” *Journal of General Physiology*, vol. 44, no. 6, pp. 1073–1088, 1961.
- [40] E. Neher and H. D. Lux, “Voltage clamp on helix pomatia neuronal membrane; Current measurement over a limited area of the soma surface,” *Pflügers Archiv European Journal of Physiology*, vol. 311, no. 3, pp. 272–277, 1969.
- [41] F. J. Sigworth and E. Neher, “Single Na⁺ channel currents observed in cultured rat muscle cells,” *Nature*, vol. 287, no. 5781, pp. 447–449, 1980.
- [42] O. P. Hamill, A. Marty, E. Neher, B. Sakmann, and F. J. Sigworth, “Improved patch-clamp techniques for high-resolution current recording from cells and cell-free membrane patches,” *Pflügers Archiv European Journal of Physiology*, vol. 391, no. 2, pp. 85–100, 1981.
- [43] R. Horn and A. Marty, “Muscarinic activation of ionic currents measured by a new whole-cell recording method,” *Journal of General Physiology*, vol. 92, no. 2, pp. 145–159, 1988.
- [44] L. Conforti, “Patch-clamp techniques,” in *Cell Physiology Source Book*, pp. 369–381, Elsevier, 2012.
- [45] W. A. Catterall, “Ion channel voltage sensors: Structure, function, and pathophysiology,” *Neuron*, vol. 67, no. 6, pp. 915–928, 2010.
- [46] G. L. Collingridge, R. W. Olsen, J. Peters, and M. Spedding, “A nomenclature for ligand-gated ion channels,” *Neuropharmacology*, vol. 56, no. 1, pp. 2–5, 2009.
- [47] D. C. Gadsby, P. Vergani, and L. Csanády, “The ABC protein turned chloride channel whose failure causes cystic fibrosis,” *Nature*, vol. 440, no. 7083, pp. 477–483, 2006.
- [48] L. J. Wu, T. B. Sweet, and D. E. Clapham, “International Union of Basic and Clinical Pharmacology. LXXVI. Current progress in the Mammalian TRP ion channel family,” *Pharmacological Reviews*, vol. 62, no. 3, pp. 381–404, 2010.
- [49] B. Nilius, J. Eggermont, T. Voets, and G. Droogmans, “Volume-activated Cl⁻ channels,” *General Pharmacology*, vol. 27, no. 7, pp. 1131–1140, 1996.
- [50] R. Sharif-Naeini, A. Dedman, J. H. Folgering, F. Duprat, A. Patel, B. Nilius, and E. Honoré, “TRP channels and mechanosensory transduction: Insights into the arterial myogenic response,” *Pflügers Archiv European Journal of Physiology*, vol. 456, no. 3, pp. 529–540, 2008.

-
- [51] A. J. Harmar, R. A. Hills, E. M. Rosser, M. Jones, O. P. Buneman, D. R. Dunbar, S. D. Greenhill, V. A. Hale, J. L. Sharman, T. I. Bonner, W. A. Catterall, A. P. Davenport, P. Delagrangé, C. L. Dollery, S. M. Foord, G. A. Gutman, V. Laudet, R. R. Neubig, E. H. Ohlstein, R. W. Olsen, J. Peters, J. P. Pin, R. R. Ruffolo, D. B. Searls, M. W. Wright, and M. Spedding, "IUPHAR-DB: The IUPHAR database of G protein-coupled receptors and ion channels," *Nucleic Acids Research*, vol. 37, pp. 680–685, 2009.
- [52] F. Ashcroft, *Ion Channels and Disease: Channelopathies*. Elsevier, 2000.
- [53] B. P. Bean, "The action potential in mammalian central neurons," *Nature Reviews Neuroscience*, vol. 8, no. 6, pp. 451–465, 2007.
- [54] B. W. Connors and M. J. Gutnick, "Intrinsic firing patterns of diverse neocortical neurons," *Trends in Neurosciences*, vol. 13, no. 3, pp. 99–104, 1990.
- [55] A. Erisir, D. Lau, B. Rudy, and C. S. Leonard, "Function of specific K⁺ channels in sustained high-frequency firing of fast-spiking neocortical interneurons," *Journal of Neurophysiology*, vol. 82, no. 5, pp. 2476–2489, 1999.
- [56] M. D. Bevan and C. J. Wilson, "Mechanisms underlying spontaneous oscillation and rhythmic firing in rat subthalamic neurons," *Journal of Neuroscience*, vol. 19, no. 17, pp. 7617–7628, 1999.
- [57] T. Tateno, A. Harsch, and H. P. Robinson, "Threshold firing frequency-current relationships of neurons in rat somatosensory cortex: Type 1 and type 2 dynamics," *Journal of Neurophysiology*, vol. 92, no. 4, pp. 2283–2294, 2004.
- [58] L. Forti, E. Cesana, J. Mapelli, and E. D'Angelo, "Ionic mechanisms of autorhythmic firing in rat cerebellar Golgi cells," *Journal of Physiology*, vol. 574, no. 3, pp. 711–729, 2006.
- [59] J. Dunlop, M. Bowlby, R. Peri, D. Vasilyev, and R. Arias, "High-throughput electrophysiology: an emerging paradigm for ion-channel screening and physiology," *Nature Reviews Drug Discovery*, vol. 7, no. 4, pp. 358–368, 2008.
- [60] A. Lepple-Wienhues, K. Ferlinz, A. Seeger, and A. Schäfer, "Flip the tip: An automated, high quality, cost-effective patch clamp screen," *Receptors and Channels*, vol. 9, no. 1, pp. 13–17, 2003.
- [61] D. Vasilyev, T. Merrill, A. Iwanow, J. Dunlop, and M. Bowlby, "A novel method for patch-clamp automation," *Pflügers Archiv European Journal of Physiology*, vol. 452, no. 2, pp. 240–247, 2006.

Bibliography

- [62] C. J. Milligan, J. Li, P. Sukumar, Y. Majeed, M. L. Dallas, A. English, P. Emery, K. E. Porter, A. M. Smith, I. McFadzean, D. Beccano-Kelly, Y. Bahnasi, A. Cheong, J. Naylor, F. Zeng, X. Liu, N. Gamper, L. H. Jiang, H. A. Pearson, C. Peers, B. Robertson, and D. J. Beech, “Robotic multiwell planar patch-clamp for native and primary mammalian cells,” *Nature Protocols*, vol. 4, no. 2, pp. 244–255, 2009.
- [63] K. Schroeder, B. Neagle, D. J. Trezise, and J. Worley, “IonWorks™ HT: A new high-throughput electrophysiology measurement platform,” *Journal of Biomolecular Screening*, vol. 8, no. 1, pp. 50–64, 2003.
- [64] D. C. Bell and M. L. Dallas, “Using automated patch clamp electrophysiology platforms in pain-related ion channel research: insights from industry and academia,” *British Journal of Pharmacology*, vol. 175, no. 12, pp. 2312–2321, 2018.
- [65] M. Scanziani and M. Häusser, “Electrophysiology in the age of light,” *Nature*, vol. 461, no. 7266, pp. 930–939, 2009.
- [66] N. Ji, H. Shroff, H. Zhong, and E. Betzig, “Advances in the speed and resolution of light microscopy,” *Current Opinion in Neurobiology*, vol. 18, no. 6, pp. 605–616, 2008.
- [67] S. W. Hell, “Far-field optical nanoscopy,” *Science*, vol. 316, no. 5828, pp. 1153–1158, 2007.
- [68] B. A. Wilt, L. D. Burns, E. T. Wei Ho, K. K. Ghosh, E. A. Mukamel, and M. J. Schnitzer, “Advances in Light Microscopy for Neuroscience,” *Annual Review of Neuroscience*, vol. 32, no. 1, pp. 435–506, 2009.
- [69] L. M. Palmer and G. J. Stuart, “Membrane potential changes in dendritic spines during action potentials and synaptic input,” *Journal of Neuroscience*, vol. 29, no. 21, pp. 6897–6903, 2009.
- [70] D. R. Hochbaum, Y. Zhao, S. L. Farhi, N. Klapoetke, C. A. Werley, V. Kapoor, P. Zou, J. M. Kralj, D. MacLaurin, N. Smedemark-Margulies, J. L. Saulnier, G. L. Boulting, C. Straub, Y. K. Cho, M. Melkonian, G. K. S. Wong, D. J. Harrison, V. N. Murthy, B. L. Sabatini, E. S. Boyden, R. E. Campbell, and A. E. Cohen, “All-optical electrophysiology in mammalian neurons using engineered microbial rhodopsins,” *Nature Methods*, vol. 11, no. 8, pp. 825–833, 2014.

-
- [71] C. Prajapati, R.-P. Po, and K. Aalto-Seta, “Simultaneous recordings of action potentials and calcium transients from human induced pluripotent stem cell derived cardiomyocytes,” *Biology open*, vol. 7, no. 7, p. 035030, 2018.
- [72] B. M. Salzberg, A. L. Obaid, D. M. Senseman, and H. Gainer, “Optical recording of action potentials from vertebrate nerve terminals using potentiometric probes provides evidence for sodium and calcium components,” *Nature*, vol. 306, no. 5938, pp. 36–40, 1983.
- [73] S. Rohr and B. M. Salzberg, “Multiple site optical recording of transmembrane voltage (MSORTV) in patterned growth heart cell cultures: assessing electrical behavior, with microsecond resolution, on a cellular and subcellular scale,” *Biophysical Journal*, vol. 67, no. 3, pp. 1301–1315, 1994.
- [74] M. Djurusic, S. Antic, W. R. Chen, and D. Zecevic, “Voltage imaging from dendrites of mitral cells: EPSP attenuation and spike trigger zones,” *Journal of Neuroscience*, vol. 24, no. 30, pp. 6703–6714, 2004.
- [75] M. Nuriya, J. Jiang, B. Nemet, K. B. Eisenthal, and R. Yuste, “Imaging membrane potential in dendritic spines,” *Proceedings of the National Academy of Sciences of the United States of America*, vol. 103, no. 3, pp. 786–790, 2006.
- [76] M. Tsodyks, T. Kenet, A. Grinvald, and A. Arieli, “Linking spontaneous activity of single cortical neurons and the underlying functional architecture,” *Science*, vol. 286, no. 5446, pp. 1943–1946, 1999.
- [77] A. Arieli, A. Sterkin, A. Grinvald, and A. Aertsen, “Dynamics of ongoing activity: Explanation of the large variability in evoked cortical responses,” *Science*, vol. 273, no. 5283, pp. 1868–1871, 1996.
- [78] M. Z. Lin and M. J. Schnitzer, “Genetically encoded indicators of neuronal activity,” *Nature Neuroscience*, vol. 19, no. 9, pp. 1142–1153, 2016.
- [79] Y. Gong, C. Huang, J. Z. Li, B. F. Grewe, Y. Zhang, S. Eismann, and M. J. Schnitzer, “High-speed recording of neural spikes in awake mice and flies with a fluorescent voltage sensor,” *Science*, vol. 350, no. 6266, pp. 1361–1366, 2015.
- [80] L. Kaestner, Q. Tian, E. Kaiser, W. Xian, A. Müller, M. Oberhofer, S. Ruppenthal, D. Sinnecker, H. Tsutsui, A. Miyawaki, A. Moretti, and P. Lipp, “Genetically Encoded Voltage Indicators in Circulation Research,” *Int. J. Mol. Sci*, vol. 16, pp. 21626–21642, 2015.

Bibliography

- [81] T. Knöpfel, J. Díez-García, and W. Akemann, “Optical probing of neuronal circuit dynamics: Genetically encoded versus classical fluorescent sensors,” *Trends in Neurosciences*, vol. 29, no. 3, pp. 160–166, 2006.
- [82] T. Knöpfel, “Genetically encoded optical indicators for the analysis of neuronal circuits,” *Nature Reviews Neuroscience*, vol. 13, no. 10, pp. 687–700, 2012.
- [83] H. H. H. Yang, F. St-Pierre, X. Sun, X. Ding, M. Z. Z. Lin, and T. R. R. Clandinin, “Subcellular Imaging of Voltage and Calcium Signals Reveals Neural Processing In Vivo,” *Cell*, vol. 166, no. 1, pp. 245–257, 2016.
- [84] G. Nagel, T. Szellas, W. Huhn, S. Kateriya, N. Adeishvili, P. Berthold, D. Ollig, P. Hegemann, and E. Bamberg, “Channelrhodopsin-2, a directly light-gated cation-selective membrane channel,” *Proceedings of the National Academy of Sciences of the United States of America*, vol. 100, pp. 13940–13945, 2003.
- [85] J. M. Kim, J. Hwa, P. Garriga, P. J. Reeves, U. L. RajBhandary, and H. G. Khorana, “Light-driven activation of β 2-adrenergic receptor signaling by a chimeric rhodopsin containing the β 2-adrenergic receptor cytoplasmic loops,” *Biochemistry*, vol. 44, no. 7, pp. 2284–2292, 2005.
- [86] O. H. Petersen, M. Michalak, and A. Verkhratsky, “Calcium signalling: Past, present and future,” *Cell Calcium*, vol. 38, no. 3-4, pp. 161–169, 2005.
- [87] M. B. Cannell, J. R. Berlin, and W. J. Lederer, “Intracellular calcium in cardiac myocytes: calcium transients measured using fluorescence imaging,” *Society of General Physiologists series*, vol. 42, pp. 201–14, 1987.
- [88] Y. Kovalchuk, R. Homma, Y. Liang, A. Maslyukov, M. Hermes, T. Thestrup, O. Griesbeck, J. Ninkovic, L. B. Cohen, and O. Garaschuk, “In vivo odourant response properties of migrating adult-born neurons in the mouse olfactory bulb,” *Nature Communications*, vol. 6, p. 6349, 2015.
- [89] W. A. Saber, F. M. Gasparoli, M. G. Dirks, F. J. Gunn-Moore, and M. Antkowiak, “All-optical assay to study biological neural networks,” *Frontiers in Neuroscience*, vol. 12, p. 451, 2018.
- [90] M. Mues, I. Bartholomäus, T. Thestrup, O. Griesbeck, H. Wekerle, N. Kawakami, and G. Krishnamoorthy, “Real-time in vivo analysis of T cell activation in the central nervous system using a genetically encoded calcium indicator,” *Nature Medicine*, vol. 19, no. 6, pp. 778–783, 2013.

-
- [91] R. Shinnawi, I. Huber, L. Maizels, N. Shaheen, A. Gepstein, G. Arbel, A. J. Tijssen, and L. Gepstein, “Monitoring human-induced pluripotent stem cell-derived cardiomyocytes with genetically encoded calcium and voltage fluorescent reporters,” *Stem Cell Reports*, vol. 5, no. 4, pp. 582–596, 2015.
- [92] G. Grynkiewicz, M. Poenie, and R. Y. Tsien, “A new generation of Ca^{2+} indicators with greatly improved fluorescence properties,” *Journal of Biological Chemistry*, vol. 260, no. 6, pp. 3440–3450, 1985.
- [93] D. A. Dombeck, A. N. Khabbaz, F. Collman, T. L. Adelman, and D. W. Tank, “Imaging Large-Scale Neural Activity with Cellular Resolution in Awake, Mobile Mice,” *Neuron*, vol. 56, no. 1, pp. 43–57, 2007.
- [94] D. S. Greenberg, A. R. Houweling, and J. N. Kerr, “Population imaging of ongoing neuronal activity in the visual cortex of awake rats,” *Nature Neuroscience*, vol. 11, no. 7, pp. 749–751, 2008.
- [95] C. Stosiek, O. Garaschuk, K. Holthoff, and A. Konnerth, “In vivo two-photon calcium imaging of neuronal networks,” *Proceedings of the National Academy of Sciences of the United States of America*, vol. 100, no. 12, pp. 7319–7324, 2003.
- [96] K. Ohki, S. Chung, Y. H. Ch’ng, P. Kara, and R. C. Reid, “Functional imaging with cellular resolution reveals precise microarchitecture in visual cortex,” *Nature*, vol. 433, no. 7026, pp. 597–603, 2005.
- [97] B. L. Sabatini and K. Svoboda, “Analysis of calcium channels in single spines using optical fluctuation analysis,” *Nature*, vol. 408, no. 6812, pp. 589–593, 2000.
- [98] J. J. Chong, X. Yang, C. W. Don, E. Minami, Y. W. Liu, J. J. Weyers, W. M. Mahoney, B. Van Biber, S. M. Cook, N. J. Palpant, J. A. Gantz, J. A. Fugate, V. Muskheli, G. M. Gough, K. W. Vogel, C. A. Astley, C. E. Hotchkiss, A. Baldessari, L. Pabon, H. Reinecke, E. A. Gill, V. Nelson, H. P. Kiem, M. A. Laflamme, and C. E. Murry, “Human embryonic-stem-cell-derived cardiomyocytes regenerate non-human primate hearts,” *Nature*, vol. 510, no. 7504, pp. 273–277, 2014.
- [99] T. J. Herron, P. Lee, and J. Jalife, “Optical imaging of voltage and calcium in cardiac cells & tissues,” *Circulation Research*, vol. 110, no. 4, pp. 609–623, 2012.
- [100] G. Buzsáki, C. A. Anastassiou, and C. Koch, “The origin of extracellular fields and currents-EEG, ECoG, LFP and spikes,” *Nature Reviews Neuroscience*, vol. 13, no. 6, pp. 407–420, 2012.

Bibliography

- [101] A. Stett, U. Egert, E. Guenther, F. Hofmann, T. Meyer, W. Nisch, and H. Haemmerle, “Biological application of microelectrode arrays in drug discovery and basic research,” *Analytical and Bioanalytical Chemistry*, vol. 377, no. 3, pp. 486–495, 2003.
- [102] A. Hierlemann, U. Frey, S. Hafizovic, and F. Heer, “Growing cells atop microelectronic chips: Interfacing electrogenic cells in vitro with CMOS-based microelectrode arrays,” *Proceedings of the IEEE*, vol. 99, no. 2, pp. 252–284, 2011.
- [103] M. J. Engelene Obien, K. Deligkaris, T. Bullmann, D. J. Bakkum, U. Frey, and A. El Hady, “Revealing neuronal function through microelectrode array recordings,” *Frontiers in Neuroscience*, vol. 8, p. 423, 2015.
- [104] K. K. D. Harris, D. D. A. Henze, J. Csicsvari, H. Hirase, G. Buzsaki, and G. Buzsáki, “Accuracy of tetrode spike separation as determined by simultaneous intracellular and extracellular measurements,” *Journal of Neurophysiology*, vol. 84, no. 1, p. 401, 2000.
- [105] C. M. Gray, P. E. Maldonado, M. Wilson, and B. McNaughton, “Tetrodes markedly improve the reliability and yield of multiple single-unit isolation from multi-unit recordings in cat striate cortex,” *Journal of Neuroscience Methods*, vol. 63, no. 1-2, pp. 43–54, 1995.
- [106] C. A. Thomas, P. A. Springer, G. E. Loeb, Y. Berwald-Netter, and L. M. Okun, “A miniature microelectrode array to monitor the bioelectric activity of cultured cells,” *Experimental Cell Research*, vol. 74, no. 1, pp. 61–66, 1972.
- [107] G. W. Gross, E. Rieske, G. W. Kreutzberg, and A. Meyer, “A new fixed-array multi-microelectrode system designed for long-term monitoring of extracellular single unit neuronal activity in vitro,” *Neuroscience Letters*, vol. 6, no. 2-3, pp. 101–105, 1977.
- [108] J. Pine, “Recording action potentials from cultured neurons with extracellular microcircuit electrodes,” *Journal of Neuroscience Methods*, vol. 2, no. 1, pp. 19–31, 1980.
- [109] A. Natarajan, M. Stancescu, V. Dhir, C. Armstrong, F. Sommerhage, J. J. Hickman, and P. Molnar, “Patterned cardiomyocytes on microelectrode arrays as a functional, high information content drug screening platform,” *Biomaterials*, vol. 32, no. 18, pp. 4267–4274, 2011.

-
- [110] P. Igelmund, B. K. Fleischmann, I. R. Fischer, J. Soest, O. Gryshchenko, M. M. Böhm-Pinger, H. Sauer, Q. Liu, and J. Hescheler, “Action potential propagation failures in long-term recordings from embryonic stem cell-derived cardiomyocytes in tissue culture,” *Pflügers Archiv European Journal of Physiology*, vol. 437, no. 5, pp. 669–679, 1999.
- [111] S. L. Beeres, D. E. Atsma, A. Van Der Laarse, D. A. Pijnappels, J. Van Tuyn, W. E. Fibbe, A. A. De Vries, D. L. Ypey, E. E. Van Der Wall, and M. J. Schalij, “Human adult bone marrow mesenchymal stem cells repair experimental conduction block in rat cardiomyocyte cultures,” *Journal of the American College of Cardiology*, vol. 46, no. 10, pp. 1943–1952, 2005.
- [112] J. Hescheler, M. Halbach, U. Egert, Z. J. Lu, H. Bohlen, B. K. Fleischmann, and M. Reppel, “Determination of electrical properties of ES cell-derived cardiomyocytes using MEAs,” *Journal of Electrocardiology*, vol. 37, pp. 110–116, 2004.
- [113] M. Imboden, E. de Coulon, A. Poulin, C. Dellenbach, S. Rosset, H. Shea, and S. Rohr, “High-speed Mechano-active MEA for Investigating Rapid Stretch Effects on Cardiac Tissue,” *Nature Communications*, vol. 10, no. 1, p. 834, 2019.
- [114] M. Taketani and M. Baudry, *Advances in Network Electrophysiology: Using Multi-electrode Arrays*. Springer, 2006.
- [115] R. A. Weale, “A new micro-electrode for electro-physiological work,” *Nature*, vol. 167, no. 4248, pp. 529–530, 1951.
- [116] R. C. Gesteland, J. Y. Lettvin, B. Howland, B. Howland, and W. H. Pitts, “Comments on Microelectrodes,” *Proceedings of the IRE*, vol. 47, no. 11, pp. 1856–1862, 1959.
- [117] M. Ballini, J. Muller, P. Livi, Y. Chen, U. Frey, A. Stettler, A. Shadmani, V. Viswam, I. L. Jones, D. Jackel, M. Radivojevic, M. K. Lewandowska, W. Gong, M. Fiscella, D. J. Bakkum, F. Heer, and A. Hierlemann, “A 1024-channel CMOS microelectrode array with 26,400 electrodes for recording and stimulation of electrogenic cells in vitro,” *IEEE Journal of Solid-State Circuits*, vol. 49, no. 11, pp. 2705–2719, 2014.
- [118] D. Tsai, D. Sawyer, A. Bradd, R. Yuste, and K. L. Shepard, “A very large-scale microelectrode array for cellular-resolution electrophysiology,” *Nature Communications*, vol. 8, no. 1, p. 1802, 2017.

Bibliography

- [119] J. Ogi, Y. Kato, Y. Matoba, C. Yamane, K. Nagahata, Y. Nakashima, T. Kishimoto, S. Hashimoto, K. Maari, Y. Oike, and T. Ezaki, “Twenty-four-micrometer-pitch microelectrode array with 6912-channel readout at 12 kHz via highly scalable implementation for high-spatial-resolution mapping of action potentials,” *Biointerphases*, vol. 12, no. 5, p. 05F402, 2017.
- [120] D. Jäckel, D. J. Bakkum, T. L. Russell, J. Müller, M. Radivojevic, U. Frey, F. Franke, and A. Hierlemann, “Combination of High-density Microelectrode Array and Patch Clamp Recordings to Enable Studies of Multisynaptic Integration,” *Scientific Reports*, vol. 7, no. 1, p. 978, 2017.
- [121] J. Dragas, V. Viswam, A. Shadmani, Y. Chen, R. Bounik, A. Stettler, M. Radivojevic, S. Geissler, M. E. J. Obien, J. Müller, and A. Hierlemann, “In Vitro Multi-Functional Microelectrode Array Featuring 59 760 Electrodes, 2048 Electrophysiology Channels, Stimulation, Impedance Measurement, and Neurotransmitter Detection Channels,” *IEEE Journal of Solid-State Circuits*, vol. 52, no. 6, pp. 1576–1590, 2017.
- [122] V. Viswam, R. Bounik, A. Shadmani, J. Dragas, C. Urwyler, J. A. Boos, M. E. J. Obien, J. Muller, Y. Chen, and A. Hierlemann, “Impedance Spectroscopy and Electrophysiological Imaging of Cells with a High-Density CMOS Microelectrode Array System,” *IEEE Transactions on Biomedical Circuits and Systems*, vol. 12, no. 6, pp. 1356–1368, 2018.
- [123] V. Emmenegger, M. E. J. Obien, F. Franke, and A. Hierlemann, “Technologies to study action potential propagation with a focus on HD-MEAs,” *Frontiers in Cellular Neuroscience*, vol. 13, p. 159, 2019.
- [124] D. J. Bakkum, U. Frey, M. Radivojevic, T. L. Russell, J. Müller, M. Fiscella, H. Takahashi, and A. Hierlemann, “Tracking axonal action potential propagation on a high-density microelectrode array across hundreds of sites,” *Nature Communications*, vol. 4, p. 2181, 2013.
- [125] R. Habibey, S. Latifi, H. Mousavi, M. Pesce, E. Arab-Tehrany, and A. Blau, “A multielectrode array microchannel platform reveals both transient and slow changes in axonal conduction velocity,” *Scientific Reports*, vol. 7, no. 1, pp. 1–14, 2017.
- [126] K. Shimba, K. Sakai, T. Isomura, K. Kotani, and Y. Jimbo, “Axonal conduction slowing induced by spontaneous bursting activity in cortical neurons cultured in a microtunnel device,” *Integrative Biology*, vol. 7, no. 1, pp. 64–72, 2015.

-
- [127] M. Radivojevic, D. Jäckel, M. Altermatt, J. Müller, V. Viswam, A. Hierlemann, and D. J. Bakkum, “Electrical Identification and Selective Microstimulation of Neuronal Compartments Based on Features of Extracellular Action Potentials,” *Scientific Reports*, vol. 6, no. 1, pp. 1–20, 2016.
- [128] M. E. Spira and A. Hai, “Multi-electrode array technologies for neuroscience and cardiology,” *Nature Nanotechnology*, vol. 8, no. 2, pp. 83–94, 2013.
- [129] M. R. Angle, B. Cui, and N. A. Melosh, “Nanotechnology and neurophysiology,” *Current Opinion in Neurobiology*, vol. 32, pp. 132–140, 2015.
- [130] J. Abbott, T. Ye, D. Ham, and H. Park, “Optimizing Nanoelectrode Arrays for Scalable Intracellular Electrophysiology,” *Accounts of Chemical Research*, vol. 51, no. 3, pp. 600–608, 2018.
- [131] W. Franks, I. Schenker, P. Schmutz, and A. Hierlemann, “Impedance characterization and modeling of electrodes for biomedical applications,” *IEEE Transactions on Biomedical Engineering*, vol. 52, no. 7, pp. 1295–1302, 2005.
- [132] C. Xie, Z. Lin, L. Hanson, Y. Cui, and B. Cui, “Intracellular recording of action potentials by nanopillar electroporation,” *Nature Nanotechnology*, vol. 7, no. 3, pp. 185–190, 2012.
- [133] Z. Carter Lin, A. F. McGuire, P. W. Burridge, E. Matsa, H.-Y. Lou, J. C. Wu, and B. Cui, “Accurate nanoelectrode recording of human pluripotent stem cell-derived cardiomyocytes for assaying drugs and modeling disease,” *Microsystems & Nanoengineering*, vol. 3, p. 16080, 2017.
- [134] J. Abbott, T. Ye, L. Qin, M. Jorgolli, R. S. Gertner, D. Ham, and H. Park, “CMOS nanoelectrode array for all-electrical intracellular electrophysiological imaging,” *Nature Nanotechnology*, vol. 12, no. 5, pp. 460–466, 2017.
- [135] J. Abbott, T. Ye, K. Krennek, R. S. Gertner, S. Ban, Y. Kim, L. Qin, W. Wu, H. Park, and D. Ham, “A nanoelectrode array for obtaining intracellular recordings from thousands of connected neurons,” *Nature Biomedical Engineering*, vol. 4, p. 232–241, 2019.
- [136] K. Y. Lee, I. Kim, S. E. Kim, D. W. Jeong, J. J. Kim, H. Rhim, J. P. Ahn, S. H. Park, and H. J. Choi, “Vertical nanowire probes for intracellular signaling of living cells,” *Nanoscale Research Letters*, vol. 9, no. 1, pp. 1–7, 2014.

Bibliography

- [137] R. Liu, R. Chen, A. T. Elthakeb, S. H. Lee, S. Hinckley, M. L. Khraiche, J. Scott, D. Pre, Y. Hwang, A. Tanaka, Y. G. Ro, A. K. Matsushita, X. Dai, C. Soci, S. Biesmans, A. James, J. Nogan, K. L. Jungjohann, D. V. Pete, D. B. Webb, Y. Zou, A. G. Bang, and S. A. Dayeh, “High Density Individually Addressable Nanowire Arrays Record Intracellular Activity from Primary Rodent and Human Stem Cell Derived Neurons,” *Nano Letters*, vol. 17, no. 5, pp. 2757–2764, 2017.
- [138] L. Hanson, Z. C. Lin, C. Xie, Y. Cui, and B. Cui, “Characterization of the cell-nanopillar interface by transmission electron microscopy,” *Nano Letters*, vol. 12, no. 11, pp. 5815–5820, 2012.
- [139] F. Santoro, W. Zhao, L. M. Joubert, L. Duan, J. Schnitker, Y. Van De Burgt, H. Y. Lou, B. Liu, A. Salleo, L. Cui, Y. Cui, and B. Cui, “Revealing the Cell-Material Interface with Nanometer Resolution by Focused Ion Beam/Scanning Electron Microscopy,” *ACS Nano*, vol. 11, no. 8, pp. 8320–8328, 2017.
- [140] M. Dipalo, H. Amin, L. Lovato, F. Moia, V. Caprettini, G. C. Messina, F. Tantussi, L. Berdondini, and F. De Angelis, “Intracellular and Extracellular Recording of Spontaneous Action Potentials in Mammalian Neurons and Cardiac Cells with 3D Plasmonic Nanoelectrodes,” *Nano Letters*, vol. 17, no. 6, pp. 3932–3939, 2017.
- [141] Z. C. Lin, C. Xie, Y. Osakada, Y. Cui, and B. Cui, “Iridium oxide nanotube electrodes for sensitive and prolonged intracellular measurement of action potentials,” *Nature Communications*, vol. 5, no. 1, p. 3206, 2014.
- [142] A. Hai, J. Shappir, and M. E. Spira, “In-cell recordings by extracellular microelectrodes,” *Nature Methods*, vol. 7, no. 3, pp. 200–202, 2010.
- [143] A. Hai and M. E. Spira, “On-chip electroporation, membrane repair dynamics and transient in-cell recordings by arrays of gold mushroom-shaped microelectrodes,” *Lab on a Chip*, vol. 12, no. 16, p. 2865, 2012.
- [144] A. Hai, J. Shappir, and M. E. Spira, “Long-Term, Multisite, Parallel, In-Cell Recording and Stimulation by an Array of Extracellular Microelectrodes,” *Journal of Neurophysiology*, vol. 104, no. 1, pp. 559–568, 2010.
- [145] S. M. Ojovan, N. Rabieh, N. Shmoel, H. Erez, E. Maydan, A. Cohen, and M. E. Spira, “A feasibility study of multi-site, intracellular recordings from mammalian neurons by extracellular gold mushroom-shaped microelectrodes,” *Scientific Reports*, vol. 5, no. 1, p. 14100, 2015.

-
- [146] M. E. Spira, N. Shmoel, S. H. M. Huang, and H. Erez, “Multisite attenuated intracellular recordings by extracellular multielectrode arrays, a perspective,” *Frontiers in Neuroscience*, vol. 12, p. 212, 2018.
- [147] A. Fendyur and M. E. Spira, “Toward on-chip, in-cell recordings from cultured cardiomyocytes by arrays of gold mushroom-shaped microelectrodes,” *Frontiers in Neuroengineering*, vol. 5, pp. 1–10, 2012.
- [148] A. Blau, “Cell adhesion promotion strategies for signal transduction enhancement in microelectrode array in vitro electrophysiology: An introductory overview and critical discussion,” *Current Opinion in Colloid and Interface Science*, vol. 18, no. 5, pp. 481–492, 2013.
- [149] J. T. Robinson, M. Jorgolli, A. K. Shalek, M.-H. Yoon, R. S. Gertner, and H. Park, “Vertical nanowire electrode arrays as a scalable platform for intracellular interfacing to neuronal circuits,” *Nature nanotechnology*, vol. 7, no. 3, pp. 180–184, 2012.
- [150] B. D. Almquist and N. A. Melosh, “Fusion of biomimetic stealth probes into lipid bilayer cores,” *Proceedings of the National Academy of Sciences*, vol. 107, no. 13, pp. 5815–5820, 2010.
- [151] B. D. Almquist, P. Verma, W. Cai, and N. A. Melosh, “Nanoscale patterning controls inorganic–membrane interface structure,” *Nanoscale*, vol. 3, no. 2, pp. 391–400, 2011.
- [152] B. D. Almquist and N. A. Melosh, “Molecular structure influences the stability of membrane penetrating biointerfaces,” *Nano Letters*, vol. 11, no. 5, pp. 2066–2070, 2011.
- [153] M. R. Angle, A. Wang, A. Thomas, A. T. Schaefer, and N. A. Melosh, “Penetration of Cell Membranes and Synthetic Lipid Bilayers by Nanoprobes,” *Biophysical Journal*, vol. 107, no. 9, pp. 2091–2100, 2014.
- [154] J. J. VanDersarl and P. Renaud, “Biomimetic surface patterning for long-term transmembrane access,” *Scientific Reports*, vol. 6, no. 1, p. 32485, 2016.
- [155] P. Verma and N. A. Melosh, “Gigaohm resistance membrane seals with stealth probe electrodes,” *Applied Physics Letters*, vol. 97, no. 3, pp. 10–13, 2010.
- [156] B. Tian, T. Cohen-Karni, Q. Qing, X. Duan, P. Xie, and C. M. Lieber, “Three-Dimensional, Flexible Nanoscale Field-Effect Transistors as Localized Bioprobes,” *Science*, vol. 329, no. 5993, pp. 830–834, 2010.

Bibliography

- [157] X. Duan, R. Gao, P. Xie, T. Cohen-Karni, Q. Qing, H. S. Choe, B. Tian, X. Jiang, and C. M. Lieber, “Intracellular recordings of action potentials by an extracellular nanoscale field-effect transistor,” *Nature Nanotechnology*, vol. 7, no. 3, pp. 174–179, 2011.
- [158] Y. Zhao, S. S. You, A. Zhang, J.-H. Lee, J. Huang, and C. M. Lieber, “Scalable ultrasmall three-dimensional nanowire transistor probes for intracellular recording,” *Nature Nanotechnology*, vol. 14, pp. 783–790, 2019.
- [159] D. Braeken, D. Jans, R. Huys, A. Stassen, N. Collaert, L. Hoffman, W. Eberle, P. Peumans, and G. Callewaert, “Open-cell recording of action potentials using active electrode arrays,” *Lab on a Chip*, vol. 12, no. 21, p. 4397, 2012.
- [160] M. Dipalo, G. Melle, L. Lovato, A. Jacassi, F. Santoro, V. Caprettini, A. Schirato, A. Alabastri, D. Garoli, G. Bruno, F. Tantussi, and F. De Angelis, “Plasmonic meta-electrodes allow intracellular recordings at network level on high-density CMOS-multi-electrode arrays,” *Nature Nanotechnology*, vol. 13, no. 10, pp. 965–971, 2018.
- [161] S. F. Cogan, “Neural Stimulation and Recording Electrodes,” *Annual Review of Biomedical Engineering*, vol. 10, no. 1, pp. 275–309, 2008.
- [162] N. Shmoel, N. Rabieh, S. M. Ojovan, H. Erez, E. Maydan, and M. E. Spira, “Multisite electrophysiological recordings by self-assembled loose-patch-like junctions between cultured hippocampal neurons and mushroom-shaped microelectrodes,” *Scientific Reports*, vol. 6, no. 1, p. 27110, 2016.
- [163] D. Joseph, G. Henry, and H. Ronald, “Innovation in the pharmaceutical industry: New estimates of R&D costs,” *Journal of Health Economics*, vol. 47, pp. 20–33, 2016.
- [164] M. Hay, D. W. Thomas, J. L. Craighead, C. Economides, and J. Rosenthal, “Clinical development success rates for investigational drugs,” *Nature Biotechnology*, vol. 32, no. 1, pp. 40–51, 2014.
- [165] C. P. Wong, Y. Li, and K. S. Moon, *Nano-Bio-Electronic, Photonic and MEMS Packaging*. Springer, 2010.
- [166] A. Biswas, I. S. Bayer, A. S. Biris, T. Wang, E. Dervishi, and F. Faupel, “Advances in top-down and bottom-up surface nanofabrication: Techniques, applications & future prospects,” *Advances in Colloid and Interface Science*, vol. 170, no. 1-2, pp. 2–27, 2012.

-
- [167] H. Kim, H. B. R. Lee, and W. J. Maeng, “Applications of atomic layer deposition to nanofabrication and emerging nanodevices,” *Thin Solid Films*, vol. 517, no. 8, pp. 2563–2580, 2009.
- [168] L. C. Palmer and S. I. Stupp, “Molecular self-assembly into one-dimensional nanostructures,” *Accounts of Chemical Research*, vol. 41, no. 12, pp. 1674–1684, 2008.
- [169] H. Li, J. D. Carter, and T. H. LaBean, “Nanofabrication by DNA self-assembly,” *Materials Today*, vol. 12, no. 5, pp. 24–32, 2009.
- [170] A. K.-K. Wong, *Resolution Enhancement Techniques in Optical Lithography*. SPIE Publications, 2001.
- [171] Y. Chen, “Nanofabrication by electron beam lithography and its applications: A review,” *Microelectronic Engineering*, vol. 135, pp. 57–72, 2015.
- [172] Y. N. Xia and G. M. Whitesides, “Soft lithography,” *Annual Review Of Materials Science*, vol. 37, no. 5, pp. 551–575, 1998.
- [173] L. J. Guo, “Nanoimprint lithography: Methods and material requirements,” *Advanced Materials*, vol. 19, no. 4, pp. 495–513, 2007.
- [174] G. Villanueva, O. Vazquez-Mena, M. A. F. van den Boogaart, K. Sidler, K. Pataky, V. Savu, and J. Brugger, “Etching of sub-micrometer structures through stencil,” *Microelectronic Engineering*, vol. 85, pp. 1010–1014, 2008.
- [175] O. Vazquez-Mena, T. Sannomiya, L. G. Villanueva, J. Voros, and J. Brugger, “Metallic nanodot arrays by stencil lithography for plasmonic biosensing applications,” *ACS Nano*, vol. 5, no. 2, pp. 844–853, 2011.
- [176] K. Sidler, G. Villanueva, O. Vazquez-Mena, V. Savu, and J. Brugger, “Compliant membranes improve resolution in full-wafer micro/nanostencil lithography,” *Nanoscale*, vol. 4, pp. 773–778, 2012.
- [177] O. Vazquez Mena, T. Sannomiya, M. Tosun, G. Villanueva, A. V. Savu, J. Voros, and J. Brugger, “High-resolution resistless nanopatterning on polymer and flexible substrates for plasmonic biosensing using stencil masks,” *ACS Nano*, vol. 6, no. 6, pp. 5474–5481, 2012.
- [178] A. A. Tseng, A. Notargiacomo, and T. P. Chen, “Nanofabrication by scanning probe microscope lithography: A review,” *Journal of Vacuum Science & Technology B: Microelectronics and Nanometer Structures*, vol. 23, no. 3, p. 877, 2005.

Bibliography

- [179] B. D. Gates, Q. Xu, M. Stewart, D. Ryan, C. G. Willson, and G. M. Whitesides, “New approaches to nanofabrication: Molding, printing, and other techniques,” *Chemical Reviews*, vol. 105, no. 4, pp. 1171–1196, 2005.
- [180] F. Lenzmann, K. Li, A. H. Kitai, and H. D. Stöver, “Thin-Film Micropatterning Using Polymer Microspheres,” *Chemistry of Materials*, vol. 6, pp. 156–159, 1994.
- [181] J. Zhao, B. Frank, F. Neubrech, C. Zhang, P. V. Braun, and H. Giessen, “Hole-mask colloidal nanolithography combined with tilted-angle-rotation evaporation: A versatile method for fabrication of low-cost and large-area complex plasmonic nanostructures and metamaterials,” *Beilstein Journal of Nanotechnology*, vol. 5, no. 1, pp. 577–586, 2014.
- [182] H. J. Jeon, K. H. Kim, Y. K. Baek, D. W. Kim, and H. T. Jung, “New top-down approach for fabricating high-aspect-ratio complex nanostructures with 10 nm scale features,” *Nano Letters*, vol. 10, no. 9, pp. 3604–3610, 2010.
- [183] H.-J. Jeon, H.-W. Yoo, E. H. Lee, S. W. Jang, J.-S. Kim, J. K. Choi, and H.-T. Jung, “Fabrication of complex 3-dimensional patterned structures on a 10 nm scale from a single master pattern by secondary sputtering lithography,” *Nanoscale*, vol. 5, no. 6, p. 2358, 2013.
- [184] H. J. Jeon, H. S. Jeong, Y. H. Kim, W. B. Jung, J. Y. Kim, and H. T. Jung, “Fabrication of 10 nm-scale complex 3d nanopatterns with multiple shapes and components by secondary sputtering phenomenon,” *ACS Nano*, vol. 8, no. 2, pp. 1204–1212, 2014.
- [185] H. R. Zafarani, K. Mathwig, E. J. R. Sudhölter, and L. Rassaei, “Electrochemical redox cycling in a new nanogap sensor: Design and simulation,” *Journal of Electroanalytical Chemistry*, vol. 760, pp. 42–47, 2016.
- [186] M. A. G. Zevenbergen, P. S. Singh, E. D. Goluch, B. L. Wolfrum, and S. G. Lemay, “Stochastic sensing of single molecules in a nanofluidic electrochemical device,” *Nano Letters*, vol. 11, no. 7, pp. 2881–2886, 2011.
- [187] B. Wolfrum, M. Zevenbergen, and S. Lemay, “Nanofluidic redox cycling amplification for the selective detection of catechol,” *Analytical Chemistry*, vol. 80, no. 4, pp. 972–977, 2008.
- [188] H. Becker, K. Lowack, and A. Manz, “Planar quartz chips with submicron channels for two-dimensional capillary electrophoresis applications,” *Journal of Micromechanics and Microengineering*, vol. 8, no. 1, pp. 24–28, 1998.

-
- [189] H. Im, K. C. Bantz, N. C. Lindquist, C. L. Haynes, and S. H. Oh, “Vertically oriented sub-10-nm plasmonic nanogap arrays,” *Nano Letters*, vol. 10, no. 6, pp. 2231–2236, 2010.
- [190] S. Passinger, M. S. M. Saifullah, C. Reinhardt, K. R. V. Subramanian, B. N. Chichkov, and M. E. Welland, “Direct 3D patterning of TiO₂ using femtosecond laser pulses,” *Advanced Materials*, vol. 19, no. 9, pp. 1218–1221, 2007.
- [191] A. Timmis, N. Townsend, C. Gale, R. Grobbee, N. Maniadakis, M. Flather, E. Wilkins, L. Wright, R. Vos, J. Bax, M. Blum, F. Pinto, and P. Vardas, “European Society of Cardiology: Cardiovascular disease statistics 2017,” *European Heart Journal*, vol. 39, no. 7, pp. 508–577, 2018.
- [192] D. P. Zipes, J. Jalife, and W. G. Stevenson, *Cardiac Electrophysiology : from Cell to Bedside*. Elsevier, 2013.
- [193] B. Sakmann and E. Neher, “Patch Clamp Techniques for Studying Ionic Channels in Excitable Membranes,” *Annual Review of Physiology*, vol. 46, no. 1, pp. 455–472, 1984.
- [194] S. Rohr and J. P. Kucera, “Optical recording system based on a fiber optic image conduit: Assessment of microscopic activation patterns in cardiac tissue,” *Biophysical Journal*, vol. 75, no. 2, pp. 1062–1075, 1998.
- [195] J. P. Kucera, M. O. Heuschkel, P. Renaud, and S. Rohr, “Power-law behavior of beat-rate variability in monolayer cultures of neonatal rat ventricular myocytes,” *Circulation research*, vol. 86, no. 11, pp. 1140–1145, 2000.
- [196] C. O’Shea, A. P. Holmes, J. Winter, J. Correia, X. Ou, R. Dong, S. He, P. Kirchhof, L. Fabritz, K. Rajpoot, and D. Pavlovic, “Cardiac optogenetics and optical mapping – Overcoming spectral congestion in all-optical cardiac electrophysiology,” *Frontiers in Physiology*, vol. 10, p. 182, 2019.
- [197] M. Dipalo, A. F. McGuire, H. Y. Lou, V. Caprettini, G. Melle, G. Bruno, C. Lubrano, L. Matino, X. Li, F. De Angelis, B. Cui, and F. Santoro, “Cells Adhering to 3D Vertical Nanostructures: Cell Membrane Reshaping without Stable Internalization,” *Nano Letters*, vol. 18, no. 9, pp. 6100–6105, 2018.
- [198] B. X. E. Desbiolles, A. Bertsch, and P. Renaud, “Ion beam etching redeposition for 3D multimaterial nanostructure manufacturing,” *Microsystems & Nanoengineering*, vol. 5, p. 11, 2019.

Bibliography

- [199] C. Ziegler, *Cell-based Biosensors*, vol. 366. Springer, 2000.
- [200] A. Héduit, I. Quinio, D. Stadmuller, and D. R. Thévenot, “Modified platinum electrodes: electrochemical characteristics and behaviour in activated sludge,” *Wat. Sci, Tech*, vol. 34, no. 4, pp. 143–150, 1996.
- [201] S. H. Lee and J. C. Rasaiah, “Proton transfer and the diffusion of H⁺ and OH⁻ ions along water wires,” *Journal of Chemical Physics*, vol. 139, no. 12, p. 124507, 2013.
- [202] T. Korhonen, S. L. Hänninen, and P. Tavi, “Model of excitation-contraction coupling of rat neonatal ventricular myocytes,” *Biophysical Journal*, vol. 96, no. 3, pp. 1189–1209, 2009.
- [203] S. Rohr, M. Schölly, and A. G. Kléber, “Patterned Growth of Neonatal Rat Heart Cells in Culture,” *Circulation research*, vol. 68, no. 1, pp. 114–130, 1991.
- [204] F. Heer, W. Franks, A. Blau, S. Taschini, C. Ziegler, A. Hierlemann, and H. Baltes, “CMOS microelectrode array for the monitoring of electrogenic cells,” *Biosensors and Bioelectronics*, vol. 20, no. 2, pp. 358–366, 2004.
- [205] G. Voskerician, M. S. Shive, R. S. Shawgo, H. Von Recum, J. M. Anderson, M. J. Cima, and R. Langer, “Biocompatibility and biofouling of MEMS drug delivery devices,” *Biomaterials*, vol. 24, no. 11, pp. 1959–1967, 2003.
- [206] M. Miragoli, N. Salvarani, and S. Rohr, “Myofibroblasts induce ectopic activity in cardiac tissue,” *Circulation Research*, vol. 101, no. 8, pp. 755–758, 2007.
- [207] T. Li and W. Hu, “Electrochemistry in nanoscopic volumes,” *Nanoscale*, vol. 3, no. 1, pp. 166–176, 2011.
- [208] P. Actis, S. Tokar, J. Clausmeyer, B. Babakinejad, S. Mikhaleva, R. Cornut, Y. Takahashi, A. López Córdoba, P. Novak, A. I. Shevchuck, J. A. Dougan, S. G. Kazarian, P. V. Gorelkin, A. S. Erofeev, I. V. Yaminsky, P. R. Unwin, W. Schuhmann, D. Klenerman, D. A. Rusakov, E. V. Sviderskaya, and Y. E. Korchev, “Electrochemical nanopores for single-cell analysis,” *ACS Nano*, vol. 8, no. 1, pp. 875–884, 2014.
- [209] L. A. Baker, “Perspective and Prospectus on Single-Entity Electrochemistry,” *Journal of the American Chemical Society*, vol. 140, no. 46, pp. 15549–15559, 2018.

-
- [210] S. Rohr, R. Flückiger-Labrada, and J. P. Kucera, “Photolithographically defined deposition of attachment factors as a versatile method for patterning the growth of different cell types in culture,” *Pflügers Archiv European Journal of Physiology*, vol. 446, no. 1, pp. 125–132, 2003.
- [211] R. Stämpfli, “Reversible electrical breakdown of the excitable membrane of a Ranvier node,” *Anais da Academia Brasileira de Ciências*, vol. 30, pp. 57–63, 1958.
- [212] A. J. Sale and W. A. Hamilton, “Effects of high electric fields on microorganisms. I. Killing of bacteria and yeasts,” *BBA - General Subjects*, vol. 148, no. 3, pp. 781–788, 1967.
- [213] T. Kotnik, W. Frey, M. Sack, S. Haberl Meglič, M. Peterka, and D. Miklavčič, “Electroporation-based applications in biotechnology,” *Trends in Biotechnology*, vol. 33, no. 8, pp. 480–488, 2015.
- [214] M. S. M. Andrei G. Pakhomov, Damijan Miklavcic, *Advanced Electroporation Techniques in Biology and Medicine*. CRC Press Book, 2010.
- [215] E. Neumann, M. Schaefer-Ridder, Y. Wang, and P. Hofschneider, “Gene transfer into mouse lyoma cells by electroporation in high electric fields,” *The EMBO Journal*, vol. 1, no. 7, pp. 841–845, 1982.
- [216] T. K. Wong and E. Neumann, “Electric field mediated gene transfer,” *Biochemical and Biophysical Research Communications*, vol. 107, no. 2, pp. 584–587, 1982.
- [217] F. André and L. M. Mir, “DNA electrotransfer: Its principles and an updated review of its therapeutic applications,” *Gene Therapy*, vol. 11, pp. 33–42, 2004.
- [218] Y. Zhan, C. Sun, Z. Cao, N. Bao, J. Xing, and C. Lu, “Release of intracellular proteins by electroporation with preserved cell viability,” *Analytical Chemistry*, vol. 84, no. 19, pp. 8102–8105, 2012.
- [219] C. T. S. Ching, L. S. Fu, T. P. Sun, T. H. Hsu, and K. M. Chang, “Use of electroporation and reverse iontophoresis for extraction of transdermal multi-biomarkers,” *International Journal of Nanomedicine*, vol. 7, pp. 885–894, 2012.
- [220] M. Sack, J. Sigler, S. Frenzel, C. Eing, J. Arnold, T. Michelberger, W. Frey, F. Attmann, L. Stukenbrock, and G. Müller, “Research on industrial-scale electroporation devices fostering the extraction of substances from biological tissue,” *Food Engineering Reviews*, vol. 2, no. 2, pp. 147–156, 2010.

Bibliography

- [221] L. M. Mir and S. Orlowski, “Mechanisms of electrochemotherapy,” *Advanced Drug Delivery Reviews*, vol. 35, no. 1, pp. 107–118, 1999.
- [222] M. J. Jaroszeski, R. Gilbert, and R. Heller, “Electrochemotherapy: An emerging drug delivery method for the treatment of cancer,” *Advanced Drug Delivery Reviews*, vol. 26, no. 2-3, pp. 185–197, 1997.
- [223] R. Heller, R. Gilbert, and M. J. Jaroszeski, “Clinical applications of electrochemotherapy,” *Advanced Drug Delivery Reviews*, vol. 35, no. 1, pp. 119–129, 1999.
- [224] X. Yajuan, L. Xin, and L. Zhiyuan, “A Comparison of the Performance and Application Differences Between Manual and Automated Patch-Clamp Techniques,” *Current Chemical Genomics*, vol. 6, pp. 87–92, 2013.
- [225] J. T. Robinson, M. Jorgolli, and H. Park, “Nanowire electrodes for high-density stimulation and measurement of neural circuits,” *Frontiers in Neural Circuits*, vol. 7, p. 38, 2013.
- [226] B. X. Desbiolles, E. De Coulon, A. Bertsch, S. Rohr, and P. Renaud, “Intracellular Recording of Cardiomyocyte Action Potentials with Nanopatterned Volcano-Shaped Microelectrode Arrays,” *Nano Letters*, vol. 19, no. 9, pp. 6173–6181, 2019.
- [227] R. Milo and R. Phillips, *Cell Biology by the Numbers*. CRC Press Book, 2015.
- [228] O. Tovar and L. Tung, “Electroporation and recovery of cardiac cell membrane with rectangular voltage pulses,” *American Journal of Physiology - Heart and Circulatory Physiology*, vol. 263, no. 4, pp. 1128–1136, 1992.
- [229] Y. Zhang, “Cell toxicity mechanism and biomarker,” *Clinical and Translational Medicine*, vol. 7, no. 1, p. 34, 2018.
- [230] M. Reberšek, “Beyond electroporation pulse parameters: From application to evaluation,” in *Handbook of Electroporation*, vol. 2, pp. 977–997, Springer, 2017.
- [231] F. Santoro, S. Dasgupta, J. Schnitker, T. Auth, E. Neumann, G. Panaitov, G. Gompper, A. Offenhä, and A. Offenhäusser, “Interfacing Electrogenic Cells with 3D Nanoelectrodes: Position, Shape, and Size Matter,” *ACS Nano*, vol. 8, no. 7, pp. 6713–6723, 2014.
- [232] M. Miragoli, G. Gaudesius, and S. Rohr, “Electrotonic modulation of cardiac impulse conduction by myofibroblasts,” *Circulation Research*, vol. 98, no. 6, pp. 801–810, 2006.

-
- [233] D. D. Carlo, L. Y. Wu, and L. P. Lee, “Dynamic single cell culture array,” *Lab on a Chip*, vol. 6, no. 11, pp. 1445–1449, 2006.
- [234] F. Yesilkoy, R. Ueno, B. X. E. Desbiolles, M. Grisi, Y. Sakai, B. J. Kim, and J. Brugger, “Highly efficient and gentle trapping of single cells in large microfluidic arrays for time-lapse experiments,” *Biomicrofluidics*, vol. 10, no. 1, p. 014120, 2016.
- [235] B. D. Hoffman, C. Grashoff, and M. A. Schwartz, “Dynamic molecular processes mediate cellular mechanotransduction,” *Nature*, vol. 475, no. 7356, pp. 316–323, 2011.
- [236] J. Howard, S. W. Grill, and J. S. Bois, “Turing’s next steps: The mechanochemical basis of morphogenesis,” *Nature Reviews Molecular Cell Biology*, vol. 12, no. 6, pp. 400–406, 2011.
- [237] A. Brugués, E. Anon, V. Conte, J. H. Veldhuis, M. Gupta, J. Colombelli, J. J. Muñoz, G. W. Brodland, B. Ladoux, and X. Trepat, “Forces driving epithelial wound healing,” *Nature Physics*, vol. 10, no. 9, pp. 683–690, 2014.
- [238] N. I. Petridou, Z. Spiró, and C. P. Heisenberg, “Multiscale force sensing in development,” *Nature Cell Biology*, vol. 19, no. 6, pp. 581–588, 2017.
- [239] G. Binnig, C. F. Quate, and C. Gerber, “Atomic force microscope,” *Physical Review Letters*, vol. 56, no. 9, pp. 930–933, 1986.
- [240] M. Radmacher, R. W. Tillmann, and H. E. Gaub, “Imaging viscoelasticity by force modulation with the atomic force microscope,” *Biophysical Journal*, vol. 64, no. 3, pp. 735–742, 1993.
- [241] M. Radmacher, R. W. Tillmann, M. Fritz, and H. E. Gaub, “From molecules to cells: Imaging soft samples with the atomic force microscope,” *Science*, vol. 257, no. 5078, pp. 1900–1905, 1992.
- [242] R. Matzke, K. Jacobson, and M. Radmacher, “Direct, high-resolution measurement of furrow stiffening during division of adherent cells,” *Nature Cell Biology*, vol. 3, no. 6, pp. 607–610, 2001.
- [243] S. Iyer, R. M. Gaikwad, V. Subba-Rao, C. D. Woodworth, and I. Sokolov, “Atomic force microscopy detects differences in the surface brush of normal and cancerous cells,” *Nature Nanotechnology*, vol. 4, no. 6, pp. 389–393, 2009.

Bibliography

- [244] S. E. Cross, Y. S. Jin, J. Rao, and J. K. Gimzewski, “Nanomechanical analysis of cells from cancer patients,” *Nature Nanotechnology*, vol. 2, no. 12, pp. 780–783, 2007.
- [245] M. B. Viani, T. E. Schäffer, A. Chand, M. Rief, H. E. Gaub, and P. K. Hansma, “Small cantilevers for force spectroscopy of single molecules,” *Journal of Applied Physics*, vol. 86, no. 4, pp. 2258–2262, 1999.
- [246] P. R. Laskowski, M. Pfreunds Schuh, M. Stauffer, Z. Ucurum, D. Fotiadis, and D. J. Müller, “High-Resolution Imaging and Multiparametric Characterization of Native Membranes by Combining Confocal Microscopy and an Atomic Force Microscopy-Based Toolbox,” *ACS Nano*, vol. 11, no. 8, pp. 8292–8301, 2017.
- [247] E. Moeendarbary, L. Valon, M. Fritzsche, A. R. Harris, D. A. Moulding, A. J. Thrasher, E. Stride, L. Mahadevan, and G. T. Charras, “The cytoplasm of living cells behaves as a poroelastic material,” *Nature Materials*, vol. 12, no. 3, pp. 253–261, 2013.
- [248] J. H. Hoh and C. A. Schoenenberger, “Surface morphology and mechanical properties of MDCK monolayers by atomic force microscopy,” *Journal of Cell Science*, vol. 107, no. 5, pp. 1105–1114, 1994.
- [249] C. Rotsch, F. Braet, E. Wisse, and M. Radmacher, “AFM imaging and elasticity measurements on living rat liver macrophages,” *Cell Biology International*, vol. 21, no. 11, pp. 685–696, 1997.
- [250] C. Rotsch, K. Jacobson, and M. Radmacher, “Dimensional and mechanical dynamics of active and stable edges in motile fibroblasts investigated by using atomic force microscopy,” *Proceedings of the National Academy of Sciences of the United States of America*, vol. 96, no. 3, pp. 921–926, 1999.
- [251] C. Rotsch and M. Radmacher, “Drug-induced changes of cytoskeletal structure and mechanics in fibroblasts: An atomic force microscopy study,” *Biophysical Journal*, vol. 78, no. 1, pp. 520–535, 2000.
- [252] C. Blaue, J. Kashef, and C. M. Franz, “Cadherin-11 promotes neural crest cell spreading by reducing intracellular tension—Mapping adhesion and mechanics in neural crest explants by atomic force microscopy,” *Seminars in Cell and Developmental Biology*, vol. 73, pp. 95–106, 2018.
- [253] J. Domke, W. J. Parak, M. George, H. E. Gaub, and M. Radmacher, “Mapping the mechanical pulse of single cardiomyocytes with the atomic force microscope,” *European Biophysics Journal*, vol. 28, no. 3, pp. 179–186, 1999.

-
- [254] W. T. Chang, D. Yu, Y. C. Lai, K. Y. Lin, and I. Liau, “Characterization of the mechanodynamic response of cardiomyocytes with atomic force microscopy,” *Analytical Chemistry*, vol. 85, no. 3, pp. 1395–1400, 2013.
- [255] A. J. Engler, M. A. Griffin, S. Sen, C. G. Bönnemann, H. L. Sweeney, and D. E. Discher, “Myotubes differentiate optimally on substrates with tissue-like stiffness : pathological implications for soft or stiff microenvironments,” *Journal of Cell Biology*, vol. 166, no. 6, pp. 877–887, 2004.
- [256] A. J. Engler, S. Sen, H. L. Sweeney, and D. E. Discher, “Matrix Elasticity Directs Stem Cell Lineage Specification,” *Cell*, vol. 126, no. 4, pp. 677–689, 2006.
- [257] L. Liu, Z. You, H. Yu, L. Zhou, H. Zhao, X. Yan, D. Li, B. Wang, L. Zhu, Y. Xu, T. Xia, Y. Shi, C. Huang, W. Hou, and Y. Du, “Mechanotransduction-modulated fibrotic microniches reveal the contribution of angiogenesis in liver fibrosis,” *Nature Materials*, vol. 16, no. 12, pp. 1252–1261, 2017.
- [258] P. D. Odermatt, M. T. M. Hannebelle, H. A. Eskandarian, A. P. Nievergelt, J. D. McKinney, and G. E. Fantner, “Overlapping and essential roles for molecular and mechanical mechanisms in mycobacterial cell division,” *Nature Physics*, vol. 16, pp. 57–62, 2020.
- [259] R. Saar Dover, A. Bitler, E. Shimoni, P. Trieu-Cuot, and Y. Shai, “Multiparametric AFM reveals turgor-responsive net-like peptidoglycan architecture in live streptococci,” *Nature Communications*, vol. 6, pp. 1–10, 2015.
- [260] P. Herman-Bausier, C. Valotteau, G. Pietrocola, S. Rindi, D. Alsteens, T. J. Foster, P. Speziale, and Y. F. Dufrêne, “Mechanical strength and inhibition of the *Staphylococcus aureus* collagen-binding protein Cna,” *mBio*, vol. 7, no. 5, pp. 01529–16, 2016.
- [261] D. Mohammed, M. Versaevel, C. Bruyère, L. Alaimo, M. Luciano, E. Vercruysse, A. Procès, and S. Gabriele, “Innovative tools for mechanobiology: Unraveling outside-in and inside-out mechanotransduction,” *Frontiers in Bioengineering and Biotechnology*, vol. 7, p. 162, 2019.
- [262] G. Caluori, J. Pribyl, V. Cmiel, M. Pesl, T. Potocnak, I. Provaznik, P. Skladal, and V. Rotrekl, “Simultaneous study of mechanobiology and calcium dynamics on hESC-derived cardiomyocytes clusters,” *Journal of Molecular Recognition*, vol. 32, no. 2, p. 2760, 2019.

Bibliography

- [263] B. M. Gaub and D. J. Müller, “Mechanical Stimulation of Piezo1 Receptors Depends on Extracellular Matrix Proteins and Directionality of Force,” *Nano Letters*, vol. 17, no. 3, pp. 2064–2072, 2017.
- [264] J. F. Cogollo, M. Tedesco, S. Martinoia, and R. Raiteri, “A new integrated system combining atomic force microscopy and micro-electrode array for measuring the mechanical properties of living cardiac myocytes,” *Biomedical Microdevices*, vol. 13, no. 4, pp. 613–621, 2011.
- [265] J. Tian, C. Tu, B. Huang, Y. Liang, J. Zhou, and X. Ye, “Study of the union method of microelectrode array and AFM for the recording of electromechanical activities in living cardiomyocytes,” *European Biophysics Journal*, vol. 46, no. 5, pp. 495–507, 2017.
- [266] K. V. Upadhye, J. E. Candiello, L. A. Davidson, and H. Lin, “Whole-cell electrical activity under direct mechanical stimulus by AFM cantilever using planar patch clamp chip approach,” *Cellular and Molecular Bioengineering*, vol. 4, no. 2, pp. 270–280, 2011.
- [267] E. Pamir, M. George, N. Fertig, and M. Benoit, “Planar patch-clamp force microscopy on living cells,” *Ultramicroscopy*, vol. 108, no. 6, pp. 552–557, 2008.
- [268] A. Meister, M. Gabi, P. Behr, P. Studer, J. Vörös, P. Niedermann, J. Bitterli, J. Polesel-Maris, M. Liley, H. Heinzelmann, and T. Zambelli, “FluidFM: Combining atomic force microscopy and nanofluidics in a universal liquid delivery system for single cell applications and beyond,” *Nano Letters*, vol. 9, no. 6, pp. 2501–2507, 2009.
- [269] O. Guillaume-Gentil, E. Potthoff, D. Ossola, C. M. Franz, T. Zambelli, and J. A. Vorholt, “Force-controlled manipulation of single cells: From AFM to FluidFM,” *Trends in Biotechnology*, vol. 32, no. 7, pp. 381–388, 2014.
- [270] D. Ossola, M.-Y. Amarouch, P. Behr, J. Vo Ro S, H. Abriel, and T. Zambelli, “Force-Controlled Patch Clamp of Beating Cardiac Cells,” *Nano Letters*, vol. 15, pp. 1743–1750, 2015.
- [271] J. E. Linley, “Perforated whole-cell patch-clamp recording,” *Methods in Molecular Biology*, vol. 998, pp. 149–157, 2013.
- [272] B. X. Desbiolles, E. De Coulon, N. Maino, A. Bertsch, S. Rohr, and P. Renaud, “Nanovolcano-microelectrode-arrays: Controlled electroporation enables long-term on-demand registration of transmembrane action potentials,” *Submitted*, 2020.

-
- [273] P. K. Hansma, B. Drake, D. Grigg, C. B. Prater, F. Yashar, G. Gurley, V. Elings, S. Feinstein, and R. Lal, “A new, optical-lever based atomic force microscope,” *Journal of Applied Physics*, vol. 76, no. 2, pp. 796–799, 1994.
- [274] N. Huebsch, P. Loskill, M. A. Mandegar, N. C. Marks, A. S. Sheehan, Z. Ma, A. Mathur, T. N. Nguyen, J. C. Yoo, L. M. Judge, C. I. Spencer, A. C. Chukka, C. R. Russell, P. L. So, B. R. Conklin, and K. E. Healy, “Automated video-based analysis of contractility and calcium flux in human-induced pluripotent stem cell-derived cardiomyocytes cultured over different spatial scales,” *Tissue Engineering - Part C: Methods*, vol. 21, no. 5, pp. 467–479, 2015.
- [275] P. Hoang, S. Jacquir, S. Lemus, and Z. Ma, “Quantification of Contractile Dynamic Complexities Exhibited by Human Stem Cell-Derived Cardiomyocytes Using Nonlinear Dimensional Analysis,” *Scientific Reports*, vol. 9, no. 1, p. 14714, 2019.
- [276] A. Lugstein, E. Bertagnolli, C. Kranz, A. Kueng, and B. Mizaikoff, “Integrating micro- and nanoelectrodes into atomic force microscopy cantilevers using focused ion beam techniques,” *Applied Physics Letters*, vol. 81, no. 2, pp. 349–351, 2002.
- [277] J. Shimada and T. Kaneko, “Development of Single Cardiomyocyte Measurement of Extracellular Potential,” *Biophysical Journal*, vol. 110, no. 3, p. 169, 2016.
- [278] J. Rothe, O. Frey, R. Madangopal, J. Rickus, and A. Hierlemann, “Robust functionalization of large microelectrode arrays by using pulsed potentiostatic deposition,” *Sensors*, vol. 17, no. 1, p. 22, 2017.
- [279] P. D. Odermatt, A. Shivanandan, H. Deschout, R. Jankele, A. P. Nievergelt, L. Feletti, M. W. Davidson, A. Radenovic, and G. E. Fantner, “High-Resolution Correlative Microscopy: Bridging the Gap between Single Molecule Localization Microscopy and Atomic Force Microscopy,” *Nano Letters*, vol. 15, no. 8, pp. 4896–4904, 2015.
- [280] D. Nečas and P. Klapetek, “Gwyddion: An open-source software for SPM data analysis,” *Central European Journal of Physics*, vol. 10, no. 1, pp. 181–188, 2012.
- [281] S. Shoham, D. H. O’Connor, and R. Segev, “How silent is the brain: Is there a “dark matter” problem in neuroscience?,” *Journal of Comparative Physiology A: Neuroethology, Sensory, Neural, and Behavioral Physiology*, vol. 192, no. 8, pp. 777–784, 2006.

Bibliography

- [282] World Health Organization, “Neurological disorders: a public health approach,” tech. rep., 2006.
- [283] W. Akemann, H. Mutoh, A. Perron, J. Rossier, and T. Knöpfel, “Imaging brain electric signals with genetically targeted voltage-sensitive fluorescent proteins,” *Nature Methods*, vol. 7, no. 8, pp. 643–649, 2010.
- [284] L. Jin, Z. Han, J. Platisa, J. R. Wooldorton, L. B. Cohen, and V. A. Pieribone, “Single Action Potentials and Subthreshold Electrical Events Imaged in Neurons with a Fluorescent Protein Voltage Probe,” *Neuron*, vol. 75, no. 5, pp. 779–785, 2012.
- [285] D. S. Peterka, H. Takahashi, and R. Yuste, “Imaging Voltage in Neurons,” *Neuron*, vol. 69, no. 1, pp. 9–21, 2011.
- [286] A. Fendyur, N. Mazurski, J. Shappir, and M. E. Spira, “Formation of Essential Ultrastructural Interface between Cultured Hippocampal Cells and Gold Mushroom-Shaped MEA- Toward ‘IN-CELL’ Recordings from Vertebrate Neurons,” *Frontiers in Neuroengineering*, vol. 4, p. 14, 2011.
- [287] G. A. Banker and W. M. Cowan, “Rat hippocampal neurons in dispersed cell culture,” *Brain Research*, vol. 126, no. 3, pp. 397–425, 1977.
- [288] M. L. Seibenhener and M. W. Wooten, “Isolation and culture of hippocampal neurons from prenatal mice,” *Journal of visualized experiments : JoVE*, no. 65, pp. 1–7, 2012.
- [289] K. Walczuch, P. Renze, C. Ingensiep, R. Degen, T. P. Bui, U. Schnakenberg, P. Bräunig, and K. Bui-Göbbels, “A new microfluidic device design for a defined positioning of neurons in vitro,” *Biomicrofluidics*, vol. 11, no. 4, p. 044103, 2017.
- [290] F. T. Jaber, F. H. Labeed, and M. P. Hughes, “Action potential recording from dielectrophoretically positioned neurons inside micro-wells of a planar micro-electrode array,” *Journal of Neuroscience Methods*, vol. 182, no. 2, pp. 225–235, 2009.
- [291] P. Steiner, J. C. Floyd Sarria, L. Glauser, S. Magnin, S. Catsicas, and H. Hirling, “Modulation of receptor cycling by neuron-enriched endosomal protein of 21 kD,” *Journal of Cell Biology*, vol. 157, no. 7, pp. 1197–1209, 2002.
- [292] G. M. Beaudoin, S. H. Lee, D. Singh, Y. Yuan, Y. G. Ng, L. F. Reichardt, and J. Arikath, “Culturing pyramidal neurons from the early postnatal mouse hippocampus and cortex,” *Nature Protocols*, vol. 7, no. 9, pp. 1741–1754, 2012.

- [293] S. S. Varricchio, H. Cyrille, B. Arnaud, and R. Philippe, “Fabrication of multilayered nanofluidic membranes through silicon templates,” *Nanoscale*, vol. 7, no. 48, pp. 20451–20459, 2015.
- [294] S. S. Varricchio, N. Piacentini, A. Bertsch, and P. Renaud, “Multimaterial Nanoporous Membranes Shaped through High Aspect-Ratio Sacrificial Silicon Nanostructures,” *ACS Omega*, vol. 2, no. 6, pp. 2387–2394, 2017.
- [295] A. Zani and A. Proverbio, *Cognitive Electrophysiology of Mind and Brain*. Academic Press, 2003.
- [296] D. Floreano and C. Mattiussi, *Bio-Inspired Artificial Intelligence*. The MIT Press, 2008.
- [297] D. O. Hebb, *The Organization of Behavior*. Wiley, 1949.
- [298] F. Jousset, A. Maguy, S. Rohr, and J. P. Kucera, “Myofibroblasts electrotonically coupled to cardiomyocytes alter conduction: Insights at the cellular level from a detailed in silico tissue structure model,” *Frontiers in Physiology*, vol. 7, pp. 1–23, 2016.

List of publications

Publications related to this thesis

- ◇ **B.X.E. Desbiolles**, A. Bertsch, and P. Renaud; “Ion beam etching redeposition for 3D multimaterial nanostructures,” *Microsystems and Nanoengineering*, vol. 9, p. 11, 2019.
- ◇ **B.X.E. Desbiolles**, E. de Coulon, A. Bertsch, S. Rohr, and P. Renaud, “Intracellular recording of cardiomyocyte action potentials with nanopatterned volcano-shaped microelectrode arrays,” *Nano Letters*, vol. 19, no. 9, pp. 6173–6181, 2019.
- ◇ **B.X.E. Desbiolles**^{*}, E. de Coulon,^{*} N. Maino, A. Bertsch, S. Rohr, and P. Renaud, “Nanovolcano-microelectrode-arrays: Controlled electroporation enables long-term on-demand registration of transmembrane action potentials,” *Under review in Microsystems and Nanoengineering*, 2020.
- ◇ **B.X.E. Desbiolles**, M.T.M. Hannebelle, E. de Coulon, A. Bertsch, S. Rohr, G.E. Fantner, and P. Renaud, “Volcano-shaped SPM probe for combined force-electrogram recordings from excitable cells,” *Submitted*, 2020.

Publications non-related to this thesis

- ◇ F. Yesilkoy, R. Ueno, **B.X.E. Desbiolles**, M. Grisi, Y. Sakai, B. J. Kim, and J. Brugger, “Highly efficient and gentle trapping of single cells in large microfluidic arrays for time-lapse experiments,” *Biomicrofluidics*, vol. 10, no. 1, p. 014120, 2016.
- ◇ **B.X.E. Desbiolles**, G. Furlan, A.M. Schwartzberg, P.D. Ashby, and D. Ziegler, “Electrostatically actuated encased cantilevers,” *Beilstein Journal of Nanotechnology*, vol. 9, pp. 1381–1389, 2018.

Bibliography

- ◇ C. Raillon, J. Che, S. Thill, M. Duchamp, **B.X.E. Desbiolles**, A. Millet, E. Sollier-Christen, and P. Renaud; “Towards microfluidic label-free isolation and enumeration of circulating tumor cells from blood samples,” *Cytometry Part A*, vol. 95, no. 10, pp. 1085-1095, 2019.

Conference proceedings

- ◇ **B.X.E. Desbiolles**, A. Bertsch, and P. Renaud; “A simple method for 3D multimaterial nanostructure manufacturing,” *MicroTAS 2019*, Basel (Switzerland), 2019.
- ◇ **B.X.E. Desbiolles**, E. de Coulon, A. Bertsch, S. Rohr, and P. Renaud, “Intracellular recording of cardiomyocyte action potentials with nanopatterned volcano-shaped microelectrode arrays,” *NanoBioTech-Montreux*, Montreux (Switzerland), 2019.



Benoît DESBIOLLES

PhD Student



ADDRESS

Avenue de la Harpe 20B
CH - 1007 Lausanne
Switzerland



OFFICE

EPFL-STI-IMT-LMIS4
BM3124 (Bâtiment BM)
Station 17
CH - 1015 Lausanne
Switzerland



EMAIL

be.desbiolles@gmail.com



PHONE

+33 6 18 54 77 56



DATE OF BIRTH

August 31st, 1992



NATIONALITY

French



SCHOLAR ID

Benoît Desbiolles



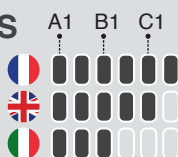
ORCID

0000-0001-6848-3289



LANGUAGES

French
English
Italian



REFERENCES

Prof. Philippe Renaud
philippe.renaud@epfl.ch

Prof. Stephan Rohr
rohr@pyl.unibe.ch

EDUCATION

◆ Ph. D. in Microsystems for life-sciences

Microsystems laboratory, Prof. P. Renaud
Ecole Polytechnique Fédérale de Lausanne (EPFL), Switzerland
Microsystems and Microelectronics Doctoral School
January 2016 - May 2020



◆ Nanoscale patterning of 3D microelectrode arrays for long-term intracellular electrophysiology

- Nanofabrication of 3D multimaterial nanostructures at wafer-scale
- Intracellular electrophysiology from neural networks and cardiomyocyte monolayers

◆ B. Sc. and M. Sc. in Microengineering

Lawrence Berkeley National Laboratory (LBNL), USA
Ecole Polytechnique Fédérale de Lausanne (EPFL), Switzerland
September 2010 - November 2015



Master EFPL-LBNL (*September 2013 - November 2015*):

- ◆ Major: Micro- and nanosystems
 - Master thesis: "Shielded and low-damping SPM probes for quantitative electrical and electrochemical characterization." D. Ziegler, P. Ashby, Prof. Renaud
 - Master internship: "Reflectometric module in a point of care biosensor." Qloudlab
 - Master semester project II: "Microfluidic cell-trapping structures for single-cell analysis." Prof. Brugger
 - Master semester project I: "Electrode arrays for fibrin sensing via smartphone's touchscreen." Prof. Renaud
 - Topics: Advanced MEMS, BioMEMS, Microfabrication, Nanotechnology, Flexible bioelectronics, Optics
 - **GPA:5.89/6**
- ◆ Minor: Biomedical technologies
 - Minor project: "3D Micropatterned stretchable electrode for biomedical applications" Prof. Brugger
 - Topics: Cellular biology and biochemistry, Neuroscience, Immunology, Cardiovascular system, Biomaterials, Biomicroscopy, Biosensors
 - **GPA:5.52/6**

Bachelor EPFL (*September 2010 - June 2013*):

- Topics: General Physics, Chemistry, Mathematics, Mechanics, Optics, Materials, Electronics, Microelectronics, Signal processing, Microinformatics, Programming, Industrialisation
- **GPA:5.16/6**

Skills

Micro-Nanoengineering

Biosensing

Electronics

Micro-Nanofabrication

- Thin film deposition
- Photolithography
- E-beam lithography
- Wet and dry etching
- Soft lithography
- Metrology:
SEM, FIB, SPM, EDX

Electrophysiology

- Multielectrode arrays
- Cell-electrode interface
- Cardiomyocytes
monolayers culture
- Neural networks culture

Biomicroscopy

- Wide-field fluorescence
microscopy
- Confocal microscopy

Interfacing

- PCB design
- Mechanical design
- Wire-bonding

Signal processing

Microinformatics and

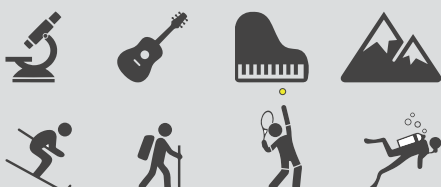
Programming

- Matlab
- C, C++
- Assembler

Optics and Photonics

Flexible electronics

Interests



PUBLICATIONS

- ◆ B.X.E. Desbiolles et al., “Nanovolcano-microelectrode-arrays: Controlled electro-poration enables long-term on-demand registration of transmembrane action potentials”, *Under review in Microsystems and Nanoengineering*, 2020.
- ◆ B.X.E. Desbiolles et al., “Volcano-shaped SPM probe for combined force-electrogram recordings from excitable cells”, *Submitted*, 2020.
- ◆ B.X.E. Desbiolles et al., “Intracellular recording of cardiomyocyte action potentials with nanopatterned volcano-shaped microelectrode arrays.”, *Nano Letters*, 2019.
- ◆ C. Raillon et al., “Towards microfluidic label-free isolation and enumeration of circulating tumor cells from blood samples.”, *Cytometry Part A*, 2019.
- ◆ B.X.E. Desbiolles et al., “Ion beam etching for 3D multimaterial nanostructures manufacturing.”, *Microsystems and Nanoengineering*, 2019.
- ◆ B.X.E. Desbiolles et al., “Electrostatically actuated encased cantilevers.”, *Beilstein Journal of Nanotechnology*, 2018.
- ◆ F. Yesilkoy et al., “Highly efficient and gentle trapping of single cells in large microfluidic arrays for time-lapse experiments.”, *Biomicrofluidics*, 2016.

CONFERENCES

Talks:

- ◆ B.X.E. Desbiolles et al., “Intracellular recording of cardiomyocyte action potentials with nanopatterned volcano-shaped microelectrode arrays”, Nanobiotech-Montreux, Montreux (Switzerland), 2019.
- ◆ B.X.E. Desbiolles et al., “Intracellular recording of cardiomyocyte action potentials with nanopatterned volcano-shaped microelectrode arrays”, MicroTAS, Basel (Switzerland), 2019.
- ◆ B.X.E. Desbiolles et al., “Intracellular recording of cardiomyocyte action potentials with nanopatterned volcano-shaped microelectrode arrays”, Troppo Breve symposium, Vlieland (Netherlands), 2019.
- ◆ B.X.E. Desbiolles et al., “Innovation probes for reliable scanning probe microscopy in liquids”, 5th Thermal Probe workshop, Zurich (Switzerland), 2018. *Invited speaker*
- ◆ B.X.E. Desbiolles et al., “Nanoscale patterning of 3D microelectrode arrays for long-term in-cell recording”, Troppo Breve symposium, Riederalp (Switzerland), 2018.
- ◆ B.X.E. Desbiolles and P. Renaud, “Getting inside human cells”, Heidelberg Instruments microfabrication workshop, Suzhou (China), 2016. *Invited speaker*

Posters:

- ◆ B.X.E. Desbiolles, A. Bertsch and P. Renaud, “A simple method for 3D multi-material nanostructure manufacturing”, MicroTAS, Basel (Switzerland), 2019.
- ◆ B.X.E. Desbiolles and P. Renaud, “Getting inside human cells”, Healthcare Diagnostics in 2025, Fiesch (Switzerland), 2016. *Best poster award*
- ◆ F. Yesilkoy et al., “Highly efficient trapping of single cells in large microfluidic arrays”, NanoBioTech Montreux, Montreux (Switzerland), 2014.

TEACHING

Master student supervision (07.2016 - 02.2019):

8 students (*1 Omega award for outstanding master thesis*)

Teaching assistant:

EPFL Bachelor: *Structural mechanics*, Prof. G. Villanueva, (09.2016 - 02.2019)
EPFL Master: *Advanced MEMS practicals*, Prof. P. Renaud, (02.2016 - 06.2019)

